BROAD-SPECTRUM CHEMOKINE-BINDING PEPTIDES FROM CLASS A EVASINS

Serena Vales

DPhil in Medical Sciences

University of Oxford

Linacre College

2024

Thesis presented for the degree of Doctor of Philosophy

DECLARATION

I declare that this thesis is my own work, except for the following figures:

Figure 3.2.2: Class A evasin phage display screen – Data contributed alongside Ms Katrin Hafner.

Figure 3.2.4: Top 30 peptides identified with broad-spectrum binding – Analysed by Prof. Shoumo Bhattacharya using R.

Figure 3.2.5.1: Neighbour-joining tree of peptides with identities indicated at the tree-tops – Analysed by Prof. Shoumo Bhattacharya using R.

Figure 3.2.5.2: Sequence alignment of wild-type peptides from EVA4 and EV672 – Analysed by Prof. Shoumo Bhattacharya using R.

Figure 3.2.5.3: Box-and-whisker plot showing the effect of Cys to Ala or Cys to Ser (MUT) mutations compared to wild-type (WT) for a subset of the top 30 peptides – Analysed by Prof. Shoumo Bhattacharya using R.

Figure 4.2.1.2: Preliminary chemotaxis screening of selected peptides from the top 30 list for inhibition of chemokine-induced migration – Buffy coat data contributed alongside Dr Philomena Mburu and Dr Gintare Smagurauskaite.

Figure 4.2.2.1: Bar chart with SD error bars showing the effect of the peptide HD2 on cell migration induced by CCL7, CCL8, CXCL6, CXCL10 and CXCL11– Panel F by Dr. Gintare Smagurauskaite, G by Ms Megan Payne, and H by Ms Jhanna Kryukova.

Figure 4.2.2.2: Potency of HD2 and EVA4 on chemotaxis response – Panel D by Dr. Gintare Smagurauskaite, E by Ms Megan Payne.

Figure 4.2.3.1: Bar chart with SD error bars showing the effect of alanine mutations in HD2 alanine mutant peptides on cell migration induced by CCL5, CCL7, CCL8, CXCL6 and CXCL10 – Panel D data by Dr. Gintare Smagurauskaite.

Figure 4.2.3.2: Effect of HD2 mutations on chemotaxis – Panel C data by Ms Jhanna Kryukova and analysed by Prof. Shoumo Bhattacharya using R.

Figure 5.2.2: Tile plots showing HD845 mutation effects on phage binding – Analysed by Prof. Shoumo Bhattacharya using R.

Figure 6.2.1.1: Box-whisker plots showing chemokines in atherosclerotic plaque – Analysed by Prof. Shoumo Bhattacharya using R.

Appendix 5: Propidium Iodide (PI)/Live dead staining of the HD2, HD845, HD845 mutants and SCRs on ATC – Data obtained by Ms Megan Payne

I confirm that the thesis gives appropriate credit where it references the work of others.

ABSTRACT

The chemokine network comprises 46 secreted chemokines that signal through 18 GPCRs, resulting in leukocyte recruitment in inflammation. Despite being a validated therapeutic target, chemokine network redundancy thwarts pharmacological intervention. Class A and Class B tick salivary proteins (evasins) bind CC and CXC-class chemokines, respectively, overcoming redundancy and allowing prolonged blood feeding. Evasins are unsuitable for therapeutic use due to potential immunogenicity and chemokine-class specificity requiring both evasin classes to be used. Peptides previously isolated from the chemokine-binding region of class A evasins inhibit a limited number of CC-class chemokines but lack the breadth of binding needed to overcome redundancy. This thesis tests the hypothesises that phage display can identify and improve peptides from class A evasins with broad chemokine binding and inhibitory activity. By screening a phage-display library from 21 class A evasins, peptides that surprisingly bind both CC and CXC chemokine classes were identified. An exemplar peptide, HD2, from evasin EVA4, inhibited both CC and CXC-class chemokines. Alanine-scanning mutagenesis of HD2 identified critical residues important for inhibitory activity, which correlated with binding activity in phage display. HD845 is a peptide derived from the evasin EV672. HD845 binds and inhibits both CC and CXC-chemokines in phage display and in chemotaxis assays. Saturation mutagenesis of HD845 identified several single mutations that show enhanced chemokine binding and inhibitory activity. Lastly, HD2 served as a template to identify improved mutant peptides capable of inhibiting an atherosclerosis-relevant chemokine pool. These results support the hypothesis that peptides with broad-spectrum chemokine-binding activity can be identified, and their binding affinity and potency improved using phage display.

TABLE OF CONTENTS

DECLARATION 2

ABSTRACT 3

TABLE OF CONTENTS 4

LIST OF FIGURES 7

LIST OF TABLES 9

ACKNOWLEDGEMENTS 10

PUBLICATIONS 11

LIST OF ABBREVIATIONS 12

1 INTRODUCTION 16

1.1 INFLAMMATION 16
1.1.1 Key Immune Cells Involved in Inflammation 17
1.1.2 Immune Cell Recruitment and Rolling Action 20
1.2 CHEMOKINES 23
1.2.1 Chemokine Structure and Classification 24
1.2.2 Classification of Chemokines 25
1.2.3 CC and CXC Class Chemokines 26
1.2.4 XC Chemokines 29
1.2.5 CX3C Class Chemokine 29
1.2.6 Chemokine Receptors and Signalling 30
1.2.7 Chemokine and Chemokine Receptor Binding 31
1.2.8 Chemokine Dimerisation 31
1.2.9 GAG Binding 32
1.2.10 Atypical Receptors 32
1.2.11 Chemokine Function 33
1.3 INFLAMMATORY DISEASE LINKED TO CHEMOKINES 34
1.3.1 Atherosclerosis 34
1.3.2 The Chemokine Role in Atherosclerosis Regression 38
1.4 THE CHEMOKINE NETWORK AND REDUNDANCY 39
1.5 TREATMENTS TARGETING CHEMOKINES 41
1.5.1 Limitations of Immune Therapy Treatments Targeting CVD 41
1.6 EVASINS: TICK-DERIVED CHEMOKINE BINDING PROTEINS 43
1.6.1 Chemokine and Evasin Binding 46
1.6.2 Evasins as Potential Therapeutics 47
1.6.3 Limitations of Evasins and Peptides as an Alternative Therapeutic Approach 47
1.6.4 Evasin Derived Peptides 48
1.7 AIMS OF THIS WORK: 49

2 MATERIALS AND METHODS 50

2.1 MATERIALS 50

2.1.1 Media and Buffers (Phage Display) ... 50
2.1.1.1 Primers (Phage Display) ... 52
2.1.2 Synthetic Peptides ... 52
2.1.2.1 Synthetic Peptides Sequences ... 53
2.1.3 Chemokines ... 55
2.1.3.1 Biotinylated Chemokines ... 55
2.1.3.2 Non-Biotinylated Chemokines ... 56
2.1.4 Media (Chemotaxis) ... 59
2.2 METHODS ... 61
2.2.1 Phage Display ... 61
2.2.1.1 EVAA Phage Display Design ... 61
2.2.1.2 EVAA Phage Display Library Construction ... 61
2.2.1.3 HD845 Saturation Mutagenesis Phage Display Library (Design) ... 62
2.2.1.4 Library Next-Generation Sequencing (NGS) and Analysis ... 63
2.2.1.5 Phage Display Library Screening ... 64
2.2.1.6 Screening Next-generation Sequencing (NGS) and Analysis ... 65
2.2.2 Polymerase Chain Reaction (PCR) ... 66
2.2.2.1 Phage Display Selection PCR ... 66
2.2.2.2 Phage Display Selection PCR steps ... 67
2.2.2.3 NGS Construction and Screening PCR ... 68
2.2.2.4 NGS Construction and Screening PCR Steps ... 69
2.2.3 Gel Electrophoresis ... 69
2.2.4 Cell Lines ... 70
2.2.4.1 THP1 ... 70
2.2.4.2 Jurkats ... 70
2.2.4.3 Human Blood Samples ... 71
2.2.4.4 Activated T cells (ATC) ... 71
2.2.4.5 Buffy Coat ... 72
2.2.4.6 Mycoplasma Tests ... 73
2.2.4.7 PI (Live/Dead) Staining ... 73
2.2.5 Chemotaxis assays (Cell Migration Assays) ... 74
2.2.5.1 Dose-Response Assays ... 74
2.2.5.2 Single Concentration Inhibition Assay ... 75
2.2.5.3 Inhibition Dose-Response Assays (IC50s) ... 76
2.2.6 Atherosclerosis (Athero) Pool Construction ... 77

3 CHAPTER 3: DISCOVERY OF PEPTIDES FROM CLASS A EVASINS ... 79

3.1 INTRODUCTION ... 79
3.2 RESULTS ... 82
3.2.1 Phage Display Library Construction and Validation ... 82
3.2.2 Phage Display Library Screening and Results ... 84
3.2.3..... Phage Display Identifies Peptides That Coincide with Established Chemokine Binding Sites ... 86
3.2.4.....Broad-Spectrum Chemokine-Binding Peptides Identified from EVAA Library Using Phage Display ... 87
3.2.5.....Sequence Alignment Uncovers a Conserved Motif Containing an Unpaired Cysteine Residue ... 89
3.3 DISCUSSION ... 92

4 CHAPTER 4: CHARACTERISATION OF THE CLASS A DERIVED PEPTIDE: HD2 ... 95

4.1 INTRODUCTION ... 95
4.2 RESULTS ... 97
4.2.1 Selection and Functional Testing of Peptides for Chemokine Inhibition ... 97
4.2.2 HD2 Peptide Possesses CC and CXC Inhibitory Activity ... 103

4.2.3.... Alanine-Scanning Mutagenesis - Correlation Between Binding Affinity and Inhibitory Activity 106
4.3 DISCUSSION 112

5 CHAPTER 5: CHARACTERISATION AND IMPROVEMENT OF HD845, A CLASS A EVASIN DERIVED PEPTIDE 115

5.1 INTRODUCTION 115
5.2 RESULTS 117
5.2.1 HD845X Library Construction and Screening 117
5.2.2 Identification and Selection of Improved HD845 Mutants 119
5.2.3 Improved Chemokine Inhibition with HD845 Mutants 122
5.2.4 Preliminary Indication of Improved Potency with HD845 Mutants 123
5.3 DISCUSSION 127

6 CHAPTER 6: CHARACTERISATION OF HD845 AND HD2 MUTANTS AGAINST A COMPLEX ATHEROSCLEROSIS CHEMOKINE POOL 130

6.1 INTRODUCTION 130
6.2 RESULTS 132
6.2.1 Development of the Atherosclerosis Chemokine Pool for Therapeutic Evaluation 132
6.2.2 Dose-Response Analysis of the Atherosclerosis Chemokine Pool 134
6.2.3..... Chemotaxis Assays Testing the Mutant Peptides using the Atherosclerosis Chemokine Pool 135
6.3 DISCUSSION 141

7 GENERAL CONCLUSION 143

7.1 SUMMARY OF FINDINGS 144
7.2 FUTURE WORK 147
7.2.1.1 HD2 Inhibition Assays 147
7.2.1.2 Phage Display 147
7.2.1.3 HD845 Mutagenesis 148
7.2.1.4 In Vivo Models 148
7.2.1.5 Improving Peptide Design for Therapeutics 149
7.2.1.6 Atherosclerosis and the Use of Anti-Inflammatory Peptides 152
7.2.1.7 Wider Academic Field: 153

8 REFERENCES 156

9 APPENDICES 170

10 PUBLICATION 178

LIST OF FIGURES

Figure 1.1.2: Schematic diagram of the multi-step process of transendothelial migration (TEM)..... 20
Figure 1.2.1: Chemokine structure of CCL8..... 24
Figure 1.2.2: Schematic image showing chemokine classification based on the arrangement of cysteines at the N-terminus..... 25
Figure 1.2.6: Structure of chemokine receptor CXCR4 30
Figure 1.3.1.2: A schematic of atherosclerosis pathogenesis..... 34
Figure 1.4: The robustness of the chemokine network..... 39
Figure 1.6: The evasin-chemokine network showing the effectiveness of evasins in disrupting the redundant chemokine network..... 45
Figure 2.2.5.1: Schematic image of a well in a dose-response assay..... 74
Figure 2.2.5.2: Schematic image of a well in an inhibition assay..... 75
Figure 3.2.1: Identifying chemokine-binding peptides using phage display..... 82
Figure 3.2.2: Class A evasin phage display screen..... 84
Figure 3.2.4: Top 30 peptides identified with broad spectrum binding..... 87
Figure 3.2.5.1: Neighbour-joining tree of peptides with identities indicated at the tree-tops..... 89
Figure 3.2.5.2: A sequence alignment of the wild-type peptides derived from EVA4 and EV672.....90
Figure 3.2.5.3: Box-and-whisker plot showing the effect of Cys mutation to Ala or Ser (MUT) compared to wild-type (WT) for a subset of 30 peptides..... 90
Figure 4.2.1.1: Preliminary screening of peptides..... 98
Figure 4.2.1.2: Preliminary screening of selected peptides from top 30 list for inhibition of chemokine-induced migration..... 100
Figure 4.2.2: Bar chart with SD error bars showing the effect of the peptide HD2 on cell migration induced by CCL7, CCL8, CXCL6, CXCL10 and CXCL11..... 103
Figure 4.2.2.2: The potency of HD2 and EVA4 on chemotaxis response..... 105
Figure 4.2.3.1: Bar chart with SD error bars showing the effect of alanine mutations in HD2 alanine mutant peptides on cell migration induced by CCL5, CCL7, CCL8, CXCL6 and CXCL10..... 107
Figure 4.2.3.2: HD2 mutations effect on chemotaxis..... 109
Figure 5.2.1: Phage display of HD845 NNK library to screen all single point mutations against chemokines..... 118
Figure 5.2.2: Tile plots depicting the effect of HD845 mutations on phage binding..... 120
Figure 5.2.3: The effect of HD845 mutants on chemotaxis..... 122
Figure 5.2.4: Preliminary potency assessment of HD845 mutants..... 125
Figure 6.2.1.1: Box-whisker plots showing chemokines in atherosclerotic plaque..... 132
Figure 6.2.2: Dose-response curves of the atherosclerosis chemokine pool in chemotaxis assays..... 134
Figure 6.2.3.1: The effect of HD2 mutant peptides against an atherosclerosis chemokine pool..... 136
Figure 6.2.3.2: The effect of HD845 mutant peptides against an atherosclerosis chemokine pool..... 139
Figure 7.2.1.4: Cyclisation on BK1.2 peptide..... 150

Appendix 1: Representative dose response curves..... 170
Appendix 2: Biological IC50 inhibitory dose-response curves for EVA4, HD2, and HD2 SCR..... 171
Appendix 3: Preliminary potency assessments of HD845 mutants..... 173
Appendix 4: Dose-response curves of the atherosclerosis chemokine pool in chemotaxis assays..... 175
Appendix 5: Propidium iodide (PI)/Live dead staining of the HD2, HD845, HD845 mutants and SCRs on ATC..... 176
Appendix 6: Propidium iodide (PI)/Live dead staining of the HD2, HD845, HD845 mutants and SCRs on THP1 cells..... 177

LIST OF TABLES

Table 1.1.1: Showing the key immune cells in inflammation and their function..... 17
Table 1.2.3.1: CC class chemokines, their receptors and their expression..... 26
Table 1.2.3.2: CXC class chemokines, their receptors and their expression..... 28
Table 1.3.1.2: Chemokines involved in atherosclerosis, and their influences.....36
Table 2.1.1: Media and buffers used in phage display, with components and supplier names and codes listed..... 50
Table 2.1.1.1: Primers used in phage display, with the primer sequence and supplier listed..... 52
Table 2.1.2.1: Peptides identified and tested used in this study, with their respective sequence, derived evasin or peptide (if mutant) and supplier name..... 53
Table 2.1.3.1: Biotinylated chemokines used in phage display with supplier and code listed..... 55
Table 2.1.3.2: Chemokines used in chemotaxis assays with supplier and code listed..... 56
Table 2.1.4: Media and buffers used in chemotaxis assays, with components and supplier names and codes listed..... 59
Table 2.2.2.1: Components and the amounts needed to construct the phage display selection PCR..... 66
Table 2.2.2.2: Selection PCR steps..... 67
Table 2.2.2.3: Components and the amounts needed to construct the NGS PCR for phage display library construction (which used the oligo_fwd and oligo_rev primers) and phage display screening (which used the GENEWIZ4_fwd and GENEWIZ4_rev primers) 68
Table 2.2.2.4: NGS PCR steps..... 69
Table 2.2.6: The athero pool chemokine table indicates the chemokines ratio determined by the mean relative expression of chemokines in the plaque RNA-seq data set (GSE198600) 77
Table 6.2.1.2: The athero pool chemokine table indicating the chemokine concentrations based on the plaque RNA-seq data set (GSE198600), used in the athero pool..... 133

ACKNOWLEDGEMENTS

I wish to express my deepest appreciation to Professor Shoumo Bhattacharya, Mr Graham Davies and Professor Charles Redwood for their mentorship and guidance. I am also truly grateful to all the members of the Bhattacharya lab, both past and present. Working alongside such talented individuals has been a privilege, and I have learnt so much from each of you; my time in the lab has been incredibly rewarding.

A sincere thank you to the postdoctoral fellows, Gintare and Soumya. It has been an absolute honour to work with you both. Your patience, generosity, and willingness to share your time and knowledge have been invaluable. I have grown not only as a researcher but also personally, and for that, I am forever grateful. To Megan and Charlie, meeting you has truly brought so much light and joy into my time at Oxford. I consider myself extremely fortunate to have had you by my side during this journey. You have made the experience all the more enjoyable, and I will cherish the memories, laughter and cake we've shared!

I would also like to extend my heartfelt thanks to Dr Philomena Mburu and Dr Kalimuthu Karuppanan for their immense support during my first year, especially during the difficulties of the COVID pandemic. Your encouragement and guidance helped me navigate through an incredibly difficult time, and I cannot thank you enough for your kindness.

To my family and friends, both back home and in Oxford (Cheryl, Jasmine and Kim Shen), your support and encouragement have always been a constant source of happiness and strength.

A special mention to my brother Jaden, my constant cheerleader—thank you for always believing in me, and know that I will always have your back too. Finally, to my parents: I have been so blessed to have such supportive and loving parents. The sacrifices you both made for me and Jaden are a testament to what we have achieved and are yet to achieve. I dedicate this thesis to the three of you.

PUBLICATIONS

Vales, S., Kryukova, J., Chandra, S., Smagurauskaite, G., Payne, M., Clark, C. J., Hafner, K., Mburu, P., Denisov, S., Davies, G., Outeiral, C., Deane, C.M., Morris G.M., and Bhattacharya, S. (2023) Discovery and pharmacophoric characterization of chemokine network inhibitors using phage-display, saturation mutagenesis and computational modelling Nature Communications 14, 5763-5763 10.1038/s41467-023-41488-z.

Kryukova, J., **Vales, S**., Payne, M., Smagurauskaite, G., Chandra, S., Davies, G. and Bhattacharya, S. Development of chemokine network inhibitors using combinatorial saturation mutagenesis. (Submitted for publication- Communications Biology).

Kelm, N., Kespohl, M., Smagurauskaite, G., **Vales, S.,** Karuppanan, K., Mburu, P., Thiele, A., Pinkert, S., Bukur, T., Mülleder, M., Berndt, N., Klingel K., Gaida, M.M., Bhattacharya, S and Beling, A. Assessing Customized Multivalent Chemokine-Binding Peptide Treatment in a Murine Model of Coxsackievirus B3 Myocarditis. (Submitted for publication- Basic Research in Cardiology).

LIST OF ABBREVIATIONS

ACKR	Atypical chemokine receptor
APC	Antigen presenting cell
ATC	Activated T cell
ATLO	Arterial tertiary lymphoid tissue
BLI	Bio-layer interferometry
BSA	Bovine serum albumin
CCR	CC chemokine Receptor
CMB	Cell migration buffer
CTL	Cytotoxic T lymphocyte
CVD	Cardiovascular disease
CXCR	CXC chemokine receptor
DAMPs	Damage-associated molecular patterns
DARC	Duffy-antigen chemokine receptor
DC	Dendritic cell
DMSO	Dimethyl sulfoxide
EC50	50% effective concentration
EC80	80% effective concentration
ECACC	European Collection of Authenticated Cell Cultures
ECM	Extracellular matrix

ECs	Endothelial cells
EDTA	Ethylenediaminetetraacetic acid
EVA4	Evasin-4
EVA1	Evasin-1
EVA3	Evasin-3
EVA672	Evasin 672
EVAA	Class A evasin
EVAB	Class B evasin
FCS	Fetal Calf Serum
FSC	Forward scatter
GAGs	Glycosaminoglycans
GD	Graham Davies
GEO	Gene Expression Omnibus
GPCR	G-coupled protein receptor
GS	Gintare Smagurauskaite
HBSS	Hanks' Balanced Salt Solution
HDX-MS	Hydrogen-deuterium exchange mass spectrometry
IC50	50% inhibitory concentration
ICAM-1	Intercellular adhesion molecule-1
ICAM-2	Intercellular adhesion molecule-2
JAM-A	Junctional adhesion molecule A

JAM-C	Junctional adhesion molecule C
JK	Jhanna Kryukova
KH	Katrin Hafner
LDL	Low-density lipoprotein
MAPK	Mitogen-activated protein kinase
MDS	Molecular dynamic simulations
MMPs	Matrix metalloproteinases
MP	Megan Payne
MUT	Mutant
NETs	Neutrophil extracellular traps
NGS	Next-Generation Sequencing
NK	Natural killer cells
NMR	Nuclear magnetic resonance
OxLDLs	Oxidised LDLs
PAMPs	Pathogen-associated molecular patterns
PBS	Phosphate buffer solution
PCR	Polymerase chain reaction
PDB	Protein database
PDGF	Platelet-derived growth factor
PECAM-1	Platelet/endothelial cell adhesion molecule 1
PI	Propidium iodide

PRRs	Pattern-recognition receptors
PSGL-1	P-selectin glycoprotein ligand 1
RBC	Red blood cells
RNA	Ribonucleic acid
RNA-seq	RNA sequencing
ROI	Regions of interest
RPM	Rounds per minute
SB	Shoumo Bhattacharya
SCR	Scrambled peptide
SMC	Smooth muscle cell
SPR	Surface plasmon resonance
SSC	Side scatter
SV	Serena Vales
TEM	Transendothelial migration
TLR	Toll-like receptor
TPM	Transcripts per million
VCAM-1	Vascular cell adhesion molecule-1
VLA-4	Very late antigen 4
VSMC	Vascular smooth muscle cells
WT	Wild type

1 INTRODUCTION

1.1 INFLAMMATION

Inflammation is an important biological response that protects the body from injury and initiates tissue repair. Inflammation can be categorised into acute and chronic inflammation based on the duration of the response. Acute inflammation is a fast, short-term protective response that typically lasts a few days, leading to the resolution or healing of the affected tissue. It is characterised by the five cardinal signs: redness (rubor), heat (calor), swelling (tumor), and pain (dolor). These were first described in the 1st century AD by the Roman medical historian Aulus Cornelius Celsus[1], with the fifth, loss of function (functio laesa) later added in the 19th century by German pathologist Rudolf Virchow[2].

The acute inflammatory response begins with the recognition of pathogen-associated molecular patterns (PAMPs) by tissue macrophages, leading to the release of proinflammatory cytokines, chemokines, and other inflammatory mediators[3]. These mediators trigger vasodilation, increasing blood flow to the area and causing redness and heat. Enhanced vascular permeability also occurs, which allows plasma containing antibodies to enter the surrounding tissue, leading to swelling[4]. Additionally, cytokines and chemokines are released at the site of injury, recruiting neutrophils, followed by monocytes and lymphocytes, to clear the pathogens, resulting in pain and loss of function[5]. Once the harmful agents are removed, the inflammatory cells undergo apoptosis, and macrophages remove apoptotic cells to prevent further tissue damage[6], initiating tissue repair and homeostasis of the inflammatory response[7].

However, when inflammation is prolonged and excessive, it can turn chronic, contributing to the development of various pathological conditions, including autoimmune disorders[8], cardiovascular diseases[9], diabetes[10], neurodegenerative diseases[11], and cancer[12].

1.1.1 Key Immune Cells Involved in Inflammation

Inflammation involves various immune cells, the movement of which needs to be carefully orchestrated to the site of injury or infection. **Table 1.1.1** shows a general overview of key immune cells involved in inflammation.

Leukocyte	**Schematic Image**	**Role**
Monocyte		- Circulates the blood stream, recruited to sites of inflammation and differentiates into macrophages or dendritic cells at the site of infection[13] - Mediate host antimicrobial defence[14] - Produced in bone marrow[13]
Macrophage	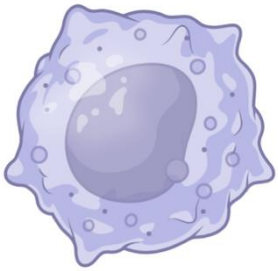	- Derived from monocytes, residing in tissues[15] - M1 macrophages have pro-inflammatory effects whereas, M2 macrophages are immune suppressive[15] - Engulf and digest pathogens (phagocytosis) as well as cell debris to maintain homeostasis[16] - Present antigens to T cells and secrete pro-inflammatory cytokines[17]
Neutrophil		- A type of granulocyte, first responder to infection or injury and produced in the bone marrow[18] - Largest leukocyte population in blood[19] - Mediate host antimicrobial defence[19] - Engulfs and kills pathogens (phagocytosis)[20] - Releases enzymes, cytokines, and reactive oxygen species to fight infection; secretion

		of proteases and neutrophil extracellular traps (NETs) formation[20]
T-cell		- Categorised broadly into CD4+, CD8+, and natural killer T (NKT) cells[21] - CD4+ T cells are activated by presentation of antigen in APCs, costimulatory stimulation, and cytokine signalling[21] - CD4+ T cells can be differentiated further into subsets such as Th1, Th2, T_{reg}, follicular helper T (Tfh), Th17, Th9, Th22, and $CD4^+$ cytotoxic T lymphocytes (CTLs) which help maintain immune regulation and peripheral tolerance[21] - CD8+ T cells recognise and kill infected cells by releasing cytotoxins[21] - CD8+ T cells can eliminate malignant cells in cancer[21] - Memory CD8+ T cells provide long-term immunity by rapidly recognising past antigens[21]
Natural killer (NK) cell	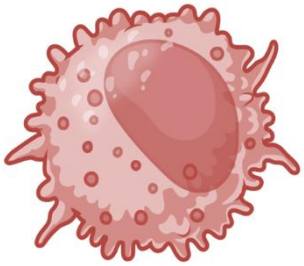	- Detect abnormal cells and kill virus-infected or tumour cells without prior sensitisation[22] - Once activated becomes cytotoxic and release lytic granules, interferons, cytokines[23], and chemokines (CCL3, CCL4, CCL5, CXCL8)[22] - Also induce death signals such as TNF-related apoptosis-inducing ligand (TRIAL) or Fas[22,23] - Maintain immune homeostasis by eliminating overactive immune cells[22]

B-cell		- Developed in bone marrow - Producing antibodies bind to many antigens[24] - Differentiate into memory B cells, offering long-lasting immunity[24]
Dendritic (DC) cell	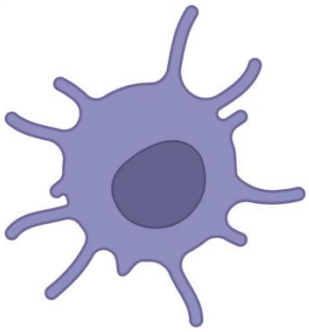	- Antigen-presenting cells - Capture microbial antigens and present them to T cells[25] - Secrete cytokines and chemokines for T-cell differentiation[25]

Table 1.1.1: Showing the key immune cells in inflammation and their function. Leukocyte images from BioRender.

1.1.2 Immune Cell Recruitment and Rolling Action

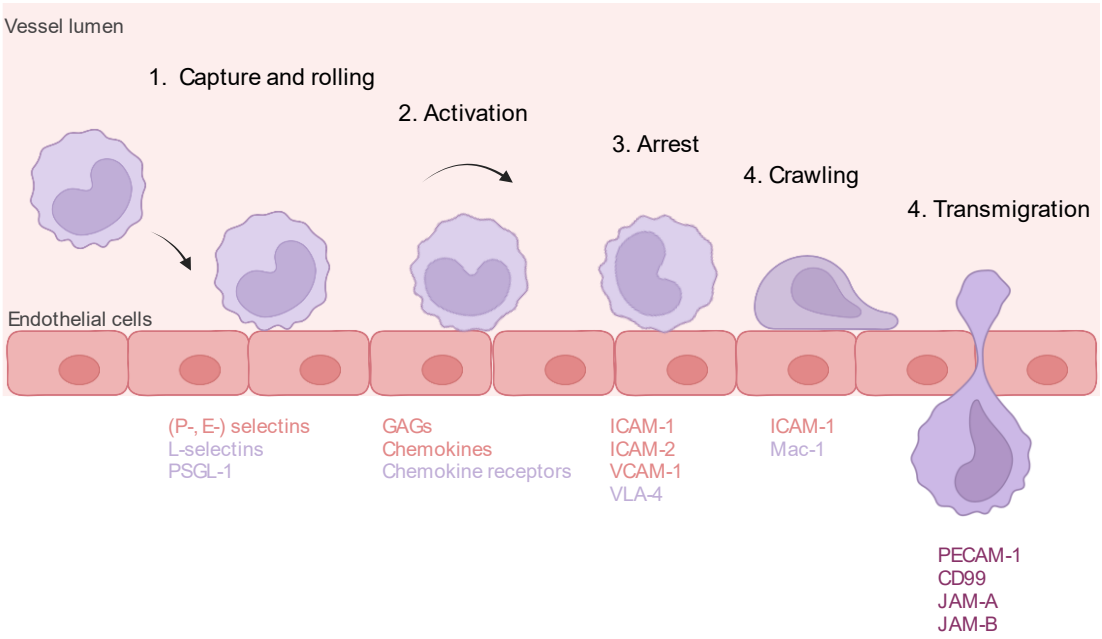

Figure 1.1.2: Schematic diagram of the multi-step transendothelial migration (TEM) process. 1. Capture and Rolling: Leukocytes first slow down and roll along the vascular endothelium, mediated by selectins on endothelial cells binding to their selectin ligands on leukocytes. 2. Activation: Chemokines presented on the endothelial surface via GAGs activate leukocyte integrins through signalling mechanisms. 3. Arrest: Activated integrins on leukocytes bind strongly to endothelial cell adhesion molecules (e.g., ICAM-1, VCAM-1), causing arrest of leukocytes to the endothelium. 4. Crawling: Leukocytes crawl along the endothelial surface to find the nearest junction between endothelial cells. This is mediated by integrins and actin cytoskeletal rearrangements in leukocytes. 5. Transmigration: Leukocytes pass through the endothelial barrier between endothelial cells into the underlying tissue. Adhesion molecules and their ligands are colour-coded according to their presentation location: Red indicates expression on endothelial cells, purple indicates expression on leukocytes, while magenta indicates expression on both endothelial cells and leukocytes. Adapted from[26]. Created using BioRender.

Transendothelial migration (TEM) is the process by which leukocytes leave the bloodstream and pass through the endothelial barrier of blood vessels to reach sites of inflammation (**Figure 1.1.2**). TEM also acts as a regulatory checkpoint, and misregulation can lead to chronic inflammation. This multi-step process involves leukocyte capture, rolling, activation, arrest, and transmigration, allowing efficient movement of leukocytes to sites of infection or injury, resulting in an immune response[27].

Capture and rolling: Circulating leukocytes travel in the centre of the bloodstream due to laminar flow. However, at sites of tissue damage or inflammation, the blood flow slows, increasing the likelihood of leukocytes attaching to adhesion molecules expressed on the endothelium, such as P-selectins and E-selectins. These selectins interact with P-selectin glycoprotein ligand 1 (PSGL-1) on the leukocyte surface. L-selectins, present on the surface of leukocytes, are involved in leukocyte-leukocyte interactions, allowing for secondary leukocyte capture[28,29]. E-selectins are upregulated on the endothelium after a few hours of exposure to pro-inflammatory cytokines[28]. Interactions between selectins and ligands are characterised by fast 'on and off' rates, allowing the leukocytes to be captured from the bloodstream and roll across the endothelium surface[30].

Activation: As leukocytes roll along the endothelium, they encounter chemokines immobilised on glycosaminoglycans (GAGs) present on the endothelial surface. These chemokines bind to corresponding chemokine receptors on the leukocyte, triggering integrin activation, also known as 'inside-out' integrin activation. This leads to conformational changes in integrins, enhancing their affinity for adhesion molecules on the endothelial surface, preparing leukocytes for firm adhesion[27].

Arrest: Once the integrins are activated, they adhere very tightly to adhesion molecules on the endothelium. This strong adhesion is mediated by interactions between integrins on leukocytes and intracellular adhesion molecules (ICAM-1 and ICAM-2) expressed on endothelial cells. Monocytes and lymphocytes present the integrin very late antigen 4 (VLA-

4), which binds to VCAM-1 on the endothelium. This firm adhesion stops the rolling leukocyte, preparing it for migration across the endothelium[27].

Crawling: Before transmigration, leukocytes crawl to locate the nearest junction between endothelial cells. This crawling is mediated by integrins on the leukocyte surface, such as Mac-1, which bind to ICAM-1 on endothelial cells. While leukocytes primarily migrate between endothelial cells (paracellular migration), they can also move through endothelial cell bodies (transcellular migration), aided by actin cytoskeletal rearrangements[26,27]. However, transcellular migration is less common and is not detailed here.

Transmigration: Transmigration occurs as leukocytes pass through the endothelial barrier. Unlike the prior steps, which involve heterophilic adhesion (binding between different molecules), transmigration involves homophilic adhesion, where molecules on leukocytes bind to the same molecules on endothelial cells. Platelet/endothelial cell adhesion molecule 1 (PECAM-1), CD99, and junctional adhesion molecules (JAM-A and JAM-C) are involved in this process. These adhesion molecules are expressed across the leukocyte surface and at endothelial cell junctions, guiding leukocytes across the endothelium and into the underlying tissue[26,27].

1.2 CHEMOKINES

Chemokines, or chemotactic cytokines, are a family of structurally related secreted proteins (8–12 kDa). They play a major role in the inflammatory response, particularly in orchestrating leukocyte migration (chemotaxis) to the site of injury or infection[31]. Chemotaxis is typically achieved by producing chemokine gradients to control leukocyte migration directionally so that leukocytes migrate from an area of low chemokine concentration to high[32].

They are also involved in various physiological functions, such as leukocyte degranulation[33], hematopoiesis[34], and angiogenesis[35]. Chemokine production is triggered by signalling pathways downstream of pattern-recognition receptors (PRRs), including Toll-like receptors (TLRs), expressed on the surface of leukocytes and endothelial cells. Upon recognition of pathogen-associated molecular patterns (PAMPs) or damage-associated molecular patterns (DAMPs), these receptors activate pathways that lead to chemokine synthesis[36].

1.2.1 Chemokine Structure and Classification

Chemokines are highly conserved proteins that generally share a common structure and folding pattern. This structure includes a flexible N-terminus stabilised by disulphide bonds between cysteine residues. Following the N-terminus is an N-terminal loop, which leads into a three-stranded antiparallel β-sheet (β1, β2 and β3), onto which a C-terminal α-helix is folded. The β-sheets and α-helix are connected by loops, referred to as the 30s, 40s, and 50s loops, named according to the residue numbers of the protein regions they link[37,38] (chemokine structure example shown in **Figure 1.2.1**).

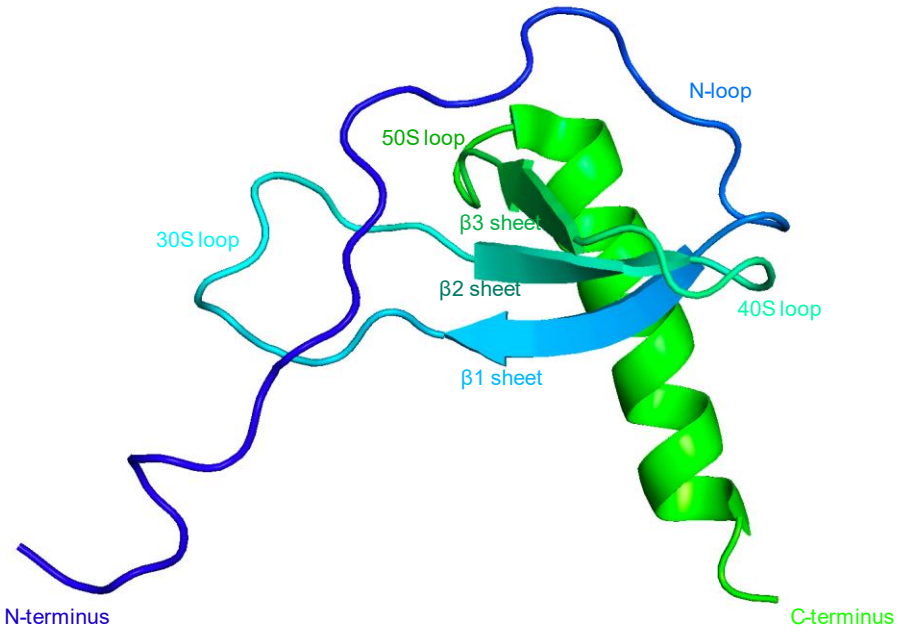

Figure 1.2.1: Chemokine structure of CCL8 (PDB 1ESR). Created using PyMol.

1.2.2 Classification of Chemokines

Chemokines are categorised based on the positioning of the conserved cysteine residues at the N-terminus: CC, CXC, XC and CX3C. In CC chemokines, the cystines are adjacent. In CXC chemokines, an amino acid is in between, while XC chemokines do not have the first or third cystine, and CX3C only possesses one chemokine, CX3CL1, also known as fractalkine, and has three amino acids in between the cysteines[39].

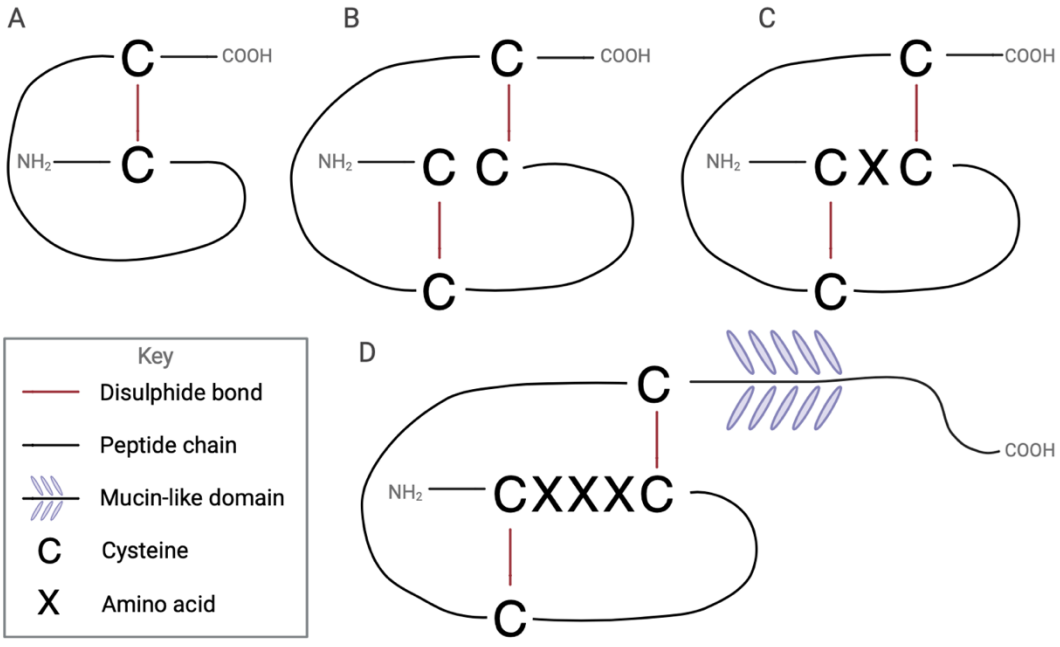

Figure 1.2.2: Schematic image showing chemokine classification based on the arrangement of cysteines at the N-terminus. A) XC class chemokines. B) CC class chemokine. C) CXC class chemokine D) CX3C class chemokine. Created using BioRender.

1.2.3 CC and CXC Class Chemokines

CC class chemokines are the largest class of chemokines and, as aforementioned, are based on the disulphide bond between the two cysteines near the N-terminus.[40] CC chemokines interact with CCR chemokine receptors and are involved and responsible for inducing various immune cells (see **Table 1.2.3.1**).

Chemokine Receptor (CCR)	CC Chemokines	Expression
CCR1	CCL2, CCL3, CCL3LI, CCL4, CCL5, CCL7, CCL8, CCL13, CCL14, CCL15, CCL16, CCL23	Neutrophil, eosinophil, basophil, monocyte/macrophage, immature DC, memory T cell, B cell, NK cell, mast cell
CCR2	CCL2, CCL7, CCL8, CCL13, CCL16	Neutrophil, eosinophil, basophil, monocyte/macrophage, immature DC, DC, B cell, memory T cell, T_{reg} cell, NK cell
CCR3	CCL5, CCL7, CCL8, CCL11, CCL13, CCL15, CCL16, CCL24, CCL26, CCL28	Neutrophil, eosinophil, basophil, T cell, T_H2 cell, mast cell, platelets, endothelial cell
CCR4	CCL17, CCL22	Eosinophil, basophil, monocyte/macrophage, DC, T_H2 cell, T_{reg} cell, NK cell, thymocyte, platelets
CCR5	CCL3, CCL3LI, CCL4, CCL5, CCL7, CCL8, CCL11, CCL13, CCL14, CCL16	Monocyte/macrophage, DC, T_H1 cell, T_{reg} cell, B cell, NK cell, thymocyte
CCR6	CCL20	Immature DC, memory T cell, T_H17 cell, T_{reg}cell, B cell

CCR7	CCL19, CCL21	DC, T_0 cell, T_H1 cell, T_H2 cell, T_{reg} cell, B cell, NK cell
CCR8	CCL1	Neutrophil, monocyte/macrophage, DC, T_H2 cell, T_{reg} cell, B cell, thymocyte
CCR9	CCL25	Memory T cell, thymocyte, epithelial cell, IgA+ plasma cell
CCR10	CCL27, CCL28	Memory T cell, B cell, fibroblast, epithelial cell

Table 1.2.3.1: CC class chemokines, their receptors and their expression. Table taken from Koelink et al[41].

CXC chemokines also induce a range of immune cells (see **Table 1.2.3.2**). CXC chemokines are further classified into two more groups, ELR+ and ELR-, depending on whether they possess the ELR (glu-leu-arg) motif present before the first cysteine. ELR+ chemokines such as CXCL1, CXCL2, CXCL3, CXCL5, CXCL6, CXCL7, CXCL8 and CXCL17 are angiogenic in nature due to their interaction with CXCR1 and CXCR2 receptors[42]. However, CXCL12, although ELR-, has been shown to induce angiogenesis via CXCR4 and CXCR7 receptors[35,43]. ELR+ chemokines are also predominately chemoattractants for neutrophils[44]. ELR- chemokines such as CXCL4, CXCL9, CXCL10, CXCL11, CXCL12, CXCL13, CXCL14 and CXCL16 lack the ELR motif and are angiostatic. They interact with the chemokine receptors CXCR3, CXCR4, CXCR5, CXCR6, and CXCR7[35,42]. ELR- chemokines mediate monocyte, basophil, eosinophil, lymphocyte, and natural killer cell migration[44].

Chemokine Receptor (CXCR)	CXC Chemokines	Expression
CXCR1	CXCL6, CXCL7, CXCL8	Neutrophil, basophil, monocyte/macrophage, immature DC, NK cell, mast cell
CXCR2	CXCL1, CXCL2, CXCL3, CXCL5, CXCL6, CXCL7, CXCL8	Neutrophil, eosinophil, monocyte/macrophage, immature DC, microvascular endothelial cell, T cell, NK cell, mast cell
CXCR3A	CXCL9, CXCL10, CXCL11	Neutrophil, eosinophil, DC, T_H1 cell, B cell, NK cell, mast cell
CXCR3B	CXCL4, CXCL9, CXCL10, CXCL11	Microvascular endothelial cell, neoplastic cell
CXCR4	CXCL12	Neutrophil, eosinophil basophil, monocyte/macrophage, DC, T_0 cell, memory T cell, T_H1 cell, T_H2 cell, T_H17 cell, T_{reg}cell, B cell, NK cell, platelets
CXCR5	CXCL13	B cell, T cell
CXCR6	CXCL16	Memory T cell, T_H1 cell, NK cell
CXCR7	CXCL11, CXCL12	Tumour cell

Table 1.2.3.2: CXC class chemokines, their receptors and their expression. Table taken from Koelink et al[41].

1.2.4 XC Chemokines

The XC chemokine class currently contains two chemokines: XCL1 and XCL2. XCL1 is an inflammatory chemokine primarily secreted by activated CD8+ T cells, which is thought to mediate interactions between antigen-presenting dendritic cells and T cells. Both XCL1 and XCL2 are also expressed by unstimulated natural killer (NK) cells, though their expression is lower in unstimulated CD8+ T cells. Functionally, XCL2 is similar to XCL1, acting as a ligand for the XCR1 receptor. While both chemokines play a role in immune responses, XCL2's role is less well-studied compared to XCL1[45].

1.2.5 CX3C Class Chemokine

CX3C class is the smallest of the chemokine classes, containing only one chemokine to date, CX3CL1, also known as fractalkine. CX3CL1 binds only to the chemokine receptor CX3CL1[46] and is synthesised as a transmembrane protein anchored to the membrane via its mucin-like domain[47]. CX3CL1 can be cleaved by metalloproteinases, creating a soluble chemotactic form[48]. Depending on its molecular form, CX3CL1 is involved in both adhesion and chemotaxis of CX3CR1-expressing leukocytes, such as monocytes, macrophages, dendritic (DC) cells, CD8+ T cells and also in certain populations of natural killer (NK) cells[47,49]. CX3CR1 is also expressed on smooth muscle cells, platelets, and activated endothelial cells[50].

1.2.6 Chemokine Receptors and Signalling

Chemokine receptors are a family of G-coupled protein receptors (GPCRs) and, upon binding to chemokines, conformationally change, triggering intracellular signalling pathways via heterotrimeric G-proteins[51]. Currently, there are 18 human chemokine receptors have been identified and classified into four subfamilies based on the chemokine groups they preferentially bind to: CC CCR, CXCR, CX3CR, and XCR[39]. The chemokine receptor is located within the phospholipid bilayer of target cells. Structurally, chemokines receptors, like other GPCRs (**Figure 1.2.6**), consist of seven transmembrane helices parallelly arranged in a barrel-like formation. The extracellular half of the receptor consists of an unstructured N-terminal region connected by three extracellular connecting loops (ECL1, ECL2 and ECL3), in which ECL2 has a β-hairpin structure. Disulphide bonds maintain formation between the N-terminus and ECL3 and between ECL1 and ECL2. The cytoplasmic half of the receptor consists of three intracellular connecting loops (ICL1, ICL2 and ICL3) and the C-terminal region[52].

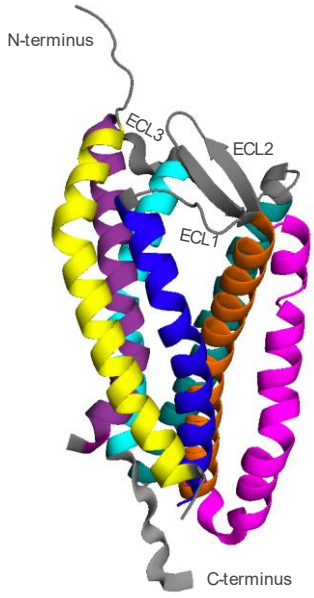

Figure 1.2.6: Structure of chemokine receptor CXCR4 (PDB 4RWS). The C-terminus has been simplified for clarity. Created using PyMol.

1.2.7 Chemokine and Chemokine Receptor Binding

A widely accepted model suggests that chemokine and chemokine receptor interactions occur through four distinct chemokine recognition sites: CRS0.5, CRS1, CRS 1.5 and CRS2. CRS0.5 is located at the distal part of the receptor's N-terminus and binds to the β1-strand of the chemokine. CRS1 is positioned in the receptor's N-terminus and engages with the N-loop and 40s loop of the chemokines. CRS1.5 is found between CRS1 and CRS2 in the N-terminus and interacts with the chemokine's conserved disulphide bond. Finally, CRS2 is located in the receptor's transmembrane pocket and engages with the chemokine's N-terminus[51]. When chemokine receptors bind to their specific chemokines, they conformationally change shape and activate intracellular effectors, such as G proteins or β-arrestins, triggering signal transduction pathways and leading to various cellular responses[52].

1.2.8 Chemokine Dimerisation

Chemokines can also bind to each other, forming homodimers, heterodimers and oligomers. Dimerisation between CC-class chemokines typically occurs between the flexible N-termini, forming a two-stranded anti-parallel β-sheet[38]. Dimerisation between CXC-class chemokines occurs through the antiparallel extension of the β-strands[38]. Molecular dynamic simulations (MDS) suggest that both CC and CXC chemokines preferentially bind within their own chemokine class, though CC-CXC heterodimers can also form, e.g. CCL5-CXCL4. CC-type heterodimers such as CCL5-CCL17 and CCL5-CCL2 have been implicated in promoting synergism, whereas CXC-type heterodimers often exhibit inhibitory effects[53].

1.2.9 GAG Binding

Chemokines, whether as monomers, homodimers, or heterodimers, interact specifically and strongly with glycosaminoglycans (GAGs) through electrostatic forces, as the negatively charged GAGs are attracted to positively charged amino acids in the chemokine[54]. This binding is crucial for anchoring chemokines to the endothelial surface, preventing their clearance by the bloodstream, maintaining chemokine gradients, prolonging chemokine half-life and ensuring efficient immune cell migration. Additionally, as previously mentioned, GAG binding supports leukocyte arrest and extravasation while maintaining chemokine gradients[55].

1.2.10 Atypical Receptors

Atypical chemokine receptors (ACKRs) are a distinct family of chemokine receptors, with four officially classified members: ACKR1 (DARC), ACKR2 (D6), ACKR3 (CXCR7), and ACKR4 (CCR11)[56]. These receptors are expressed on leukocytes, endothelial cells, and other tissues[56]. ACKRs differ from the classical chemokine GPCR receptors in that they lack, or have a variance of, the conserved DRYLAIV motif, which is important for Gαi protein coupling, leading to calcium ion release and activation of signalling pathways involved in cell polarisation, integrin activation, and migration[57]. Instead, ACKRs primarily regulate chemokine levels by modulating chemokine availability and receptor signalling dynamics. This regulation is achieved in different ways by different receptors. ACKR2 and ACKR4 both internalise chemokines via the β-arrestin pathway. ACKR4 targets chemokines for degradation, while ACKR2 recycles them through endosomes, preventing excessive chemokine activity. ACKR3 modulates the trafficking, subcellular localisation, and signal transduction of classical chemokine receptors like CXCR4, thus altering their response to chemokines. ACKR1 transports and presents chemokines to leukocytes and forms heteromers with chemokine receptors such as CCR5. On erythrocytes, ACKR1 acts

as a "chemokine buffer," sequestering chemokines when levels are high and releasing them when levels are low, thereby modulating local chemokine availability[56,57].

1.2.11 Chemokine Function

Chemokines are further grouped based on their functional roles: inflammatory, homeostatic, and dual-function. Inflammatory chemokines are produced in response to injury or infection and are important in directing leukocytes to sites of damage and tissue repair. These chemokines are not produced constitutively but are synthesised in response to inflammatory stimuli[44,58]. In contrast, homeostatic chemokines are constitutively produced in specific tissues, especially in lymphoid organs. They regulate the routine migration of cells for immune surveillance, as well as regulate haematopoiesis, maintain tissue structure, and support both organogenesis and the development of lymphoid organs[44,58,59]. Dual-function chemokines exhibit both inflammatory and homeostatic properties, meaning they maintain normal immune function while responding to inflammatory signals[39].

1.3 INFLAMMATORY DISEASE LINKED TO CHEMOKINES

1.3.1 Atherosclerosis

While chemokine-induced inflammation plays an important role in defending against infection, many chemokines have also been implicated in driving immunoinflammatory diseases. Cardiovascular disease (CVD), the leading cause of death globally[60], is a prime example. Atherosclerosis, a common form of CVD, is characterised by the formation of atherosclerotic plaques within arteries. Atherosclerosis is initiated by damage to the endothelial lining of large blood vessels, which can be triggered by factors such as hyperlipaemia[61] and haemodynamic shear stress[62], as well as risk factors such as diabetes, ageing, and cigarette smoking[63].

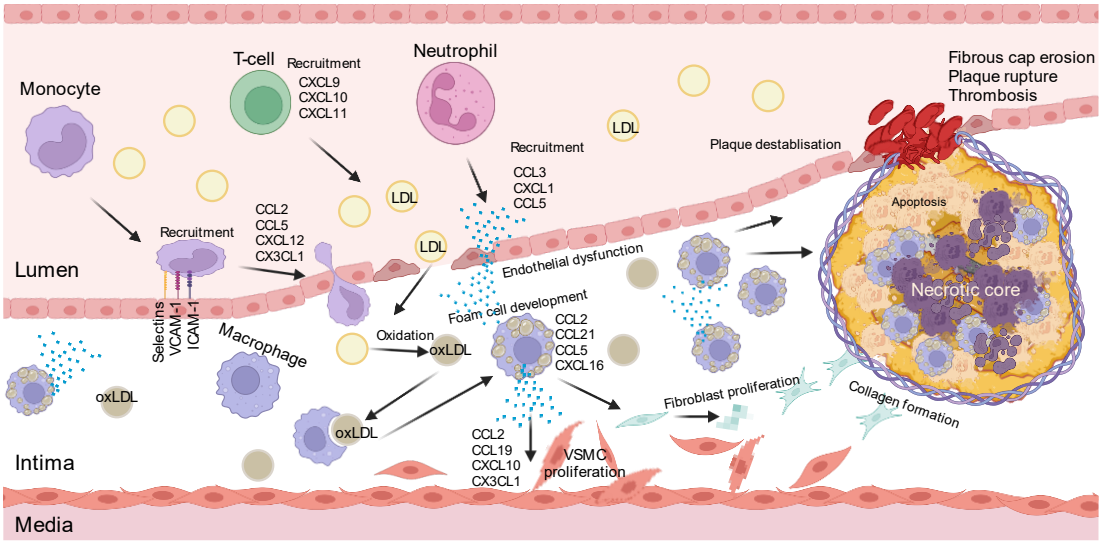

Figure 1.3.1.1: A schematic of atherosclerosis pathogenesis. Atherosclerosis starts with endothelial dysfunction and LDL entering the intima. LDLs undergo oxidation turning into oxLDLs, which induce the expression of adhesion molecules (selectins, VCAM-1 ICAM-1) on the

surface of the endothelium. This, in turn, recruits macrophages to enter the site of damage. Macrophages attempt to remove the oxLDL through phagocytosis but become overloaded and transform into foam cells. Foam cells start losing their mobility and begin to develop the plaque, eventually undergoing apoptosis and forming a necrotic lipid core. Foam cells and other recruited immune cells release chemokines, further exacerbating the progression. Growth factors from foam cells induce smooth muscle cell (SMC) proliferation, leading to fibroblast proliferation, which deposits collagen, further contributing to plaque development. Over time, the plaque thins due to the thinning of the blood vessel and collagenases, resulting in a thrombus formation. Adapted from[64]. Made in Biorender.

This endothelial damage activates the cells and initiates an inflammatory response through the nuclear factor kappa B (NF-κB) pathway[65]. The resulting endothelial dysfunction compromises the barrier (**Figure 1.3.1.1**), allowing circulating low-density lipoproteins (LDLs) to penetrate the intima, where they are oxidised by reactive oxygen species into oxidised LDLs (oxLDLs) and accumulate[63,66]. OxLDLs stimulate the p38 mitogen-activated protein kinase (MAPK) pathway, leading to the upregulation of vascular cell adhesion molecule-1 (VCAM-1), E-selectins, and chemokine CCL2[67]. The activation of the NF-κB pathway also promotes the expression of adhesion molecules, cytokines, and matrix metalloproteinases (MMPs)[65]. Chemokines (see **Table 1.3.1.2**) recruit circulating monocytes, which adhere to the activated endothelial cells via adhesion molecules such as VCAM-1, intercellular adhesion molecule-1 (ICAM-1), and P/E-selectins. The monocytes then transmigrate into the intima[66]. Once inside the intima, monocytes differentiate into macrophages, which are tasked with clearing oxLDLs. As macrophages engulf the oxLDLs, they become overloaded and transform into foam cells[68]. The compromised endothelial barrier further allows monocytes to infiltrate the intima[66]. Activated platelets secrete chemokines and also recruit other leukocytes, further aggravating the inflammatory response[69]. Foam cells have impaired mobility, and their continual accumulation, along with high lipid content, leads to the secretion of proinflammatory cytokines. Growth factors such as platelet-derived growth factor (PDGF) contribute to smooth muscle cell (SMC)

migration and proliferation, forming a fatty streak—the initial stage of plaque development[70]

Plaque formation is slow but progressive. As foam cells die, they create a necrotic core within the plaque, which triggers SMCs to migrate from the media to the intima. These SMCs proliferate and release extracellular matrix (ECM) components, forming a fibrous cap over the plaque[66,71]. As the plaque grows, blood flow through the vessel lumen becomes increasingly restricted. Over time, enzymes such as collagenases, released by foam cells or other inflammatory mediators, thin the fibrous cap, making it more prone to rupture[66]. Plaque rupture can lead to thrombus formation, which blocks blood flow to surrounding or downstream tissues, potentially resulting in ischemic events such as heart attacks or strokes[72].

Chemokine	Produced by	Role in Atherosclerosis
CX3CL1	Activated endothelial cells, apoptotic cells	- Acts as an adhesion molecule, binding to CX3CR1 on leukocytes (monocytes, NK cells, cytotoxic T lymphocytes), enabling transmigration[73] - Recruits monocytes to clear apoptotic debris, promoting foam cell accumulation[73] - Recruitment of NK cells, cytotoxic T lymphocytes contributes to endothelial damage by triggering lytic granules[73] - Promotes platelet aggregation[74] - Involved in SMC migration/proliferation[75]
CXCL4	Activated platelets	- Prolongs monocyte survival and promotes differentiation into macrophages, aiding in foam cell formation[76]
CXCL1	Activated endothelial cells	- Induced by oxLDLs[77] - Recruits monocytes and neutrophils to sites of endothelial injury by binding to CXCR2[78]
CXCL8	Macrophages, Foam cells	- Induced by oxLDLs[41] - Recruit neutrophils into the plaque[41] - Direct macrophages to atherosclerotic lesions[41]
CCL5	Platelets on activated endothelium	- Recruits monocytes and neutrophils, promoting their activation and extravasation[72]

		- Aids in foam cell formation and plaque development[72]
CCL2	Activated endothelial cells, MSCs	- Critical for monocyte recruitment to sites of injury, contributing to inflammation and foam cell formation[79] - Involved in SMC migration/proliferation[75]
CCL3	Activated macrophage	- Aids in the recruitment of immune cells such as neutrophils[72]
CCL7	Smooth muscle cells (SMCs) when cytokine stimulated	- Suggested to promote human coronary artery SMC and VSMC proliferation[80]
CXCL9, CXCL10, CXCL11	Endothelial cells	- Recruit immune cells, including T cells[72] - CXCL10 destabilises plaque[72] - CXCL10 involved in SMC migration /proliferation[75]
CXCL12	Smooth muscle cells (SMCs), endothelial cells (ECs), macrophages, platelets	- Modulates monocyte migration, adhesion, and survival[81] - Involved in monocyte differentiation into macrophages[81] - Stimulates platelet aggregation and is released by activated platelets[82]
CXCL13	Medial Vascular Smooth Muscle Cells (VSMCs)	- Recruits B cells to arterial tertiary lymphoid tissues (ATLOs), contributing to local immune responses and the development of atherosclerosis[83]
CCL21	Medial VSMCs	- Involved in B cell recruitment to ATLOs, supporting local immune responses in arterial walls during atherosclerosis[83] - Involved in foam cell formation[75]
CCL19	Secreted by dendritic cells and endothelium	- Induces SMC proliferation[72] - Induces maturation of DCs[72]
CXCL16	Dendritic cells, macrophages, B cells, T cells, SMCs, ECs	- Acts as an adhesion molecule for CXCR6-presenting leukocytes[84] - Involved in foam cell formation by acting as an oxLDL scavenger receptor in macrophages and SMCs[84] - Activates platelets and promotes platelet aggregation[85]
CCL22	Macrophages	- Recruitment of monocytes[86] - Stimulates platelet aggregation[87]

Table 1.3.1.2: Chemokines involved in atherosclerosis, and their influences.

1.3.2 The Chemokine Role in Atherosclerosis Regression

Chemokine and chemokine receptors also have roles in the regression of atherosclerosis, such as CCR1 and CXCR4. CCR1 is a receptor for pro-inflammatory CC chemokines like CCL3 and CCL5, found in atherosclerotic plaques. While CCR1 is expressed on human monocytes, macrophages, and T cells, it also functions on mouse neutrophils[88]. Despite the pro-atherogenic role of CCL5, studies have shown that Ccr1 deficiency in mouse models leads to larger atherosclerotic lesions and increased T-cell activity. However, macrophage content in the lesions remained unchanged[89,90]. CCR1 is also involved in the CCL5-induced arrest of monocytes and Th1 cells on activated endothelium[91]. This shows that CCR1 may have an atheroprotective role in regulating T-cell activation and movement of monocytes and T-cells to the vessel wall[88].

CXCR4 is expressed in endothelial and smooth muscle cells within atherosclerotic plaques and serves as a receptor for the chemokine CXCL12. The CXCL12–CXCR4 axis is known to regulate haematopoietic stem cell mobilisation, organ development, angiogenesis and has a significant role in atherosclerosis[92]. Lower levels of CXCL12 have been observed in coronary artery disease patients and aged ApoE−/− mice, which are prone to developing atherosclerosis[93,94]. Mice deficient in Cxcr4 develop larger atherosclerotic lesions, and blocking CXCR4 using the antagonist AMD3465 increases neutrophil recruitment while decreasing smooth muscle cell and T cell content in plaques[95]. These findings suggest that the CXCL12–CXCR4 axis may exert an atheroprotective role by regulating neutrophil homeostasis and limiting excessive immune cell recruitment, which can destabilise plaques[88].

1.4 THE CHEMOKINE NETWORK AND REDUNDANCY

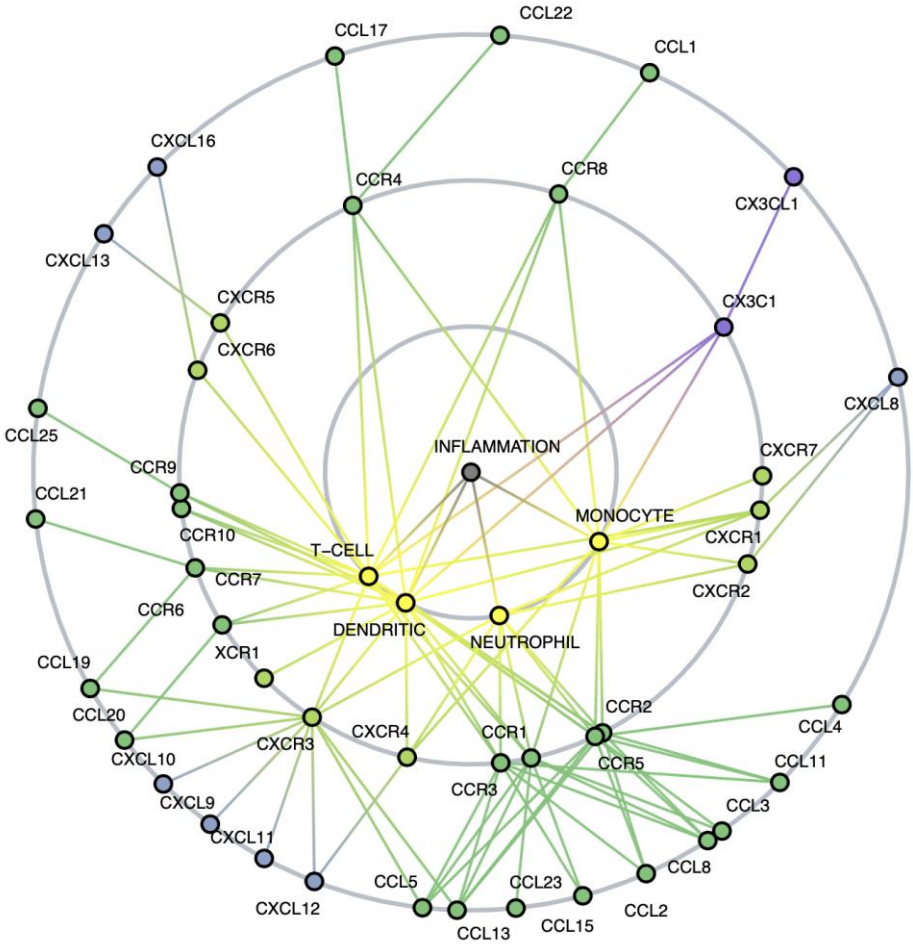

Figure 1.4: The robustness of the chemokine network, with chemokines associated with atherosclerosis. The outermost circle represents chemokines, while the next circle inward shows chemokine receptors and binding is indicated. The second innermost circle shows the leukocytes that express these receptors, leading to inflammation, represented in the innermost circle. Created by SB.

The chemokine network is highly complex and redundant[96], compromising of 46 human chemokines and 18 chemokine receptors[39]. As seen in **Figure 1.4**, this redundancy arises from multiple chemokines being expressed at the site of injury or infection, multiple receptor subtypes expressed on the surface of leukocytes and the ability of different chemokines to bind to multiple receptors[97]. Furthermore, chemokines can be expressed in a "feedforward loop," where the initial release of chemokines triggers the production of additional chemokines within the inflamed tissue, amplifying the inflammatory response[98]. This redundancy is essential for maintaining flexibility and resilience within the chemokine system, ensuring that the immune response can continually be effective even if one pathway is disrupted and the redundancy makes the network robust[96].

1.5 TREATMENTS TARGETING CHEMOKINES

Chemokines and their receptors play a crucial role in the immune system, making them appealing drug targets for inflammatory and immune-mediated diseases. However, the redundancy within the chemokine system, where multiple chemokines can signal through overlapping pathways, has limited the success of therapies targeting a single chemokine or receptor. This redundancy allows the immune system to maintain robust signalling, even when individual pathways are blocked, explaining why such targeted therapies have had limited clinical success[41,99]. Over the past two decades, only three out of 45 drugs targeting the chemokine system have achieved clinical approval[100]. Among them is Maraviroc, a CCR5 allosteric antagonist initially approved for HIV treatment. Despite its success in treating HIV, it failed to reduce inflammation in rheumatoid arthritis patients[101].

1.5.1 Limitations of Immune Therapy Treatments Targeting CVD

Immune therapy has many limitations for treating inflammation in cardiovascular disease (CVD). One limitation stems from the dual role of inflammatory pathways. Pathways such as NF-ϰB[102], TNFα[103], and the NLRP3 inflammasome[104] are vital for normal immune functions, such as cell survival and defence against infection, but also drive chronic inflammatory conditions like atherosclerosis. This dual role creates a huge challenge in developing therapies targeting harmful inflammation without disrupting beneficial immune responses. For example, in the clinical trial inhibiting a single cytokine, IL-6, patients with myocardial infarction failed to show clear benefits, suggesting that the IL-6 pathway, though pro-inflammatory, may aid early tissue repair[105].

Moreover, broad immunosuppressive treatments like IL-1 inhibitors[106] and colchicine[107,108], while reducing cardiovascular inflammation, were found to show a slight increase in adverse side effects such as increased infections and sepsis, especially in chronic disease

management. Furthermore, immune therapies must be stage-specific for treatments to be more effective. For example, monocyte recruitment is important in early-stage atherosclerosis but becomes less relevant in advanced stages where local proliferation within lesions dominates. The risk of long-term immunosuppression also remains a significant obstacle, which limits the use of these therapies in chronic conditions, making them more suitable for acute injuries. In response to these challenges, optimising the delivery and timing (such as with chrono-pharmacology) may be a potential solution to improve safety and efficacy for long-term use[105].

1.6 EVASINS: TICK-DERIVED CHEMOKINE BINDING PROTEINS

Ticks are small hematophagous arachnids that have evolved over millions of years to secrete proteins in their saliva that possess a range of immunomodulatory functions to help prolong feeding and survival. These include analgesic, anticoagulant, vasodilatory, and anti-inflammatory properties[109].

Evasins are a class of tick salivary glycoproteins with anti-chemokine activity and are aptly named as they 'evade' the host's immune defences[110]. Initial studies identified anti-chemokine activity in tick salivary gland extracts, specifically targeting CXCL8, across various ixodid tick species. Later research revealed that tick saliva can neutralise additional chemokines such as CCL2, CCL3, CCL5, and CCL11[111,112].

Subsequent research from the Proudfoot group, led to the first three characterised evasins from *Rhipicephalus* ticks: Evasin-1 (EVA1), Evasin-3 (EVA3) and Evasin-4 (EVA4)[113,114]. The identification process for all three evasins involved isolating and cloning tick cDNA, expressing the proteins in HEK293 cells, and screening for chemokine-binding properties using surface plasmon resonance (SPR). EVA1 was shown to bind to a small subset of CC chemokines, CCL3, CCL4, CCL14 and CCL18[113,115]. EVA4, which shares a similar sequence with EVA1, was also seen to bind exclusively to CC chemokines but exhibited a broader binding range, binding to CCL1, CCL2, CCL3, CCL4, CCL7, CCL8, CCL11, CCL13, CCL14, CCL15, CCL16, CCL17, CCL18, CCL19, CCL21, CCL22, CCL23, CCL24, CCL25, and CCL26[114,115]. EVA4 was also seen to functionally inhibit CCL2, CCL3, CCL3L1, CCL5, CCL7, CCL8, CCL11, CCL13, CCL14, CCL15, CCL16, CCL17, CCL22, CCL23, CCL24 and CCL26 using chemokine inhibition assays[114]. Notably, both EVA1 and EVA4 showed no binding affinity for CXC chemokines. In contrast, EVA3 is distinct in that it exclusively binds to ELR+ CXC chemokines, such as CXCL1 and CXCL8[113].

In the following years, hundreds of evasins were discovered from various tick species through bioinformatics analyses and identification via yeast surface display or *E. coli* expression systems, followed by fluorescence anisotropy-binding assays to assess their chemokine-binding capabilities[97,116-120].

Since then, 50 characterised evasins from *Ixodes*, *Amblyomma* and *Rhipicephalus* ticks have been classified into two families: Class A (EVAA) and Class B (EVAB), which bind to multiple CC or CXC- class chemokines, respectively and based on sequence homology to with Evasin 1 and 4 or Evasin 3[97,121]. Class A evasins range from 89 to 126 amino acids in length[122] and include the structurally characterised proteins EVA1 and EVA4. Of the 21 known Class A evasins, 19 contain eight cysteine residues, which form four intramolecular disulfide bonds, a feature shared by both EVA1 and EVA4[97,121]. The structure of Class A evasins also includes a discontinuous N-terminus, which is linked by a disulphide bond to two antiparallel β-sheets. The C-terminal domain consists of two additional antiparallel β-sheets, comprising five antiparallel β-strands and an α-helix[123]. Using x-ray crystallography, the structure of EVA1 was solved, and it was reported that the N-terminal of CCL3 interacts with the N-terminal and the C-terminal of EVA1[124]. Another example of a class A evasin is EV672, also from *Rhipicephalus* ticks, pulled from selection to CCL8 using yeast surface display. Using Bio-layer interferometry (BLI) EV672 was able to bind to the chemokines CCL1, CCL2, CCL3, CCL3L1, CCL7, CCL8, CCL11, CCL13, CCL14, CCL15, CCL16, CCL18 and CCL23 and also showed inhibition against the chemokines CCL2, CCL3, CCL3L1, CCL7 and CCL8. Similar to EVA1 and EVA4, it was reported that EV672's N-terminus is involved in binding to CCL8[119].

Class B evasins range from 60 to 100 amino acids in length[122] and include the structurally characterised protein EVA3, which was reported to bind to CXCL1, CXCL2, CXCL3, CXCL5, CXCL6 and CXCL8[113,118]. All 29 class B evasins possess six cysteine residues, creating three intramolecular disulphide bonds in a knottin structure[118]. This knottin

scaffold has been reported to be important in chemokine binding because different segments of the knottin scaffold bind to specific CXC chemokines[118,125].

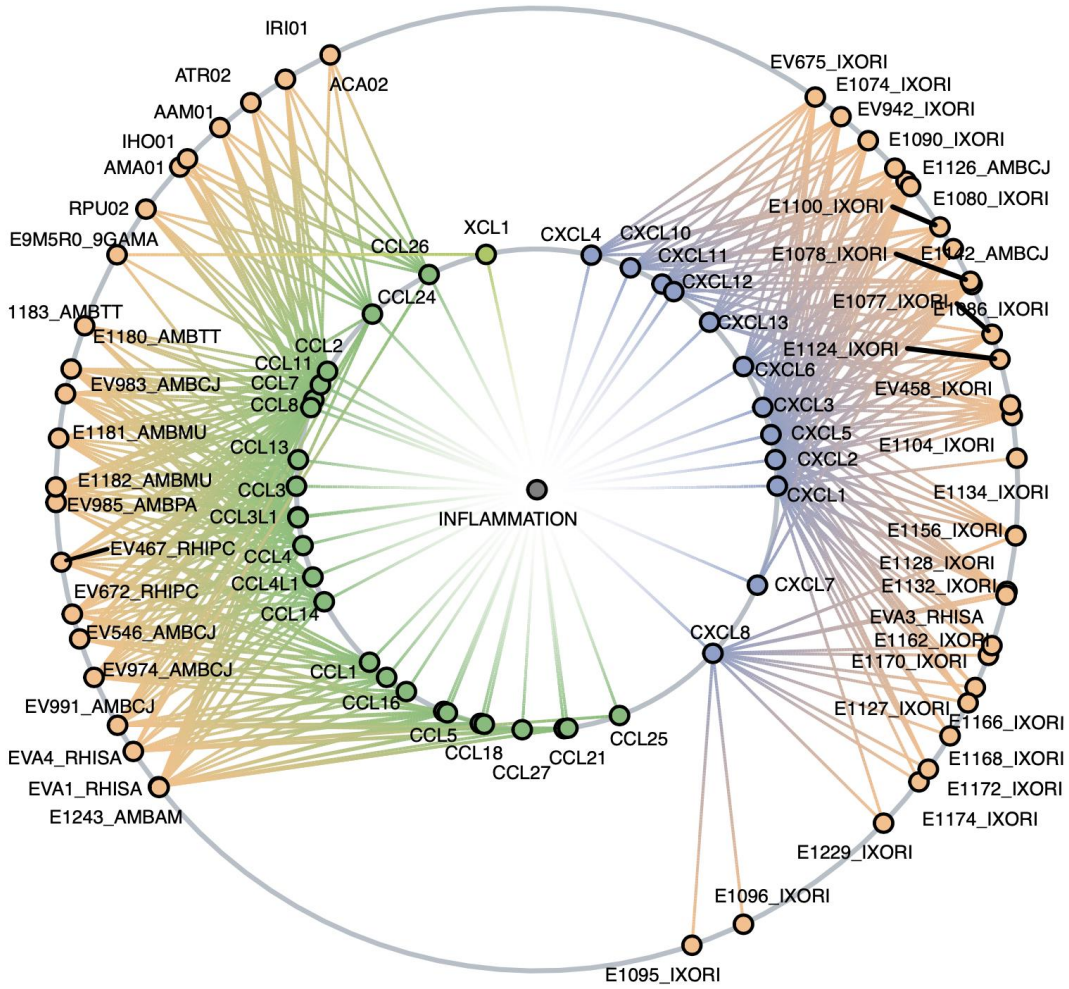

Figure 1.6: The evasin-chemokine network shows the effectiveness of evasins in disrupting the redundant chemokine network. The outermost circle represents evasins, with Class A evasins on the left and Class B evasins on the right. The second circle shows the chemokines these evasins target, with CC chemokines on the left and CXC chemokines on the right. Created by SB.

1.6.1 Chemokine and Evasin Binding

The use of phage display and in silico models confirms that EVA1 requires both its N-terminus and C-terminus for effective binding to CCL3, while EVA4 engages chemokines primarily through its N-terminus[126]. Both EVA1 and EVA4 target the N-terminus of chemokines, disrupting their interaction with chemokine receptors. Recent work confirms the importance of the evasin's N-terminus in chemokine recognition, but it works in conjunction with the body of the evasin to ensure binding specificity. For example, the chimera CHI-4R, formed from segments of EVA4 and EVA-R, found that chemokine binding occurs only when the N-terminal region of the evasin is compatible with the body of the same evasin, demonstrating the cooperative interaction between these regions in binding chemokines[115].

Evasins are highly promiscuous and capable of binding to multiple chemokines. Interestingly, the two classes of evasins show specific chemokine binding preferences: Class A evasins exclusively bind to CC chemokines, while Class B evasins specifically target CXC chemokines. A few hypotheses exist regarding how evasins can bind to multiple chemokines within the same class. One possibility is different ligand positioning, where different chemokines bind to distinct regions of the evasin structure[98]. Class A evasins have been reported to show CC class chemokine specificity due to structurally conserved backbone-backbone interactions, with additional residues in CXC chemokines potentially sterically hindering this binding[127]. In addition to rigid backbone interactions, side-chain interactions at key hotspots in flexible regions of the evasin structure were also found to be important for targeting specific chemokines within the CC class[127]. This possibly suggests another hypothesis: conformational plasticity, where the evasin can change its conformation to accommodate different chemokines binding at the same site[98].

1.6.2 Evasins as Potential Therapeutics

The promiscuous nature of chemokine binding allows ticks to overcome the redundant nature of the chemokine network and inhibit inflammation at the bite site[98] (**Figure 1.6**). This has led to an interest in utilising evasins as anti-inflammatory agents to disrupt chemokine function and treat inflammatory diseases. Success has been demonstrated in reducing inflammation in several animal models, including atherosclerosis[128], colitis[110], post-infarction myocardial injury and remodelling[129], pulmonary fibrosis[130], chronic liver disease[131] , ischemic reperfusion injury and psoriasis[113].

1.6.3 Limitations of Evasins and Peptides as an Alternative Therapeutic Approach

As evasins can only bind to one chemokine class, at least two different evasins classes must be administered to overcome the redundancy of the chemokine network. One approach to overcome this was the two-warhead or multi-warhead evasin. This involved linking two (or more) evasins together to create a single therapeutic possessing complementary anti-chemokine activity that was seen to be effective in inhibiting CC (CCL3, CCL5) and CXC (CXCL8) chemokines *in-vitro*[117].

While evasins show great potential as therapeutics, their application is limited by potential immunogenicity, high production costs, and the challenges of parenteral delivery. Moreover, the binding specificity of evasins requires using both Class A and Class B evasins to effectively target both CC and CXC chemokines. Peptides derived from the chemokine-binding sites of these evasins could help overcome these limitations, offering a more cost-effective, less immunogenic, and versatile alternative[98].

Peptides and peptidomimetics have been successful as therapeutics. A few such examples include captopril (to regulate blood pressure), eptifibatide, and tirofiban (to act on platelet aggregation and prevent blood clotting), which were derived from peptides found in snake venom toxins[132]. These peptide-derived replicate the desired biological activity of their naturally found parental peptide. They also offer increased safety profiles, improved bioavailability, and ease of production, making peptides a promising avenue for therapeutic development[132].

1.6.4 Evasin Derived Peptides

In our laboratory, we have previously reported a series of BK peptides (named after Shoumo **B**hattacharya and Akane **K**awamura) derived from the evasin EVA672, identified using hydrogen-deuterium exchange mass spectrometry (HDX-MS). The peptides BK1.2 and BK1.3 have shown significant efficacy in inhibiting multiple CC chemokines *in vitro,* and BK1.3 reduced inflammation *in vivo*[133]. Additionally, others have identified a peptide derived from the evasin EVA4 using nuclear magnetic resonance spectroscopy (NMR) that inhibits the activity of the CCL5 chemokine *in vitro*[134]. These findings suggest that peptide-based approaches can potentially circumvent the need to use full-length evasins to target the chemokine system.

1.7 Aims of This Work:

Previous work has demonstrated the potential of evasin-derived peptides as promising candidates for anti-inflammatory therapeutics. However, while these peptides have shown efficacy, they have not been shown to target multiple chemokine classes, a crucial requirement for effectively disrupting the chemokine network and overcoming redundancy. This project explores the therapeutic potential of evasin-derived peptides as broad-spectrum chemokine inhibitors, capable of simultaneously targeting multiple chemokines and disrupting redundant chemokine signalling pathways.

- **Chapter 3** focuses on identifying peptides with broad chemokine-binding capabilities using phage display. The goal is to discover peptides that can target multiple chemokine classes.
- **Chapter 4** aims to characterise the lead candidate peptide, HD2, in detail and assess its functional activity as an anti-chemokine agent, evaluating its ability to inhibit chemokine-induced migration.
- **Chapter 5** builds on findings from Chapter 3, exploring a related chemokine-targeting peptide to improve its binding profile through saturation mutagenesis followed by phage display.
- **Chapter 6** evaluates these improved mutant peptides in functional inhibition assays to determine their ability to inhibit complex chemokine mixtures associated with inflammatory conditions such as atherosclerosis.

The discovery of broad-spectrum chemokine-binding peptides in this project could lead to novel therapeutic strategies. These peptides could target multiple chemokine classes at once by eliminating the need to combine full-length Class A and B evasins. This approach may offer a novel way to address inflammatory diseases by effectively disrupting the chemokine network in a more efficient and targeted manner.

2 MATERIALS AND METHODS

2.1 MATERIALS

2.1.1 Media and Buffers (Phage Display)

Media	Components	Supplier
PT buffer	PBS (0.05%) Tween20	Gibco™ (10010023) Sigma-Aldrich (P9416)
PBT buffer	PBS (0.2% BSA) (0.05%) Tween20	Gibco™ (10010023) Sigma-Aldrich (A7030) Sigma-Aldrich (P9416)
(10X) PBT buffer	(10X) PBS (2% BSA) (0.5%) Tween20	Sigma-Aldrich (P4417) Sigma-Aldrich (A7030) Sigma-Aldrich (P9416)
Blocking buffer	PBS (0.2% BSA)	Gibco™ (10010023) Sigma-Aldrich (A7030)
SOC media	0.5% Yeast Extract 2% Tryptone 10 mM NaCl 2.5 mM KCl	Gibco™ (212750) Gibco™ 211705 Sigma-Aldrich (S3014) Sigma-Aldrich (P9541)

	10 mM MgCl2 10 mM MgSO4 20 mM Glucose. Glucose was added after autoclaving. Media was later filtered using 0.2 μm filter.	Sigma-Aldrich (M8266) Sigma-Aldrich (M7506) Sigma-Aldrich (D9434)
2YT (pH 7.0) (with Kan and Carb)	MP Biomedicals OR (10g) Bacto yeast extract (16g) Tryptone (5g) NaCl MilliQ water (add to 1L) Plus (150 μg/mL) Carbenicillin (75 μg/mL) Kanamycin	MP Biomedicals (113012031) Gibco (212750) Gibco (211705) Sigma-Aldrich (S9888) Sigma-Aldrich (C9231) Sigma-Aldrich (K1377)
LB (with Carb)	LB Agar (100 μg/mL) Carbenicillin	 Sigma-Aldrich (C9231)
LB broth (with Carb)	LB (100 μg/mL) Carbenicillin	 Sigma-Aldrich (C9231)

Table 2.1.1: Media and buffers used in phage display, with components and supplier names and codes listed.

2.1.1.1 Primers (Phage Display)

Primers	Sequence	Supplier
pRSTOP4Nsi_fwd	5'-GGAGGCGCCGAGGGTGAC	Sigma-Aldrich
pRSTOP4Nsi_rev	5'-ATAGGCATTTGTAGCAATAGAAAAAACGAACATAGATGCAAG	Sigma-Aldrich
oligo_fwd	5'-CTATTGCTACAAATGCCTATGCAGCCTCTTCATCTGGC	Sigma-Aldrich
oligo_rev2	5'-TCGTCACCCTCGGCGCCTCCTCCG-GATCCTCCACC	Sigma-Aldrich
GENEWIZ4_fwd	ACACTCTTTCCCTACACGACGCTCTTCCGATCTctagcgctATGCCTATGCAGCCTCTTCA	Life Technologies
GENEWIZ4_rev	GACTGGAGTTCAGACGTGTGCTCTTCCGATCTCGTCTGCGATGACAACAACCATCGCCCA	Life Technologies

Table 2.1.1.1: Primers used in phage display, with the primer sequence and supplier listed.

2.1.2 Synthetic Peptides

Peptides were synthesised using Fmoc solid-phase synthesis ordered from Thermofisher or GenScript as 16-amino acids in length with an amide C-terminal. They were synthesised with >95% purity, and their molecular weights were confirmed by liquid chromatography-mass spectrometry (LC–MS) performed by the suppliers. All peptides arrived as lyophilised powder and were dissolved in 100% DMSO (D4540, Sigma) with PBS added for a final concentration of 1000 μM peptide and 5% DMSO. Peptides were aliquoted out and stored in a -20 °C freezer. Scrambled (SCR) versions of respective peptides (HD2SCR,

HD845SCR) were designed by SB, by using an R-package that randomly reorders the sequence and finds the maximally distant sequence compared to the originating sequence.

2.1.2.1 Synthetic Peptides Sequences

Peptide Name	Peptide Sequence	Parental Evasin/Peptide	Supplier
HD2	EEDDYTAYAPLTCYFT	EVA4	ThermoFisher, GenScript
HD2 SCR	TLETDTFYECPDAYAY	EVA4	ThermoFisher, GenScript
HD2 E1A	AEDDYTAYAPLTCYFT	HD2	GenScript
HD2 E2A	EADDYTAYAPLTCYFT	HD2	GenScript
HD2 D3A	EEADYTAYAPLTCYFT	HD2	GenScript
HD2 D4A	EEDAYTAYAPLTCYFT	HD2	GenScript
HD2 Y5A	EEDDAAYAPLTCYFT	HD2	GenScript
HD2 T6A	EEDDYAAYAPLTCYFT	HD2	GenScript
HD2 Y8A	EEDDYTADAPLTCYFT	HD2	GenScript
HD2 P10A	EEDDYTAYADLTCYFT	HD2	GenScript
HD2 L11A	EEDDYTAYAPATCYFT	HD2	GenScript
HD2 T12A	EEDDYTAYAPLDCYFT	HD2	GenScript
HD2 C13A	EEDDYTAYAPLTAYFT	HD2	GenScript
HD2 Y14A	EEDDYTAYAPLTCAFT	HD2	GenScript
HD2 F15A	EEDDYTAYAPLTCYAT	HD2	GenScript

HD2 T16A	EEDDYTAYAPLTCYFA	HD2	GenScript
HD845	EDEDYEDFFKPVTCYF	EV672	GenScript
HD845SCR	PVFTFYEYCEDKFDD	EV672	GenScript
HD845 E6F	EDEDYFDFFKPVTCYF	HD845	GenScript
HD845 E6W	EDEDYWDFFKPVTCYF	HD845	GenScript
HD845 K10A	EDEDYEDFFAPVTCYF	HD845	GenScript
HD845 K10W	EDEDYEDFFWPVTCYF	HD845	GenScript
HD7	EEEDDYTAYAPLTCYF	EVA4	GenScript
HD540	DEDYEDFFKPVTCYFA	EV672	GenScript
HD883	EDYEDFFKPVTCYFAN	EV672	GenScript
HD1	TESLGISDKVANRMQG	ATR02	GenScript
HD3	PDIPYTCWLGWCSKGE	P1181	GenScript
HD5	ECYNVTEEVAKRMTPD	P1181	GenScript
HD6	SIPKETYEVSYRRNWR	EVA1	GenScript
HD8	KLLGSHYFSNGTLSTA	P1243	GenScript
HD9	TECIDLTQQASDVMQS	AMA01	GenScript

Table 2.1.2.1: Peptides identified and tested used in this study, with their respective sequence, derived evasin or peptide (if mutant) and supplier name.

2.1.3 Chemokines

2.1.3.1 Biotinylated Chemokines

Biotinylated chemokines were dissolved in (1X) PBS at 1µg/µl stocks, 3.3 µL aliquots, and stored at -20 °C.

Biotinylated Chemokines	Supplier	Code
CCL1	ALMAC	CB-07
CCL2	ALMAC	CB-02
CCL3	ALMAC	CB-01
CCL4	ALMAC	CB-23
CCL5	ALMAC	CB-08
CCL8	ALMAC	CB-18
CCL11	ALMAC	CB-03
CCL15	ALMAC	CB-19
CCL17	ALMAC	CB-16
CCL18	ALMAC	CB-21
CCL19	ALMAC	CB-06
CCCL20	ALMAC	CB-05
CCL22	ALMAC	CB-04
CCL25	ALMAC	CB-15
CCL28	ALMAC	CB-20

CXCL1	Protein Foundry	PFP029TBL
CXCL5	Protein Foundry	PFP004TBL
CXCL8	ALMAC	CB-09
CXCL10	ALMAC	CB-10
CXCL11	ALMAC	CB-13
CXCL12A	ALMAC	CB-11
CXCL12B	ALMAC	CB-22
CXCL13	ALMAC	CB-12
CXCL14	ALMAC	CB-17
CX3CL1	ALMAC	CB-14

Table 2.1.3.1: Biotinylated chemokines used in phage display with supplier and code listed.

2.1.3.2 Non-Biotinylated Chemokines

Chemokines were dissolved in PBSA (1X PBS and 0.1% BSA) at 10 µM stocks, in 10 µL aliquots and stored at -20 °C.

Chemokines	Supplier	Code
CCL1	PeproTech	300-37
CCL2	PeproTech	300-04
CCL3	PeproTech	300-08
CCL4	PeproTech	300-09

CCL4L1	PeproTech	300-58
CCL5	PeproTech	300-06
CCL7	PeproTech	300-17
CCL8	PeproTech	300-15
CCL11	PeproTech	300-21
CCL13	PeproTech	300-24
CCL14s (66aa)	PeproTech	300-38B
CCL15s (68aa)	Novus Biologicals	NBP2-35043
CCL16	PeproTech	300-44
CCL17	PeproTech	300-30
CCL18	PeproTech	300-34
CCL19	PeproTech	300-29B
CCCL20	PeproTech	300-29A
CCL21	PeproTech	300-35
CCL22	PeproTech	300-36A
CCL23s (75aa)	Biolegend	587002
CCL24	PeproTech	300-33
CCL25	PeproTech	300-45
CCL26	PeproTech	300-48
CCL27	PeproTech	300-54
CCL28	PeproTech	300-57
CXCL1	PeproTech	300-11

CXCL2	PeproTech	300-39
CXCL3	PeproTech	300-40
CXCL4	PeproTech	300-16
CXCL5	PeproTech	300-22
CXCL6	PeproTech	300-41
CXCL7	PeproTech	300-14
CXCL8	PeproTech	200-08
CXCL9	PeproTech	300-26
CXCL10	PeproTech	300-12
CXCL11	PeproTech	300-46
CXCL12A	PeproTech	300-28A
CXCL12B	PeproTech	300-28B
CXCL13	PeproTech	300-47
CXCL14	PeproTech	300-50
CXCL16	PeproTech	300-55
XCL1	PeproTech	300-20
CX3CL1	PeproTech	300-31

Table 2.1.3.2: Chemokines used in chemotaxis assays with supplier and code listed.

2.1.4 Media (Chemotaxis)

Media	Components	Supplier
THP-1/Jurkat cell culture media	RMPI-1640 4 mM L-Glutamine 10% heat inactivated Fetal Calf Serum (FCS)	Sigma-Aldrich (R0883) Sigma-Aldrich (G7513) Sigma-Aldrich (F9665)
T-cell activation and expansion	TexMACS Medium IL-2 T-cell activator	Miltenyi Biotec (130-097-196) PeproTech (200-02) STEMCELL Technologies (10971)
THP1 cell migration buffer (CMB)	RPMI-1640 4 mM L-Glutamine 0.5% Fetal Bovine Serum (Heat Inactivated)	Sigma-Aldrich (R0883) Sigma-Aldrich (G7513) Sigma-Aldrich (F9665)
Jurkat CXCR1 cell migration buffer (CMB)	RPMI-1640 4 mM L-Glutamine 0.25% Fetal Bovine Serum (Heat Inactivated)	Sigma-Aldrich (R0883) Sigma-Aldrich (G7513) Sigma-Aldrich (F9665)
Activated T cells and Buffy coat cell migration buffer (CMB)	HBSS 0.1% Protease free BSA Filter sterilised	Life Technologies (14025-092) Sigma-Aldrich (A7030)
PBSA	PBS 0.1% BSA (Protease Free)	Gibco™ (10010023) Sigma-Aldrich (A7030)

	Filter sterilised	
MACs buffer	PBS 0.5% BSA 2 mM ETDA (pH adjusted to 7.2 and filter sterilised)	Gibco™ (10010023) Sigma-Aldrich (A7030) Sigma-Aldrich (E9884)

Table 2.1.4: Media and buffers used in chemotaxis assays, with components and supplier names and codes listed.

2.2 METHODS

2.2.1 Phage Display

2.2.1.1 EVAA Phage Display Design

Wild-type class A evasin nucleotide sequences (excluding the signal peptide region) were codon-optimised for *E. coli* expression using GeneDesigner with default settings. This included a codon bias threshold of 0.1, removal of splicing signals, RNA destabilising elements, prokaryotic ribosome binding sites, Shine-Dalgarno sequences, optimisation of the 5' structure, and elimination of repeats. Codon optimisation was also performed after mutating each Cys residue to Ala or Ser. 81-mer oligonucleotides were designed, encoding for hexadecapeptides (16 aa length peptides). They overlap by a single residue, with the sequences 5'-GCAGCCTCTTCATCTGGC and GGTGGAGGATCCGGA-3' at respective ends to allow amplification and cloning. A total of 4741 distinct peptides, including Cys-to-Ala or Ser mutations, were (GenScript, 12K chip).

2.2.1.2 EVAA Phage Display Library Construction

Oligonucleotides were amplified using the primers oligo_fwd and oligo_rev2 (**Table 2.1.1.1**). The resulting PCR products were cloned into the prSTOP4Nsi plasmid using the NEB Builder HiFi Assembly Kit (E5520, NEB) according to the manufacturer's instructions. The prSTOP4Nsi plasmid was first amplified with primers pRSTOP4Nsi_fwd and pRSTOP4Nsi_rev (**Table 2.1.1.1**). The assembled vector pool was then transformed into ElectroMAX™ DH5α-E™ cells (11319019, Invitrogen), and

the plasmid DNA was purified using the GeneJet Plasmid Maxiprep Kit (K0491, Thermo Scientific). The purified plasmid DNA was subsequently transformed into SS320 phage display electrocompetent cells (60512, Lucigen) following the manufacturer's protocol.

After electroporation, the cells were resuspended in 950 µL of recovery media, transferred to 50 mL Falcon tubes, and infected with 100 µL of M13KO7 helper phage (10^{11} CFU/mL, N0315S, NEB). The mixture was incubated at 37°C and 220 RPM for 1 hour. After recovery, 1 mL of the culture was added to 2YT medium containing 50 µg/mL carbenicillin (C9231, Sigma-Aldrich) and 25 µg/mL kanamycin (K1377, Sigma-Aldrich) and incubated and shaken overnight at 37°C, 220 RPM. To precipitate the phage, 22.5 mL of the culture supernatant was mixed with 4.5 mL of 20% PEG 8000 (89510, Sigma-Aldrich) and 2.5 M NaCl (S9625, Sigma-Aldrich), incubated on ice for 30 mins, and centrifuged at 12,857 g for 10 mins at 4°C. The phage pellet was then resuspended in 1 mL of PBT buffer (PBS (P4417, Sigma-Aldrich), 0.20% BSA (A7030, Sigma-Aldrich), 0.05% Tween 20 (P1379, Sigma-Aldrich)). Anything undissolved was removed by centrifugation at 15,871 g for 10 mins at 4°C. Finally, glycerol (G5516, Sigma-Aldrich) was added to a final concentration of 10% (v/v), and aliquots were stored at -80°C.

2.2.1.3 HD845 Saturation Mutagenesis Phage Display Library (Design)

HD845 mutant oligonucleotides (81-mer), containing NNK substitution at each of the 16 peptide-encoding residues, were designed with 5'-GCAGCCTCTTCATCTGGC and GGTGGAGGATCCGGA-3' sequence arms for amplification and cloning. Oligonucleotides (GenScript) were pooled, amplified and cloned into plasmid prSTOP4Nsi (library construction was then performed as described above).

2.2.1.4 Library Next-Generation Sequencing (NGS) and Analysis

The library was amplified by PCR (**Table 2.2.2.3** and **Table 2.2.2.4**) using the primers oligo_fwd and oligo_rev2 (**Table 2.1.1.1**) to prepare it for next-generation sequencing (NGS). PCR products were verified on a 2% agarose gel to ensure the expected band size of approximately 271 bp. The products were then purified using the Monarch PCR & DNA Cleanup Kit (5 μg) (T1030, NEB), following the manufacturer's instructions.

The concentration of each PCR product was measured using both a Nanodrop (260/280 ratio) and the Qubit dsDNA High Sensitivity Quantitation Kit (Q32851, Thermo Scientific). PCR products were diluted to approximately 20 ng/μL and sent to Azenta/GeneWiz for sequencing using the AmpliconEZ protocol.

NGS Analysis: The forward and reverse Fastq files were paired using the "read ID." Only sequences that contained both forward (5'-CTAGCGCT) and reverse (5'-CGCAGACG) demultiplexing regions, as well as both constant regions (5'-ATGCCTATGCAGCCTCTTCATCTGGC and 5'-GGTGGAGGATCCGGAGGAGGCGCCGAGGGTGACGATCCCGCAAAAGCG GCCTTTAACTCCCTGCAAGCCTCAGCGACCGAATATATCGGTTATGCGTGG GCGATGGTTGTTGTCAT) (Life Technologies), were included in the analysis. Insert sequences from each read were identified and reads with non-matching or ambiguous insert sequences were excluded. Additionally, reads with incorrect insert sizes (i.e., not 48 nucleotides) were filtered out.

Only peptide sequences from the designed library were counted, and their frequencies were determined. Library cloning efficiency was calculated as the ratio of distinct cloned peptide inserts to the total number of designed inserts. The cloning efficiency was 98% for the EVAA library and 100% for the HD845X library.

2.2.1.5 Phage Display Library Screening

Phage display library screening involved four main stages: binding, washing, elution, and amplification.

Binding: In a flat-bottomed 96-well plate (655180, Greiner Bio-one), 1 μg of biotinylated chemokines or complement C5a was added to 5 μl streptavidin-coated magnetic Dynabeads (Dynabeads™ M-280 Streptavidin, 11205D, Invitrogen) per well in 100 μl PBS. The Dynabeads were pre-washed with PBS, and the chemokine-bead mixture was incubated overnight at 4°C on a plate shaker to allow chemokine immobilisation. Plates were covered with breathable film during incubation. After incubation, the plate was placed on a magnetic plate to immobilise the beads, and unbound chemokines and PBS were removed. Wells were washed once with blocking buffer. The beads were then transferred to a fresh 96-well plate containing 200 μl of blocking buffer to prevent non-specific binding, followed by a 2-hour incubation on a shaker. After blocking, the buffer was removed, and wells were washed four times with 200 μl of PT buffer. The phage library, diluted to ~10^{10} CFU (colony-forming unit)/mL in PBT buffer, was added (100 μl per well) and incubated for 2 hours at room temperature on a plate shaker.

Washing: The magnetic plate was used to wash the beads 15 times with 200 μl of PT buffer, and the beads were transferred to a fresh 96-well plate.

Elution: Each well received 100 μL of *Omnimax* phage-resistant *E. coli* (OD600 ~0.4-0.6), and the plate was incubated at 37°C for 30 mins with shaking. Next, 10 μL of M13K07 helper phage (10^{10} CFU/mL, N0315S, NEB) was added, and incubation continued at 37°C for 45 mins.

Amplification: The cells were transferred to a V-bottom 96-deep well plate (CLS3960, Corning) containing 1 mL of 2YT medium supplemented with carbenicillin and kanamycin. The plate was incubated overnight at 37°C with shaking. After incubation, the

plate was centrifuged at 2000 g for 30 mins at 4°C. Then, 540 µL of the supernatant from each well was transferred to a fresh deep-well plate containing 60 µL of 10X PBT for storage at 4°C. The selection process was repeated three times, with the newly amplified library used for each round of binding.

Selection PCR: After the third selection round, PCR was performed to confirm the presence of phage binders for each chemokine tested. First, a selection PCR OneTaq polymerase was performed (selection PCR construction and steps described in **Table 2.2.2.1** and **Table 2.2.2.1**, respectively), with the amplified phage library from the third round as the template. The pRSTOP4 Nsi empty vector served as the negative control, while the EVAA library was used as a positive control.

2.2.1.6 Screening Next-generation Sequencing (NGS) and Analysis

NGS: As previously described, NGS was performed after the third selection round using the GENEWIZ4_fwd and GENEWIZ4_rev primers (**Table 2.1.1.1**), with NGS PCR construction and steps described in **Table 2.2.2.3** and **Table 2.2.2.4**, respectively.

NGS Analysis: The enrichment (E) was calculated as the log2 ratio of output-to-input peptide frequencies. If the input proportion was unavailable, the lowest input value in the experiment was used to avoid an infinite E value. Similarly, the lowest output value was used if the output proportion was unavailable to avoid a log2E of -Infinity. Peptides binding to the control (C5a, log2E > 0) were excluded from further analysis. For HD845 mutagenesis screening, Δlog2E was calculated by subtracting the log2E of the parental HD845 peptide from that of the peptide of interest.

2.2.2 Polymerase Chain Reaction (PCR)

2.2.2.1 Phage Display Selection PCR

Component	Volume per 50 µL reaction	Final Concentration
5X OneTaq Standard Reaction Buffer (B9027S, NEB)	10 µl	1X
10 mM dNTPs (N0447S, NEB)	1 µl	200 µM
10 µM Forward Primer **GENEWIZ4_fwd**	1µl	0.2 µM
10 µM Reverse Primer **GENEWIZ4_rev**	1 µl	0.2 µM
OneTaq® DNA Polymerase (M0480S, NEB)	0.25 µl	1.25 units/50 µl PCR
Nuclease-free water	Up to 50 µl	
Template DNA	1 µl	

Table 2.2.2.1: Components and the amounts needed to construct the phage display selection PCR.

2.2.2.2 Phage Display Selection PCR steps

Step	Temperature (°C)	Time
Initial Denaturation	98°C	30 seconds
20 Cycles	98°C	10 seconds
	60°C	30 seconds
	72°C	30 seconds
Final Extension	72°C	2 mins
Hold	4°C	

Table 2.2.2.2: Selection PCR steps.

2.2.2.3 NGS Construction and Screening PCR

Component	Volume per 50 µL reaction	Final Concentration
5X Q5 Reaction Buffer (B9027S, NEB)	10 µl	1
10 mM dNTPs (N0447S, NEB)	1 µl	200 µM
10 µM Forward Primer **(Construction: oligo_fwd)** **(Screening: GENEWIZ4_fwd)**	2.5 µl	0.5 µM
10 µM Reverse Primer **(Construction: oligo_rev2)** **(Screening: GENEWIZ4_rev)**	2.5 µl	0.5 µM
Q5 High-Fidelity DNA Polymerase (M0491S, NEB)	0.5 µl	1.0 units/50 µl PCR
Nuclease-free water	Up to 50 µl	
Template DNA	2 µl	< 1000 ng

Table 2.2.2.3: Components and the amounts needed to construct the NGS PCR for phage display library construction (which used the oligo_fwd and oligo_rev primers) and phage display screening (which used the GENEWIZ4_fwd and GENEWIZ4_rev primers).

2.2.2.4 NGS Construction and Screening PCR Steps

Step	Temperature (°C)	Time
Initial Denaturation	98°C	30 seconds
20 Cycles	98°C	10 seconds
	60°C	30 seconds
	72°C	30 seconds
Final Extension	72°C	2 mins
Hold	4°C	

Table 2.2.2.4: NGS PCR steps.

2.2.3 Gel Electrophoresis

DNA fragments from PCR were analysed using a 2 % agarose gel. To prepare the gel, 1 g of agarose (A9539-500G, Sigma-Aldrich) was dissolved in 150 mL of TAE buffer (40 mM Tris, 20 mM acetic acid, 1 mM EDTA, pH 8.3) by heating. Ethidium bromide was added to the molten agarose at a final concentration of 0.5 μg/mL before pouring the gel. Once the gel was set, the DNA samples were loaded, and electrophoresis was performed at 120V for 60 mins. DNA bands were visualised under UV light, and images were captured using a BioRad ChemiDoc Imager.

2.2.4 Cell Lines

2.2.4.1 THP1

THP-1 cells (ECACC 88081201) were obtained from the European Collection of Authenticated Cell Cultures (ECACC) and cultured in suspension in THP1 cell culture media (**Table 2.1.4**). Cells were maintained at 0.3 × 10^6 cells/mL in T175 flasks (CLS431080-50EA, Corning) in a humidified incubator at 37°C, 5% CO_2.

Cell Migration: For migration assays, 300,000 THP1 cells/well were added to the top chamber of a 5-μm Transwell insert (3388, Corning) in 50 μL of THP1 cell migration media. Cells were allowed to migrate for 4 hours at 37°C in 5% CO_2.

2.2.4.2 Jurkats

Jurkat E6.1 cells (ATCC TIB-152) were provided by Pauline van Diemen (Oxford). The Jurkat:CXCR1 cell line was generated by Dr. Gintare Smagurauskaite through electroporation of Jurkat E6.1 cells with a PvuI-linearised plasmid (D1398) and selection in Jurkat cell culture media (**Table 2.1.4**), and 5 μg/mL blasticidin (203350, Sigma-Aldrich). The cell line was cultured and maintained in Jurkat cell culture media (**Table 2.1.4**) with an additional 5 μg/mL blasticidin in T175 flasks at 37°C, 5% CO_2.

Cell Migration: For migration assays, 300,000 Jurkat CXCR1 cells/well were added to the top chamber of a 3-μm Transwell insert (3385, Corning) in 50 μL of Jurkat cell culture media. Migration was allowed for 4 hours at 37°C in 5% CO_2.

2.2.4.3 Human Blood Samples

Peripheral blood cells were isolated from anonymised donor leukocyte cones and buffy coats obtained from NHS Blood Transfusion Services. Ethical approval was granted by the University of Oxford Medical Sciences Interdivisional Research Ethics Committee (CUREC1, reference R75963/RE001).

2.2.4.4 Activated T cells (ATC)

Activated T cells were isolated from peripheral blood mononuclear cells (PBMCs) from human leukocyte cones. Isolation: 5 mL of blood was gently mixed with 10 mL of Lymphoprep™ density gradient (07801, STEMCELL Technologies) and added in a SepMate™ isolation tube (85450, STEMCELL Technologies). A modified protocol was later used to exclude the SepMateTM isolation tube to reduce the number of spins and directly lyse red blood cells with (1X) RBC lysis buffer (170-080-033, Miltenyi Biotec). RBC lysis buffer was added in a 1:1 ratio to the blood and incubated for 10 mins at room temperature. The sample was spun down at 1400 rpm for 10 mins at room temperature to aspirate the supernatant and was resuspended with the RBS lysis buffer to repeat the lysis step. After the second centrifugation, the pellet was resuspended with 10 ml of MACS buffer (**Table 2.1.4**). Cells were then passed through a 70-μm cell strainer, and CD8+ T cells were isolated using a CD8+ T-cell isolation kit (480011, BioLegend).

Activation: Isolated CD8+ T cells were activated in ImmunoCult™-XF T-cell expansion medium (10982, STEMCELL Technologies) supplemented with 25 μl/ml of anti-CD3/anti-CD28 activator (10991, STEMCELL Technologies) and with 10 ng/mL recombinant human IL-2 (200-02, PeproTech), along with 1% penicillin/streptomycin (Miltenyi Biotec), and cultured at 37°C in 5% CO_2. The T-cells were passaged every 2–3

days and cryopreserved at ~day 10-13 at 20 × 10^6 cells/mL in TexMACS medium supplemented with 10% DMSO (D2650, Sigma-Aldrich) in liquid nitrogen. 24 hours before use, activated CD8+ T cells were thawed, spun down to remove DMSO, and resuspended in TexMACS medium at 0.3 × 10^6 cells/mL, and incubated in a humified incubator at 37 °C in 5% CO2.

Cell Migration: For migration assays, 100,000 ATCs/well were added to the top chamber of a 3-μm Transwell insert in 50 μL of ATC cell migration media (**Table 2.1.4**). Cells were allowed to migrate at 37 °C in 5% CO2 for 2 hours in a humified incubator.

2.2.4.5 Buffy Coat

Monocytes, granulocytes and lymphocytes were isolated from buffy coats (National Blood Service, Bristol) collected from John Radcliffe Hospital, Oxford. For every 5 mL of blood, 1 mL of HetaSep™ (#07906, STEMCELL Technologies) was added in 15 mL falcon tubes. After 15 mins incubation at 37 °C in a 5% CO2 incubator, the top layer containing the buffy coat from every tube was carefully removed and placed (max 10 mL buffy coat/tube) in a fresh 50 mL falcon tube. To this, MACs buffer was added, gently inverted, and centrifuged for 10 mins at 1400 rpm. The supernatant was removed, and the pellet was resuspended with 1X RBC lysis buffer (130-094-183, Miltenyi Biotec) and incubated at room temperature for 10 mins. MACs buffer was added to stop the lysis, and the falcon was centrifuged for 10 mins at 1400 rpm. The pellet was resuspended MACs and centrifuged twice again. On the last spin, the pellet was resuspended in 2.5 mL of MACs buffer, counted on the Attune flow cytometer, and resuspended using cell migration media based on the monocyte count to 2 million cells/mL for migration assays.

Cell migration: For migration assays, 50 μL of cells (2 million cells/mL) were added to the top chamber of a 3-μm Transwell insert and incubated for 2 hours at 37°C in 5% CO_2.

For each batch of buffy coat collected, dose-response assays must be performed for every chemokine being tested in the inhibition assays.

2.2.4.6 Mycoplasma Tests

All cell lines were tested monthly for mycoplasma contamination using the MycoAlert™ Mycoplasma Detection Kit (LT07-318, Lonza) following the manufacturer's instructions.

2.2.4.7 PI (Live/Dead) Staining

Cell viability was assessed to determine whether the peptides were toxic to the cells, using propidium iodide (PI) staining. 300,000 THP-1 cells/mL or 100,000 cells/mL for ATCs, were incubated with 10 μM peptide for 2-4 hours (depending on the cell type). Control samples of live and heat-killed cells were included. After incubation, one drop of PI (R37169, Invitrogen) was added, followed by 15 mins of incubation in the dark at room temperature. Samples were analysed by flow cytometry (ATTUNE) to quantify live vs. dead cells relative to the controls.

2.2.5 Chemotaxis assays (Cell Migration Assays)

2.2.5.1 Dose-Response Assays

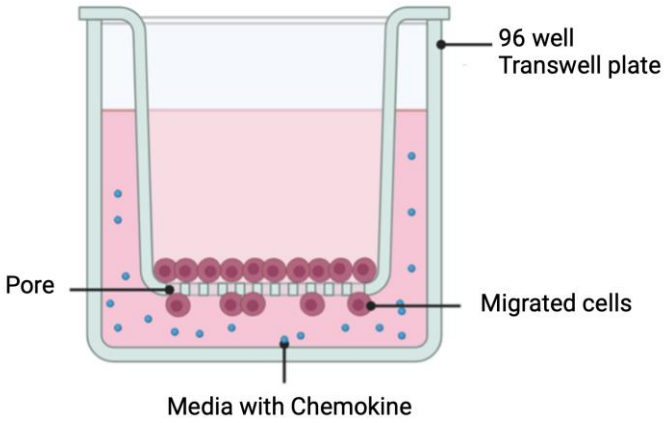

Figure 2.2.5.1: Schematic image of a well in a dose-response assay. Created in BioRender.

For every chemokine tested, a dose-response assay was performed to determine the chemokine EC50 or EC80, which represents the concentration of chemokine required for 50% or 80% of maximum cell migration, respectively. This concentration was then used to test the effect of the peptide. Each migration assay included three technical replicates and three biological replicates.

Chemokine dilutions were prepared as follows: 0–50 nM for THP1 cells, 0–200 nM for Jurkats, and 0–300 nM for ATC and buffy coat cells, respectively. These dilutions were added to the bottom chambers of a migration assay plate in a volume of 150 μL of cell migration buffer (CMB). An appropriate number of cells (depending on the cell type) were added in the top chambers.

The plate was incubated in a humidified incubator at 37°C with 5% CO2 for the required duration. Following incubation, the plate was placed on a shaker for 10 mins. The top chamber insert was then carefully removed, and 150 μL of the migrated cells and media were transferred into a new U-bottomed plate containing 50 μL of CMB for counting of migrated cells.

Migrated cells were counted using the ATTUNE flow cytometer, using forward scatter (FSC) and side scatter (SSC) dot plots for analysis. Data were analysed using GraphPad Prism, with migration responses fitted to a four-parameter agonist response curve.

2.2.5.2 Single Concentration Inhibition Assay

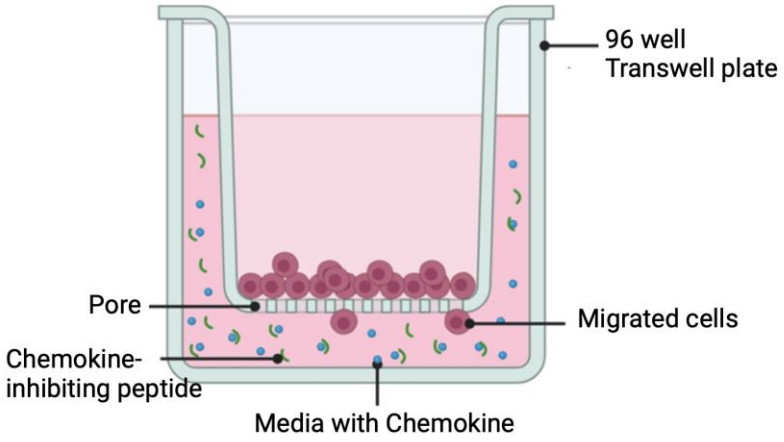

Figure 2.2.5.2: Schematic image of a well in an inhibition assay. Created in BioRender.

For the single-concentration inhibition assay, the EC50 or EC80 concentration of the chemokine and 10 μM of the test peptide were pre-incubated together at 37°C for 30 mins to allow for optimal binding. After this, 150 μL of the chemokine-peptide mixture was added to the bottom chamber of the Transwell plate. Based on the cell type, the appropriate number of cells was added to the top chamber in 50 μL per well. The plate was incubated at 37°C in a humidified incubator with 5% CO_2 for the required duration. After incubation, the plate was placed on a shaker for 10 mins. The top chamber insert was then removed, and 150 μL of the migrated cells and media were transferred into a fresh U-bottom plate containing 50 μL of CMB.

Migrated cells were then counted using the ATTUNE flow cytometer-based FSC versus SSC dot plot. Each migration assay was performed in triplicate (three technical replicates

and three biological replicates). The data were analysed in GraphPad Prism using one-way ANOVA followed by Dunnett's test for multiple comparisons.

2.2.5.3 Inhibition Dose-Response Assays (IC50s)

Inhibition dose-response assays were conducted similarly to the single-concentration inhibition assays. The EC50 or EC80 concentration of the chemokine was incubated with varying concentrations of the peptide at 37°C for 30 mins to allow binding. A 150 μL aliquot of the chemokine-peptide mixture was then added to the bottom chamber of the Transwell plate, and the respective number of cells was added to the top chamber in 50 μL per well.

The plate was incubated at 37°C in a humidified incubator with 5% CO_2 for the required amount of time. Following incubation, the plate was placed on a shaker for 10 mins. The top chamber insert was removed, and 150 μL of migrated cells and media were transferred into a fresh U-bottom plate containing 50 μL of CMB. The migrated cells were quantified using an ATTUNE flow cytometer and analysed with FSC versus SSC dot plots. The results were analysed using GraphPad Prism, fitting the data to a four-parameter antagonist response curve.

2.2.6 Atherosclerosis (Athero) Pool Construction

To construct the atherosclerosis chemokine pool, the relative quantities of each chemokine were derived from their mean expression in the RNA-seq dataset (**Table 2.2.6**). Chemokines were added to the pool in proportion to these relative amounts. All chemokines were freshly synthesised, resuspended, and stored at a concentration of 1000 μM.

Two key calculations were performed for pool preparation: the sum of the relative amounts and the scaling factor. The scaling factor was obtained by dividing the target final concentration of the pool (10 μM) by the sum of the relative amounts. The concentration of each chemokine in the pool was calculated by multiplying its relative amount by the scaling factor. The volume of each chemokine needed for the pool (final volume = 1 mL) was calculated by dividing its concentration by the target concentration (10 μM) and multiplying by 1000 μL.

Chemokines present in lower relative amounts were added in smaller volumes. The smaller pools were combined to create the final athero pool, accurately representing the chemokine composition found in the plaque environment.

Chemokine	Relative Amount	Concentration (μM)
CCL2	100	2.6107
CCL18	70.891	1.85075
CXCL12	47.19	1.23199
CCL3	23.75	0.62004
CXCL16	21.638	0.5649
CCL4	16.484	0.43035
CXCL8	13.172	0.34388
CCL14s	12.426	0.32441
CCL8	10.623	0.27733
CCL4L1	8.393	0.21912
CCL5	7.858	0.20515

CXCL7	7.122	0.18593
CCL19	6.731	0.17573
CXCL10	5.824	0.15205
CCL13	4.931	0.12873
CXCL2	3.925	0.10247
CCL21	3.23	0.08433
CXCL9	2.905	0.07584
CX3CL1	2.786	0.07273
CXCL1	2.395	0.06253
CXCL3	1.579	0.04122
CCL7	1.34	0.03498
CCL28	1.315	0.03433
CXCL4	1.299	0.03391
CXCL5	0.949	0.02478
CXCL11	0.733	0.01914
CCL23s	0.441	0.01151
XCL1	0.396	0.01034
CCL26	0.388	0.01013
CXCL6	0.387	0.0101
CCL16	0.343	0.00895
CXCL13	0.328	0.00856
CCL20	0.315	0.00822
CCL22	0.27	0.00705
CCL24	0.264	0.00689
CCL17	0.128	0.00334
CCL11	0.121	0.00316
CXCL14	0.069	0.0018
CCL15s	0.057	0.00149
CCL27	0.027	0.0007
CCL1	0.016	0.00042

Table 2.2.6 The athero pool chemokine table indicates the chemokines ratio determined by the mean relative expression of chemokines in the plaque RNA-seq data set (GSE198600). The mean relative chemokine expression levels were analysed by SB. Four chemokines (CCL3L3, XCL2, CXCL4L1, and CXCL17) were excluded from the athero pool due to their unavailability.

CHAPTER 3: DISCOVERY OF PEPTIDES FROM CLASS A EVASINS

3.1 INTRODUCTION

Chemokines are a family of 46 structurally related secreted proteins that play a key role in leukocyte chemotaxis and inflammation[39]. Chemokines are classified into four main classes -CC, CXC, CX3C and XC- based on the arrangement of cysteine residues at the N-termini, each of which has differing specificities for inflammatory cells[135,136]. While chemokine-induced inflammation protects against infection, many chemokines have been found to drive immunoinflammatory diseases. Elevated levels of multiple CC and CXC chemokines have been observed in patients with conditions such as atherosclerosis, rheumatoid arthritis, psoriasis, inflammatory bowel disease, and multiple sclerosis[78,137,138]. These elevated chemokine levels promote the recruitment of additional leukocytes, which, upon activation, release more chemokines, thereby creating a feed-forward loop that exacerbates disease progression[137]. Studies using gene knockout models in mice have shown that the absence of certain chemokines or their receptors can significantly reduce inflammation in several inflammatory diseases[138]. These findings highlight the pivotal role of chemokines as potential therapeutic targets in treating inflammatory disorders.

Chemokines are also functionally characterised into three main groups: inflammatory, homeostatic, and dual-function. Inflammatory chemokines are secreted in response to tissue injury or infection, driving leukocyte chemotaxis to the site of inflammation. Homeostatic chemokines are produced by tissue cells and play a role in basal leukocyte trafficking, such as lymphocyte homing and recirculation. Dual-function chemokines exhibit both inflammatory and homeostatic roles[135].

Targeting inflammatory diseases is challenging due to the redundancy within the chemokine network. This redundancy arises from the expression of multiple inflammatory CC and CXC chemokines coupled with the promiscuous interactions between these

chemokines and their respective receptors[139]. The ability of a single receptor to bind multiple chemokine ligands, and vice versa, creates a complex and robust signalling network that is difficult to target effectively[98]. Conventional approaches targeting individual chemokines or receptors have historically failed to achieve successful therapeutic outcomes, as seen by the failure of CCR5 inhibition with Maraviroc in reducing inflammation in rheumatoid arthritis patients[101]. This highlights the need for novel strategies simultaneously targeting multiple chemokines to overcome network redundancy.

Interestingly, nature has provided a potential solution in the form of evasins, a class of salivary proteins produced by ticks. Ticks secrete these evasins at the bite site; these remarkable proteins have evolved to bind and neutralise multiple chemokines to overcome chemokine redundancy promiscuously, enabling extended feeding periods. Evasins are classified into two distinct classes: Class A evasins (EVAA) bind and inhibit multiple CC chemokines, while Class B evasins (EVAB) bind and inhibit multiple CXC chemokines[97].

Despite their potential to reduce inflammation in several inflammatory models[110,113,128-131]. The therapeutic development of full-length evasins has been hindered by limitations such as high production costs and potential immunogenicity[140]. To overcome these limitations, researchers have explored utilising peptides derived from the chemokine binding sites of evasins as an alternative therapeutic approach.

In our laboratory, we have previously reported a series of BK peptides derived from the evasin EVA672, identified using hydrogen-deuterium exchange mass spectrometry (HDX-MS). These peptides, including BK1.2 and BK1.3, have demonstrated remarkable efficacy in inhibiting several CC chemokines *in vitro* and BK1.3 reducing inflammation *in vivo*[133]. Additionally, others have identified a peptide derived from the evasin EVA4, using NMR, that inhibits the activity of the CCL5 chemokine *in vitro*[134].

However, the ability of these peptides to overcome chemokine redundancy in immuno-inflammatory diseases has yet to be extensively evaluated. This project aims to explore the potential of evasin-derived peptides as broad-spectrum chemokine inhibitors, capable of simultaneously targeting multiple chemokines and disrupting the redundant signalling network. The chapter hypothesises that short linear peptides with broad CC-chemokine binding derived from tick class A evasins can be identified using phage display. To test this hypothesis, a phage-display-NGS method was used to screen evasin-derived peptides for their ability to bind chemokines.

This work has been published in Vales *et al.*[141]

3.2 RESULTS

3.2.1 Phage Display Library Construction and Validation

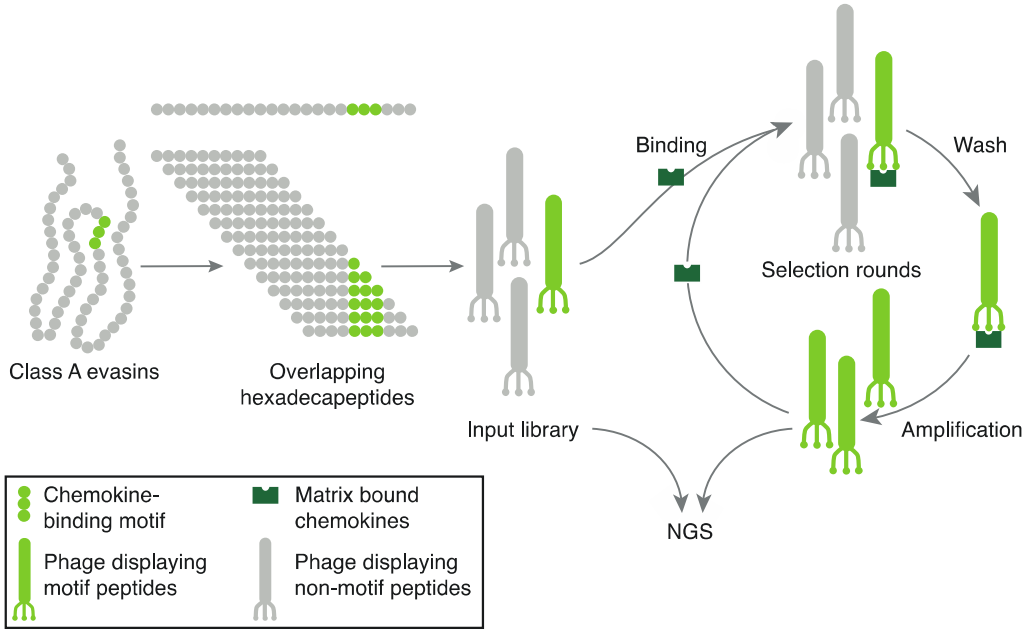

Figure 3.2.1: Identifying chemokine-binding peptides using phage display. Phage Display NGS Pipeline: 21 class A evasins were divided into 16aa (amino acid) oligonucleotides, each overlapping by one amino acid. These oligonucleotides were cloned into a prSTOP4 phagemid vector, creating a phagemid pool. The pools were then transfected into *E. coli* and helper phage to generate the input phage display library. The library was PCR amplified, and the amplicon was analysed by next-generation sequencing (NGS) to verify correct sequences and ensure high coverage. The phage library was incubated with matrix-bound chemokines to identify and select chemokine-binding peptides. Wells were washed to remove weak or non-specific binders. T1-phage-resistant *E. coli* and helper phage were used to amplify the chemokine-bound peptide binders. This amplified library underwent subsequent selection rounds to filter for strong binders. After three rounds, phage inserts were PCR amplified and analysed using NGS. Peptides binding to each chemokine were identified and expressed as log2E, calculated based on enrichment (E),

the ratio of each peptide in the output library to the input library. Peptides binding to the negative control complement C5a were excluded.

Our lab utilised a phage-display platform using the phagemid prSTOP4 combined with next-generation sequencing (NGS) to systematically identify chemokine-binding peptides derived from class A evasins. The class A evasin phage display library, also named EVAA library, was designed by SB and constructed by GD and KH. As seen in **Figure 3.2.1**, the phage display library was created such that single residue resolution overlapping peptides 16 aa in length derived from 21 mature class A evasin sequences were displayed onto the p8 protein coat of the phage. The 16 aa peptide length was chosen based on the previous work with the BK1 peptide, which mapped the binding region interface between CCL8 and EV672 using HDX-MS[133]. It was also thought that a 16 aa length would strike a balance. Peptides that are too short might lose structural context, while those too long could result in less specific interactions or steric hindrance. The phage display technique allows multiple peptides to be displayed on the phage, allowing the selection of low-affinity interactions[142].

Class A evasins served as the initial focus for exploring linear chemokine-binding peptides to validate the phage display method. This approach builds on previously reported chemokine-binding peptides derived from class A evasins, which were identified using structural methods[133,134]. The library was constructed with both wild-type and Cys to Ser and Cys to Ala mutations. These mutations removed the side chains after the β-carbon without affecting conformational flexibility[143]. These mutations were included as it was thought that unpaired Cys residues could affect phage display by forming disulphide bonds.

The input library was sent for NGS (GeneWiz Amplicon EZ) to verify that the sequences were correct and that it had a high cloning efficiency of 98%. Furthermore, the wild type, Cys to Ser, and Cys to Ala mutations showed little to no impact on the count numbers. Any peptides that were not found in the original design (mutations) were not used in analyses.

3.2.2 Phage Display Library Screening and Results

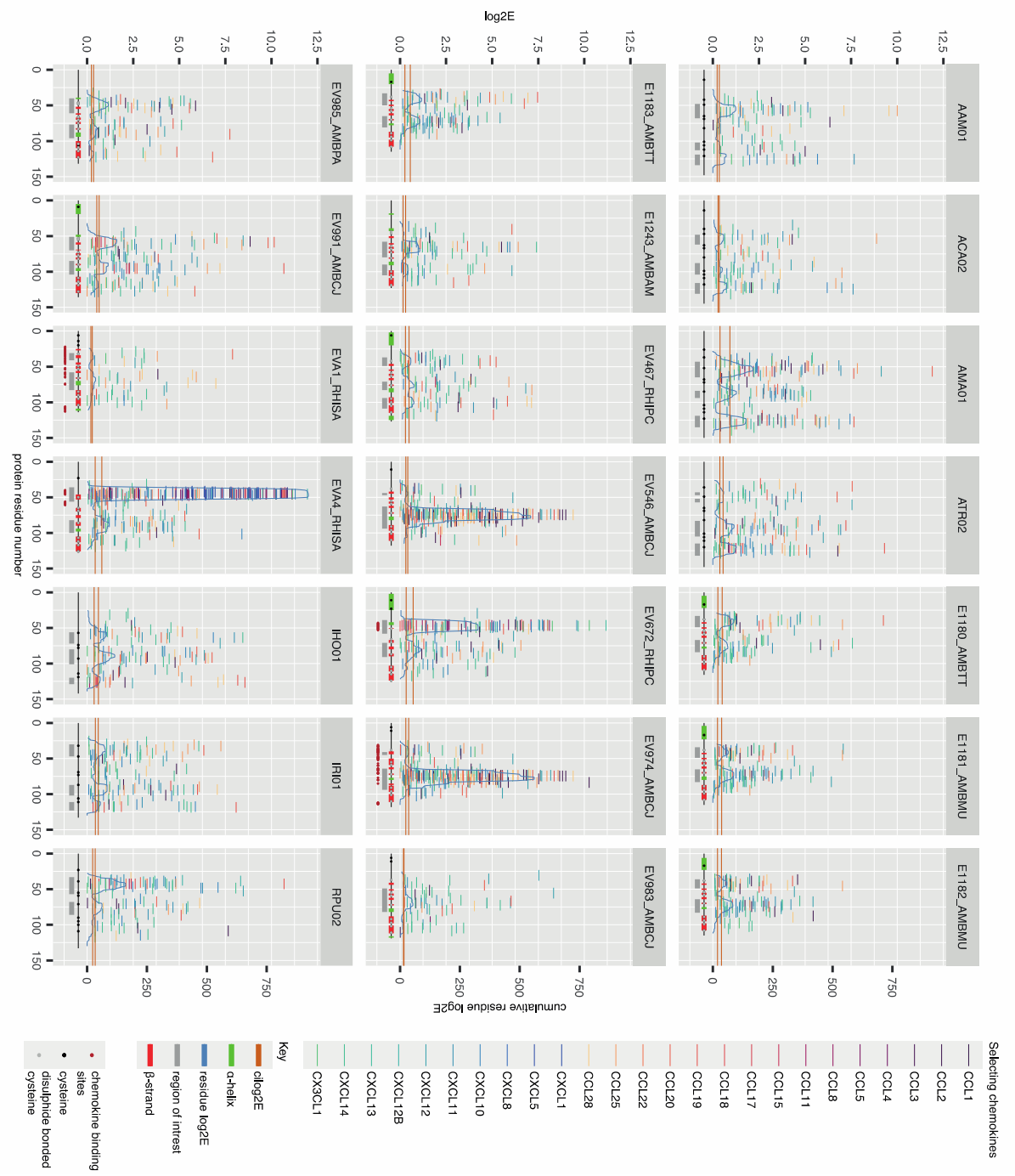

Figure 3.2.2: Class A evasin phage display screen. The names of the 21 class A evasins used to create the EVAA phage display library are displayed above each sub-panel. Enriched peptides derived from each evasin are represented as colour-coded tiles, indicating the specific chemokine to which the peptide binds. The x-axis shows the protein residue numbers, indicating the location of each peptide within the evasin protein. The left y-axis displays the peptide log2E (binding affinity). The right y-axis represents the cumulative residue log2E (rlog2E). The rlog2E for each residue was calculated by summing the log2E values of all peptides overlapping that residue, and the resulting curve was smoothed using a rolling median over seven residues. Regions of interest (ROI) were identified where rlog2E exceeded the upper boundary of the 95% confidence interval of the median rlog2E. Structural features, including AlphaFold model data, were obtained from the UniProt database. Known chemokine binding sites are indicated. Chemokine-binding sites for EV672 with CCL8 and EVA4 with CCL5 were obtained from published data sources[133,134] The chemokine-binding site for EVA1 with CCL3 was extracted from PDB structure 3FPU. Binding sites for EV974 with CCL17 and CCL7 were extracted from PDB structures 7S4N and 7SO029[127]. Abbreviations: ck:bind, chemokine binding sites; cys, cysteine; dsb, disulphide-bonded cysteine; ROI, region of interest; cilog2E, 95% confidence interval of the median rlog2E for the entire protein. Figure was constructed by SB, with data generated by SV and KH[141].

The phage display library was screened against 25 biotinylated chemokines attached to streptavidin-coated magnetic beads. Alongside the chemokines, biotinylated complement C5a was added as a negative control to remove any non-specific binders (during analysis), as it shares similar characteristics with chemokines, including molecular weight, extracellular location, GPCR binding, and chemotactic function[144]. I screened the EVAA phage display library against CXC and CX3C chemokines, and Katrin Hafner screened the library against CC chemokines. As seen in **Figure 3.2.1**, after three selection rounds, the enrichment (E) for each peptide with each chemokine was calculated and compared to the input library to be expressed as log2E, which correlates to binding affinity[145].

3.2.3 Phage Display Identifies Peptides That Coincide with Established Chemokine Binding Sites

As seen in **Figure 3.2.2**, each peptide was mapped to the parental evasin sequence based on the log2E for each peptide and chemokine. Certain regions in the parental sequences (namely EVA4, EV672, EV974, EV546) were clustered due to overlapping hexadecapeptides binding to a large range of chemokines at a high binding affinity. Within these clusters, regions of interest (ROI) were calculated to find specific regions on the parental sequence that could bind to multiple chemokines at a high binding affinity. Regions of interest were calculated when the residue log2E, the sum of log2Es of peptides overlapping a residue, exceeded the upper boundary of the 95% confidence interval of the median rlog2E. ROIs were seen to overlap with known chemokine binding sites for EVA4, EV672 and EV974. Interestingly, it was unexpected that the class A-derived hexadecapeptides could bind to multiple chemokine classes, including CX3CL1 and CXC chemokines like CXCL1, CXCL5, CXCL8, CXCL10, CXCL11, CXCL12B and CXCL13 given that class A evasins are known to specifically bind only to CC class chemokines.

3.2.4 Broad-Spectrum Chemokine-Binding Peptides Identified from EVAA Library Using Phage Display

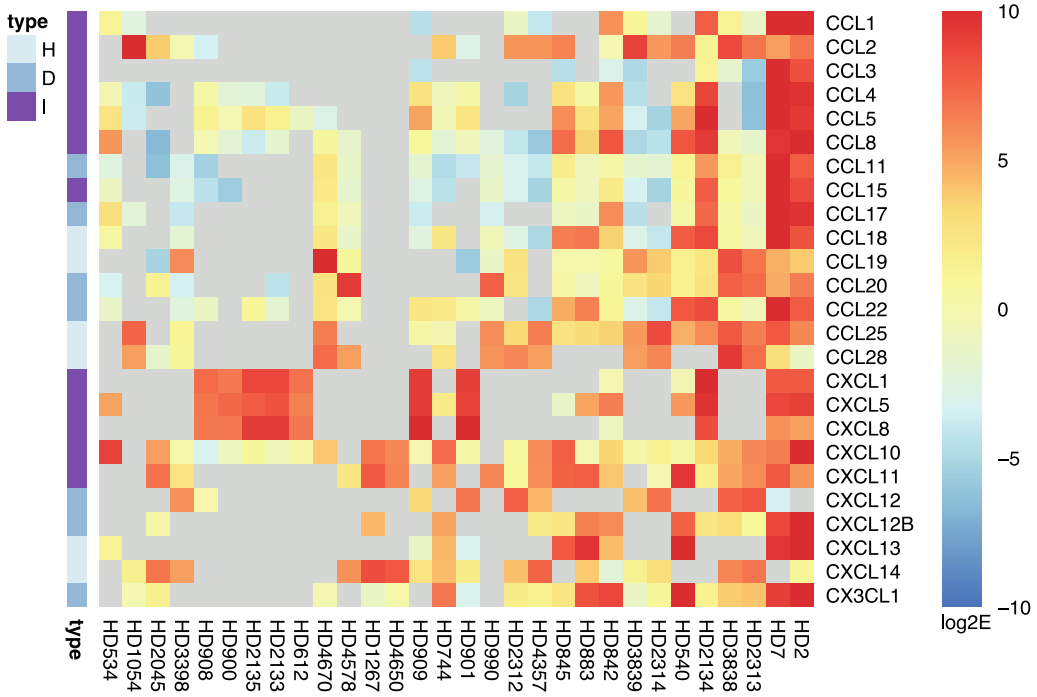

Figure 3.2.4: Top 30 peptides identified with broad-spectrum binding. Tile plot heatmap displaying the log2E values of 30 peptides that specifically bind to at least three chemokines with log2E > 5. Rows represent the selected chemokines, while columns represent the peptides. Peptides are organised by the total number of chemokines they bind to with log2E > 5. The scale bar indicates log2E values. Grey tiles denote peptides not recovered following the screen. Chemokine types are shown: I = inflammatory, D = dual, H = homeostatic. Figure created by SB[141].

To overcome the redundant chemokine network, the list of peptides was filtered for high binding affinity and binding to a broad number of chemokines. This filter included peptides that bound to at least three chemokines and possessed a log2E>5. This narrowed the list to 30 peptides. Nine of the peptides that contained the Cys to Ala or Cys to Ser mutation were mutant versions of the 12 wild-type peptides, and the other 18 were wild-type containing one or more Cys residues. **Figure 3.2.4** shows a heatmap of the 30 peptides and their individual log2E values; some of these peptides, namely HD2 and HD7, are highly promiscuously binding to the majority of the chemokines and to different chemokine classes. There are notable differences in the binding pattern of CXCL12 and CXCL12B, its isoform; this may be due to the tag placement on CXCL12[146,147], as well as extra residues at the C-terminus of CXCL12B could alter the distance of the biotin tag from the peptide-binding site.

3.2.5 Sequence Alignment Uncovers a Conserved Motif Containing an Unpaired Cysteine Residue

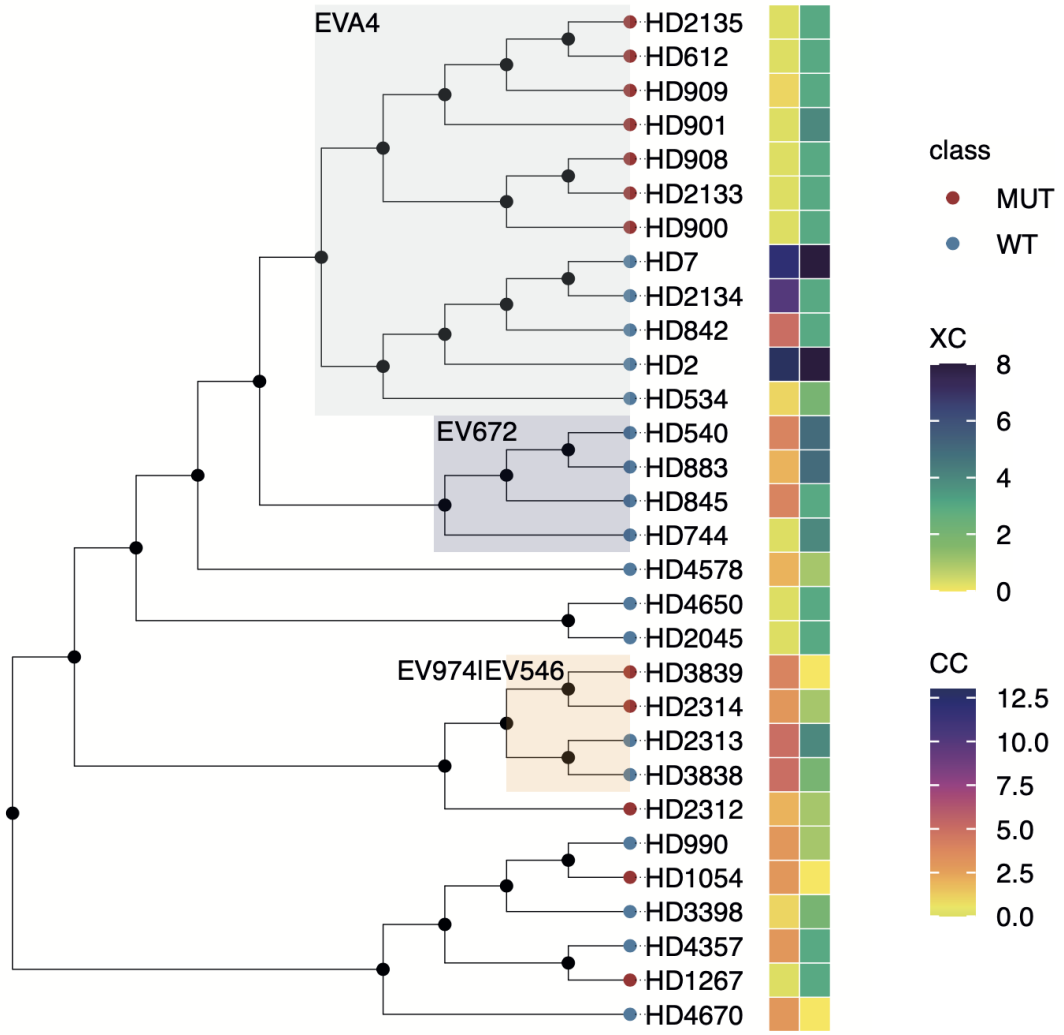

Figure 3.2.5.1: Neighbour-joining tree of peptides with identities indicated at the tree-tops. The ancestral node is defined by midpoint rooting. Peptides derived from EVA4, EV672, and EV974 are highlighted in azure, navy, and orange. The accompanying heat map displays the number of CC or XC chemokines bound with log2E > 5. Mutant (MUT) and wild-type (WT) tip nodes are also indicated. Figure created by SB[141].

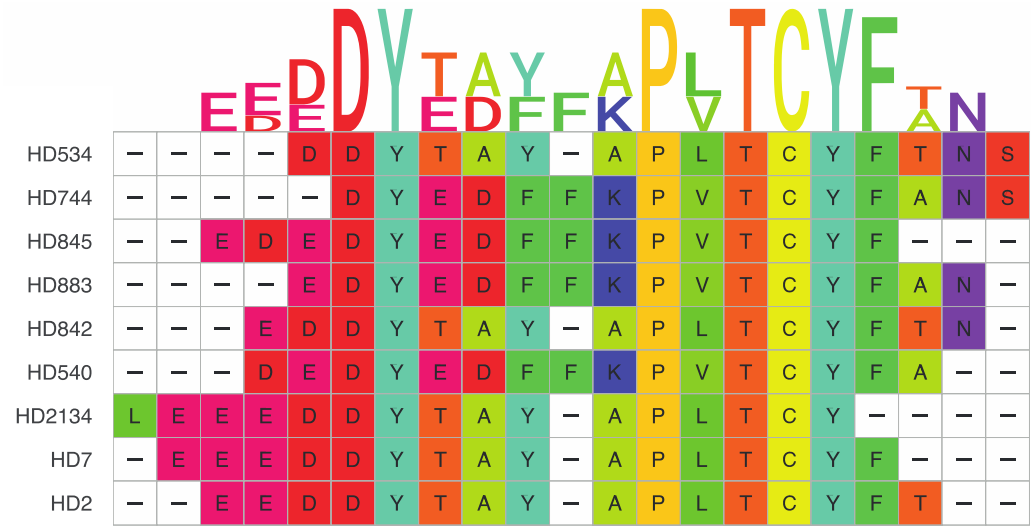

Figure 3.2.5.2: A sequence alignment of the wild-type peptides derived from EVA4 and EV672. The logo represents the amino acid residues coloured according to the Taylor scale, with the size of the logo correlating to the alignment. Figure created by SB[141].

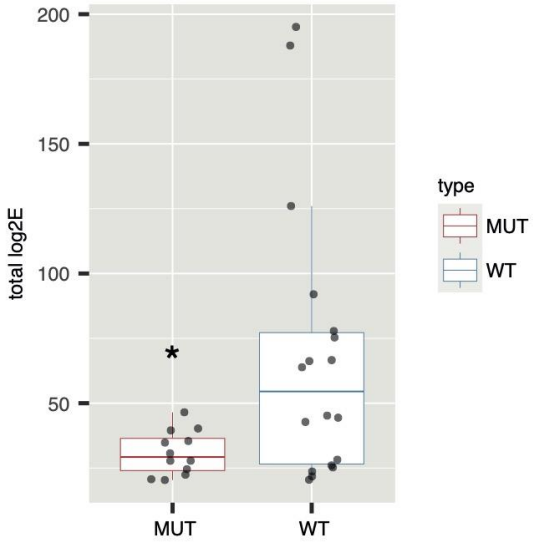

Figure 3.2.5.3: Box-and-whisker plot showing the effect of Cys to Ala or Cys to Ser (MUT) mutations compared to wild-type (WT) for a subset of the top 30 peptides. The y-axis shows the total log2E, with individual peptide data points. The box-and-whisker plot displays the median as the centre line, the 25th and 75th percentiles as the box bounds, and 1.5 times the interquartile range as the whiskers. A statistically significant difference between the WT (18 peptides) and the MUT (12 peptides) groups was observed using one-way ANOVA). Figure created by SB[141].

The two evasins with the largest overlapping wild-type peptides were EVA4 and EV672, followed by EV974 and EV546. These evasins EVA4 and EV672 are quite similar to each other as being in the neighbour-joining tree in **Figure 3.2.5.1**, and so multiple sequence alignment was performed on the peptides from 30 peptides derived from these two evasins. Two conserved regions were identified, as seen in **Figure 3.2.5.2**: E(E/D)(E/D)DY near the N-terminus and P(L/V)TCYF near the C terminus.

The effect of mutating the Cys residues in phage display was investigated. The log2E for each peptide with all chemokines tested was measured to give the overall binding affinity. As seen in **Figure 3.2.5.3**, the wild-type peptides have significantly higher total log2E compared to the Cys to Ser or Cys to Ala mutant peptides, indicating that the unpaired Cys residues in the second conserved motif are vital for chemokine binding affinity.

3.3 DISCUSSION

In this chapter, phage display successfully identified peptides from class A tick evasins that bound to chemokines across multiple chemokine classes, supporting the hypothesis. This is a significant and novel discovery, as it demonstrates that these peptides have a broader chemokine-binding capability compared to previously identified evasin-derived peptides, which were known to bind only to a single chemokine class. This broader binding specificity was not previously recognised in the field. The ability of these peptides to target multiple chemokine classes suggests they could serve as broad-spectrum chemokine inhibitors, offering potential therapeutic applications for complex inflammatory conditions like atherosclerosis, where multiple chemokine classes contribute to disease progression[78].

There is confidence in the peptides pulled from phage display as regions of interest align with previously identified chemokine binding peptides such as EV672:CCL8[133] complex identified by HDXMS, EVA4:CCL5[134] identified by NMR and EV974 complexes with CCL7 and CCL17 by X-ray crystallography[127]. The exemplar peptide, HD2, is in the same region as the EVA:CCL5 peptide, identified from NMR spectroscopy; compared to HD2, it contains a Cys to Ala mutation and is revealed only to inhibit CCL5. As aforementioned, EVA4 and EV672 are very similar, and so are their respective peptides, such as HD2 and HD845. HD845 was previously reported as BK1.5, which was part of the BK series identified using HDXMS[133]. Similar to the EVA4:CCL5 peptide, no CXC chemokine class interaction was reported with the BK peptides. These peptides were not tested against CXC chemokines due to the belief that they would not bind or inhibit them, as they came from a CC-only binding class A evasin.

This broader binding capability seen by the peptides may be due to them being shortened sequences of the evasins, potentially allowing access to binding sites on CXC chemokines that are inaccessible to full-length evasins. An alternative explanation is that the peptides have a novel binding mode to chemokines that evasins do not possess, possibly due to the

smaller size of these peptides reducing steric hindrance, facilitating binding to a broader range of chemokine classes.

A potential limitation of phage display is its ability to select chemokine peptide binders. Peptides with potential chemokine binding ability may be overlooked if they do not display well on the phage or are not effectively enriched during the selection process. Additionally, the phage display library may not encompass all possible peptide sequences, potentially missing highly effective chemokine-binding candidates. To mitigate this, cloning efficiency quality checks (QC) of the input library were performed using next-generation sequencing (NGS), which confirmed that 98% of the inserts were present. A high coverage ensures a wide variety of peptides is represented.

Another limitation is that peptides are fused to the p8 phage coat via the C-terminus. This fusion position may restrict the peptides' exposure to the chemokine and may prevent interactions with the C-terminal region of the peptides. This configuration could potentially exclude peptides that inhibit chemokines through their C-terminal residues. Future iterations of the library design could consider alternative fusion strategies to diversify peptide exposure and interaction with the chemokine.

Non-specific binding is another challenge, as peptides might bind non-specifically to the plastic of the plate wells or the chemokine itself. To address this issue, strict washing steps were implemented after each incubation period, and the chemokine and peptide were transferred to a fresh plate to minimise non-specific interactions. Additionally, a negative control, complement C5a, was included. Any peptide that was bound to C5a was excluded from the dataset to ensure that only peptides pulled from phage display specifically targeted chemokines.

An important consideration is that chemokine binding does not necessarily equate to chemokine inhibition. Several factors could affect the results despite phage display identifying peptides with high binding affinity. Biotinylated chemokines immobilised to the bottom of the well may not adopt the same conformation as they do in physiological

conditions, potentially leading to the selection of non-optimal inhibitors. Furthermore, the selection process might favour peptides that display well on phage rather than those that are the most effective inhibitors. Peptides displayed on the phage coat can exhibit higher avidity due to multivalent interactions (peptide displayed 2700 times on phage coat), which might lead to the selection of peptides that possess lower binding affinity when tested as individual peptides. Furthermore, chemokine binding may not occur at the functional binding site, which again may limit the effectiveness of inhibition.

Identifying binding peptides is just the first step, and functional assays are required to confirm that these peptides can effectively and specifically inhibit chemokine activity. This important aspect of the research will be explored in the next chapter.

CHAPTER 4: CHARACTERISATION OF THE CLASS A DERIVED PEPTIDE: HD2

4.1 INTRODUCTION

Chapter 3 focused on the identification of short hexadecapeptides derived from class A evasins, identified through a phage display screening process. This screening involved the EVAA library, which was tested against 24 biotinylated chemokines simultaneously. Several peptides were identified from this process, demonstrating the ability to bind to chemokines. Certain regions of interest (ROI) from the results aligned with previously established chemokine binding sites, with a particularly distinct peak observed in the EVA4 subpanel. Unexpectedly, these peptides showed binding to multiple chemokines across different classes, a surprising finding given that class A evasins typically bind to only one chemokine class, CC chemokines[97].

Further analysis of the phage display results focused on binding affinity (log2E > 5) and the ability to bind at least three chemokine classes. Among the identified peptides, HD2 stood out, demonstrating the highest binding affinity and the broadest range of chemokine interactions.

The identification of peptides with broad chemokine-binding capabilities is particularly significant, as it suggests potential for broader therapeutic applications. Chemokine redundancy is a major challenge in therapeutic development because targeting a single chemokine or receptor often fails to produce the desired therapeutic outcome. This is due to compensatory mechanisms within the chemokine network[139]. An example is the CCR5 antagonist Maraviroc, effective in other contexts but was unsuccessful in reducing inflammation in patients with rheumatoid arthritis[101]. To overcome this redundancy, effective therapeutic strategies must simultaneously target multiple chemokines or receptors.

Building on the findings from Chapter 3, Chapter 4 focuses on assessing whether the identified peptides exhibit functional activity by inhibiting chemokine function, specifically through chemotaxis assays. Evaluating the functional activity of these peptides is crucial, as some peptides may demonstrate strong binding affinity, but they could still be poor inhibitors. This discrepancy might occur if the peptides bind strongly to the chemokine but not at its active site, where it interacts with the receptor. Chemotaxis assays will reveal whether their binding translates into effective inhibition of chemokine-driven processes, such as cell migration (chemotaxis).

Through these experiments, I anticipate identifying peptides that not only bind to chemokines but also effectively inhibit their activity, paving the way for the development of new therapeutic agents. This chapter specifically explores the hypothesis that the hexadecapeptides identified through phage display in Chapter 3, especially HD2, can functionally inhibit multiple chemokines and possess a broad chemokine-binding range, potentially overcoming chemokine redundancy. The aim is to characterise the exemplar peptide HD2 and identify its key residues responsible for binding.

This work has been published in Vales *et al.*[141]

4.2 RESULTS

4.2.1 Selection and Functional Testing of Peptides for Chemokine Inhibition

To identify peptides with the broadest chemokine-inhibiting potential, the class A evasin phage display screen was initially examined (**Figure 3.2.2**). The high peak clearly observed in the EVA4 subpanel indicated that HD2 was particularly interesting due to its high binding affinity and ability to bind to the greatest number of chemokines. Based on this finding, HD2 was selected for further investigation to determine its chemokine inhibitory activity.

In addition to HD2, other peptides, specifically HD1, HD3, HD5, HD6, HD8, and HD9, were selected for preliminary testing. These peptides, derived from various class A evasins, were initially chosen based on their binding affinity to myocarditis-associated chemokines before the top 30 peptide list was generated (**Figure 3.2.4**). The primary objective was to assess whether these peptides, identified through phage display, exhibited functional chemokine inhibition.

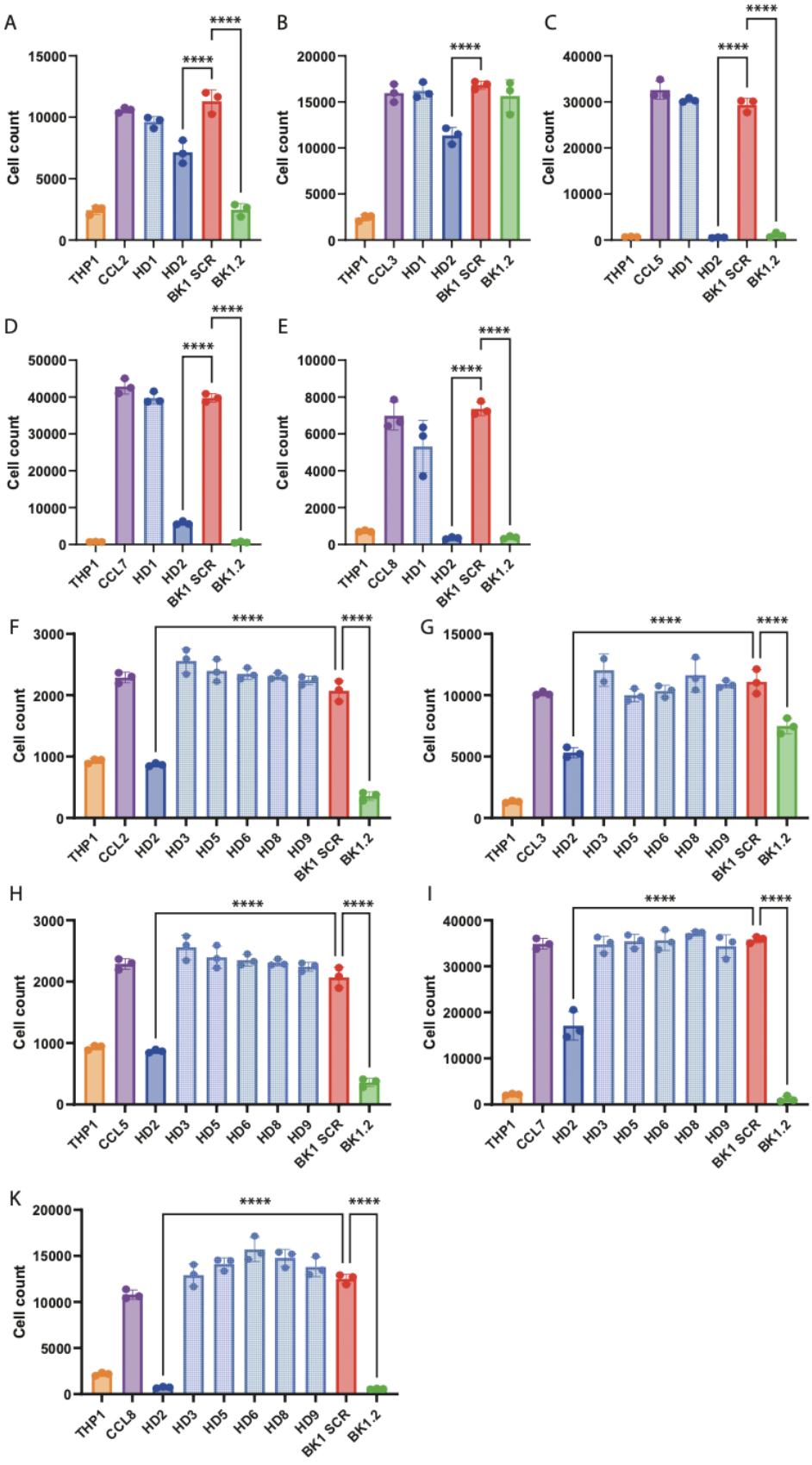
A
B
C
D
E
F
G
H
I
K
Cell count
****
THP1
CCL2
CCL3
CCL5
CCL7
CCL8
HD1
HD2
HD3
HD5
HD6
HD8
HD9
BK1 SCR
BK1.2

Figure 4.2.1.1: Preliminary chemotaxis screening of peptides. Each experiment was performed with three technical replicates, with individual data points shown. The y-axis represents the cell count, while the x-axis indicates the chemokines and peptides tested using THP1 cells. BK1SCR (scrambled BK1) was used as a negative control and BK1.2 as a positive control. All peptides tested were at 10 μM final concentration with chemokines used at EC80 concentrations. Statistically significant differences (compared to control HD2SCR, coloured red) were assessed using one-way ANOVA followed by Dunnett's test for multiple comparisons, indicated by asterisks: ****p ≤ 0.0001, ***p ≤ 0.001, **p ≤ 0.01, *p ≤ 0.1.

HD2, the other HD peptides, BK1.2 (positive control) and BK1 SCR (negative control) were tested in cell migration assays to assess their ability to inhibit chemokine-induced migration of THP1 cells. Each peptide was tested at 10 μM final concentration against the respective chemokine EC80 dose (CCL2, CCL3, CCL5, CCL7, CCL8). From this preliminary testing, as it is clear in **Figure 4.2.1.1**, HD2 demonstrated superior inhibitory activity across all these chemokines compared to the other tested peptides. This preliminary finding displays the effectiveness of phage display in identifying potent chemokine-inhibiting peptides. However, biological replicates will need to be performed on HD2 to validate this finding, which will be explored later in the chapter.

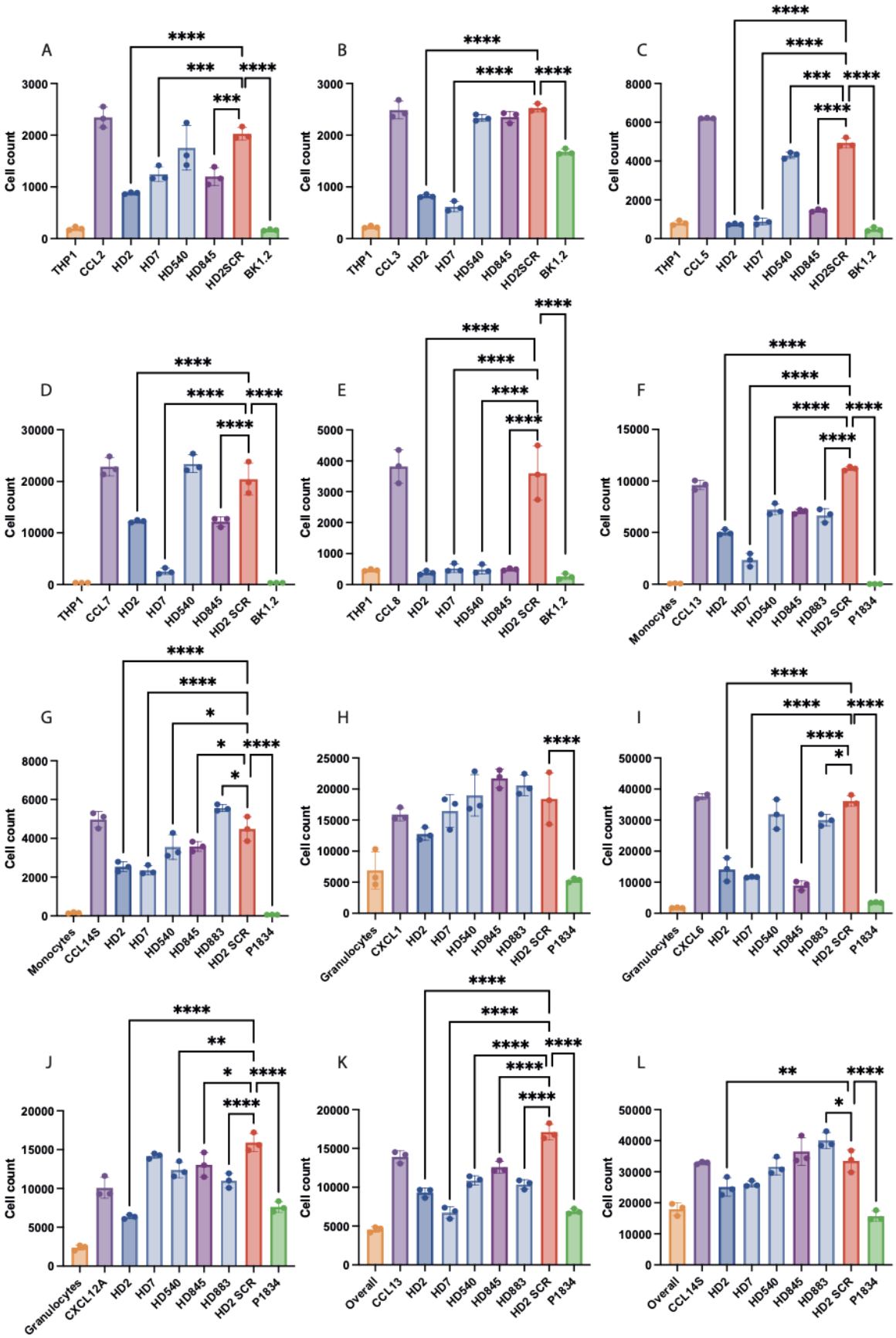
A
Cell count
THP1
CCL2
HD2
HD7
HD540
HD845
HD2SCR
BK1.2
B
CCL3
C
CCL5
D
CCL7
HD2 SCR
E
CCL8
F
Monocytes
CCL13
HD883
P1834
G
CCL14S
H
Granulocytes
CXCL1
I
CXCL6
J
CXCL12A
K
Overall
L

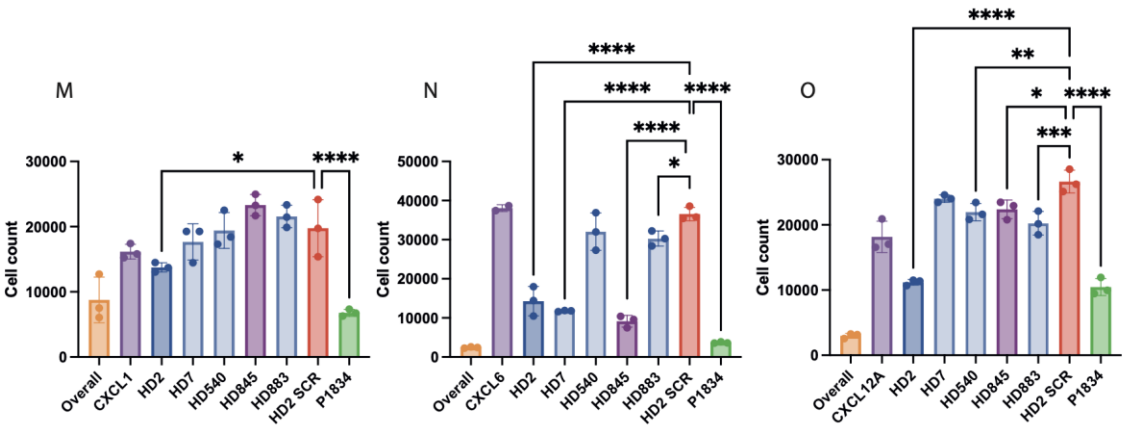

Figure 4.2.1.2: Preliminary chemotaxis screening of selected peptides from the top 30 list for inhibition of chemokine-induced migration. Each experiment was conducted with three technical replicates, with individual data points shown. The y-axis in each panel represents cell count. The x-axis shows the constituents of each experiment, with chemokine and cell type names indicated. Panels **A-E** use THP1 cells, while panels **F-O** use buffy coat cells. HD2SCR is a scrambled version of HD2 used as a negative control. BK1.2 and P1834 were used as a positive control. All peptides tested were at 10 μM final concentration and chemokines at EC80 doses. Statistically significant differences (compared to control HD2SCR, coloured red) were identified using one-way ANOVA followed by Dunnett's test for multiple comparisons, indicated by asterisks: ****$p \leq 0.0001$, ***$p \leq 0.001$, **$p \leq 0.01$, *$p \leq 0.1$.

Following the generation of the top 30 peptide list (**Figure 3.2.4**), additional peptides were chosen and screened alongside HD2 in preliminary screenings. The additional peptides included HD7 (also an EVA4-derived peptide, with a single amino acid difference from HD2), HD540, HD845, and HD883 (EV672-derived peptides). The choice of HD7, HD845, and HD883 was guided by their initial binding profiles, which were bound to at least three different chemokine classes and the log2E>5.

Figure 4.2.1.2 shows that when tested against the chemokines CCL2, CCL3, CCL5, CCL7 and CCL8 with THP1 cells and CCL13, CCL14S, CXCL1, CXCL6 and CXCL12A using buffy coat cells. The HD2, HD7, HD845, and HD540 peptides displayed varying degrees of inhibition. HD2 consistently demonstrated the broadest range of inhibition, excitingly extending to CXC chemokines despite being derived from a CC-specific evasin. HD7 also showed broad chemokine binding, to CCL2, CCL3 CCL5, CCL7, CCL8, CCL13, CCL14S and CXCL6 (granulocytes and buffy coat). HD845, derived from EV672, showed moderate inhibition, significantly affecting all tested CC chemokines, except CCL3 and CCL14S, and showed inhibition to CXCL6 and CXCL12A. HD883, tested specifically on buffy coat cells against CCL13, CCL14S, CXCL1, CXCL6, and CXCL12A, exhibited only slight inhibition of CCL13, CXCL6 and CXCL12A.

Overall, HD2 emerged as the most potent peptide, with the broadest chemokine inhibition profile, including CXC chemokines. This interesting result led to the decision to characterise HD2 in detail further to understand its potential as a broad-spectrum chemokine inhibitor.

4.2.2 HD2 Peptide Possesses CC and CXC Inhibitory Activity

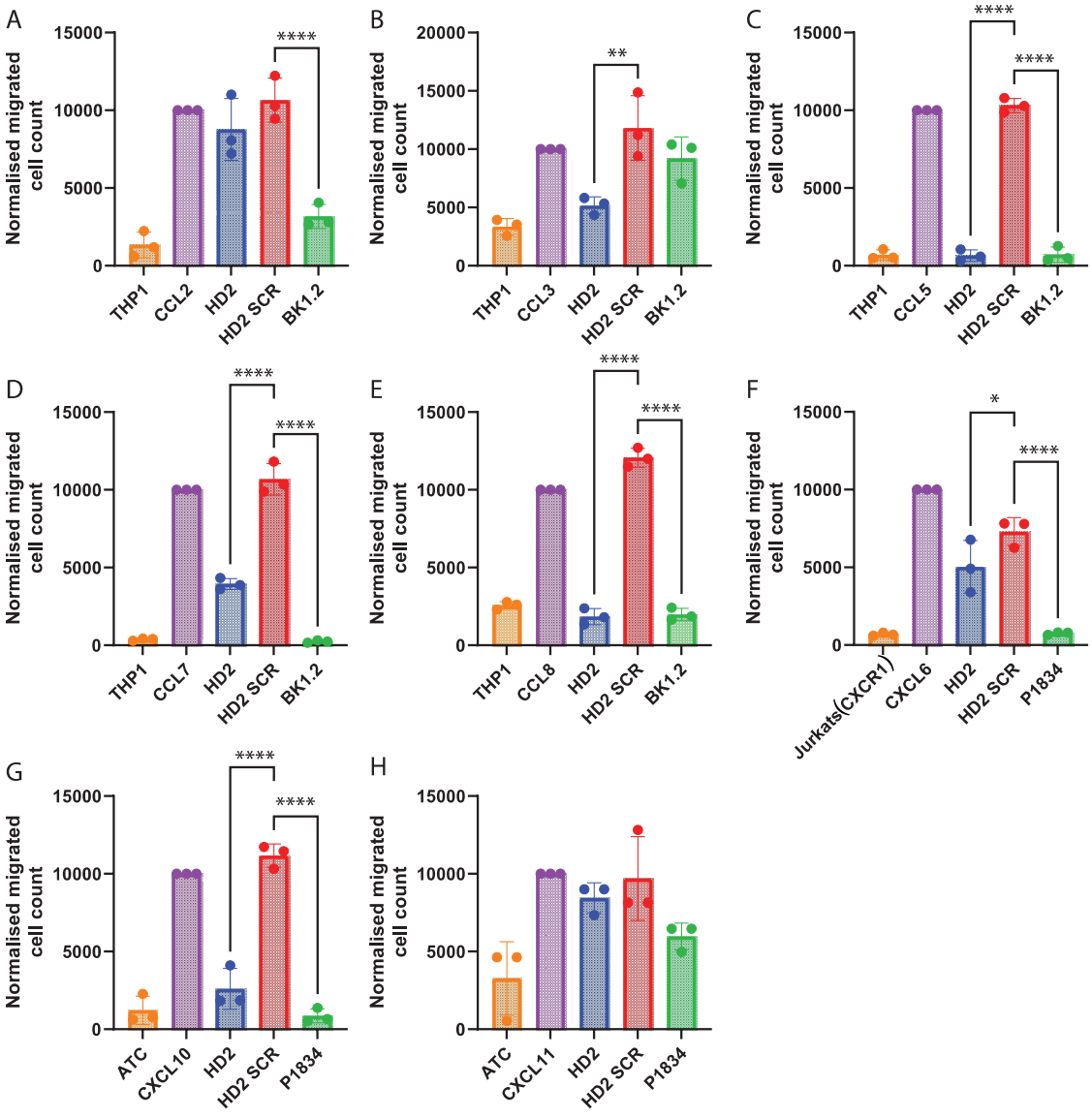

Figure 4.2.2.1: Bar chart with SD error bars showing the effect of the peptide HD2 on cell migration induced by CCL7, CCL8, CXCL6, CXCL10 and CXCL11. Each experiment was performed with three technical and three biological replicates, with individual biological replicate data points (mean of technical replicates) displayed. The y-axis in each panel represents cell count, normalised to the mean value of migrated cells in the presence of chemokine only, set at 10,000 cells. The x-axis shows the constituents of each experiment, with chemokine and cell type names indicated. HD2SCR is a scrambled version of HD2 used as a negative control. All peptides tested

were at 10 μM final concentration and chemokines at EC80 doses. Statistically significant differences (compared to control HD2SCR, coloured red) were identified using one-way ANOVA followed by Dunnett's test for multiple comparisons, indicated by asterisks: ****$p \leq 0.0001$, ***$p \leq 0.001$, **$p \leq 0.01$, *$p \leq 0.05$.

After confirming that HD2 possesses functional inhibitory activity, I wanted to validate and further characterise its effects on specific chemokines. Chemotaxis assays were performed with HD2 and its scrambled version (HD2 SCR) as a negative control to determine whether inhibition was due to the specific sequence or the amino acid composition. For comparison, BK1.2, a previously reported CC chemokine inhibitor[133], was used as the positive control, or P1834, a triple-warhead protein developed in our lab (unpublished), which is known to inhibit CC and CXC chemokines, was also used as a positive control against CXC chemokines.

As shown in **Figure 4.2.2.1**, HD2 significantly inhibited cell migration in response to chemokines from both the CC (CCL3, CCL5, CCL7, CCL8) and CXC (CXCL6, CXCL10) classes compared to the HD2 SCR control. While HD2 also showed slight inhibition of CCL2 and CXCL11, these effects were not statistically significant.

Live/dead staining was conducted with HD2 and HD2SCR peptides to confirm that the reduction in cell migration was not due to peptide toxicity (**Appendix 5 and 6**), and no toxicity was observed.

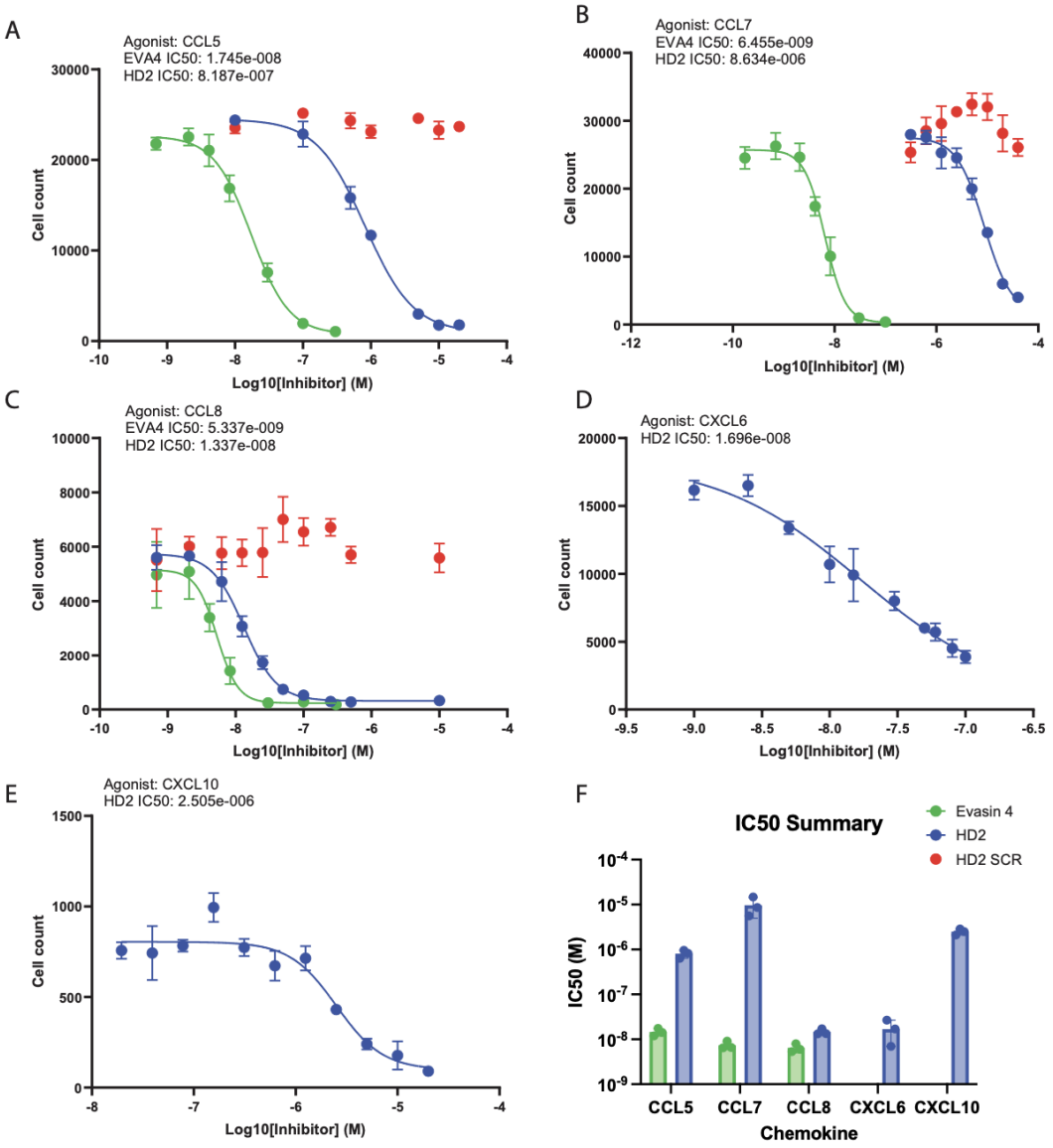

Figure 4.2.2.2: The potency of HD2 and EVA4 on chemotaxis response. (**A-E**) Inhibitory dose-response curves showing the effect of HD2 (blue) and EVA4 (green) on human-induced chemokine migration of THP1 (CCL5, CCL7 and CCL8) or Jurkat CXCR1 (CXCL6) or activated T cells (ATC) (CXCL10). HD2 SCR (red) was used as the negative control. The y-axis shows the migrated cell count. The x-axis shows the inhibitor concentration (M). These IC50 curves were calculated using a 4-parameter log-logistic fit. The EVA4 IC50 curves could not be produced for CXCL6 and CXCL10 because EVA4 does not inhibit CXC chemokines. (**F**) Summary of IC50 average values of HD2 and EVA4 against the respective chemokines. The y-axis shows the IC50 values in molar (M), and the x-axis indicates the chemokine. Each inhibitory experiment was performed as three biological replicates, and each data point was performed as three technical replicates. CXCL6 and CXCL10 experiments were performed by GS and MP, respectively.

To investigate the potency of HD2, inhibitory dose-response curves (IC50 curves) were performed for several chemokines, including CCL5, CCL7, CCL8, CXCL6, and CXCL10 (**Figure 4.2.2.2**). The IC50 value represents the concentration of HD2 required to inhibit cell migration by 50%, providing a measure of its potency. As EVA4 specifically binds and inhibits CC chemokines, therefore IC50 curves for EVA4 could not be generated against the CXC chemokines CXCL6 and CXCL10. The average IC50 values for HD2 ranged from as low as 0.015 μM for CCL8 to 2.49 μM for CXCL10, indicating variable potency across different chemokines.

4.2.3 Alanine-Scanning Mutagenesis - Correlation Between Binding Affinity and Inhibitory Activity

To assess the impact of alanine mutations on HD2's inhibitory function, synthetic alanine-substituted peptides were tested in chemotaxis assays against a range of chemokines, including CCL5, CCL7, CCL8, CXCL6, and CXCL10, with HD2 as the control (**Figure 4.2.3.1**). For CCL5, significant reductions in inhibition were observed with alanine substitutions at positions 4 (D), 8 (Y), 10 (P), 13 (C), and 14 (Y). In the case of CCL7, substitutions at positions 1 (E), 4 (D), 5 (Y), 8 (Y), 10 (P), 13 (C), and 14 (Y) also led to decreased inhibition. CCL8 inhibition was primarily affected by the proline-to-alanine substitution at position 10. For CXCL6, significant effects were seen with substitutions at positions 10 (P), 11 (L), 13 (C), and 15 (F). Similarly, CXCL10 inhibition was impaired by mutations at positions 8 (Y), 11 (L), 13 (C), 14 (Y), and 15 (F). These results highlight the critical role of specific residues in HD2's ability to inhibit various chemokines.

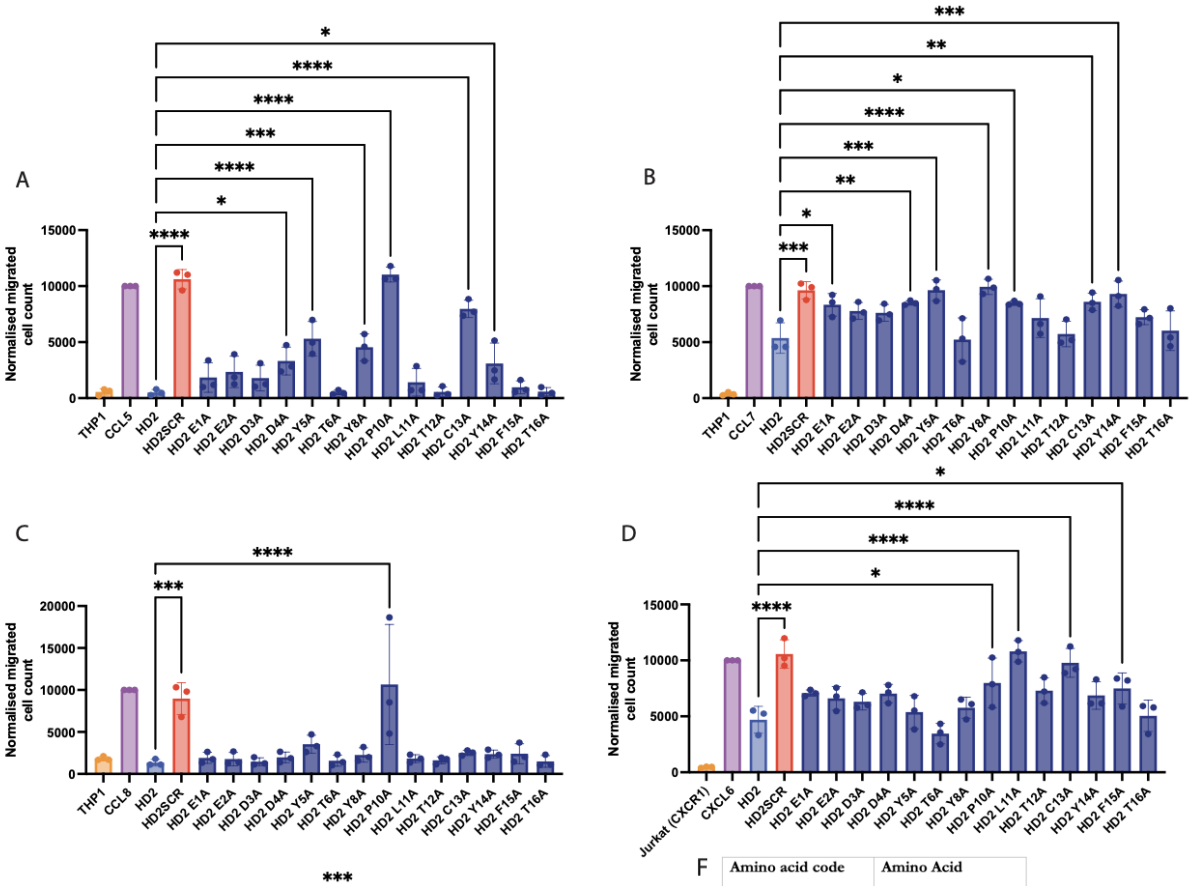

F

Amino acid code	Amino Acid
E	Glutamic acid
D	Aspartic acid
Y	Tyrosine
T	Threonine
P	Proline
L	Lysine
C	Cysteine
F	Phenylalanine
A	Alanine

Figure 4.2.3.1: Bar chart with SD error bars showing the effect of alanine mutations in HD2 alanine mutant peptides on cell migration induced by CCL5, CCL7, CCL8, CXCL6 and CXCL10. The y-axis in each panel represents the cell count, normalised to the mean number of migrated cells in the presence of chemokine alone, set at 10,000 cells. The x-axis indicates the peptide tested, with corresponding chemokines (CCL5 (**A**), CCL7 (**B**), CCL8 (**C**), CXCL6 (**D**),

and CXCL10 (**E**)) and cell types (THP1 (**A-C**), Jurkat CXCR1 (**D**), and ATC (**E**)) noted. HD2SCR, a scrambled version of HD2, was used as a control. All peptides were tested at a final concentration of 10 μM and chemokines at EC80 doses. Each experiment was conducted with three technical and three biological replicates, with individual biological replicate data points (mean of technical replicates) shown. Statistically significant differences (compared to HD2 control, coloured in light blue) were determined by one-way ANOVA followed by Dunnett's test for multiple comparisons, with asterisks indicating significance levels: ****$p \leq 0.0001$, ***$p \leq 0.001$, **$p \leq 0.01$, *$p \leq 0.05$. CXCL6 assays were performed by GS. F) Table of amino acid abbreviations.

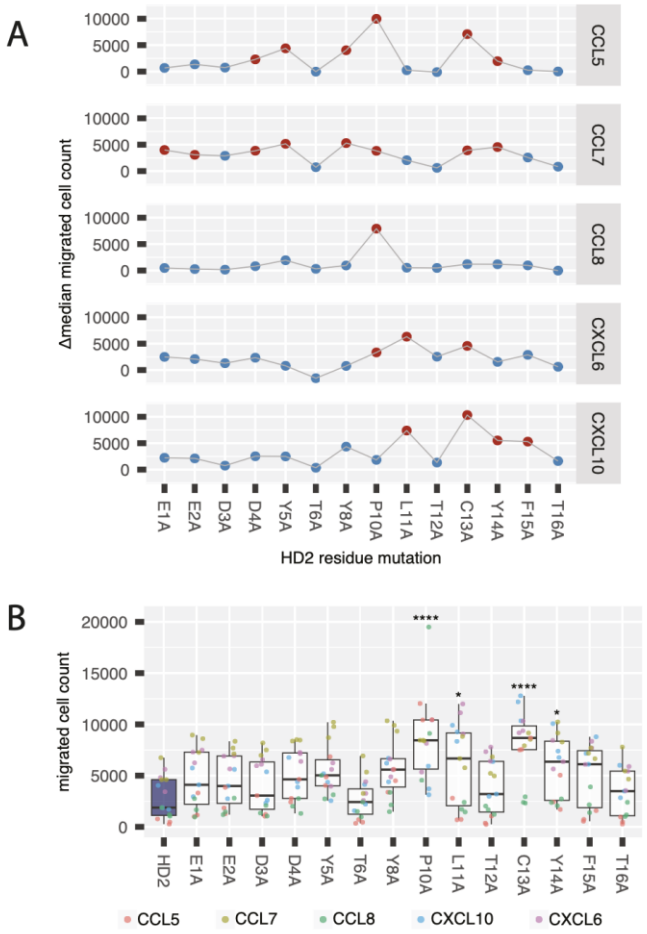

Figure 4.2.3.2: HD2 mutations effect on chemotaxis. A) Faceted plots illustrate the difference in median migrated cell count between alanine-mutant and wild-type HD2 peptides from cell migration assays (y-axis, Δmedian migrated cell count) relative to the alanine-substituted residue (x-axis). The chemokines used for each experiment are indicated at the end of each plot. Statistically significant differences compared to parental HD2 are marked as red dots. **B**) Box-whisker plot illustrating the impact of HD2 residue mutation to alanine (x-axis) on migrated cell count (y-axis) for all chemokines studied. Each experiment was performed as three biological replicates, with individual data points coloured according to the chemokine. The box-and-whisker plot displays the median at the centre, with the 25th and 75th percentiles forming the bounds and whiskers extending to 1.5 times the interquartile range. Statistically significant differences, compared to the control (shown in blue), are marked with asterisks using Dunnett's test with

correction for multiple comparisons: ****p ≤ 0.0001, ***p ≤ 0.001, **p ≤ 0.01, *p ≤ 0.05, with n = 15 observations per group (three biological replicates per chemokine).

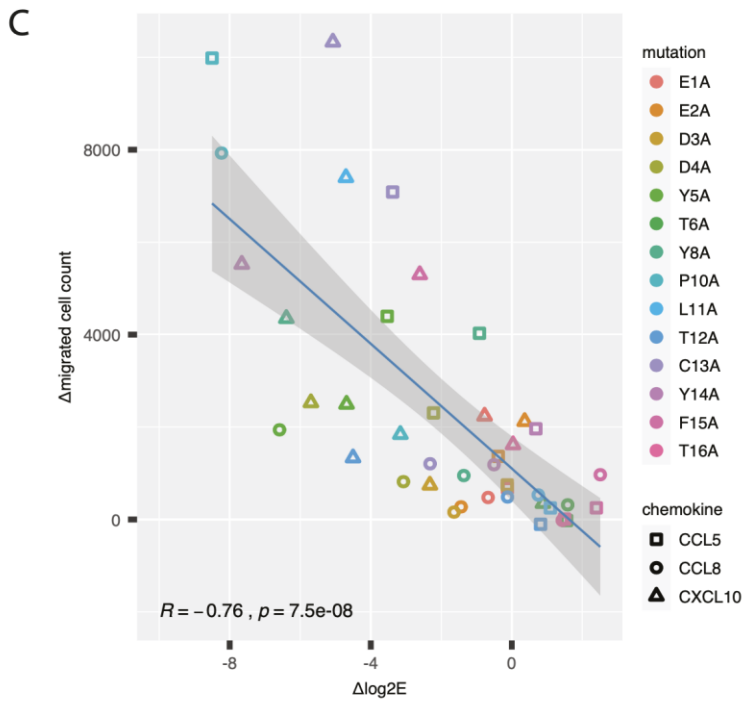

C) Phage binding and inhibitory potency correlation for alanine mutant HD2 peptides. Scatterplot of Δmedian migrated cell count (y-axis, cell migration assays) versus Δlog2E (X-axis, phage-display experiments) for peptide pairs. Individual data points represent peptide pairs for which cell migration and Δlog2E data were available. Linear regression plots show a 95% confidence interval, Spearman correlation coefficient (R), and statistical significance (p). Phage-display data generated by JK, chemotaxis data generated by SV and figure constructed by SB[141].

Figure 4.2.3.1 is summarised and simplified in **Figure 4.2.3.2A**. Overall, mutations at residues E1, E2, D4, Y5, Y8, P10, L11, C13, Y14, and F15 significantly impaired inhibition across all tested chemokines, as evidenced by the difference in migrated cell count compared to HD2. Notably, P10 was the only residue that specifically affected CCL8

inhibition. A meta-analysis of the alanine mutagenesis chemotaxis data (**Figure 4.2.3.2B**) identified P10, L11, C13, and Y14 as particularly critical for chemokine inhibition. Additionally, HD2 underwent saturation mutagenesis, where each residue was systematically mutated using an NNK codon (conducted by JK) to explore these interactions further. By comparing the binding affinity (Δlog2E—the difference in binding between the alanine-mutant HD2 and the parental HD2) from the mutagenesis phage display to inhibition (Δmigrated) in chemotaxis assays, a strong correlation was observed (**Figure 4.2.3.2C**). This correlation indicates that reduced chemotaxis inhibition is associated with reduced binding affinity, reinforcing the importance of binding affinity in effective chemokine inhibition.

4.3 DISCUSSION

In this chapter, peptides identified from phage display were also shown to possess functional chemokine inhibition using chemotaxis assays. A significant and novel finding was the inhibition seen by the exemplar peptide HD2, particularly as its parental evasin, EVA4, is known to target CC chemokines exclusively[121]. HD2 was shown to functionally inhibit CC chemokines (e.g., CCL2, CCL3, CCL5, CCL7, and CCL8) as well as CXC chemokines (e.g., CXCL6 and CXCL10). This broad-spectrum inhibitory ability suggests that HD2 has the potential to be developed into a therapeutic agent and overcome chemokine redundancy, which is currently lacking in many chemokine-targeting therapeutics[101].

Structural modelling efforts in the Bhattacharya lab provided insights into how HD2 may inhibit chemokine function. Using AlphaFold-2 Multimer predictions, we found that HD2 binding likely occludes chemokine receptor binding sites. For CCL8, HD2 is predicted to interact with key regions, including the N-terminus, N-loop, β3-strand, and the 30s and 40s loops. For CXCL10, HD2 is predicted to bind near the β1-strand and α-helix[141]. EVA4 was reported to interact between the N-loop and β3-strand of CC class chemokines, and HD2 may also bind to this region[134]. This suggests that HD2 exerts its inhibitory effect by preventing chemokines from interacting with their receptors and so disrupting their normal function[141]. However, structural experiments such as NMR or X-ray crystallography would need to be performed to confirm these in silico predictions.

Alanine scanning mutagenesis combined with chemotaxis assays investigate the importance of residues in functional inhibition of both CC and CXC chemokines. Saturation mutagenesis highlighted the importance of proline, indicated by the loss of inhibition when substituted, particularly for inhibition of CCL8, which is conserved within the HD2 sequence. Similarly, the mutation of proline in BK1.1 eliminated chemokine binding[133]. This suggests that structural rigidity may play a critical role in the peptide's function, with proline facilitating the necessary conformation[148].

An important limitation to consider is that although chemotaxis assays are valuable for testing the inhibitory effects of peptides on individual chemokines, they do not fully replicate the *in vivo* environment, where multiple chemokines influence cell migration. In inflammatory diseases, multiple chemokines are expressed, such as 16 CC and 7 CXC chemokines in atherosclerotic plaques[98] and 15 CC and 11 CXC chemokines in joint tissue with rheumatoid arthritis[149]. This contributes to a dynamic and complex environment that is difficult to replicate *in vitro*. As a result, chemotaxis assays may oversimplify the migratory responses of cells, potentially leading to results that only partially translate to physiological conditions.

The peptides tested in the chemotaxis assays used in this chapter were primarily tested on THP1 (to model monocytes/macrophages) or Jurkat cells (to model T lymphocytes). There are immense benefits to using immortalised cell lines, such as greater consistency and reproducibility, ease of culturing and cost-effectiveness, to name a few[150]. However, it is important to note the limitations of using immortalised cell lines, such as that they may not accurately represent primary cell receptor expression, signalling pathways, or cellular responses[150]. This can lead to responses to chemokine that may differ from primary cells derived directly from tissues. This discrepancy can impact the reliability of chemotaxis assays in predicting the behaviour of primary cells *in vivo*.

Complementing chemotaxis assays with other experimental approaches, such as *in vivo* models and animal studies, can provide additional representation of chemokine-mediated cell migration and allow for assessing peptide inhibitors in a physiological context. Moreover, using primary cells and organoids from relevant tissues in chemotaxis assays can help bridge the gap between *in vitro* and *in vivo* findings.

In the Bhattacharya lab, saturation mutagenesis was successfully performed on the HD2 sequence to improve its therapeutic potential (Kryukova, Vales *et al.*, manuscript submitted). In the next chapter, molecular evolution was similarly performed on a different peptide, HD845, to investigate whether this pipeline could be used with a

different peptide with a different starting point and also to improve its breadth and potency.

CHAPTER 5: CHARACTERISATION AND IMPROVEMENT OF HD845, A CLASS A EVASIN DERIVED PEPTIDE

5.1 INTRODUCTION

This chapter investigates the potential to expand the binding profile and affinity of the HD845 peptide through *in vitro* molecular evolution, using saturation mutagenesis followed by phage display. The hexadecapeptide HD845, derived from the class A evasin EV672, was identified in the EVAA phage display screen. This peptide was chosen for further study due to its ability to bind (as briefly discussed in Chapter 3) and inhibit multiple chemokines classes (as demonstrated in preliminary chemotaxis assays in Chapter 4). However, compared to HD2, HD845 exhibits a relatively narrower chemokine-binding range, binding to 18 chemokines compared to HD2's 22 chemokines, as shown in the phage display data (**Figure 3.2.4**).

Chemokine redundancy is a major challenge in therapeutic development because targeting a single chemokine or receptor often fails to produce the desired effect due to compensatory mechanisms within the chemokine network[139]. For example, Maraviroc, a CCR5 antagonist, did not succeed in reducing inflammation in patients with rheumatoid arthritis[101]. To overcome such redundancy, developing peptides that can target multiple chemokines or receptors is crucial. Improving the binding profile of HD845 could increase its potential as an effective therapeutic agent.

Using HDX-MS, a series of BK peptides were derived from the binding interface between the class A evasin EV672 and CCL8. BK1.1, a peptide from the series, is closely related to HD845, differing only by a Cys to Ala mutation at position 14. BK1.1 was reported to bind CCL7, CCL8, and CCL18 and proved to be a highly potent inhibitor of CCL8. Modifications to BK1.1 led to the creation of BK1.2 and BK1.3. BK1.2 was cyclised by

substituting alanine with cysteine at position 14, which formed a thioether bond with the tyrosine added at the N-terminus. BK1.3 was dimerised by adding a tyrosine at position 0 and replacing alanine with cysteine at position 14 to allow disulphide bond formation. These modifications significantly enhanced the inhibition of CCL2, CCL3, CCL7, and CCL8 and notably, the BK1.3 dimer demonstrated anti-inflammatory activity in an *in vivo* air pouch model[133]. The success of BK1.3, in particular, suggests that modifications could also be applied to HD845 to improve the chemokine-binding and inhibition profile.

The HD2 peptide discovered and characterised in my previous chapters underwent saturation mutagenesis followed by phage display to expand and improve the binding profile (Kryukova, Vales *et al.*, manuscript submitted). From this screen, a number of improved binders were identified and characterised in chemotaxis assays, but more importantly, the binding profile and affinity of HD2 were improved.

Building on findings from Chapter 3 and previous molecular evolution work on HD2 and the BK peptides and given that HD845 currently exhibits a narrower binding profile compared to HD2, this chapter aims to determine whether the binding profile and affinity of the HD845 peptide can be expanded and enhanced through saturation mutagenesis followed by phage display, leading to the identification of mutant peptides with improved functional inhibition of chemokines. This chapter hypothesises that these modifications will result in improved inhibition of chemokine-induced cell migration, overcoming the challenge of chemokine redundancy and potentially leading to more effective therapeutic agents.

5.2 RESULTS

5.2.1 HD845X Library Construction and Screening

To create the HD845X library, each residue in the HD845 sequence was systematically mutated by replacing the corresponding codon with an NNK codon (**Figure 5.2.1**). This allowed for the substitution of any of the 20 canonical amino acids at each position (where N represents any nucleotide: A, C, G, or T, and K represents G or T)[151]. The HD845X library also contained the parental HD845 peptide for comparison. The phage library was screened against a panel of 25 biotinylated chemokines (CC, CXC and CX3C chemokine classes) attached to streptavidin-coated beads to identify mutant HD845 peptides with improved chemokine binding breadth and affinity. Biotinylated complement C5a was added as a negative control to exclude non-specific binders from phage display analysis, as it shares similar characteristics with chemokines, including molecular weight, extracellular location, GPCR binding, and chemotactic function[144]. The phage library underwent three selection rounds, each using the previous amplified library, to filter weak or non-specific binders. After three rounds of selection, the samples were analysed for NGS to identify which peptide bound to which chemokine. Each mutant peptide's enrichment (E) with each chemokine was compared to the input library and expressed as log2E, which correlates with binding affinity[145]. The log2E value for each mutant peptide was then compared to the log2E of the parental HD845 for the corresponding chemokine to calculate the Δlog2E (difference in log2E).

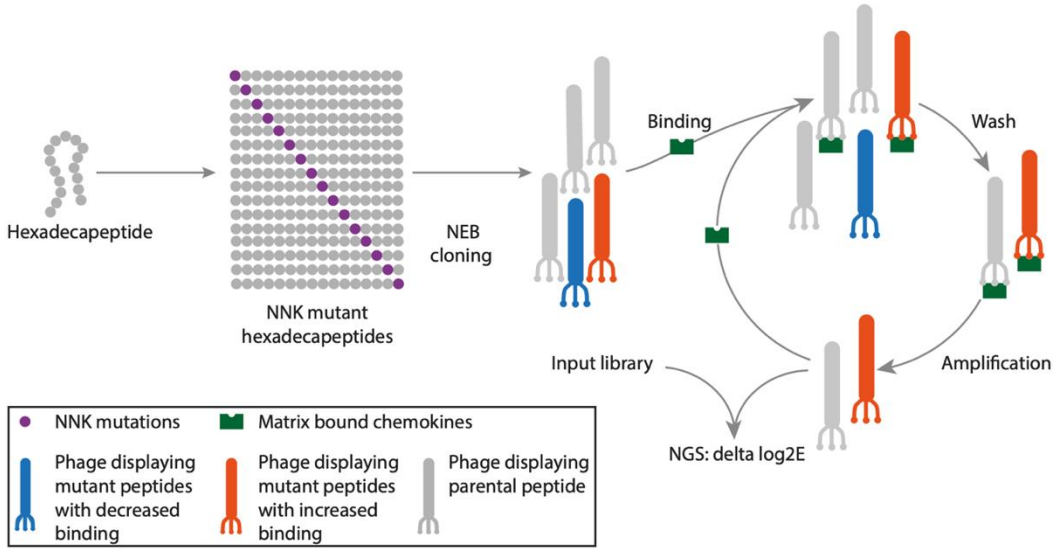

Figure 5.2.1: Phage display of HD845 NNK library to screen all single point mutations against chemokines. Each amino acid position in the HD845 sequence was randomly substituted with any of the 20 amino acids by an NNK codon. The oligonucleotides were pooled together, PCR amplified and cloned into a prSTOP4 phagemid vector, creating a phagemid pool. The pools were then transfected into *E. coli* and helper phage were added to generate the input phage display library. The phage library was amplified by PCR, and the amplicon was analysed using next-generation sequencing (NGS) to verify correct sequences and ensure high coverage. The phage library was incubated with matrix-bound 25 biotinylated chemokines to identify and select chemokine-binding peptides. Wells were washed to remove weak, non-specific binders. Bound phage were retrieved and allowed to infect T1-phage-resistant *E. coli* in the presence of helper phage to amplify the chemokine-bound binders. After three selection rounds, phage inserts were PCR amplified and analysed using NGS. Peptides binding to each chemokine were identified and expressed as log2E values, which were calculated as a ratio of enrichment (E), each peptide in the output library compared to the input library. The log2E value of each mutant peptide was compared to the log2E value of the parental HD845 for the corresponding chemokine to determine the Δlog2E (difference in log2E). Peptides binding to the negative control complement C5a were excluded from the analysis.

5.2.2 Identification and Selection of Improved HD845 Mutants

To identify the binding profiles of mutant peptides, the delta log2E (Δlog2E) for each mutant peptide across all tested chemokines was calculated. Two key metrics were used: the mean Δlog2E, which identifies mutant peptides with an overall improved binding affinity compared to the parental HD845, and the peak Δlog2E, which highlights mutant peptides with enhanced breadth of binding to specific chemokines. Both metrics were further categorised based on chemokine classes: CC and CXC (including CX3C) chemokines.

In the mean CC group (**Figure 5.2.2A**), the mutant peptide E6F showed the most significant improvement, with enhanced binding to CCL3, CCL4, and CCL5. In the mean CXC group (**Figure 5.2.2B**), the focus was on peptides with overall improved binding to CXC chemokines, where K10A stood out, demonstrating significant binding improvements to CX3CL1, CXCL8, and CXCL10. Across all chemokines based on mean Δlog2E (**Figure 5.2.2C**), E6W and K10A emerged as peptides of interest, with E6W showing enhanced binding to CCL1, CCL3, CCL4, CCL15, and CXCL8, and K10A showing improved binding to CXCL10. E6W was not included in the mean CC group because E6F displayed a greater binding affinity to CC chemokines, despite E6W also showing improved binding to these chemokines. When examining the peak Δlog2E groups for both CC and CXC chemokines, E6W showed greater chemokine breadth, while K10A again demonstrated improved binding to CXCL10 (**Figure 5.2.2D** and **E**). Based on overall improved binding breadth and affinity, a select number of peptides, particularly E6F, E6W, K10A, and K10W, were chosen for further characterisation (**Figure 5.2.2F**).

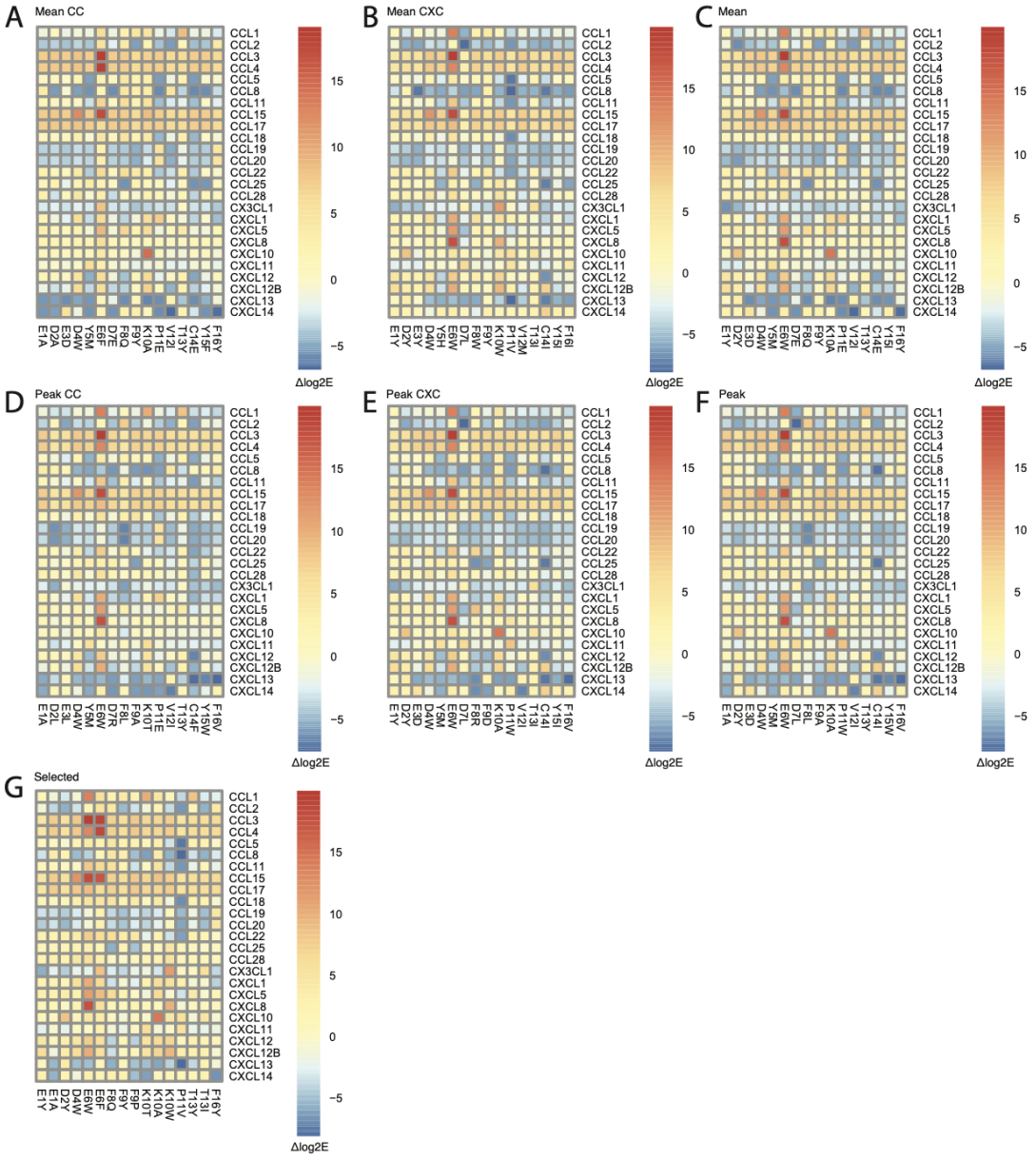

Figure 5.2.2: Tile plots depicting the effect of HD845 mutations on phage binding. The heatmap scale bar shows Δlog2E values, with enhanced binding (positive Δlog2E values) indicated in red and loss of binding (negative Δlog2E values) in blue. Tile colour representing the Δlog2E. Δlog2E is the difference in log2E between the parental peptide (HD845) and its mutant variants following phage display selection at each residue. (**A-C**) Tile plots displaying mutations selected for maximal enhancement of mean delta log2E. (**D-F**) Tile plots displaying mutations selected for maximal enhancement of peak delta log2E. (**A** and **D**) Enhancing mutations based on CC

chemokines. (**B** and **E**) Enhancing mutations based on CXC (including CX3C) chemokines. (**C** and **F**) Overall chemokine enhancement based on mean or peak analysis. (**G**) Summary of selected peptides taken forward for further analysis. Analysis of library performed by SB.

5.2.3 Improved Chemokine Inhibition with HD845 Mutants

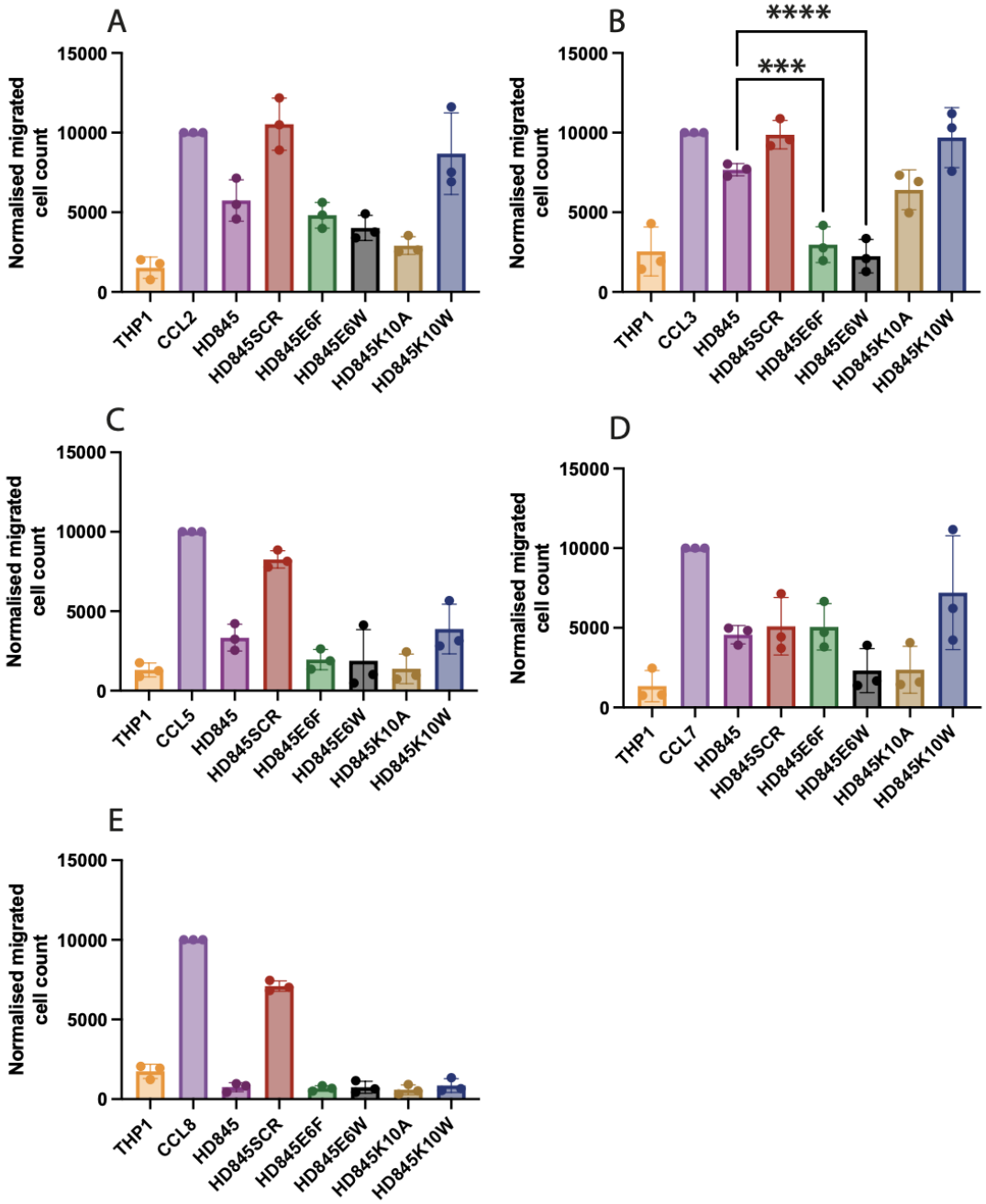

Figure 5.2.3: The effect of HD845 mutants on chemotaxis. Bar chart with SD error bars showing the impact of HD845 mutations on migration. Each experiment was performed in three technical and biological replicates, with individual biological replicate data points (mean of

technical replicates) displayed. The y-axis in each panel represents the cell count normalised to the mean value of migrated THP1 cells in the presence of chemokine only, set at 10,000 cells. The x-axis indicates the peptides and chemokines tested in each experiment. All peptides were tested at a 10 μM concentration against the chemokines at EC80 doses. Statistically significant differences compared to HD845, in darker purple, were identified using a one-way ANOVA followed by Dunnett's test for multiple comparisons and indicated by asterisks: ****$p \leq 0.0001$, ***$p \leq 0.001$, **$p \leq 0.01$, *$p \leq 0.05$.

Chemotaxis assays were conducted with the HD845 mutant peptides to assess whether they possessed improved functional inhibition compared to the parental HD845 (**Figure 5.2.3**). All mutant peptides (apart from K10W) appeared to inhibit all chemokines tested, most potently CCL8, where all peptides achieved complete inhibition. However, only E6F and E6W showed statistically significant improved inhibition compared to HD845 among the tested peptides, which strongly correlates with their improved binding profiles observed in the phage display assays. While K10A appeared to show enhanced inhibition compared to HD845 against CCL2, CCL5, and CCL7, and E6W against CCL5 and CCL7, these improvements were not statistically significant.

5.2.4 Preliminary Indication of Improved Potency with HD845 Mutants

To evaluate the potency of HD845 and its mutant peptides, chemotaxis assays were performed using a range of peptide concentrations (10, 5, 1, and 0.5 μM). This allowed for the determination of the concentration at which the peptides lose their inhibitory effects (**Appendix 3**). The best HD2 mutant inhibitor for each chemokine was added for comparison (Kryukova, Vales *et al.*, manuscript submitted).

In **Appendix 3**, most peptides lost their inhibitory activity at concentrations below 5 μM, allowing for observation of differences in inhibitory effectiveness. **Figure 5.2.4** shows

chemotaxis inhibition results using 5 μM peptide concentration. The HD845 mutant E6W showed statistically significant improvement in inhibition against CCL3 and CCL5 chemotaxis with THP1 cells compared to HD845, while K10A demonstrated significant enhancement in inhibiting CCL5 and CCL7. E6F also showed a statistically significant improvement in inhibition of CCL3 compared to HD845, which overall suggests a slight improvement in potency.

Several mutant peptides performed comparably to the most potent HD2 mutant peptides. For example, in **Figure 5.2.4A**, at 5 μM against CCL2, HD845 K10A showed similar inhibition to HD2 CM307, a combinatorial mutant with two mutations in the HD2 sequence. Similarly, in panel **B**, E6W showed similar levels of inhibition to HD2T12W against CCL3. In panel **D**, K10A also matched HD2 CM304 in inhibiting CCL7, while E6F, E6W, and K10 exhibited comparable inhibition to HD2 T5W against CCL8 in panel **E**.

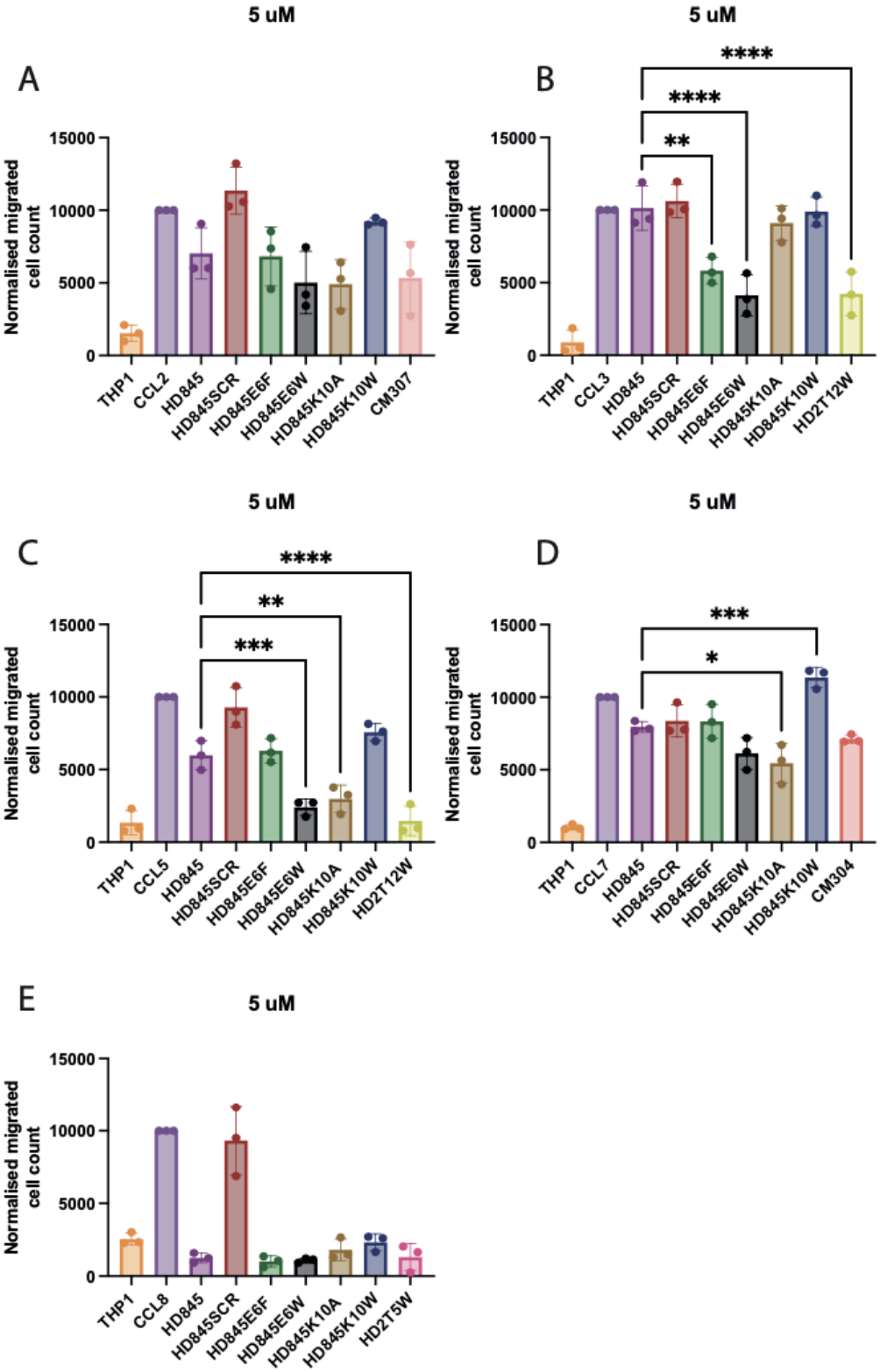
A
5 uM
Normalised migrated cell count
15000
10000
5000
0
THP1
CCL2
HD845
HD845SCR
HD845E6F
HD845E6W
HD845K10A
HD845K10W
CM307
B
5 uM
****
****
**
Normalised migrated cell count
15000
10000
5000
0
THP1
CCL3
HD845
HD845SCR
HD845E6F
HD845E6W
HD845K10A
HD845K10W
HD2T12W
C
5 uM
****
**
***
Normalised migrated cell count
15000
10000
5000
0
THP1
CCL5
HD845
HD845SCR
HD845E6F
HD845E6W
HD845K10A
HD845K10W
HD2T12W
D
5 uM
***
*
Normalised migrated cell count
15000
10000
5000
0
THP1
CCL7
HD845
HD845SCR
HD845E6F
HD845E6W
HD845K10A
HD845K10W
CM304
E
5 uM
Normalised migrated cell count
15000
10000
5000
0
THP1
CCL8
HD845
HD845SCR
HD845E6F
HD845E6W
HD845K10A
HD845K10W
HD2T5W

Figure 5.2.4: Preliminary potency assessment of HD845 mutants. Bar chart with SD error bars illustrating the effect of HD845 mutants on chemokine-induced cell migration, compared to the parental HD845 peptide at 5 μM, with chemokines concentration tested at EC80 doses. The x-axis indicates the specific peptide tested. Each experiment included three technical replicates, with individual data points indicated. The y-axis shows the normalised migrated cell count. Cell counts were normalised to the mean value of migrated cells in the presence of chemokine alone, which was set at 10000 cells.

5.3 DISCUSSION

In this chapter, saturation mutagenesis coupled with phage display successfully identified mutant peptides E6F, E6W, K10A, and K10W with broader and improved chemokine binding. Chemotaxis assays validated that only the mutant peptides E6F and E6W displayed significantly improved inhibition of CCL3. Similar to HD2, HD845 displayed a binding profile predominantly favouring CC chemokines and was the most potent inhibitor of CCL8 chemotaxis. This explains why the mutant peptides, despite showing effective inhibition, when compared to HD845, did not achieve statistical significance compared to HD845. Furthermore, in the original EVAA phage display, parental HD845 showed weak binding to CCL3, as indicated by the blue tile in the phage display results (**Figure 3.2.4**). This likely contributes to the significantly improved inhibition of the mutant peptides compared to HD845, as the parental peptide was initially a poor binder to CCL3.

The mutant peptide HD845K10A, containing lysine (K) to alanine (A) mutation, showed improved inhibition against CCL2, CCL5, and CCL7. This may appear counterintuitive as alanine is a small, non-polar amino acid that, when substituted, removes the side chain at the β-carbon and abolishes any contacts that the side chain might form with the binding partner. Therefore, alanine scanning is commonly used to determine the roles of amino acid side chains in proteins and was also performed on the HD2 sequence in Chapter 4 to investigate which residues were important for chemokine binding. The observed improvement in binding and inhibitory chemokine activity of HD845K10A suggests that the lysine side chain is not important for HD845 binding to chemokine and chemokine activity can be improved by alanine substitution, perhaps allowing for greater flexibility[152].

The mutant peptide HD845 E6W, which contained a glutamic acid (E) to tryptophan (W) substitution at position 6, has significantly improved inhibition against CCL3 and CCL5 and slight improvement with CCL2 and CCL7 at 5 μM. This may be due to the intrinsic

properties of the tryptophan. Tryptophan contains an indole ring, which can participate in greater cation-π interactions, and tryptophan can engage in π-π interactions. These interactions could stabilise the peptide's binding to the chemokine[153,154]. Furthermore, the bulky side chain of tryptophan can introduce rigidity into the peptide structure[155], which may help maintain an optimal conformation for binding to the chemokine. However, when tryptophan was substituted at position 10 in HD845 K10W, the mutant peptide was not as potent as the parental HD845 but was showing inhibition against CCL5 and strong inhibition against CCL8.

The mutant peptide HD845 E6F, containing a glutamic acid (E) to phenylalanine (F) substitution at position 6, has improved inhibition against CCL2, CCL3 and CCL5. Like tryptophan, phenylalanine is a hydrophobic amino acid that can form strong hydrophobic interactions with chemokine, enhancing binding affinity. Phenylalanine's aromatic ring can engage in π-π interactions with other aromatic residues in the chemokine, further stabilising the peptide-chemokine complex[154].

One limitation of this study is that the CXC chemokines were not extensively studied. Phage display revealed that the mutant peptides E6W and K10A exhibited enhanced binding to the CXC chemokines CXCL8 and CXCL10, respectively. Further investigation of whether these peptides inhibit more effectively to additional CXC chemokines would be valuable. Doing so could significantly improve the potential of these peptides to address chemokine redundancy, a major challenge in targeting chemokines therapeutically.

Inhibitory dose-response curves, which provide IC50 values, are generally a more accurate measure of potency. Although the chemotaxis assays were conducted at various concentrations, preliminary findings suggest a modest improvement in potency, particularly with E6F and E6W against CCL3 and E6W and K10A against CCL5 at 5 μM. To better define potency, future work could include inhibitory dose-response assays to determine precise IC50 values, particularly testing peptide concentrations lower than 0.5 μM against CCL8. The strong CCL8 inhibition observed with these mutants is not

unexpected. HD845 differs by only one amino acid from BK1.1, which has been identified as part of the binding interface between CCL8 and EV672, the peptides from which BK1.1 and HD845 are derived[133]. Additionally, future research might explore combining mutations, as was done with the HD2 mutations (Kryukova, Vales *et al.*, manuscript submitted), to enhance binding affinity and breadth. Other potential modifications include peptide cyclisation and creating a peptide dimer, similar to BK1.2 and BK1.3, respectively, which could potentially enhance potency even further[133].

CHAPTER 6: CHARACTERISATION OF HD845 AND HD2 MUTANTS AGAINST A COMPLEX ATHEROSCLEROSIS CHEMOKINE POOL

6.1 INTRODUCTION

Chapter 5 led to the discovery of improved mutant peptides by utilising saturation mutagenesis on EV672-derived HD845 peptide followed by phage display. A few HD845 mutants exhibited improved chemokine binding breadth and potency in *in vitro* functional assays compared to the parental HD845. HD2 had previously undergone two rounds of saturation mutagenesis and screening, where improved mutations were identified in the first round, and the most effective single mutations were combined into more potent combinatorial mutants in the second round. This resulted in superior combinatorial HD2 mutants, which showed an increased breadth of action against multiple chemokines (Kryukova, Vales *et al*., manuscript submitted).

As aforementioned, the chemokine network is highly complex. While chemokines protect against infection, chemokine-induced inflammation also plays a significant role in driving various immunoinflammatory diseases. Elevated levels of multiple CC and CXC chemokines are commonly observed in conditions such as atherosclerosis, rheumatoid arthritis, psoriasis, inflammatory bowel disease, and multiple sclerosis[78,137,138]. These elevated chemokine levels recruit more leukocytes, which, once activated, release more chemokines, creating feed-forward loops that exacerbate the disease procession[137]. Moreover, chemokines can form homo- or hetero-dimers, which can enhance their inflammatory effects through synergistic hetero-dimerisation. For instance, the synergy between CCL5:CXCL4, CCL5:CCL17 and CCL5:CCL2 has been shown to amplify leukocyte migration. Disrupting these synergistic interactions has proven effective in reducing leukocyte migration in models of acute lung injury and atherosclerosis[53]. Additionally, chemokine redundancy is a major challenge in chemokine-targeted drug

development. Targeting single or too few chemokines may result in insufficient disruption of the inflammatory process[101], while broad inhibition can have detrimental effects, such as opportunistic infections or disruption of homeostatic functions of chemokines such as leukocyte maturation and stem cell homing[156,157].

Given the network's complexities, the next step was to evaluate whether the mutated peptides could effectively inhibit a complex chemokine mixture associated with inflammatory diseases rather than targeting individual chemokines. This chapter focuses on chemokines linked to atherosclerosis, hypothesising that the mutant peptides selected from phage display mutagenesis can inhibit a complex chemokine mixture associated with this disease. The aim is to test the HD845 mutants and HD2 combinatorial mutants against a complex atherosclerosis chemokine pool in chemotaxis assays, evaluating their potential as therapeutic agents.

This work has been included in (Kryukova, Vales *et al.*, manuscript submitted)

6.2 RESULTS

6.2.1 Development of the Atherosclerosis Chemokine Pool for Therapeutic Evaluation

To mimic the chemokine environment associated with atherosclerosis and assess the potential of mutant peptides as therapeutic agents, an atherosclerosis chemokine pool (athero pool) was developed. This pool was based on data from bulk RNA sequencing (GSE198600) obtained from the Gene Expression Omnibus (GEO) database. The dataset included ribosome-depleted total RNA from 11 carotid plaques: six from 'recently ruptured' and five from 'asymptomatic' plaques. Analysis of the bulk RNA-seq data analysis identified 45 chemokines, as illustrated in **Figure 6.2.1.1**, which shows the chemokine expression levels in transcripts per million (TPM). A synthetic chemokine pool was constructed with 41 chemokines (**Table 6.2.1.2**). Individual chemokine molar concentrations in the pool were at ratios determined by the mean relative expression of chemokines in the RNA-sequencing dataset.

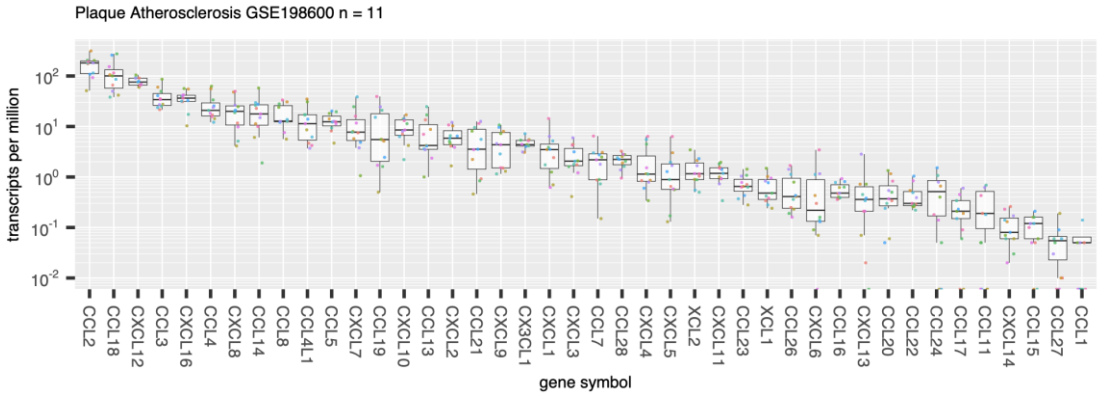

Figure 6.2.1.1: Box-whisker plots showing chemokines in atherosclerotic plaque. The y-axis shows the transcript count per million, and the x-axis shows the chemokine. GEO database

source identity is GSE198600, n = the number of samples. Individual data points are shown. Chemokine expression levels were analysed, and the figure created by SB.

Chemokine	Concentration (μM)
CCL2	2.6107
CCL18	1.85075
CXCL12	1.23199
CCL3	0.62004
CXCL16	0.5649
CCL4	0.43035
CXCL8	0.34388
CCL14s	0.32441
CCL8	0.27733
CCL4L1	0.21912
CCL5	0.20515
CXCL7	0.18593
CCL19	0.17573
CXCL10	0.15205
CCL13	0.12873
CXCL2	0.10247
CCL21	0.08433
CXCL9	0.07584
CX3CL1	0.07273
CXCL1	0.06253
CXCL3	0.04122
CCL7	0.03498
CCL28	0.03433
CXCL4	0.03391
CXCL5	0.02478
CXCL11	0.01914
CCL23s	0.01151
XCL1	0.01034
CCL26	0.01013
CXCL6	0.0101
CCL16	0.00895
CXCL13	0.00856
CCL20	0.00822
CCL22	0.00705
CCL24	0.00689

CCL17	0.00334
CCL11	0.00316
CXCL14	0.0018
CCL15s	0.00149
CCL27	0.0007
CCL1	0.00042

Table 6.2.1.2: The athero pool chemokine table indicating the chemokine concentrations based on the plaque RNA-seq data set (GSE198600) used in the athero pool. Four chemokines (CCL3L3, XCL2, CXCL4L1, and CXCL17) were excluded from the athero pool due to their unavailability.

6.2.2 Dose-Response Analysis of the Atherosclerosis Chemokine Pool

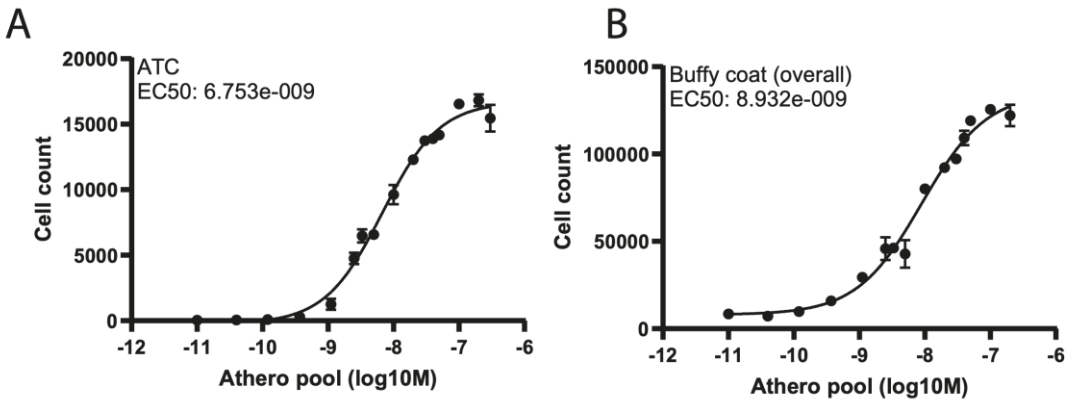

Figure 6.2.2: Dose-response curves of the atherosclerosis chemokine pool in chemotaxis assays. Representative dose-response curves of atherosclerosis chemokine pool (athero pool) - induced activated T cells (ATC) (**A**) and buffy coat (**B**). The data are shown as individual data points observed for different chemokine doses, with each dose performed with three technical replicates. The x-axis shows athero pool concentration (molar). The y-axis shows the migrated cell count of cells. The curve was fitted on GraphPad Prism using a 4-parameter log-logistic fit. The data are shown as representative examples of at least three biological replicates.

As seen in **Figure 6.2.2**, dose-response curves in chemotaxis assays were analysed for each cell type tested (ATC and buffy coat cells) to generate an EC50. ATC and buffy coat (lymphocytes, granulocytes, and monocytes) cells were used in these experiments due to their higher biological relevance compared to cancer cell lines. These dose-response assays were performed with three biological replicates, and the mean EC50 values were calculated for use in subsequent chemotaxis assays testing the mutant peptides. EC50 concentrations were selected over EC80 concentrations to minimise the volume and cost of chemokines required for these assays.

6.2.3 Chemotaxis Assays Testing the Mutant Peptides using the Atherosclerosis Chemokine Pool

After establishing the EC50 athero pool dose for activated T cells and buffy coat cells, mutant peptides were tested against this pool. I first tested HD2 and its single and combinatorial mutants (CM peptides), which were previously identified through saturation mutagenesis phage display for their broad selectivity against different chemokines (Kryukova, Vales *et al.*, manuscript submitted). All peptides and controls were tested at 10 μM, against the athero chemokine pool. Inhibition was compared to the scrambled control (HD2 SCR) to assess whether combinatorial saturation mutagenesis produced effective mutant peptides against a chemokine pool, rather than just improving upon the parental HD2 peptide. Controls included EVA4 (the parental evasin from which HD2 was derived, known to inhibit multiple CC chemokines[97,141]), EVA3 (a CXC-binding evasin[127]), and P1834 (a triple warhead evasin protein capable of inhibiting both CC and CXC chemokine classes, unpublished).

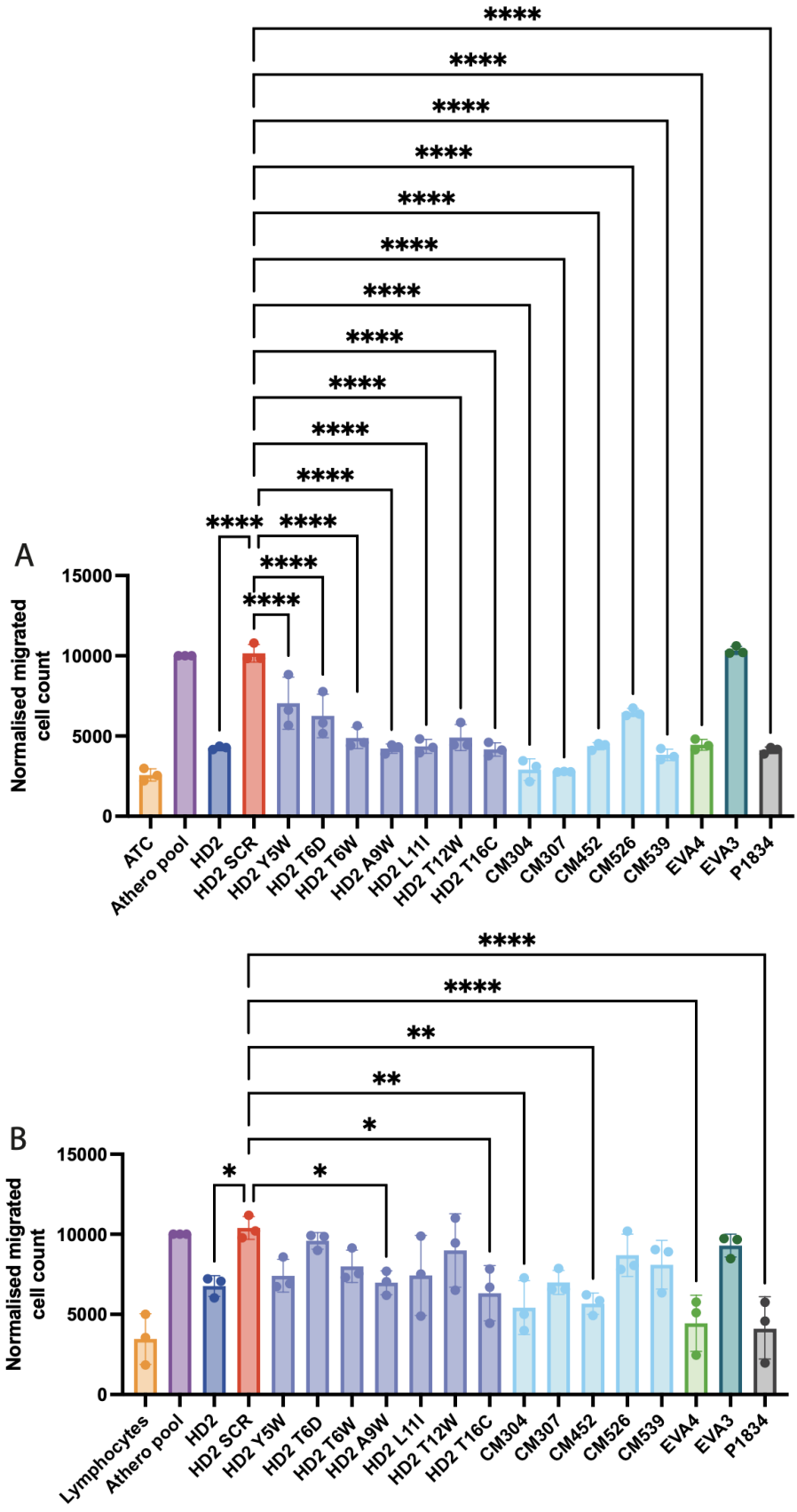
A
Normalised migrated cell count
15000
10000
5000
0
****
ATC
Athero pool
HD2
HD2 SCR
HD2 Y5W
HD2 T6D
HD2 T6W
HD2 A9W
HD2 L11I
HD2 T12W
HD2 T16C
CM304
CM307
CM452
CM526
CM539
EVA4
EVA3
P1834
B
Normalised migrated cell count
15000
10000
5000
0
*
**
****
Lymphocytes
Athero pool
HD2
HD2 SCR
HD2 Y5W
HD2 T6D
HD2 T6W
HD2 A9W
HD2 L11I
HD2 T12W
HD2 T16C
CM304
CM307
CM452
CM526
CM539
EVA4
EVA3
P1834

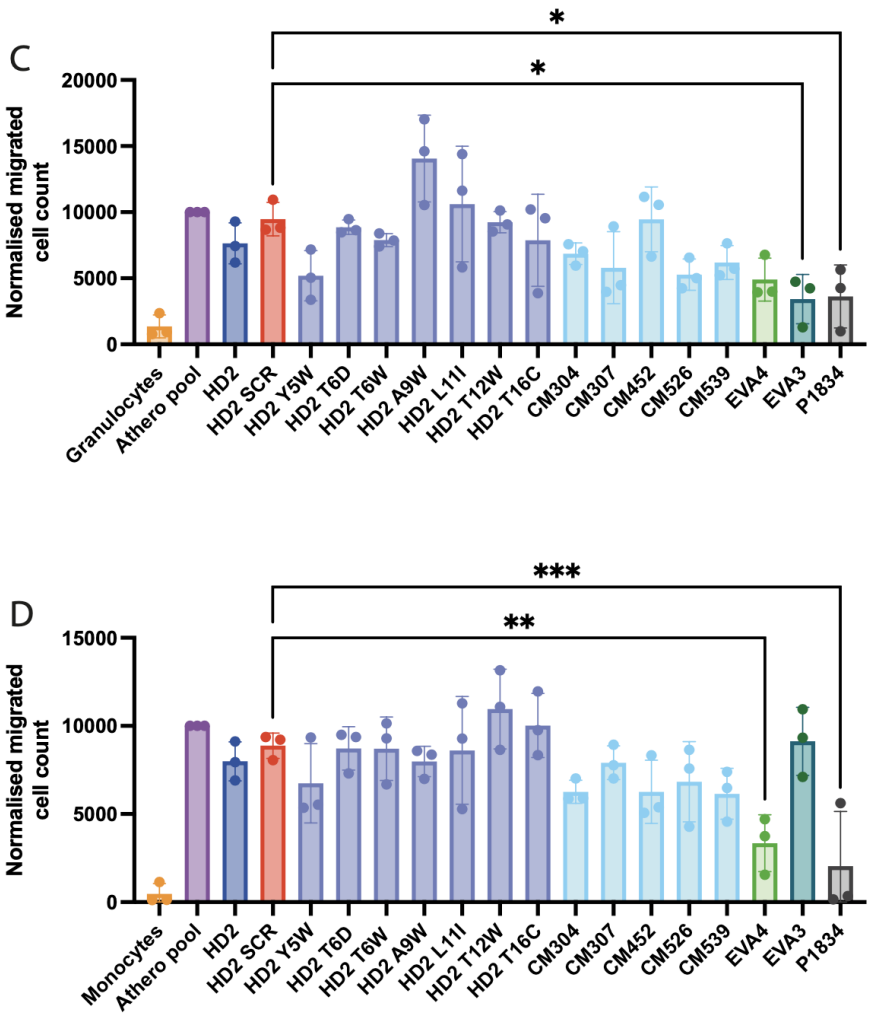

Figure 6.2.3.1: The effect of HD2 mutant peptides against an atherosclerosis chemokine pool. Bar chart with SD error bars showing the impact of the mutant peptides against an athero chemokine pool. The x-axis shows the peptide and cell type tested; the y-axis represents the cell count normalised to the mean value of migrated cells in the presence of the athero pool alone, set at 10,000 cells. Each experiment was performed as three technical and biological replicates, with individual biological replicate data points (mean of technical replicates) displayed. All peptides were tested at a final concentration of 10 μM and athero pool at EC50 doses. Statistically significant differences compared to HD2SCR, in red, were identified using a one-way ANOVA followed by

Dunnett's test for multiple comparisons and indicated by asterisks: ****$p \leq 0.0001$, ***$p \leq 0.001$, **$p \leq 0.01$, *$p \leq 0.05$.

For the athero pool tested against ATC cells, all HD2 mutants, including HD2 itself, showed significant inhibition compared to the SCR control (**Figure 6.2.3.1**). Among these, CM304 and CM307 exhibited the greatest inhibition, reducing ATC migration to baseline levels. For lymphocytes, HD2, HD2 A9W, HD2 T16C, CM304, and CM452 showed significant inhibition. However, no significant inhibition was observed for granulocytes or monocytes with any of the peptides tested.

Additionally, single-concentration inhibition assays were conducted with the athero pool to test the HD845 peptide and its mutants (**Figure 6.2.3.2**), as identified in Chapter 5. Similar controls were included, along with EV672, a CC-inhibiting evasin from which HD845 was derived. Unfortunately, neither HD845 nor its mutants showed significant inhibition in any cell type tested, compared to HD845 SCR. As a result, further testing of the HD845 mutant peptides was not taken further.

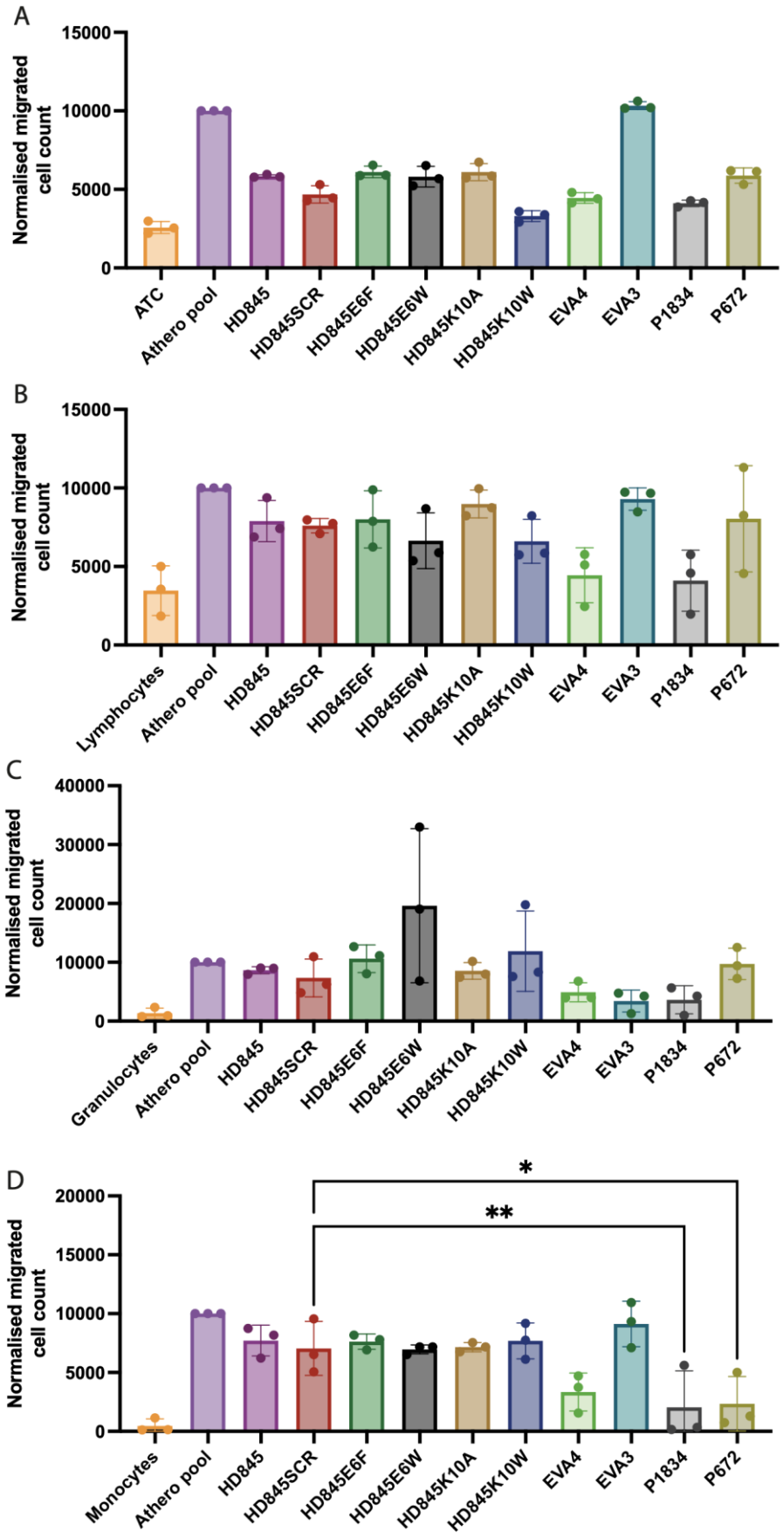
A
Normalised migrated cell count
15000
10000
5000
0
ATC
Athero pool
HD845
HD845SCR
HD845E6F
HD845E6W
HD845K10A
HD845K10W
EVA4
EVA3
P1834
P672
B
Normalised migrated cell count
15000
10000
5000
0
Lymphocytes
Athero pool
HD845
HD845SCR
HD845E6F
HD845E6W
HD845K10A
HD845K10W
EVA4
EVA3
P1834
P672
C
Normalised migrated cell count
40000
30000
20000
10000
0
Granulocytes
Athero pool
HD845
HD845SCR
HD845E6F
HD845E6W
HD845K10A
HD845K10W
EVA4
EVA3
P1834
P672
D
Normalised migrated cell count
20000
15000
10000
5000
0
*
**
Monocytes
Athero pool
HD845
HD845SCR
HD845E6F
HD845E6W
HD845K10A
HD845K10W
EVA4
EVA3
P1834
P672

Figure 6.2.3.2: The effect of HD845 mutant peptides against an atherosclerosis chemokine pool. Bar chart with SD error bars showing the impact of the mutant peptides against an athero chemokine pool. The x-axis shows the peptide and cell type tested; the y-axis represents the cell count normalised to the mean value of migrated cells in the presence of the athero pool alone, set at 10,000 cells. Each experiment was performed as three technical and biological replicates, with individual biological replicate data points (mean of technical replicates) displayed. All peptides were tested at a final concentration of 10 μM and athero pool at EC50 doses. Statistically significant differences compared to HD845SCR, in burgundy, were identified using a one-way ANOVA followed by Dunnett's test for multiple comparisons and indicated by asterisks: ****$p \leq 0.0001$, ***$p \leq 0.001$, **$p \leq 0.01$, *$p \leq 0.05$.

6.3 DISCUSSION

This chapter investigated the potential of peptides, enhanced through saturation mutagenesis followed by phage display, to inhibit a complex mixture of chemokines associated with atherosclerosis. The HD2 mutant peptides, particularly CM304 and CM307, demonstrated significant inhibition of the athero chemokine pool. In some instances, the efficacy of the combinatorial peptides was comparable to EVA4, which was previously shown to be effective in several inflammatory disease models[110,129,158]. These findings highlight the success of targeted combinatorial mutations in enhancing the binding affinity, specificity, and inhibitory potency of peptides.

The disparity in effectiveness between the HD2 mutants and those derived from the HD845 sequence suggests that the starting sequence is crucial in mutagenesis outcomes. None of the HD845 mutant peptides displayed significant inhibition compared to the scrambled control. HD2 may possess favourable binding motifs or conformational flexibility that allows interactions with a broad range of chemokines, and these advantageous features can be further amplified through mutagenesis, leading to more potent, broad-spectrum inhibitors. Conversely, the HD845 sequence may lack these critical attributes, resulting in less effective mutants despite applying similar mutagenesis techniques. This difference can be seen when comparing the levels of inhibition between HD2 and HD845 against the athero pool, with HD2 emerging as the more potent inhibitor. This highlights the importance of selecting a robust starting sequence with inherent binding potential to increase the likelihood of developing powerful inhibitors capable of targeting complex chemokine networks in various diseases. Furthermore, performing structural analysis on HD845, similar to that performed on HD2,[141] could help elucidate any differences in binding to chemokines.

The chemokine pool offers a more biologically relevant approach to evaluating the functional inhibition of the mutant peptides. Unlike tests against individual chemokines, the chemokine pool better simulates the complex chemokine interactions present in disease conditions, where chemokines act synergistically and antagonistically to regulate cell migration and signalling[53,159]. Furthermore, the use of buffy coat and activated T cells instead of immortalised cell lines further improves the biological relevance of the findings. These cells (buffy coat and ATC) better replicate the conditions found in diseased tissues. This methodology increases the likelihood of identifying peptide candidates with greater therapeutic potential.

The chemokine pool was constructed using bulk RNA-seq data from carotid plaques[160] to determine the chemokine profile associated with atherosclerosis. This approach was preferred over single-cell RNA-seq data, which, while informative, does not capture the total chemokine production landscape by all cells within the tissue. However, there are limitations to the RNA-seq approach, such as temporal variability, degradation rates of transcripts and chemokines, and post-transcriptional mechanisms that result in the observed chemokine levels not matching the mRNA levels[160,161]. Despite limitations, the chemokine pool remains a useful method for assessing the inhibitory potential of peptides in a more disease-relevant context.

Future work may include testing the peptides in animal models to validate their therapeutic potential and assess their effects within a complex organism. These studies are essential for understanding pharmacokinetics, tissue-specific targeting, and potential off-target effects, which *in vitro* assays cannot fully capture. It is important that the peptides selectively target inflammatory chemokines in diseased tissues without globally affecting normal immune functions is vital to avoid unintended consequences such as impaired leukocyte maturation[157] or increased risk of opportunistic infections. This could be achieved by conjugating the peptide to a targeting agent, such as nanobodies[162] that specifically bind an inflammation-specific or tissue-specific biomarker. This approach would localise the peptide to diseased tissues, enhancing safety and efficacy.

7 GENERAL CONCLUSION

Nature has long been a source of inspiration for drug development. Various drugs, such as Arteether (for malaria) and Galantamine (for Alzheimer's), have been derived from plants[163]. Similarly, Captopril (for hypertension) and Eptifibatide (for preventing blood clotting) were developed from snake venom peptides[132]. In this project, I turned to ticks, particularly their salivary proteins known as evasins, to address one of the most challenging aspects of developing anti-inflammatory therapeutics: the redundancy of the chemokine system.

Chemokines are among the key players involved in driving inflammation, guiding the migration of immune cells to the site of damage and injury[31]. Chemokines are classified into CC, CXC, CX3C, and XC chemokines based on the arrangement of the conserved cysteine residues[39]. Chemokines have been implicated in a range of inflammatory diseases such as atherosclerosis, rheumatoid arthritis, psoriasis, inflammatory bowel disease, and multiple sclerosis[78,137,138], making them an attractive target for developing anti-inflammatory therapeutics. However, targeting the chemokine network is a great challenge due to its redundant nature[139]. The chemokine system is highly redundant, with multiple chemokines binding to multiple receptors, creating a complex and robust signalling network[98]. This explains why there is great difficulty in developing therapeutics that target just one chemokine or one chemokine receptor[101].

Evasins are tick salivary proteins which possess an extraordinary ability to bind to promiscuously multiple chemokines, overcoming the redundant nature of the chemokine system[97]. This evolutionary mechanism allows ticks to prolong feeding and evade detection from the host by preventing an immune response at the bite site[110]. Evasins are categorised into classes A and B, which exclusively bind to CC or CXC class chemokines, respectively[97]. Evasins are effective in several anti-inflammatory models, such as

atherosclerosis[128], colitis[110], pulmonary fibrosis[130], chronic liver disease[131] , ischemic reperfusion injury and psoriasis[113].

Despite their efficacy, the development of full-length evasins as therapeutics faces challenges, such as high production costs and potential immunogenicity concerns[140]. To overcome these limitations, utilising peptides derived from the chemokine binding sites of evasins could serve as an alternative therapeutic approach.

Previous work in our lab has reported a series of BK peptides derived from the evasin EVA672, identified using hydrogen-deuterium exchange mass spectrometry (HDX-MS). These peptides (BK1.2 and BK1.3) have demonstrated remarkable efficacy in inhibiting several CC chemokines *in vitro,* and BK1.3 reducing inflammation *in vivo*[133]. Additionally, others have identified a peptide derived from the evasin EVA4 using NMR that inhibits the activity of the CCL5 chemokine *in vitro*[134]. Despite the success of these peptides, a major limitation is that, like the evasin protein they are derived from, they can only target a select few chemokines and only one chemokine class. This project explored the potential of evasin-derived peptides as broad-spectrum chemokine inhibitors, capable of simultaneously targeting multiple chemokines and disrupting the redundant signalling network.

7.1 SUMMARY OF FINDINGS

Chapter 3 discovered broad-spectrum chemokine-binding peptides, a novel finding as evasin-derived peptides had not previously been reported to bind multiple chemokine classes. Here, they were shown to bind three classes: CC, CXC, and CX3C chemokines. These peptides were identified using phage display by screening 25 biotinylated chemokines against the EVAA library consisting of 21 class A evasins that were fragmented into overlapping 16-mer peptides and cloned into bacteriophage. Three selection rounds were performed to ensure only the strong, specific chemokine binders

were identified and samples were sent for NGS analyses. Analyses revealed a great number of peptides bound to a diverse range of chemokines from multiple classes, a novel and exciting finding considering that class A evasins only bind to CC class chemokines. There was also great confidence in the results of the phage display screen as regions of interest overlapped with known chemokine binding sites. To identify the peptides most likely to overcome chemokine redundancy, the list of peptides was filtered based on the following criteria: a binding affinity (log2E) greater than five and binding to at least three different chemokine classes. The peptide at the top of the list that bound to the greatest number of chemokines with high binding affinity was the HD2 peptide. This validated that phage display can identify broad-spectrum evasin-derived chemokine binding peptides.

Chapter 4 tested the functional inhibition by peptides identified from phage display. From preliminary testing, HD2 exhibited a superior chemokine binding profile, which led to its characterisation in chemotaxis assays. HD2 showed significant inhibition to the chemokines CCL3, CCL5, CCL7, CCL8, CXCL6 and CXCL10. Dose-response inhibition assays were performed to determine the IC50 value and potency, which ranged from 0.015 μM for CCL8 to 2.49 μM for CXCL10.

The critical residues of HD2 required for binding were identified through alanine saturation mutagenesis. This involved substituting every residue on the HD2 sequence with alanine and testing the HD2 alanine mutant peptides in chemotaxis assays to assess the impact on inhibition. The results indicate that different chemokines interact with distinct regions on the HD2 peptide, as different residues were found to be critical for inhibition across various chemokines, suggesting unique interaction sites on the peptide. Furthermore, these results were supported by saturation mutagenesis phage display results, which correlated with chemotaxis data. This also indicated a correlation between binding affinity in phage display and functional inhibition in chemotaxis assays. Results from this chapter further support that the peptides pulled from phage display also possess functional chemokine inhibitory activity.

Chapter 5 describes the successful mutation and identification of improved HD845 mutants using saturation mutagenesis followed by phage display. Work from this chapter was based on mutagenesis improvement on HD2, which saw improvement in its binding and potency profile, performed in the lab. This chapter used HD845 as a different starting sequence and involved mutagenesis of every residue from the HD845 sequence with an NNK codon. This allowed the random substitution of any of the 20 amino acids to create an HD845 mutagenesis phage display library. Results from the screen identified four improved HD845 mutants compared to the parental HD845 peptide: E6F, E6W, K10A and K10W. These mutant peptides were tested for improved functional inhibition in chemotaxis assays. Despite improved inhibition observed from the mutant peptides, only E6F and E6W showed significantly improved inhibition against CCL3 compared to the parental HD845 peptide. Varying concentrations of the HD845 mutant peptides were also preliminarily evaluated. At 5 μM, the concentration where the most noticeable differences could be seen, E6W showed improved potency against CCL3 and CCL5. Similarly, K10A showed improved potency against CCL7 and CCL5, and E6F showed improved potency against CCL3 compared to HD845. Results from this chapter further indicate that peptide mutagenesis can improve and expand the binding profile and potency of peptides pulled from phage display.

Chapter 6 investigated whether the HD845 mutants and the single and combinatorial HD2 mutant peptides could inhibit a disease-relevant complex chemokine mixture. To obtain the chemokines associated with atherosclerosis, RNA-seq data (GSE198600) was obtained from the GEO database, and the relative amounts of chemokine were determined and formed the basis of the chemokine pool, whereby the athero chemokine pool was reflective of the dataset. Dose-response curves were established with the athero pool against ATC and buffy coat to calculate the EC50 value to test in the inhibition assays. Inhibition assays revealed that only the HD2 peptide and its mutants were able to significantly inhibit athero pool-induced migration, with HD2 and all HD2 mutant peptides significantly inhibiting migration against ATC, and against lymphocytes, HD2, HD2 A9W, HD2 T16C, CM304 and CM452 showed significant inhibition. This showed

that saturation mutagenesis followed by phage display could identify peptides that inhibit a complex mixture of chemokines.

7.2 FUTURE WORK

7.2.1.1 HD2 Inhibition Assays

The novel finding of this thesis is the discovery of the EVA4-derived peptide HD2. Unlike previously reported evasin-derived peptides[133,134] reported in this field, HD2 had surprisingly exhibited multi-class chemokine binding. However, despite HD2 showing binding to CX3CL1 in phage display, HD2 is yet to be tested in chemotaxis assays to determine whether it can inhibit CX3CL1-induced migration. It would be interesting to validate that HD2 can functionally inhibit chemokines across three classes.

7.2.1.2 Phage Display

To date, there are 46 human chemokines[39], but due to limited availability, only 25 chemokines were screened in this study. Synthesis of biotinylated chemokines that are not commercially available may further reveal the binding potential of the peptides in the EVAA library. Furthermore, the peptides in phage display library were fused to the phage via their C-terminus. This could limit potential C-terminal peptide interactions with chemokine that may prove to be effective in chemokine inhibition. Future work could explore alternative fusion strategies to identify new chemokine binders from the EVAA library. Furthermore, the peptides used on phage display are 16-mer in length. This length was based on the BK1 peptide, designed from the HDX-MS data indicating the binding interface between P672 and CCL8[133]. This length was selected to capture key chemokine-

binding regions, but optimising peptide length could increase binding affinity and functional activity.

7.2.1.3 HD845 Mutagenesis

Further investigation is needed to evaluate HD845 and its mutants, particularly against CXC-class chemokines, to fully assess improvements in HD845 mutants. Most tested chemokines, except CCL3, are already strongly inhibited by HD845. Testing chemokines that HD845 cannot inhibit would provide a clearer measure of improvement. However, neither HD845 nor its mutants were able to inhibit the complex athero chemokine pool as effectively as HD2 and its single or combinatorial mutants, indicating they are unlikely to overcome chemokine redundancy or for atherosclerosis at least. In the future, screening peptides and their mutants against a complex chemokine mixture could streamline the selection of peptides better suited to overcome redundancy. Additionally, combinatorial mutagenesis of HD845 mutants, similar to HD2, could enhance inhibition, which is currently lacking when tested against the athero pool.

7.2.1.4 *In Vivo* Models

These peptides and their mutants will need to be tested in *in vivo* models to verify safety and efficacy. For example, BK1.3 successfully reduced inflammation in the air pouch model[133], providing a promising starting point for similar evaluations of HD2 and its mutants in inflammation and atherosclerosis models.

7.2.1.5 Improving Peptide Design for Therapeutics

Peptides such as HD2, identified from phage display, act as pan-chemokine inhibitors that bind and inhibit multiple chemokines. Broad-spectrum inhibition is needed to overcome the chemokine network, which is central in driving inflammation in conditions such as atherosclerosis[72]. Currently, therapeutic development in this area is lacking, and although HD2 demonstrates promising activity, it is not yet ready for clinical application. Despite their different mechanisms and therapeutic targets, looking towards successful peptides like Lanreotide and Ozempic (semaglutide) could provide valuable insights into how HD2 can be optimised to enhance its efficacy, stability, and delivery for inflammation and immune modulation.

Mechanism of action and specificity:

Briefly, lanreotide works as a somatostatin analogue, which binds to somatostatin receptors (SSTR2, SSTR5) to inhibit hormone secretion in conditions such as acromegaly and neuroendocrine tumours. Its specificity for somatostatin receptors ensures precise modulation of hormone release, minimising off-target effects[164,165]. Similarly, Ozempic (semaglutide) is a GLP-1 receptor agonist. It mimics the action of the GLP-1 hormone to regulate insulin secretion and promote satiety and shows high specificity for its target receptors[166]. HD2 is not yet in the desirable therapeutic potency range. However, saturation mutagenesis has already been performed in the lab, generating single and combined mutation peptides with improved potency (Kryukova, Vales *et al.*, manuscript submitted). Another potential approach is designing peptidomimetics based on HD2. Peptidomimetics can be engineered to enhance affinity[167]. This could be achieved by using a genetic-code expansion phage display to incorporate non-canonical amino acids into peptides[168].

Pharmacokinetics and stability:

A significant factor contributing to the success of peptides like Lanreotide and Ozempic is their long-acting formulations. Lanreotide is administered as a monthly injection with a sustained-release formulation, allowing for consistent therapeutic levels over time[164]. Similarly, Ozempic is a weekly injectable, offering convenience and long-lasting effects due to its extended half-life and optimised pharmacokinetics[166]. In contrast, linear peptides, such as HD2, often suffer from poor *in vivo* stability due to their susceptibility to enzymatic degradation, causing short half-life, rapid clearance from the body, and poor chemical and physical stability[140], significantly limiting their therapeutic potential. To address these limitations, HD2 could incorporate modifications that enhance stability, such as cyclisation, as successfully reported by one of the BK series peptides (**Figure 7.2.1.4**), BK1.2, but was yet to be tested *in vivo*[133]. Peptidomimetic development, again, could also make the peptide less prone to proteolysis and increase *in vivo* stability[140,169]. Other modifications could include PEGylation[170], lipid conjugation[171] or encapsulation techniques[172]. These approaches could extend HD2's circulation time, reduce dosing frequency, and improve patient compliance by maintaining consistent chemokine inhibition over time.

Figure 7.2.1.4 Cyclisation on BK1.2 peptide. Cyclisation occurred via the tyrosine (Y) and cysteine (C). Taken from Darlot et al[133].

Tissue target and delivery:

As mentioned, Lanreotide, a somatostatin analogue, is designed to target endocrine tissues and Ozempic is a GLP-1 receptor agonist that acts primarily in pancreatic beta cells to

enhance insulin secretion and in gut and brain tissues[166,173]. Currently, HD2 lacks tissue-targeting and delivery mechanisms. HD2, in its current state, is systematic and non-specific in terms of areas to target, which could lead to potentially diluting its effects in the areas where chemokine activity is highest, such as inflamed tissues in diseases like atherosclerosis, rheumatoid arthritis, or other chronic inflammatory conditions. More importantly, it could lead to many side effects, such as opportunistic infection or impaired leukocyte maturation[157]. Utilising nanobodies[54] that could bind to inflammation or tissue-specific markers that could direct these peptides to affected tissues, increasing its therapeutic efficacy while minimising off-target systemic effects on normal chemokine signalling, enhancing both efficacy and safety.

Long-term efficacy and safety:

The long-term efficacy of Lanreotide, Ozempic, and Maraviroc is well-documented, with each having demonstrated sustained therapeutic benefits over time in their respective indications. Lanreotide and Ozempic provide hormone and glucose regulation with minimal long-term safety concerns[165,166]. In contrast, HD2's long-term efficacy is yet to be explored. To achieve similar success, HD2 (or its mutants) will need to undergo extensive long-term studies to evaluate its safety, particularly in chronic inflammation. While broad chemokine inhibition offers therapeutic promise, immune modulation risks of unintended consequences, such as increased susceptibility to infections or impaired immune surveillance. Future work should also focus on optimising HD2's specificity to minimise these risks and ensure its long-term use is safe and effective.

While HD2 shows promise in its current form, these improvements would enable it to fully realise its potential as a broad-spectrum chemokine inhibitor and a valuable addition to the therapeutic landscape for immune-related diseases.

7.2.1.6 Atherosclerosis and the Use of Anti-Inflammatory Peptides

Anti-inflammatory peptides have the potential to target inflammation at all stages of atherosclerosis progression.

Early Stages (Fatty Streak Formation): In the early stages, peptides conjugated with fluorescence could serve as biomarkers to detect elevated levels of systemic inflammation, such as specific chemokines, aiding in early diagnosis. Early administration of these peptides could prevent progression by inhibiting the chemokine-driven recruitment of monocytes and macrophages[174].

Intermediate Stages (Plaque Expansion): During disease progression, when chemokine-driven inflammation coincides with lipid accumulation[174], combining these peptides with lipid-lowering therapies like statins[175] could provide a synergistic effect. This dual approach could more effectively stabilise plaques, reduce inflammation, and slow disease progression than monotherapies.

Late Stages (Plaque Rupture and Post-Event Inflammation): In the advanced stages of atherosclerosis, following plaque rupture or a heart attack, persistent inflammation often exacerbates complications[174]. Administering peptides at this stage could help resolve residual inflammation, stabilise the vascular environment, and reduce the risk of recurrent cardiovascular events.

However, to determine the optimal stage for peptide intervention, data collection from sources such as the Biobank could prove useful. Identifying chemokine profiles and their concentrations at various stages of atherosclerosis (fatty streak, fibrous lesion, and rupture) can guide experimental designs. Conducting athero pool inhibition experiments with primary cells, as demonstrated in Chapter 6, would provide useful insights into the peptides' stage-specific efficacy.

Addressing Residual Risk and SMuRF-Less Patients

In addition to addressing inflammatory pathways at different stages of atherosclerosis, these peptides could play a crucial role in managing residual risk, the cardiovascular risk that can persist despite optimal control of Standard Modifiable Risk Factors (SMuRFs). SMuRFs, which include hypertension, hyperlipidemia, diabetes, smoking, and obesity, are key targets for the prevention and treatment of cardiovascular disease (CVD) through lifestyle changes (e.g., diet, exercise, smoking cessation) and medical interventions (e.g., statins and antihypertensives)[176,177]. However, even with effective management, unresolved inflammation often drives continued disease progression and recurrent cardiovascular events[178]. By targeting chemokine-driven inflammatory pathways, these peptides could complement SMuRF-focused therapies, offering a solution for the residual inflammatory risk that SMuRF-directed strategies alone cannot resolve. Furthermore, these peptides could also offer promise for SMuRF-less patients, a subset of individuals with atherosclerosis or CVD who present without traditional SMuRFs but experience disease progression due to inflammation[179,180]. In these cases, targeting inflammation directly with these peptides could expand therapeutic options to include both SMuRF-driven and non-SMuRF-driven atherosclerosis, filling an important gap in the cardiovascular therapeutic landscape.

7.2.1.7 Wider Academic Field:

The phage display pipeline and multiplex selection techniques could be used to improve and expand the therapeutic potential of peptides like HD2. These methods could be used to mutagenise and improve HD2, enhancing its binding affinity, stability, and specificity. Iterative rounds of phage selection and screening would allow for the identification of mutant peptides with improved broad-spectrum activity against CC and CXC chemokines (Kryukova, Vales *et al.*, manuscript submitted). Beyond optimising HD2, the phage display pipeline could identify biologically active peptide segments derived from evolutionarily

honed proteins. Examples include another class of tick-derived evasins, such as evasin B, which selectively binds and inhibits CXC chemokines[113,118]. Similarly, viral chemokine-binding proteins (vCKBPs) from pathogens like poxviruses and herpesviruses neutralise the chemokine network effectively by targeting multiple chemokine classes[181,182]. Other promising proteins include tick-derived molecules like OmCI, which binds to complement components, and anticoagulant proteins[183,184]. Additionally, the phage display pipeline could target families of structurally related proteins that contribute to inflammatory pathways, such as the TNF family. While current TNF inhibitors like infliximab are effective, they face challenges related to intravenous administration and treatment adherence[185]. Developing orally administered peptides targeting TNF-related molecules[186] or interleukins (e.g., IL-6, IL-17) [187-189] could offer more accessible and versatile alternatives.

Beyond atherosclerosis, HD2 or its derived peptides could address a range of chemokine-driven diseases, including rheumatoid arthritis (RA)[149], type 1 diabetes (T1D)[190], inflammatory bowel disease[191] and cytokine storms[192]. These conditions are characterised by redundant chemokine networks, where multi-targeted approaches are essential. For example, in RA, chemokine inhibition could reduce synovial inflammation, while in T1D, peptides could mitigate the recruitment of autoreactive T cells, potentially preserving pancreatic beta cells[149,190]. Broad-spectrum or disease-specific chemokine-binding peptides could complement immunotherapies, disrupting these processes and improving therapeutic outcomes. Work in the lab has already begun exploring the potential of evasin-derived peptides to treat conditions like RA and T1D (Kryukova, Vales *et al.*, manuscript submitted), further exhibiting their versatility and therapeutic promise.

In summary, this thesis identified first-of-its-kind evasin-derived peptides through phage display, demonstrating multi-class chemokine binding and functional inhibition. This finding marks a breakthrough, as evasin-derived peptides were previously limited to binding a single chemokine class. Screening the EVAA library led to the discovery of HD2, which, unlike its parent EVA4 (restricted to CC chemokines), can target CC, CXC, and CX3C chemokines. The phage-display-NGS technique reliably identified these broad-spectrum peptides by their binding to known chemokine sites, suggesting the potential for similar discoveries in other evasin classes, like EVAB.

The thesis also validated saturation mutagenesis, expanding the binding profile of the HD845 peptide. HD2 mutagenesis performed in the lab was shown here to possess functional inhibition against complex chemokine mixtures, such as those linked to atherosclerosis. This highlights HD2's potential in biologically relevant, multi-chemokine environments, a critical step toward translating *in vitro* findings into clinical applications. Overall, this research advances the understanding of evasin-derived peptides, addressing chemokine redundancy and providing a strong foundation for future therapies to treat inflammatory diseases.

8 REFERENCES

1 Celsus, A. C. & Spencer, W. G. *De medicina*. (Heinemann, 1935).

2 Lin, J. I. Rudolf Virchow: Creator of Cellular Pathology. *Laboratory Medicine* **14**, 791-794 (1983). https://doi.org/10.1093/labmed/14.12.791

3 Medzhitov, R. Origin and physiological roles of inflammation. *Nature* **454**, 428-435 (2008). https://doi.org/10.1038/nature07201

4 Headland, S. E. & Norling, L. V. The resolution of inflammation: Principles and challenges. *Seminars in immunology* **27**, 149-160 (2015). https://doi.org/10.1016/j.smim.2015.03.014

5 Chen, L. *et al.* Inflammatory responses and inflammation-associated diseases in organs. *Oncotarget* **9**, 7204-7218 (2018). https://doi.org/10.18632/oncotarget.23208

6 Savill, J. & Serhan, C. N. Resolution of inflammation: the beginning programs the end. *Nature Immunology* **6**, 1191-1197 (2005). https://doi.org/10.1038/ni1276

7 Fullerton, J. N. & Gilroy, D. W. Resolution of inflammation: A new therapeutic frontier. *Nature reviews. Drug discovery* **15**, 551-567 (2016). https://doi.org/10.1038/nrd.2016.39

8 Xiang, Y., Zhang, M., Jiang, D., Su, Q. & Shi, J. The role of inflammation in autoimmune disease: a therapeutic target. *Frontiers in immunology* **14**, 1267091-1267091 (2023). https://doi.org/10.3389/fimmu.2023.1267091

9 Henein, M. Y., Vancheri, S., Longo, G. & Vancheri, F. The Role of Inflammation in Cardiovascular Disease. *International journal of molecular sciences* **23**, 12906 (2022). https://doi.org/10.3390/ijms232112906

10 Tsalamandris, S. *et al.* The role of inflammation in diabetes: Current concepts and future perspectives. *European cardiology* **14**, 50-59 (2019). https://doi.org/10.15420/ecr.2018.33.1

11 Zhang, W., Xiao, D., Mao, Q. & Xia, H. Role of neuroinflammation in neurodegeneration development. *Signal transduction and targeted therapy* **8**, 267-267 (2023). https://doi.org/10.1038/s41392-023-01486-5

12 Kawanishi, S., Ohnishi, S., Ma, N., Hiraku, Y. & Murata, M. Crosstalk between DNA damage and inflammation in the multiple steps of carcinogenesis. *International journal of molecular sciences* **18**, 1808 (2017). https://doi.org/10.3390/ijms18081808

13 Pamer, E. G. & Shi, C. Monocyte recruitment during infection and inflammation. *Nature reviews. Immunology* **11**, 762-774 (2011). https://doi.org/10.1038/nri3070

14 Serbina, N. V., Jia, T., Hohl, T. M. & Pamer, E. G. Monocyte-mediated defense against microbial pathogens. *Annual review of immunology* **26**, 421-452 (2008). https://doi.org/10.1146/annurev.immunol.26.021607.090326

15 Bystrom, J. *et al.* Resolution-phase macrophages possess a unique inflammatory phenotype that is controlled by cAMP. *Blood* **112**, 4117-4127 (2008). https://doi.org/10.1182/blood-2007-12-129767
16 Mosser, D. M., Hamidzadeh, K. & Goncalves, R. Macrophages and the maintenance of homeostasis. *Cellular & molecular immunology* **18**, 579-587 (2021). https://doi.org/10.1038/s41423-020-00541-3
17 Guerriero, J. L. Macrophages: Their Untold Story in T Cell Activation and Function. *International Review of Cell and Molecular Biology* **342**, 73-93 (2019). https://doi.org/10.1016/bs.ircmb.2018.07.001
18 Kraus, R. F. & Gruber, M. A. Neutrophils—From Bone Marrow to First-Line Defense of the Innate Immune System. *Frontiers in immunology* **12**, 767175-767175 (2021). https://doi.org/10.3389/fimmu.2021.767175
19 Kolaczkowska, E. & Kubes, P. Neutrophil recruitment and function in health and inflammation. *Nature reviews. Immunology* **13**, 159-175 (2013). https://doi.org/10.1038/nri3399
20 Nathan, C. Neutrophils and immunity: challenges and opportunities. *Nature Reviews: Immunology* **6**, 173-182 (2006). https://doi.org/10.1038/nri1785
21 Sun, L., Su, Y., Jiao, A., Wang, X. & Zhang, B. T cells in health and disease. *Signal transduction and targeted therapy* **8**, 235-235 (2023). https://doi.org/10.1038/s41392-023-01471-y
22 Zitti, B. & Bryceson, Y. T. Natural killer cells in inflammation and autoimmunity. *Cytokine & growth factor reviews* **42**, 37-46 (2018). https://doi.org/10.1016/j.cytogfr.2018.08.001
23 Tosello-Trampont, A., Surette, F. A., Ewald, S. E. & Hahn, Y. S. Immunoregulatory role of NK cells in tissue inflammation and regeneration. *Frontiers in immunology* **8**, 301-301 (2017). https://doi.org/10.3389/fimmu.2017.00301
24 Pieper, K. M., Grimbacher, B. M. D. & Eibel, H. P. B-cell biology and development. *Journal of allergy and clinical immunology* **131**, 959-971 (2013). https://doi.org/10.1016/j.jaci.2013.01.046
25 Hilligan, K. L. & Ronchese, F. Antigen presentation by dendritic cells and their instruction of CD4+ T helper cell responses. *Cellular & molecular immunology* **17**, 587-599 (2020). https://doi.org/10.1038/s41423-020-0465-0
26 Cybulsky, M. I., Nourshargh, S., Ley, K. & Laudanna, C. Getting to the site of inflammation: the leukocyte adhesion cascade updated. *Nature Reviews: Immunology* **7**, 678-689 (2007). https://doi.org/10.1038/nri2156
27 Muller, W. A. Getting Leukocytes to the Site of Inflammation. *Veterinary pathology* **50**, 7-22 (2013). https://doi.org/10.1177/0300985812469883
28 Kansas, G. S. Selectins and Their Ligands: Current Concepts and Controversies. *Blood* **88**, 3259-3287 (1996). https://doi.org/10.1182/blood.V88.9.3259.bloodjournal8893259
29 Eriksson, E. E., Xie, X., Werr, J., Thoren, P. & Lindbom, L. Importance of primary capture and L-selectin-dependent secondary capture in leukocyte

accumulation in inflammation and atherosclerosis in vivo. *The Journal of experimental medicine* **194**, 205-217 (2001). https://doi.org/10.1084/jem.194.2.205
30 Alon, R., Hammer, D. A. & Springer, T. A. Lifetime of the P-selectin-carbohydrate bond and its response to tensile force in hydrodynamic flow. *Nature (London)* **374**, 539-542 (1995). https://doi.org/10.1038/374539a0
31 Baggiolini, M. Chemokines and leukocyte traffic. *Nature* **392**, 565 (1998). https://doi.org/10.1038/33340
32 Moore, J. E., Brook, B. S. & Nibbs, R. J. B. Chemokine transport dynamics and emerging recognition of their role in immune function. *Current opinion in biomedical engineering* **5**, 90-95 (2018). https://doi.org/10.1016/j.cobme.2018.03.001
33 Mackay, C. R. Chemokines: immunology's high impact factors. *Nature Immunology* **2**, 95 (2001). https://doi.org/10.1038/84298
34 Youn, B. S., Mantel, C. & Broxmeyer, Hal e. Chemokines, chemokine receptors and hematopoiesis. *Immunological Reviews* **177**, 150-174 (2000). https://doi.org/10.1034/j.1600-065X.2000.17701.x
35 Strieter, R. M., Burdick, M. D., Gomperts, B. N., Belperio, J. A. & Keane, M. P. CXC chemokines in angiogenesis. *Cytokine & growth factor reviews* **16**, 593-609 (2005). https://doi.org/10.1016/j.cytogfr.2005.04.007
36 Kawasaki, T. & Kawai, T. Toll-like receptor signaling pathways. *Frontiers in immunology* **5**, 461-461 (2014). https://doi.org/10.3389/fimmu.2014.00461
37 Deshmane, S. L., Kremlev, S., Amini, S. & Sawaya, B. E. Monocyte chemoattractant protein-1 (MCP-1): An overview. *Journal of interferon & cytokine research* **29**, 313-325 (2009). https://doi.org/10.1089/jir.2008.0027
38 Blanchet, X., Weber, C. & von Hundelshausen, P. Chemokine Heteromers and Their Impact on Cellular Function-A Conceptual Framework. *International journal of molecular sciences* **24**, 10925 (2023). https://doi.org/10.3390/ijms241310925
39 Zlotnik, A. & Yoshie, O. The Chemokine Superfamily Revisited. *Immunity (Cambridge, Mass.)* **36**, 705-716 (2012). https://doi.org/10.1016/j.immuni.2012.05.008
40 Hughes, C. E. & Nibbs, R. J. B. A guide to chemokines and their receptors. *The FEBS journal* **285**, 2944-2971 (2018). https://doi.org/10.1111/febs.14466
41 Koelink, P. J. *et al.* Targeting chemokine receptors in chronic inflammatory diseases: An extensive review. *Pharmacology & therapeutics (Oxford)* **133**, 1-18 (2012). https://doi.org/10.1016/j.pharmthera.2011.06.008
42 Wu, T., Yang, W., Sun, A., Wei, Z. & Lin, Q. The Role of CXC Chemokines in Cancer Progression. *Cancers* **15**, 167 (2022). https://doi.org/10.3390/cancers15010167
43 Kiefer, F. & Siekmann, A. F. The role of chemokines and their receptors in angiogenesis. *Cellular and molecular life sciences : CMLS* **68**, 2811-2830 (2011). https://doi.org/10.1007/s00018-011-0677-7
44 Bachelerie, F. *et al.* International union of pharmacology. LXXXIX. Update on the extended family of chemokine receptors and introducing a new

nomenclature for atypical chemokine receptors. *Pharmacological reviews* **66**, 1-79 (2014). https://doi.org/10.1124/pr.113.007724

45 Jiang, S. *et al.* The role of CXCL1/CXCR2 axis in neurological diseases. *International immunopharmacology* **120**, 110330-110330 (2023). https://doi.org/10.1016/j.intimp.2023.110330

46 Combadiere, C. *et al.* Identification of CX3CR1. A chemotactic receptor for the human CX3C chemokine fractalkine and a fusion coreceptor for HIV-1. *The Journal of biological chemistry* **273**, 23799-23804 (1998). https://doi.org/10.1074/jbc.273.37.23799

47 Bazan, J. F. *et al.* A new class of membrane-bound chemokine with a CX3C motif. (1997).

48 Garton, K. J. *et al.* Tumor necrosis factor-alpha-converting enzyme (ADAM17) mediates the cleavage and shedding of fractalkine (CX3CL1). (2001).

49 Lee, M., Lee, Y., Song, J., Lee, J. & Chang, S. Y. Tissue-specific role of CX3CR1 expressing immune cells and their relationships with human disease. *Immune network* **18**, e5-e5 (2018). https://doi.org/10.4110/in.2018.18.e5

50 Rowinska, Z. *et al.* Role of the CX3C chemokine receptor CX3CR1 in the pathogenesis of atherosclerosis after aortic transplantation. *PloS one* **12**, e0170644-e0170644 (2017). https://doi.org/10.1371/journal.pone.0170644

51 Kufareva, I., Gustavsson, M., Zheng, Y., Stephens, B. S. & Handel, T. M. What Do Structures Tell Us About Chemokine Receptor Function and Antagonism? *Annu Rev Biophys* **46**, 175-198 (2017). https://doi.org/10.1146/annurev-biophys-051013-022942

52 Stone, M. J., Hayward, J. A., Huang, C., Huma, Z. E. & Sanchez, J. Mechanisms of regulation of the chemokine-receptor network. *International journal of molecular sciences* **18**, 342-342 (2017). https://doi.org/10.3390/ijms18020342

53 von Hundelshausen, P. *et al.* Chemokine interactome mapping enables tailored intervention in acute and chronic inflammation. *Sci Transl Med* **9**, eaah6650 (2017). https://doi.org/10.1126/scitranslmed.aah6650

54 Miller, M. C. & Mayo, K. Chemokines from a Structural Perspective. *Int. J. Mol. Sci.* **18** (2017). https://doi.org/10.3390/ijms18102088

55 Hughes, C. E. & Nibbs, R. J. B. A guide to chemokines and their receptors. *FEBS Journal* **285**, 2944-2971 (2018). https://doi.org/10.1111/febs.14466

56 Nibbs, R. J. B. & Graham, G. J. Immune regulation by atypical chemokine receptors. *Nature reviews. Immunology* **13**, 815-829 (2013). https://doi.org/10.1038/nri3544

57 Comerford, I. & McColl, S. R. Atypical chemokine receptors in the immune system. *Nature reviews. Immunology* (2024). https://doi.org/10.1038/s41577-024-01025-5

58 Luster, A. D. Chemokines - Chemotactic cytokines that mediate inflammation. *N. Engl. J. Med.* **338**, 436-445 (1998). https://doi.org/10.1056/NEJM199802123380706

59 Zlotnik, A., Burkhardt, A. M. & Homey, B. Homeostatic chemokine receptors and organ-specific metastasis. *Nature reviews. Immunology* **11**, 597-606 (2011). https://doi.org/10.1038/nri3049

60 Nedkoff, L., Briffa, T., Zemedikun, D., Herrington, S. & Wright, F. L. Global trends in atherosclerotic cardiovascular disease. (2023).

61 Pirillo, A., Bonacina, F., Norata, G. D. & Catapano, A. L. The Interplay of Lipids, Lipoproteins, and Immunity in Atherosclerosis. *Current atherosclerosis reports* **20**, 12-12 (2018). https://doi.org/10.1007/s11883-018-0715-0

62 Davies, P. F. Flow-mediated endothelial mechanotransduction. *Physiological reviews* **75**, 519-560 (1995). https://doi.org/10.1152/physrev.1995.75.3.519

63 Rafieian-Kopaei, M., Setorki, M., Doudi, M., Baradaran, A. & Nasri, H. Atherosclerosis: Process, indicators, risk factors and new hopes. *International journal of preventive medicine* **5**, 927-946 (2014).

64 Zhang, X., Kang, Z., Yin, D. & Gao, J. Role of neutrophils in different stages of atherosclerosis. *Innate Immunity* **29**, 97-109 (2023). https://doi.org/10.1177/17534259231189195

65 Pamukcu, B., Lip, G. Y. H. & Shantsila, E. The nuclear factor – kappa B pathway in atherosclerosis: A potential therapeutic target for atherothrombotic vascular disease. *Thrombosis research* **128**, 117-123 (2011). https://doi.org/10.1016/j.thromres.2011.03.025

66 Libby, P. Inflammation and Atherosclerosis. *Circulation : journal of the American Heart Association.* **105**, 1135-1143 (2002). https://doi.org/info:doi/

67 Reustle, A. & Torzewski, M. Role of p38 MAPK in atherosclerosis and aortic valve sclerosis. *International journal of molecular sciences* **19**, 3761 (2018). https://doi.org/10.3390/ijms19123761

68 Chistiakov, D. A., Melnichenko, A. A., Myasoedova, V. A., Grechko, A. V. & Orekhov, A. N. Mechanisms of foam cell formation in atherosclerosis. *Journal of molecular medicine (Berlin, Germany)* **95**, 1153-1165 (2017). https://doi.org/10.1007/s00109-017-1575-8

69 Nording, H. M., Seizer, P. & Langer, H. F. Platelets in inflammation and atherogenesis. *Frontiers in immunology* **6**, 98-98 (2015). https://doi.org/10.3389/fimmu.2015.00098

70 Poznyak, A. V., Nikiforov, N. G., Starodubova, A. V., Popkova, T. V. & Orekhov, A. N. Macrophages and foam cells: Brief overview of their role, linkage, and targeting potential in atherosclerosis. *Biomedicines* **9**, 1221 (2021). https://doi.org/10.3390/biomedicines9091221

71 Libby, P. *et al.* Atherosclerosis. *Nat Rev Dis Primers* **5**, 56-56 (2019). https://doi.org/10.1038/s41572-019-0106-z

72 Gencer, S., Evans, B. R., Van Der Vorst, E. P. C., Döring, Y. & Weber, C. Inflammatory chemokines in atherosclerosis. *Cells (Basel, Switzerland)* **10**, 1-26 (2021). https://doi.org/10.3390/cells10020226

73 Liu, H. & Jiang, D. Fractalkine/CX3CR1 and atherosclerosis. *Clinica chimica acta* **412**, 1180-1186 (2011). https://doi.org/10.1016/j.cca.2011.03.036

74 Postea, O. *et al.* Contribution of Platelet CX3CR1 to Platelet–Monocyte Complex Formation and Vascular Recruitment During Hyperlipidemia. *Arteriosclerosis, thrombosis, and vascular biology* **32**, 1186-1193 (2012). https://doi.org/10.1161/ATVBAHA.111.243485

75 Evans, B. R. *et al.* Inflammatory Mediators in Atherosclerotic Vascular Remodeling. *Frontiers in cardiovascular medicine* **9**, 868934-868934 (2022). https://doi.org/10.3389/fcvm.2022.868934

76 Scheuerer, B. *et al.* The CXC-chemokine platelet factor 4 promotes monocyte survival and induces monocyte differentiation into macrophages. *Blood* **95**, 1158-1166 (2000). https://doi.org/10.1182/blood.V95.4.1158.004k31_1158_1166

77 Zhou, Z. *et al.* Lipoprotein-Derived Lysophosphatidic Acid Promotes Atherosclerosis by Releasing CXCL1 from the Endothelium. *Cell metabolism* **13**, 592-600 (2011). https://doi.org/10.1016/j.cmet.2011.02.016

78 Zernecke, A. & Weber, C. Chemokines in Atherosclerosis. *Arteriosclerosis, thrombosis, and vascular biology* **34**, 742 (2014). https://doi.org/10.1161/ATVBAHA.113.301655

79 Georgakis, M. K. *et al.* Circulating Monocyte Chemoattractant Protein-1 and Risk of Stroke: Meta-Analysis of Population-Based Studies Involving 17 180 Individuals. *Circulation research* **125**, 773-782 (2019). https://doi.org/10.1161/CIRCRESAHA.119.315380

80 Chang, T.-T., Chen, C. & Chen, J.-W. CCL7 as a novel inflammatory mediator in cardiovascular disease, diabetes mellitus, and kidney disease. *Cardiovascular diabetology* **21**, 1-185 (2022). https://doi.org/10.1186/s12933-022-01626-1

81 Chatterjee, M. *et al.* Platelet-derived CXCL12 regulates monocyte function, survival, differentiation into macrophages and foam cells through differential involvement of CXCR4-CXCR7. *Cell death & disease* **6**, e1989-e1989 (2015). https://doi.org/10.1038/cddis.2015.233

82 van der Vorst, E. P. C., Döring, Y. & Weber, C. Chemokines and their receptors in Atherosclerosis. *Journal of Molecular Medicine* **93**, 963-971 (2015). https://doi.org/10.1007/s00109-015-1317-8

83 Gräbner, R. *et al.* Lymphotoxin β receptor signaling promotes tertiary lymphoid organogenesis in the aorta adventitia of aged ApoE mice. *The Journal of experimental medicine* **206**, 233-248 (2009). https://doi.org/10.1084/jem.20080752

84 Gutwein, P. *et al.* CXCL16 Is Expressed in Podocytes and Acts as a Scavenger Receptor for Oxidized Low-Density Lipoprotein. *The American journal of pathology* **174**, 2061-2072 (2009). https://doi.org/10.2353/ajpath.2009.080960

85 Santos, S. M. d. *et al.* Platelets from flowing blood attach to the inflammatory chemokine CXCL16 expressed in the endothelium of the human vessel wall. *Thrombosis and haemostasis* **113**, 297-312 (2015). https://doi.org/10.1160/TH14-11-0911

86 Greaves, D. *et al.* Linked chromosome 16q13 chemokines, macrophage-derived chemokine, fractalkine, and thymus- and activation-regulated chemokine, are expressed in human atherosclerotic lesions. (2001).

87 Gear, A. R. L. & Camerini, D. Platelet Chemokines and Chemokine Receptors: Linking Hemostasis, Inflammation, and Host Defense. *Microcirculation (New York, N.Y. 1994)* **10**, 335-350 (2003). https://doi.org/10.1038/sj.mn.7800198
88 Wan, W. & Murphy, P. M. Regulation of Atherogenesis by Chemokines and Chemokine Receptors. *Archivum Immunologiae et Therapiae Experimentalis* **61**, 1-14 (2013). https://doi.org/10.1007/s00005-012-0202-1
89 Potteaux, S. *et al.* Chemokine receptor CCR1 disruption in bone marrow cells enhances atherosclerotic lesion development and inflammation in mice. *Molecular medicine (Cambridge, Mass.)* **11**, 16-20 (2005). https://doi.org/10.2119/2005-00028.Potteaux
90 Braunersreuther, V. *et al.* Ccr5 But Not Ccr1 Deficiency Reduces Development of Diet-Induced Atherosclerosis in Mice. *Arteriosclerosis, thrombosis, and vascular biology* **27**, 373-379 (2007). https://doi.org/10.1161/01.ATV.0000253886.44609.ae
91 Weber, C. *et al.* Specialized roles of the chemokine receptors CCR1 and CCR5 in the recruitment of monocytes and T(H)1-like/CD45RO(+) T cells. *Blood* **97**, 1144-1146 (2001). https://doi.org/10.1182/blood.V97.4.1144
92 Zernecke, A. & Weber, C. Chemokines in the vascular inflammatory response of atherosclerosis. *Cardiovascular research* **86**, 192-201 (2010). https://doi.org/10.1093/cvr/cvp391
93 Damås, J. K. *et al.* Stromal cell-derived factor-1α in unstable angina potential antiinflammatory and matrix-stabilizing effects. *Circulation (New York, N.Y.)* **106**, 36-42 (2002). https://doi.org/10.1161/01.CIR.0000020001.09990.90
94 Xu, Q. *et al.* Impaired CXCR4 expression and cell engraftment of bone marrow-derived cells from aged atherogenic mice. *Atherosclerosis* **219**, 92-99 (2011). https://doi.org/10.1016/j.atherosclerosis.2011.07.118
95 Zernecke, A. *et al.* Protective Role of CXC Receptor 4/CXC Ligand 12 Unveils the Importance of Neutrophils in Atherosclerosis. *Circulation research* **102**, 209-217 (2008). https://doi.org/10.1161/CIRCRESAHA.107.160697
96 Mantovani, A. Redundancy and robustness versus division of labour and specialization in innate immunity. *Seminars in immunology* **36**, 28-30 (2018). https://doi.org/10.1016/j.smim.2017.12.006
97 Bhusal, R. P. *et al.* Evasins: Tick Salivary Proteins that Inhibit Mammalian Chemokines. *Trends in biochemical sciences (Amsterdam. Regular ed.)* **45**, 108-122 (2020). https://doi.org/10.1016/j.tibs.2019.10.003
98 Bhattacharya, S. & Kawamura, A. Using evasins to target the chemokine network in inflammation. *Adv Protein Chem Struct Biol* **119**, 1-38 (2020). https://doi.org/10.1016/bs.apcsb.2019.09.003
99 Schall, T. J. & Proudfoot, A. E. I. Overcoming hurdles in developing successful drugs targeting chemokine receptors. *Nature reviews. Immunology* **11**, 355-363 (2011). https://doi.org/10.1038/nri2972

100 Zhao, S., Wu, B. & Stevens, R. C. Advancing Chemokine GPCR Structure Based Drug Discovery. *Structure (London)* **27**, 405-408 (2019). https://doi.org/10.1016/j.str.2019.02.004

101 Fleishaker, D. L. *et al.* Maraviroc, a chemokine receptor-5 antagonist, fails to demonstrate efficacy in the treatment of patients with rheumatoid arthritis in a randomized, double-blind placebo-controlled trial. *Arthritis Res Ther* **14**, R11-R11 (2012). https://doi.org/10.1186/ar3685

102 Roberti, A., Chaffey, L. E. & Greaves, D. R. NF-κB Signaling and Inflammation—Drug Repurposing to Treat Inflammatory Disorders? *Biology (Basel, Switzerland)* **11**, 372 (2022). https://doi.org/10.3390/biology11030372

103 Rolski, F. & Błyszczuk, P. Complexity of TNF-α signaling in heart disease. *Journal of clinical medicine* **9**, 1-25 (2020). https://doi.org/10.3390/jcm9103267

104 Deftereos, S. G. *et al.* Colchicine in Cardiovascular Disease: In-Depth Review. *Circulation (New York, N.Y.)* **145**, 61-78 (2022). https://doi.org/10.1161/CIRCULATIONAHA.121.056171

105 Chaffey, L., Roberti, A. & Greaves, D. R. Drug repurposing in cardiovascular inflammation: Successes, failures, and future opportunities. *Frontiers in pharmacology* **13**, 1046406 (2022). https://doi.org/10.3389/fphar.2022.1046406

106 Ridker, P. M. *et al.* Antiinflammatory Therapy with Canakinumab for Atherosclerotic Disease. *The New England journal of medicine* **377**, 1119-1131 (2017). https://doi.org/10.1056/NEJMoa1707914

107 Tardif, J.-C. *et al.* Efficacy and Safety of Low-Dose Colchicine after Myocardial Infarction. *The New England journal of medicine* **381**, 2497-2505 (2019). https://doi.org/10.1056/NEJMoa1912388

108 Tong, D. C. *et al.* Colchicine in Patients With Acute Coronary Syndrome: The Australian COPS Randomized Clinical Trial. *Circulation (New York, N.Y.)* **142**, 1890-1900 (2020). https://doi.org/10.1161/CIRCULATIONAHA.120.050771

109 Šimo, L., Kazimirova, M., Richardson, J. & Bonnet, S. I. The Essential Role of Tick Salivary Glands and Saliva in Tick Feeding and Pathogen Transmission. *Frontiers in cellular and infection microbiology* **7**, 281 (2017). https://doi.org/10.3389/fcimb.2017.00281

110 Vieira, A. T. *et al.* Treatment with a Novel Chemokine-Binding Protein or Eosinophil Lineage-Ablation Protects Mice from Experimental Colitis. *The American journal of pathology* **175**, 2382-2391 (2009). https://doi.org/10.2353/ajpath.2009.090093

111 Hajnická, V. *et al.* Anti-interleukin-8 activity of tick salivary gland extracts. *Parasite immunology* **23**, 483 (2001). https://doi.org/10.1046/j.1365-3024.2001.00403.x

112 HajnickÁ, V. *et al.* Manipulation of host cytokine network by ticks: a potential gateway for pathogen transmission. *Parasitology* **130**, 333-342 (2005). https://doi.org/10.1017/S0031182004006535

113 Déruaz, M. *et al.* Ticks produce highly selective chemokine binding proteins with antiinflammatory activity. *The Journal of experimental medicine* **205**, 2019-2031 (2008). https://doi.org/10.1084/jem.20072689

114 Déruaz, M. *et al.* Evasin- 4, a tick- derived chemokine- binding protein with broad selectivity can be modified for use in preclinical disease models. *FEBS Journal* **280**, 4876-4887 (2013). https://doi.org/10.1111/febs.12463
115 Aryal, P. *et al.* Swapping N-terminal regions among tick evasins reveals cooperative interactions influencing chemokine binding and selectivity. *The Journal of biological chemistry* **298**, 102382-102382 (2022). https://doi.org/10.1016/j.jbc.2022.102382
116 Singh, U. P. *et al.* Chemokine and cytokine levels in inflammatory bowel disease patients. *Cytokine* **77**, 44-49 (2016). https://doi.org/10.1016/j.cyto.2015.10.008
117 Alenazi, Y. *et al.* Genetically engineered two-warhead evasins provide a method to achieve precision targeting of disease-relevant chemokine subsets. *Scientific reports* **8**, 6333-6314 (2018). https://doi.org/10.1038/s41598-018-24568-9
118 Lee, A. W. *et al.* A knottin scaffold directs the CXC-chemokine-binding specificity of tick evasins. *Journal of Biological Chemistry* **294** (2019). https://doi.org/10.1074/jbc.RA119.008817
119 Eaton, J. R. O. *et al.* The N-terminal domain of a tick evasin is critical for chemokine binding and neutralization and confers specific binding activity to other evasins. (2018).
120 Hayward, J. *et al.* Ticks from diverse genera encode chemokine-inhibitory evasin proteins. *The Journal of biological chemistry* **292**, 15670-15680 (2017). https://doi.org/10.1074/jbc.M117.807255
121 Bhattacharya, S. & Nuttall, P. A. Phylogenetic Analysis Indicates That Evasin-Like Proteins of Ixodid Ticks Fall Into Three Distinct Classes. *Frontiers in cellular and infection microbiology* **11**, 769542-769542 (2021). https://doi.org/10.3389/fcimb.2021.769542
122 Denisov, S. S. & Dijkgraaf, I. Immunomodulatory Proteins in Tick Saliva From a Structural Perspective. *Frontiers in cellular and infection microbiology* **11**, 769574-769574 (2021). https://doi.org/10.3389/fcimb.2021.769574
123 Mans, B. J., Andersen, J. F. & Ribeiro, J. M. C. A Deeper Insight into the Tick Salivary Protein Families under the Light of Alphafold2 and Dali_ Introducing the TickSialoFam 2.0 Database. *International journal of molecular sciences* **23**, 15613 (2022). https://doi.org/10.3390/ijms232415613
124 Dias, J. M. *et al.* Structural Basis of Chemokine Sequestration by a Tick Chemokine Binding Protein: The Crystal Structure of the Complex between Evasin-1 and CCL3. *PloS one* **4**, e8514 (2009). https://doi.org/10.1371/journal.pone.0008514
125 Denisov, S. S. *et al.* Tick saliva protein Evasin-3 modulates chemotaxis by disrupting CXCL8 interactions with glycosaminoglycans and CXCR2. *The Journal of biological chemistry* **294**, 12370-12379 (2019). https://doi.org/10.1074/jbc.RA119.008902
126 Bonvin, P. *et al.* Identification of the Pharmacophore of the CC Chemokine-binding Proteins Evasin-1 and -4 Using Phage Display. *The Journal of biological chemistry* **289**, 31846-31855 (2014). https://doi.org/10.1074/jbc.M114.599233

127 Bhusal, R. P. *et al.* Structure-guided engineering of tick evasins for targeting chemokines in inflammatory diseases. *Proceedings of the National Academy of Sciences - PNAS* **119**, 1 (2022). https://doi.org/10.1073/pnas.2122105119
128 Copin, J.-C. *et al.* Treatment with Evasin-3 Reduces Atherosclerotic Vulnerability for Ischemic Stroke, but Not Brain Injury in Mice. *Journal of cerebral blood flow and metabolism* **33**, 490-498 (2013). https://doi.org/10.1038/jcbfm.2012.198
129 Braunersreuther, V. *et al.* Treatment with the CC chemokine-binding protein Evasin-4 improves post-infarction myocardial injury and survival in mice. *Thrombosis and haemostasis* **109**, 807-825 (2013). https://doi.org/10.1160/TH13-04-0297
130 Russo, R. C. *et al.* Therapeutic effects of evasin-1, a chemokine binding protein, in bleomycin-induced pulmonary fibrosis. *American journal of respiratory cell and molecular biology* **45**, 72-80 (2011). https://doi.org/10.1165/rcmb.2009-0406OC
131 Mohs, A. *et al.* Functional role of CCL5/RANTES for HCC progression during chronic liver disease. *Journal of hepatology* **66**, 743-753 (2017). https://doi.org/10.1016/j.jhep.2016.12.011
132 Oliveira, A. L. *et al.* The chemistry of snake venom and its medicinal potential. *Nature reviews. Chemistry* **6**, 451-469 (2022). https://doi.org/10.1038/s41570-022-00393-7
133 Darlot, B. *et al.* Engineered anti-inflammatory peptides inspired by mapping an evasin-chemokine interaction. *The Journal of biological chemistry* **295**, 10926 (2020). https://doi.org/10.1074/jbc.RA120.014103
134 Denisov, S. S. *et al.* Structural characterization of anti-CCL5 activity of the tick salivary protein evasin-4. *The Journal of biological chemistry* **295**, 14367 (2020). https://doi.org/10.1074/jbc.RA120.013891
135 Zlotnik, A. & Yoshie, O. Chemokines: A New Classification System and Their Role in Immunity. *Immunity* **12**, 121-127 (2000). https://doi.org/10.1016/S1074-7613(00)80165-X
136 Mortier, A., Van Damme, J. & Proost, P. Overview of the mechanisms regulating chemokine activity and availability. *Immunology letters* **145**, 2-9 (2012). https://doi.org/10.1016/j.imlet.2012.04.015
137 Miyabe, Y., Lian, J., Miyabe, C. & Luster, A. D. Chemokines in rheumatic diseases: pathogenic role and therapeutic implications. *Nat Rev Rheumatol* **15**, 731-746 (2019). https://doi.org/10.1038/s41584-019-0323-6
138 Garin, A. & Proudfoot, A. E. I. Chemokines as targets for therapy. *Exp Cell Res* **317**, 602-612 (2011). https://doi.org/10.1016/j.yexcr.2010.12.021
139 Mantovani, A. Redundancy and robustness versus division of labour and specialization in innate immunity. *Semin Immunol* **36**, 28-30 (2018). https://doi.org/10.1016/j.smim.2017.12.006
140 Wang, L. *et al.* Therapeutic peptides: current applications and future directions. *Signal transduction and targeted therapy* **7**, 48-48 (2022). https://doi.org/10.1038/s41392-022-00904-4

141 Vales, S. *et al.* Discovery and pharmacophoric characterization of chemokine network inhibitors using phage-display, saturation mutagenesis and computational modelling. *Nature communications* **14**, 5763-5763 (2023). https://doi.org/10.1038/s41467-023-41488-z

142 McLaughlin, M. E. & Sidhu, S. S. in *Methods Enzymol* Vol. 523 *Methods in Enzymology* 327-349 (Elsevier Science & Technology, 2013).

143 Weiss, G. A., Watanabe, C. K., Zhong, A., Goddard, A. & Sidhu, S. S. Rapid Mapping of Protein Functional Epitopes by Combinatorial Alanine Scanning. *Proceedings of the National Academy of Sciences - PNAS* **97**, 8950-8954 (2000). https://doi.org/10.1073/pnas.160252097

144 Feng, Y. *et al.* Mechanism of activation and biased signaling in complement receptor C5aR1. *Cell research* **33**, 312-324 (2023). https://doi.org/10.1038/s41422-023-00779-2

145 Rogers, J. M., Passioura, T. & Suga, H. Nonproteinogenic deep mutational scanning of linear and cyclic peptides. *Proceedings of the National Academy of Sciences - PNAS* **115**, 10959-10964 (2018). https://doi.org/10.1073/pnas.1809901115

146 Gustavsson, M., Dyer, D. P., Zhao, C. & Handel, T. M. Kinetics of CXCL12 binding to atypical chemokine receptor 3 reveal a role for the receptor N terminus in chemokine binding. *Science signaling* **12** (2019). https://doi.org/10.1126/scisignal.aaw3657

147 Kawamura, T. *et al.* A general method for site specific fluorescent labeling of recombinant chemokines. *PloS one* **9**, e81454 (2014). https://doi.org/10.1371/journal.pone.0081454

148 Ganguly, H. K. & Basu, G. Conformational landscape of substituted prolines. *Biophysical reviews* **12**, 25-39 (2020). https://doi.org/10.1007/s12551-020-00621-8

149 Szekanecz, Z. & Koch, A. E. Successes and failures of chemokine-pathway targeting in rheumatoid arthritis. *Nature reviews. Rheumatology* **12**, 5-13 (2016). https://doi.org/10.1038/nrrheum.2015.157

150 Qin, Z. The use of THP-1 cells as a model for mimicking the function and regulation of monocytes and macrophages in the vasculature. *Atherosclerosis* **221**, 2-11 (2012). https://doi.org/10.1016/j.atherosclerosis.2011.09.003

151 Nov, Y. When Second Best Is Good Enough: Another Probabilistic Look at Saturation Mutagenesis. *Applied and Environmental Microbiology* **78**, 258-262 (2012). https://doi.org/10.1128/AEM.06265-11

152 Senthil, R., Usha, S. & Saravanan, K. M. Importance of fluctuating amino acid residues in folding and binding of proteins. *Avicenna journal of medical biotechnology* **11**, 339-344 (2019).

153 Dougherty, D. A. Cation-π Interactions in Chemistry and Biology: A New View of Benzene, Phe, Tyr, and Trp. *Science (American Association for the Advancement of Science)* **271**, 163-168 (1996). https://doi.org/10.1126/science.271.5246.163

154 Vaideeswaran, S. & Ramaiah, S. Investigations on the role of π–π interactions and π–π networks in eNOS and nNOS proteins. *Bioorganic chemistry* **49**, 16-23 (2013). https://doi.org/10.1016/j.bioorg.2013.06.005

155 Anishetty, S., Pennathur, G. & Anishetty, R. Tripeptide analysis of protein structures. *BMC structural biology* **2**, 1-8 (2002). https://doi.org/10.1186/1472-6807-2-1

156 Blanchet, X., Langer, M., Weber, C., Koenen, R. R. & Hundelshausen, P. V. Touch of chemokines. **3** (2012). https://doi.org/10.3389/fimmu.2012.00175

157 Anders, H.-J., Romagnani, P. & Mantovani, A. Pathomechanisms: homeostatic chemokines in health, tissue regeneration, and progressive diseases. *Trends in molecular medicine* **20**, 154-165 (2014). https://doi.org/10.1016/j.molmed.2013.12.002

158 Bonvin, P., Power, C. A. & Proudfoot, A. E. I. Evasins: Therapeutic Potential of a New Family of Chemokine-Binding Proteins from Ticks. *Frontiers in Immunology* **7** (2016). https://doi.org/10.3389/fimmu.2016.00208

159 Gouwy, M., Schiraldi, M., Struyf, S., Van Damme, J. & Uguccioni, M. Possible mechanisms involved in chemokine synergy fine tuning the inflammatory response. *Immunology letters* **145**, 10-14 (2012). https://doi.org/10.1016/j.imlet.2012.04.005

160 Bazan, H. A. *et al.* A pro-inflammatory and fibrous cap thinning transcriptome profile accompanies carotid plaque rupture leading to stroke. *Scientific reports* **12**, 13499-13499 (2022). https://doi.org/10.1038/s41598-022-17546-9

161 Wu, L. *et al.* Variation and genetic control of protein abundance in humans. *Nature (London)* **499**, 79-82 (2013). https://doi.org/10.1038/nature12223

162 Blanchetot, C. *et al.* Neutralizing Nanobodies targeting diverse chemokines effectively inhibit chemokine function. (2013). https://doi.org/10.1074/jbc.M113.467969

163 Veeresham, C. Natural products derived from plants as a source of drugs. *Journal of advanced pharmaceutical technology and research* **3**, 200-201 (2012). https://doi.org/10.4103/2231-4040.104709

164 Enzler, T. & Fojo, T. Long-acting somatostatin analogues in the treatment of unresectable/metastatic neuroendocrine tumors. *Seminars in oncology* **44**, 141-156 (2017). https://doi.org/10.1053/j.seminoncol.2017.07.001

165 Roelfsema, F., Biermasz, N. R., Pereira, A. M. & Romijn, J. A. Therapeutic options in the management of acromegaly: Focus on lanreotide Autogel. *Biologics* **2**, 463-479 (2008). https://doi.org/10.2147/btt.s3356

166 Mahapatra, M. K., Karuppasamy, M. & Sahoo, B. M. Semaglutide, a glucagon like peptide-1 receptor agonist with cardiovascular benefits for management of type 2 diabetes. *Reviews in endocrine & metabolic disorders* **23**, 521-539 (2022). https://doi.org/10.1007/s11154-021-09699-1

167 Zhang, G. *et al.* Rapid de novo discovery of peptidomimetic affinity reagents for human angiotensin converting enzyme 2. *Communications chemistry* **5**, 8-10 (2022). https://doi.org/10.1038/s42004-022-00625-3

168 Oller-Salvia, B. & Chin, J. W. Efficient Phage Display with Multiple Distinct Non-Canonical Amino Acids Using Orthogonal Ribosome-Mediated Genetic

Code Expansion. *Angewandte Chemie International Edition* **58**, 10844-10848 (2019). https://doi.org/10.1002/anie.201902658

169 Castro, T. G., Melle-Franco, M., Sousa, C. E. A., Cavaco-Paulo, A. & Marcos, J. C. Non-Canonical Amino Acids as Building Blocks for Peptidomimetics: Structure, Function, and Applications. *Biomolecules (Basel, Switzerland)* **13**, 981 (2023). https://doi.org/10.3390/biom13060981

170 Veronese, F. M. & Pasut, G. PEGylation, successful approach to drug delivery. *Drug discovery today* **10**, 1451-1458 (2005). https://doi.org/10.1016/S1359-6446(05)03575-0

171 Dissanayake, T., Sun, X., Abbey, L. & Bandara, N. Recent advances in lipid-protein conjugate-based delivery systems in nutraceutical, drug, and gene delivery. *Food hydrocolloids for health* **2**, 100054 (2022). https://doi.org/10.1016/j.fhfh.2022.100054

172 Aguilar-Toala, J. E., Quintanar-Guerrero, D., Liceaga, A. M. & Zambrano-Zaragoza, M. L. Encapsulation of bioactive peptides: A strategy to improve the stability, protect the nutraceutical bioactivity and support their food applications. *RSC advances* **12**, 6449-6458 (2022). https://doi.org/10.1039/d1ra08590e

173 Reed, J., Bain, S. & Kanamarlapudi, V. Recent advances in understanding the role of glucagon-like peptide 1 [version 1; peer review: 2 approved]. *F1000 research* **9**, 239 (2020). https://doi.org/10.12688/f1000research.20602.1

174 Yan, Y., Thakur, M., van der Vorst, E. P. C., Weber, C. & Döring, Y. Targeting the chemokine network in atherosclerosis. *Atherosclerosis* **330**, 95-106 (2021). https://doi.org/10.1016/j.atherosclerosis.2021.06.912

175 Almeida, S. O. & Budoff, M. Effect of statins on atherosclerotic plaque. *Trends Cardiovasc Med* **29**, 451-455 (2019). https://doi.org/10.1016/j.tcm.2019.01.001

176 Kong, G. *et al.* Higher mortality in acute coronary syndrome patients without standard modifiable risk factors: Results from a global meta-analysis of 1,285,722 patients. *Int J Cardiol* **371**, 432-440 (2023). https://doi.org/10.1016/j.ijcard.2022.09.062

177 Knuuti, J. *et al.* 2019 ESC Guidelines for the diagnosis and management of chronic coronary syndromes The Task Force for the diagnosis and management of chronic coronary syndromes of the European Society of Cardiology (ESC). *European heart journal* **41**, 407-477 (2020). https://doi.org/10.1093/eurheartj/ehz425

178 Reijnders, E., van der Laarse, A., Jukema, J. W. & Cobbaert, C. M. High residual cardiovascular risk after lipid-lowering: prime time for Predictive, Preventive, Personalized, Participatory, and Psycho-cognitive medicine. *Frontiers in cardiovascular medicine* **10**, 1264319-1264319 (2023). https://doi.org/10.3389/fcvm.2023.1264319

179 Figtree, G. A. *et al.* Clinical Pathway for Coronary Atherosclerosis in Patients Without Conventional Modifiable Risk Factors: JACC State-of-the-Art Review. *J Am Coll Cardiol* **82**, 1343-1359 (2023). https://doi.org/10.1016/j.jacc.2023.06.045

180 Vernon, S. T. *et al.* Increasing proportion of ST elevation myocardial infarction patients with coronary atherosclerosis poorly explained by standard modifiable risk factors. *Eur J Cardiovasc Prev Rehabil* **24**, 1824-1830 (2017). https://doi.org/10.1177/2047487317720287

181 Heidarieh, H., Hernáez, B. & Alcamí, A. Immune modulation by virus-encoded secreted chemokine binding proteins. *Virus research* **209**, 67-75 (2015). https://doi.org/10.1016/j.virusres.2015.02.028

182 González-Motos, V., Kropp, K. A. & Viejo-Borbolla, A. Chemokine binding proteins: An immunomodulatory strategy going viral. *Cytokine & growth factor reviews* **30**, 71-80 (2016). https://doi.org/10.1016/j.cytogfr.2016.02.007

183 Roversi, P. *et al.* The Structure of OMCI, a Novel Lipocalin Inhibitor of the Complement System. *J Mol Biol* **369**, 784-793 (2007). https://doi.org/10.1016/j.jmb.2007.03.064

184 Chmelar, J., Kotál, J., Kovaríková, A. & Kotsyfakis, M. The use of tick salivary proteins as novel therapeutics. *Front Physiol* **10**, 812-812 (2019). https://doi.org/10.3389/fphys.2019.00812

185 Lauton, P. M. *et al.* Adherence to infliximab treatment in patients with immune-mediated inflammatory diseases from a referral center in Brazil: a cohort study. *BMC Gastroenterol* **24**, 384-313 (2024). https://doi.org/10.1186/s12876-024-03455-w

186 Song, Y. & Buchwald, P. TNF superfamily protein-protein interactions: feasibility of small- molecule modulation. *Curr Drug Targets* **16**, 393-408 (2015).

187 Jones, S. A. & Jenkins, B. J. Recent insights into targeting the IL-6 cytokine family in inflammatory diseases and cancer. *Nat Rev Immunol* **18**, 773-789 (2018). https://doi.org/10.1038/s41577-018-0066-7

188 Dinarello, C. A. The IL-1 family of cytokines and receptors in rheumatic diseases. *Nat Rev Rheumatol* **15**, 612-632 (2019). https://doi.org/10.1038/s41584-019-0277-8

189 McGeachy, M. J., Cua, D. J. & Gaffen, S. L. The IL-17 Family of Cytokines in Health and Disease. *Immunity* **50**, 892-906 (2019). https://doi.org/10.1016/j.immuni.2019.03.021

190 Christen, U. & Kimmel, R. Chemokines as Drivers of the Autoimmune Destruction in Type 1 Diabetes: Opportunity for Therapeutic Intervention in Consideration of an Optimal Treatment Schedule. *Front Endocrinol (Lausanne)* **11**, 591083-591083 (2020). https://doi.org/10.3389/fendo.2020.591083

191 Camba-Gómez, M., Arosa, L., Gualillo, O. & Conde-Aranda, J. Chemokines and chemokine receptors in inflammatory bowel disease: Recent findings and future perspectives. *Drug Discov Today* **27**, 1167-1175 (2022). https://doi.org/10.1016/j.drudis.2021.12.004

192 Coperchini, F., Chiovato, L., Croce, L., Magri, F. & Rotondi, M. The cytokine storm in COVID-19: An overview of the involvement of the chemokine/chemokine-receptor system. *Cytokine & growth factor reviews* **53**, 25-32 (2020). https://doi.org/10.1016/j.cytogfr.2020.05.003

9 APPENDICES

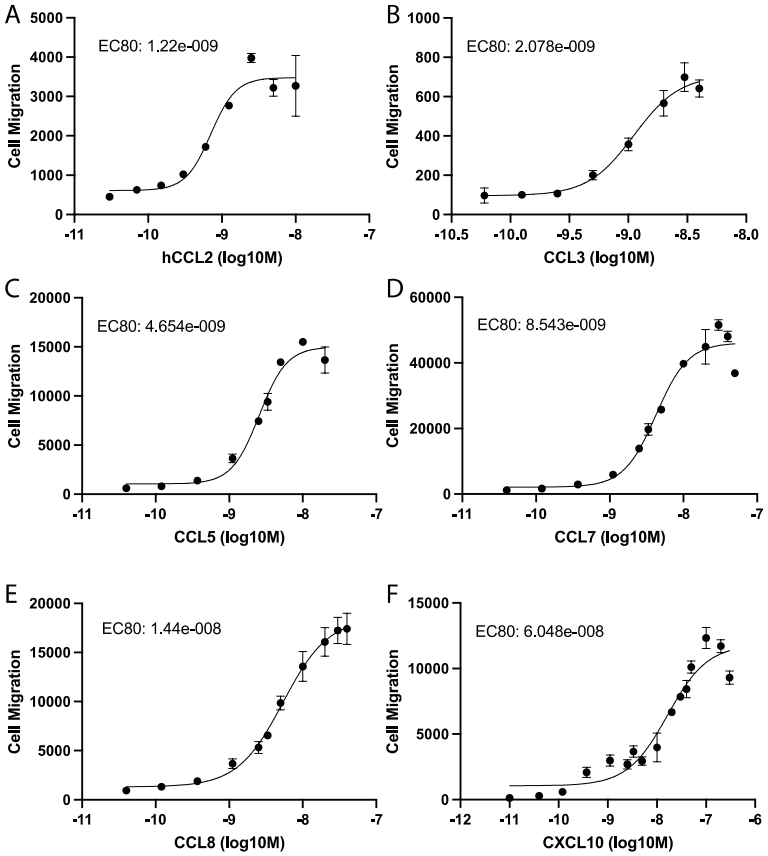

Appendix 1: Representative dose-response curves. The x-axis represents the indicated chemokine concentration (in molar), and the y-axis represents the migrated cell count (**A-E**, THP1 cells and **F** ATC). Curves were fitted using a 4-parameter log-logistic model. Data are shown as individual data points for each chemokine dose, with three technical replicates per dose. For each dose-response, biological replicates were performed, and the average EC80 was used in inhibition assays.

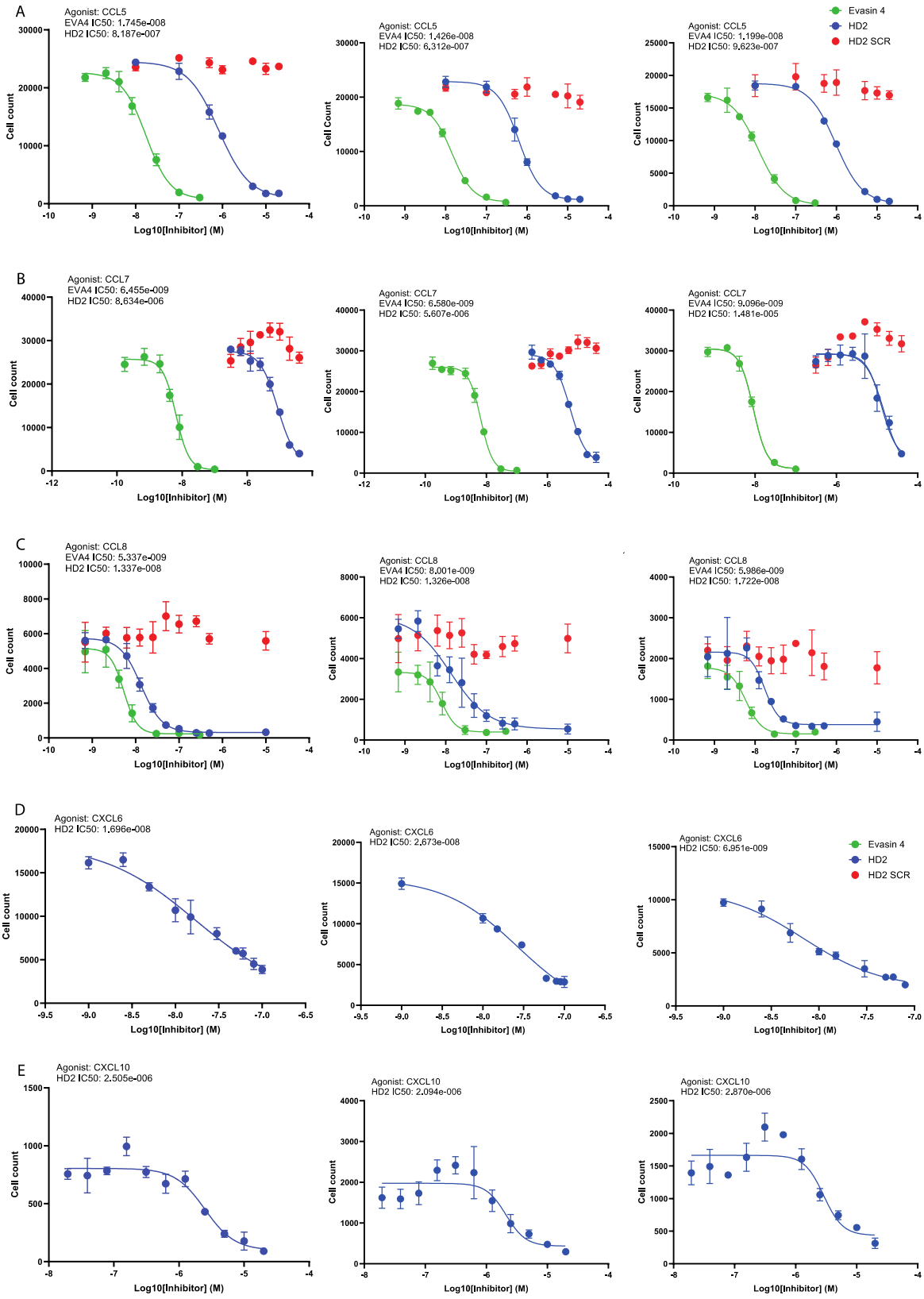
A
Agonist: CCL5
EVA4 IC50: 1.745e-008
HD2 IC50: 8.187e-007
Agonist: CCL5
EVA4 IC50: 1.426e-008
HD2 IC50: 6.312e-007
Agonist: CCL5
EVA4 IC50: 1.199e-008
HD2 IC50: 9.623e-007
Evasin 4
HD2
HD2 SCR
B
Agonist: CCL7
EVA4 IC50: 6.455e-009
HD2 IC50: 8.634e-006
Agonist: CCL7
EVA4 IC50: 6.580e-009
HD2 IC50: 5.607e-006
Agonist: CCL7
EVA4 IC50: 9.096e-009
HD2 IC50: 1.481e-005
C
Agonist: CCL8
EVA4 IC50: 5.337e-009
HD2 IC50: 1.337e-008
Agonist: CCL8
EVA4 IC50: 8.001e-009
HD2 IC50: 1.326e-008
Agonist: CCL8
EVA4 IC50: 5.986e-009
HD2 IC50: 1.722e-008
D
Agonist: CXCL6
HD2 IC50: 1.696e-008
Agonist: CXCL6
HD2 IC50: 2.673e-008
Agonist: CXCL6
HD2 IC50: 6.951e-009
Evasin 4
HD2
HD2 SCR
E
Agonist: CXCL10
HD2 IC50: 2.505e-006
Agonist: CXCL10
HD2 IC50: 2.094e-006
Agonist: CXCL10
HD2 IC50: 2.870e-006
Cell count
Cell Count
Log10[Inhibitor] (M)

Appendix 2: Biological IC50 inhibitory dose-response curves for EVA4, HD2, and HD2 SCR. Row **A**: Biological IC50 replicates against CCL5 using THP1 cells. Row **B**: Biological IC50 replicates against CCL7 using THP1 cells. Row **C**: Biological IC50 replicates against CCL8 using THP1 cells. Row **D**: IC50 replicates of HD2 only against CXCL6 using Jurkat (CXCR1) cells (performed by GS). Row **E**: IC50 replicates of HD2 only against CXCL10 using activated T cells (ATC) (performed by MP). Data are presented as individual data points for each chemokine dose, with three technical replicates per dose. The x-axis represents inhibitor concentration (in molar), while the y-axis shows the number of migrated cells. Curves were fitted using a 4-parameter log-logistic model.

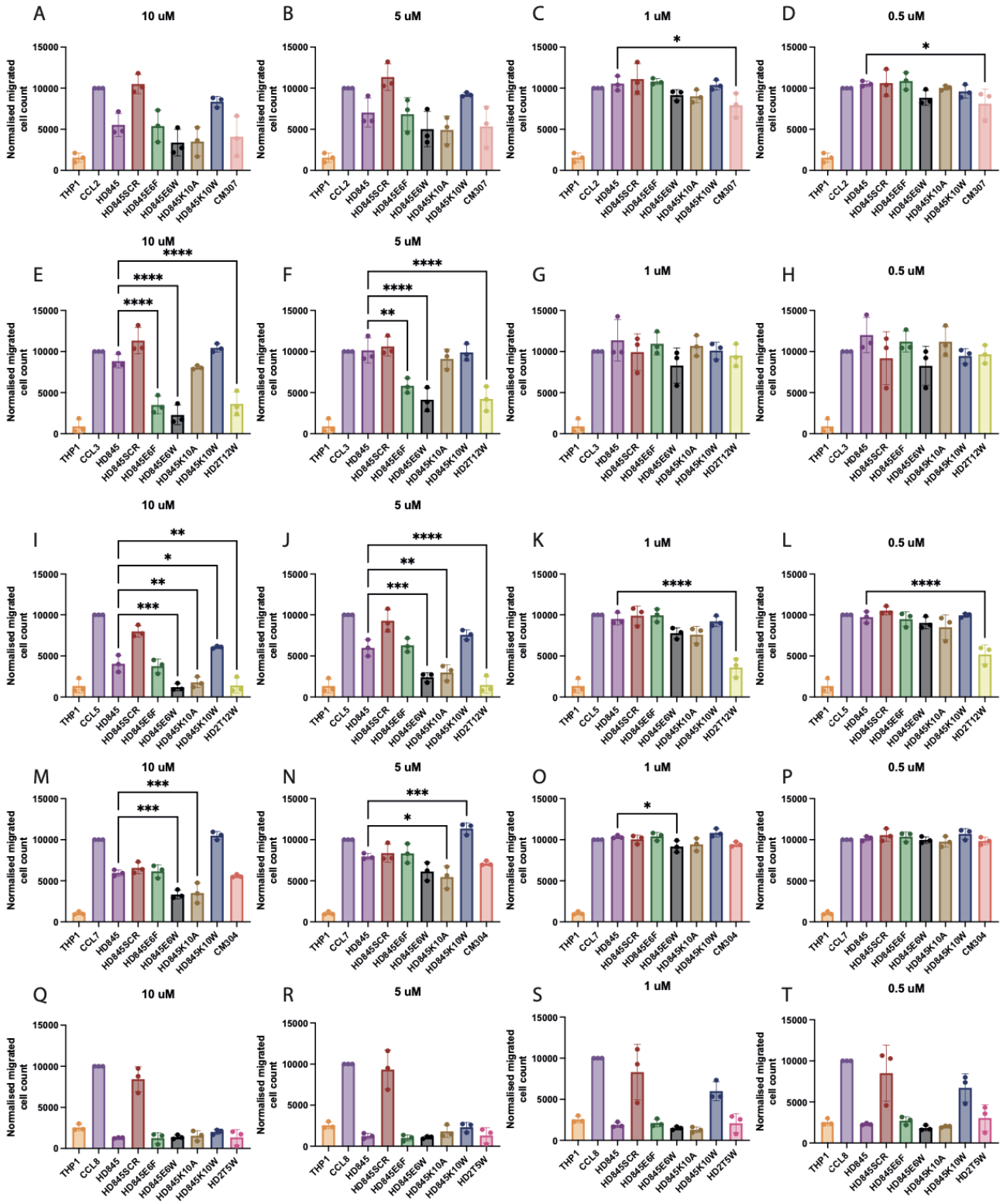
A
10 uM
B
5 uM
C
1 uM
D
0.5 uM
E
10 uM
F
5 uM
G
1 uM
H
0.5 uM
I
10 uM
J
5 uM
K
1 uM
L
0.5 uM
M
10 uM
N
5 uM
O
1 uM
P
0.5 uM
Q
10 uM
R
5 uM
S
1 uM
T
0.5 uM
Normalised migrated cell count
THP1
CCL2
CCL3
CCL5
CCL7
CCL8
HD845
HD845SCR
HD845E6F
HD845E6W
HD845K10A
HD845K10W
CM307
CM304
HD2T12W
HD2T5W

Appendix 3: Preliminary potency assessments of HD845 mutants. Bar chart with SD error bars show the effects of HD845 mutants on chemokine-induced cell migration compared to the parental HD845. The x-axis indicates the specific peptide tested. The peptides were tested at concentrations of 10, 5, 1, and 0.5 μM. Chemokines were tested at EC80 concentrations with Panels **A-D**: CCL2, Panels **E-H**: CCL3, Panels **I-L**: CCL5, Panels **M-P**: CCL7 and Panels **Q-T**: CCL8. Each experiment included three technical replicates, with individual data points indicated. The y-axis shows the normalised migrated cell count. Cell counts were normalised to the mean value of migrated cells in the presence of chemokine alone, which was set at 10000 cells. The x-axis indicates the specific peptide tested. Data was analysed using one-way ANOVA followed by Dunnett's test for multiple comparisons and indicated by asterisks: ****$p \leq 0.0001$, ***$p \leq 0.001$, **$p \leq 0.01$, *$p \leq 0.05$.

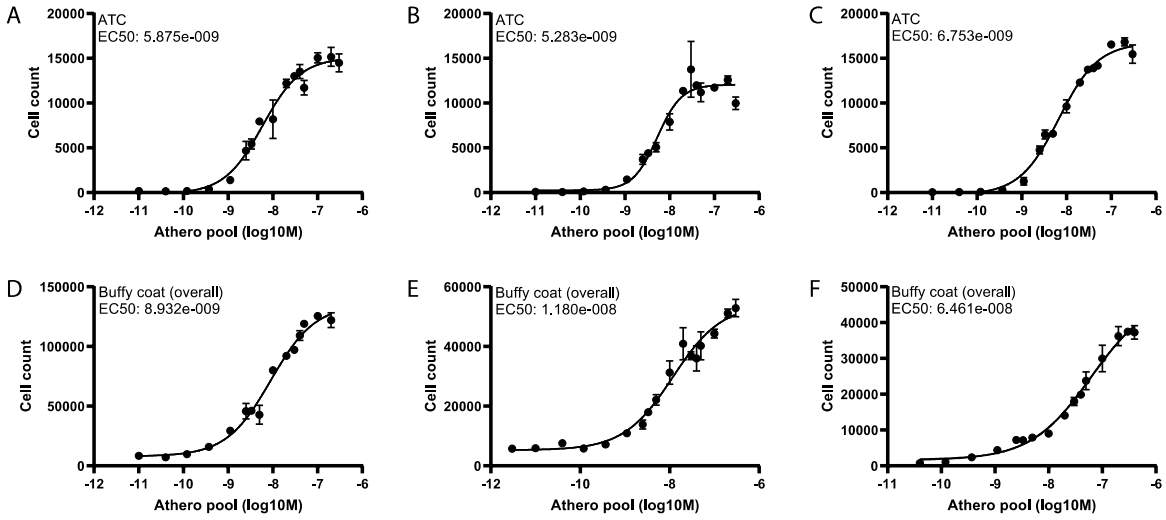

Appendix 4: Dose-response curves of the atherosclerosis chemokine pool in chemotaxis assays. Dose-response replicate curves of atherosclerosis chemokine pool (athero pool) -induced activated T cells (ATC) (**A**, **B** and **C**) and buffy coat (**D**, **E** and **F**). Data are shown as individual data points for each chemokine dose, with three technical replicates per dose. The x-axis represents athero pool concentration (in molar), and the y-axis represents the migrated cell count. Curves were fitted using a 4-parameter log-logistic model.

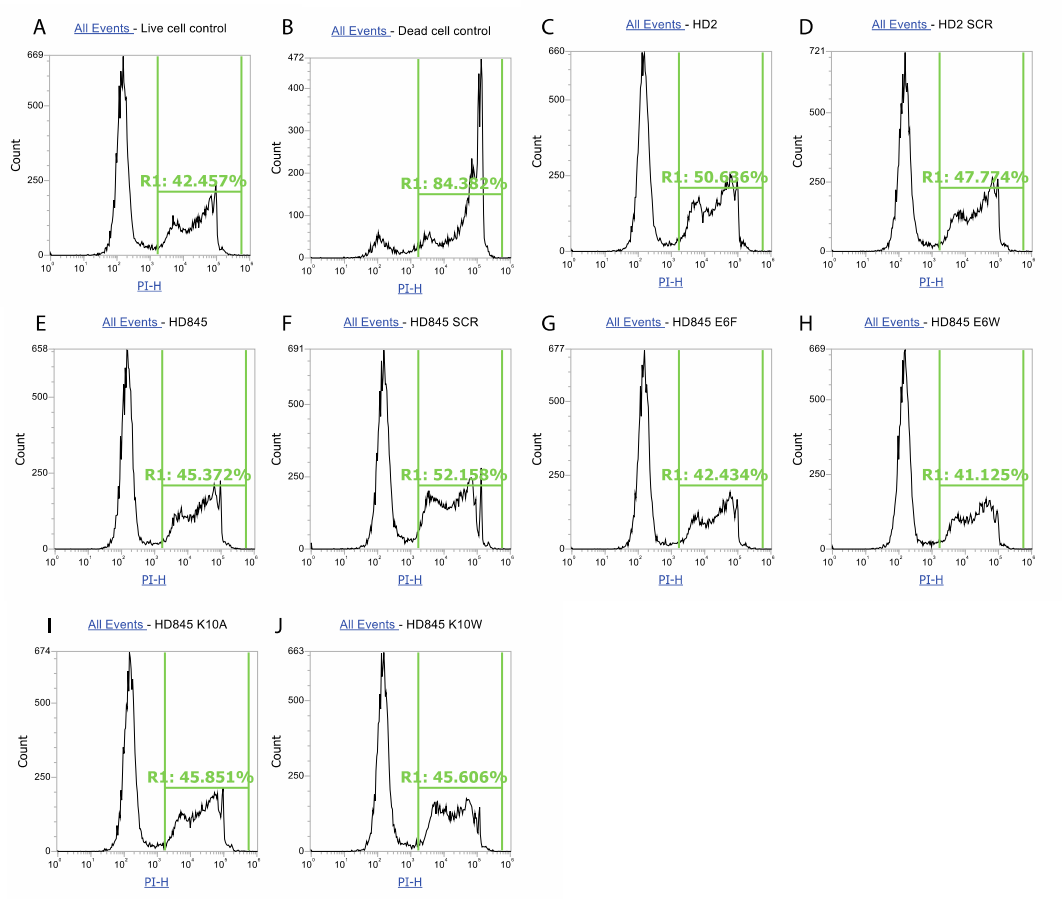

Appendix 5: Propidium iodide (PI)/Live dead staining of the HD2, HD845, HD845 mutants and SCRs on ATC. **A**) Live cells, indicated by the left peak. **B**) Dead cells in the R1 gate after cell boiling. Staining results for the specific peptides: **C**) HD2, **D**) HD2SCR, **E**) HD845, **F**) HD845SCR, **G**) HD845E6F, **H**) HD845E6W, **I**) HD845K10A and **J**) HD845K10W. Performed by MP.

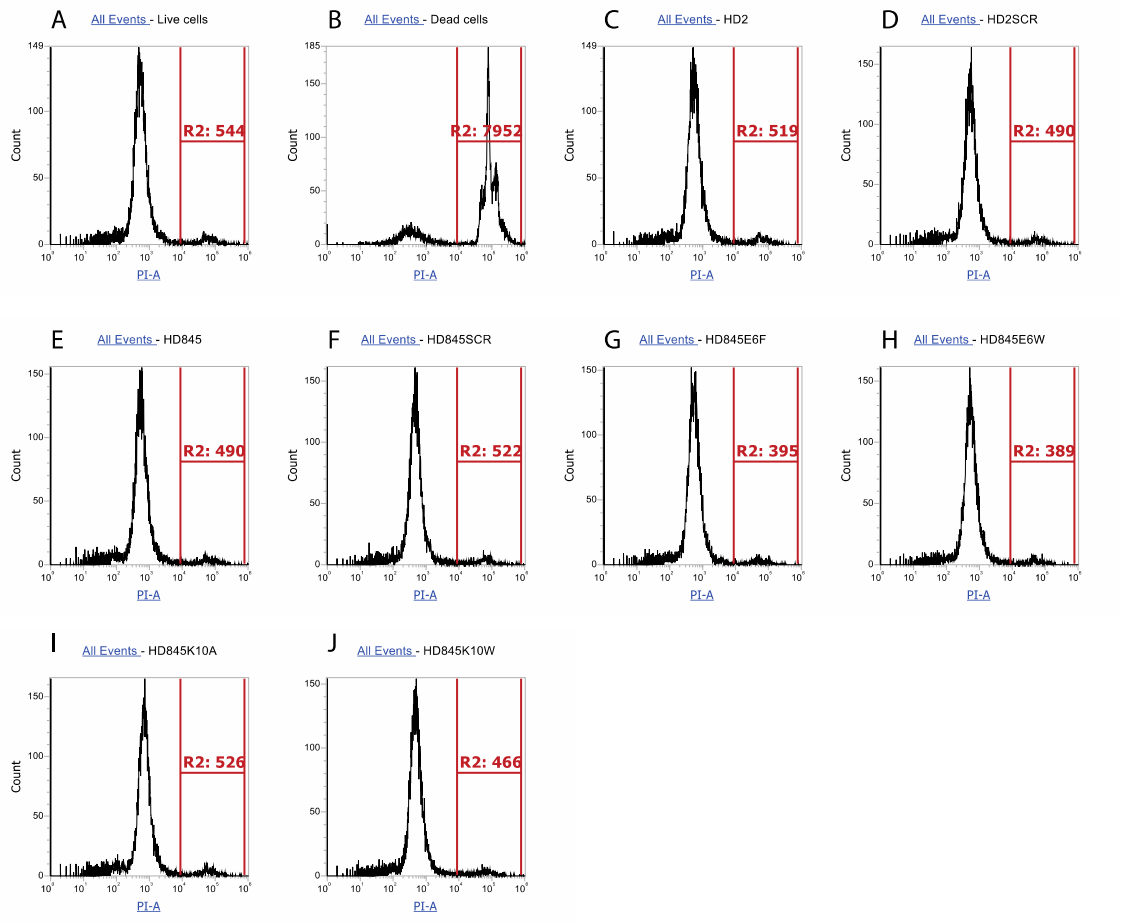

Appendix 6: Propidium iodide (PI)/Live dead staining of the HD2, HD845, HD845 mutants and SCRs on THP1 cells. A) Live cells, indicated by the left peak. **B**) Dead cells in the R2 gate after cell boiling. Staining results for the specific peptides: **C**) HD2, **D**) HD2SCR, **E**) HD845, **F**) HD845SCR, **G**) HD845E6F, **H**) HD845E6W, **I**) HD845K10A and **J**) HD845K10W.

nature communications

Article

https://doi.org/10.1038/s41467-023-41488-z

Discovery and pharmacophoric characterization of chemokine network inhibitors using phage-display, saturation mutagenesis and computational modelling

Received: 9 February 2023

Accepted: 6 September 2023

Published online: 16 September 2023

Check for updates

Serena Vales[1,3], Jhanna Kryukova[1,3], Soumyanetra Chandra[1], Gintare Smagurauskaite[1], Megan Payne[1], Charlie J. Clark[1], Katrin Hafner[1], Philomena Mburu[1], Stepan Denisov[1], Graham Davies[1], Carlos Outeiral[2], Charlotte M. Deane[2], Garrett M. Morris[2] & Shoumo Bhattacharya[1]

CC and CXC-chemokines are the primary drivers of chemotaxis in inflammation, but chemokine network redundancy thwarts pharmacological intervention. Tick evasins promiscuously bind CC and CXC-chemokines, overcoming redundancy. Here we show that short peptides that promiscuously bind both chemokine classes can be identified from evasins by phage-display screening performed with multiple chemokines in parallel. We identify two conserved motifs within these peptides and show using saturation-mutagenesis phage-display and chemotaxis studies of an exemplar peptide that an anionic patch in the first motif and hydrophobic, aromatic and cysteine residues in the second are functionally necessary. AlphaFold2-Multimer modelling suggests that the peptide occludes distinct receptor-binding regions in CC and in CXC-chemokines, with the first and second motifs contributing ionic and hydrophobic interactions respectively. Our results indicate that peptides with broad-spectrum anti-chemokine activity and therapeutic potential may be identified from evasins, and the pharmacophore characterised by phage display, saturation mutagenesis and computational modelling.

Chemokines are structurally related secreted proteins that drive the migration of neutrophils, monocytes, T-cells and other leucocytes during the inflammatory response to injury or infection and in immune system homoeostasis[1]. They play a major role in immune-inflammatory diseases ranging from atherosclerosis, rheumatoid arthritis, inflammatory bowel disease and cytokine-storm[2–5]. The 46 human chemokines are grouped into CC, CXC, CX3C and XC classes based on the spacing of their N-terminal cysteine residues[1]. CC-chemokines constitute the largest class, with 26 members in humans, while CXC chemokines have 17 members[1]. The binding of chemokines to a family of 18 G-protein coupled receptors (GPCRs) activates signalling, leading to chemotaxis or directed migration of leucocytes to the site of chemokine expression[1]. Chemokines are also functionally grouped into inflammatory or homoeostatic types with inflammatory chemokines causing leucocyte recruitment to the sites of inflammation, and constitutively expressed homoeostatic chemokines mediating immune cell homoeostasis[1]. Several homoeostatic chemokines also have inflammatory roles, and thus have dual functions[1,6].

Chemokines have a conserved disulfide-bonded tertiary structure with an unstructured N-terminal domain, followed by a N loop, a

[1]Wellcome Centre for Human Genetics and RDM Cardiovascular Medicine, University of Oxford, Roosevelt Drive, Oxford OX3 7BN, UK. [2]Department of Statistics, University of Oxford, 24-29 St Giles, Oxford OX1 3LB, UK. [3]These authors contributed equally: Serena Vales, Jhanna Kryukova.
e-mail: shoumo.bhattacharya@cardiov.ox.ac.uk

three-stranded β-sheet (linked by loops, known as 30s—between β1 and β2, and 40s—between β2 and β3), and an α-helix[7]. A consensus view is that chemokine receptors engage with chemokines through four chemokine recognition sites (CRS) − 0.5, 1, 1.5 and 2[7]. CRS0.5, i.e., the receptor distal N-terminus, interacts with the β1-strand. CRS1, located in the receptor N-terminus, interacts with the N and 40 s loops of the chemokine. CRS1.5, in the receptor N-terminus between CRS1 and CRS2, targets the conserved disulfide of the chemokine[7]. CRS2, i.e., the transmembrane pocket of the receptor, interacts with the N-terminus of the chemokine[7]. Chemokines often homodimerize, with CC-chemokines dimerising by interactions between CC motifs and preceding N-terminal residues, while CXC-chemokines dimerise by interactions between the β1-strands[7]. Chemokines also heterodimerize, with CC-type heterodimers activating and CXC-type heterodimers inhibiting chemokine activity[8]. Dimerisation impacts receptor binding: CC-class chemokines cannot bind their receptors as dimers, whereas CXC-class chemokines can[7].

The chemokine network is characterised by redundancy and robustness to genetic or environmental variation[9]. Functional redundancy is a driver of biological network robustness[10], and inflamed tissues are characterised by the expression of multiple chemokines with functionally redundant activities[11]. For instance, in rheumatoid arthritis, 15 CC and 11 CXC chemokines are expressed in joint tissues[3]. The human atherosclerotic plaque expresses 16 CC and 7 CXC chemokines[11]. Functional redundancy in chemokine-driven inflammatory leucocyte recruitment is likely created by promiscuous (i.e., "one-to-many") interactions between chemokines and their receptors[12], and the expression of multiple chemokine receptors by each leucocyte class[13]. The robustness to environmental variation has frustrated the development of therapeutics that target the chemokine network in inflammatory disease[3,14].

Following initial observations on the modulation of host immunity by ticks (reviewed in ref. 15), chemokine-binding proteins were identified in the saliva of Ixodid ticks[16]. Molecular cloning identified three chemokine-binding proteins, referred to as evasins, from the salivary glands of the dog tick *Rhipicephalus pulchellus*[17,18]. Evasins EVA1 and EVA4 specifically bind CC chemokines, whereas EVA3 specifically binds CXC chemokines[17,18]. Fifty evasin proteins from diverse tick species have been expressed and characterised to date[19–24]. They may be classified into two functional groups, A and B, with exclusive binding to either CC- or CXC- chemokines, respectively[25]. Sequence-based phylogenetic analysis of tick transcriptomes indicates that CC-chemokine binding class A evasin-like proteins segregate into three subclasses, A1, A2 and A3[25,26]. Structural characterisation shows that class A1 evasins have a four-disulfide-bonded core structure, with CC-chemokine binding specificity arising within the CC motif itself[27–29], whereas A3 evasins have a five-disulfide-bonded core structure[26]. Class B evasins have a three-disulfide-bonded "knottin" structure[23].

An important feature of both class A and class B evasins is that they typically bind and inhibit *multiple* chemokines in a "one-to-many" or promiscuous manner[19–23,25]. This facility, achieved by natural selection in ticks over several million years, very likely underlies their ability to maintain the prolonged skin attachment needed for blood feeding, despite local chemokine expression[25]. A key challenge is to exploit or mimic the ability of evasins to bind multiple chemokines for developing therapeutics that target the chemokine network in disease. Studies with evasins have shown that they are effective in diverse inflammatory disease models including arthritis, myocardial infarction, lung inflammation, pancreatitis and psoriasis (reviewed in ref. 30). Despite success in models of inflammatory disease, evasins have not been clinically developed as therapeutics, at least in part due to the perceived obstacles of foreign proteins as biological therapeutics such as immunogenicity, coupled with relatively high manufacturing costs, and binding specificity requiring that both class A and B evasins be used in combination. Alternative approaches to target chemokines have exploited evolution of broadly cross reactive antibodies using yeast surface display[31], and the isolation of promiscuous chemokine-binding peptides using phage-display followed by conversion into peptibody (IgG1-Fc) fusions[32].

Peptides and peptidomimetics that mimic the activity of parental proteins have been successfully developed from several naturally occurring proteins into viable clinical therapeutics. Exemplars include the peptidomimetics captopril, eptifibatide and tirofiban, which are based on peptides derived from the snake venom toxins bradykinin-potentiating-peptide, barbourin and echistatin respectively[33]. Peptides derived from the chemokine CCL5 have been shown to bind and inhibit chemokine function in vitro and in vivo by interfering with chemokine dimerisation[8]. Inspired by these exemplars, by using hydrogen-deuterium-exchange mass spectrometry (HDX-MS), we previously identified the chemokine-binding site of the tick class A evasin P672 (EV672_RHIPU) and developed a hexadecapeptide series that binds and inhibits the CC-class chemokines CCL8, CCL7, CCL3 and CCL2. We showed that one of these peptides inhibits inflammation in vivo[34]. In parallel, the chemokine-binding site of the tick class A evasin EVA4 was identified using NMR, and an EVA4-derived octadecapeptide Ev4Glu^{14}-Asn^{31} that inhibits CCL5 function thereby developed[28]. The finding that a short peptide sequence derived from an evasin could bind more than one chemokine raised the possibility that other promiscuous chemokine-binding peptides may be identified in the sequences of evasin proteins. The time-consuming and labour-intensive nature of HDX-MS or NMR approaches however render challenging their application to study the 386 pairwise evasin-chemokine interactions that have been documented to date[18–23,35].

Phage-display coupled to deep sequencing is a powerful approach that can be used to rapidly identify short linear interacting motifs (SLiMs) that mediate protein-protein interactions[36–39]. A phage-displayed peptide library derived from the first protein is selected using the second protein and bound phage are analysed using next-generation sequencing. Such approaches have focussed on identifying SLiMs from intrinsically disordered unstructured regions of proteins and have recently been applied to map domain-SLiM binding sites in the human proteome[39]. We hypothesised that phage-display selection coupled to deep sequencing, performed in parallel with multiple chemokines, could be exploited to identify promiscuous chemokine-binding peptides from evasins. Here we develop a pipeline combining phage-display, saturation mutagenesis and computational modelling to discover promiscuous chemokine-binding peptides from class A evasins and characterise the pharmacophore.

Results

Library construction and screening

We constructed a phage-display library where the major bacteriophage coat protein p8 was fused to hexadecapeptides derived from the mature sequences of 21 class A evasins[28,34] (see Fig. 1 and methods for details). This approach results in multivalent phage display, and allows identification of low affinity interactions[40]. We initiated our studies with class A evasins as linear chemokine-binding peptides had already been identified from this evasin class using structural methods[28,34], and would give us an opportunity to test the phage-display method. As unpaired Cys residues may compromise phage-display, they are mutated during library construction to alanine[38], a substitution that removes side-chains beyond the β-carbon without affecting conformational flexibility[41]. We constructed the library so that it included peptides with Cys residues intact, and also had peptides with mutations of Cys to Ala, and the conservative substitution, Cys to Ser[42]. Comparing counts in the wild-type Cys containing peptides, and those with Cys-Ser and Cys-Ala mutations obtained by next-generation sequencing of the input library show however that there was little or no impact on count numbers (Supplementary Fig. 1). The library was selected with 25 biotinylated chemokines as baits (Supplementary Table 1), individually attached to a

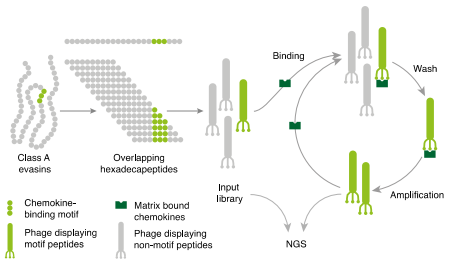

Fig. 1 | Phage display selection of chemokine binding peptides. Schematic of phage display nextGen sequencing pipeline. Class A evasins were deconstructed into DNA sequences encoding overlapping hexadecapeptides at single amino acid residue resolution and cloned into prSTOP4 phagemid vector. Phagemid pools were converted to phage library ('input') by transfecting *E.coli* together with helper phage. The phage-display library was amplified using PCR and the amplicon analysed using next-generation sequencing (NGS). Phage-display libraries were incubated with matrix-bound human chemokines and washed to remove any weak/non-binders. The matrix-bound phage was amplified using T1 phage-resistant *E. coli* and helper phage, and the amplified library was incubated again with the matrix-bound chemokine to further purify strong binders. Following three selection rounds the phage-inserts were amplified using PCR and the amplicon analysed using NGS. Hexadecapeptide enrichment (E) following selection was calculated as ratio of output peptide frequency to input peptide frequency and expressed as log2E. Peptides binding complement C5a (negative control) were excluded.

streptavidin matrix. Following library selection with each chemokine we calculated the enrichment (E) of each peptide in comparison to the input library, and expressed the enrichment as log2E, as this metric is correlated with binding affinity[43].

Phage display identifies regions overlapping with known chemokine binding sites

Mapping each peptide to the parental sequence (Fig. 2) by log2E obtained for each chemokine identified overlapping hexadecapeptides that clustered in regions of the parental sequences. This is most evident for instance for EVA4, EV672, EV974 and EV546. To identify regions of the parental protein that contribute to chemokine-binding hexadecapeptides, we calculated the contribution of each residue (rlog2E) as the sum of log2Es of peptides overlapping a residue. We defined regions of interest where rlog2E exceeded the upper boundary of the 95% confidence interval of median rlog2E. The regions of interest overlap the known chemokine-binding sites for EVA4, EV672, and EV974 (Fig. 2). Surprisingly, we observed that hexadecapeptides from these regions, in addition to binding CC chemokines as expected, also bind CX3CL1 and several CXC chemokines (CXCL1, CXCL10, CXCL11, CXCL12B, CXCL13, CXCL5 and CXCL8) which are not known to bind the parental proteins.

Phage-display identifies promiscuous chemokine binding peptides

To characterise peptides that bound chemokines promiscuously, we selected those that bound at least three chemokines with log2E > 5. We find that of 30 peptides thus identified (Supplementary Table 2), 18 that are wild-type have one or more Cys residues. In each case (i.e., EVA4, EV991, EV974, EV672, E1243, E1180) where disulfide bond data was available in UniProt or from Alphafold, this Cys residue was disulfide bonded in the parental evasin sequence. Nine of 12 Cys-mutant peptides are mutant versions of the 18 wild-type peptides. The heatmap of individual log2E values indicated that certain peptides (e.g., HD2, HD7) are highly promiscuous, and bind over 15 different chemokines including exemplars from CC, CXC and CX3C classes (Fig. 3a). Interestingly, there is a clear distinction in the binding patterns of CXCL12 and its isoform CXCL12B. The cause for the differences may reside in the known effects of tag placement on CXCL12[44,45]. Additional residues present at the C-terminus of CXCL12B would change the distance of the biotin tag from the peptide-binding epitope and may alter the effect of the tag. The neighbour-joining cladogram (Fig. 3b) shows that EVA4, EV672, and the highly homologous evasins EV974 and EV546 contribute overlapping peptides.

Sequence alignment reveals a conserved motif containing an unpaired Cys residue

The two largest groups of overlapping wild-type peptides are from EVA4 and EV672. Multiple sequence alignment of these peptides (Fig. 3c) identifies two linear motifs with conserved residues: E(E/D)(E/D)DY and P(L/V)TCYF. We next examined the importance of having an unmutated Cys residue by evaluating the total log2E for each peptide aggregated over all chemokines as a summary measure of binding affinity (Fig. 3d). This shows that wild-type peptides have significantly higher total log2E compared to mutant peptides i.e., where Cys had been mutated to either Ser or Ala. These results suggest that the unpaired Cys residue in the PL/VTCYF motif contributes to chemokine binding affinity.

Biolayer interferometry confirms binding of HD2 to CC- and CXC- chemokines

We next evaluated the ability of the exemplar peptide HD2 to bind a panel of chemokines (Supplementary Table 3) using biolayer interferometry (BLI). We generated HD2 and a scrambled control (HD2SCR) as HIS:SUMO fusion proteins in *E.coli*. This approach results in soluble proteins that can be immobilised on to BLI sensors through the N-terminal HIS tag. In comparison to control, we observed that several CC and CXC-class chemokines (CCL1, CCL5, CCL7, CCL8, CCL11, CXCL10 and CXCL13) specifically and reproducibly bind to the immobilised HD2 peptide fusion (Supplementary Fig. 2). The binding of HD2 to these chemokines was characterised at different chemokine doses to evaluate binding affinity (K_D). We performed dose-response experiments for all chemokines in parallel and show that dose-dependent responses occur in each case (Fig. 4). We found that a 1:1 binding model was able to fit the data for CCL8 (Fig. 4a), allowing calculation of binding affinity (Supplementary Table 4). However, this binding model does not fit the data for the other chemokines, where we observed the signal accumulating over time at higher chemokine concentrations (Fig. 4b–h). As chemokines are known to oligomerize in solution and also upon glycosaminoglycan binding[46], the most parsimonious explanation for this binding profile is chemokine oligomerization at the BLI sensor. All chemokines bound in BLI were also bound by phage-displayed-HD2 where a phage-display experiment was performed. However, not all chemokines that bound HD2 in phage display were observed to bind by biolayer interferometry. The most likely explanation is that multivalent phage peptide-display allows identification of lower affinity interactions in comparison to BLI[40].

HD2 inhibits both CC- and CXC- chemokines

We next studied the ability of the exemplar peptide HD2 to inhibit chemotaxis by CC and CXC chemokines (Fig. 5 and Supplementary Fig. 3). In comparison with a scrambled control (HD2SCR), we find that it significantly inhibits cell migration induced by the CC chemokines CCL3, CCL5, CCL7, CCL8, CXCL6, and CXCL10. Inhibition of migration in response to CCL2, CCL23 and CXCL11 was also observed, although this was not statistically significant. No inhibition was observed for CCL14 and 15. These results are generally concordant with the binding results obtained in phage-display and BLI except for CCL15, which bound in phage-display but did not inhibit cell migration. We did not test other peptides extensively, but where tested, observed inhibition of CCL8 by HD845 and HD540 (Supplementary Fig. 3a). We performed

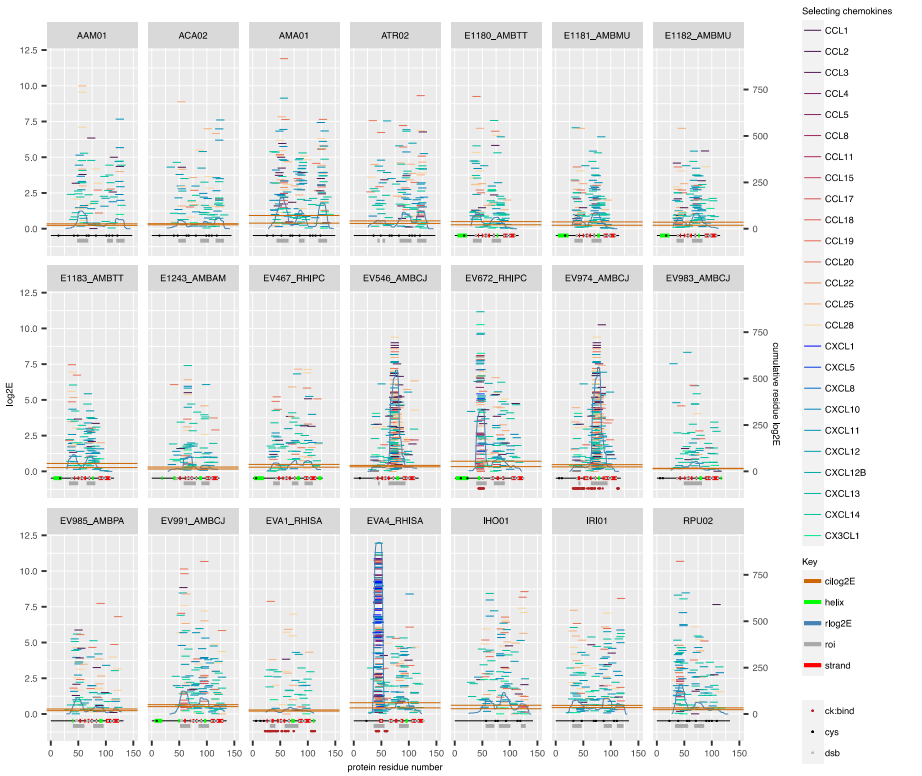

Fig. 2 | Mapping of enriched hexadecapeptides to parental proteins. Parental class A evasins are identified in the strip above each subpanel by UniProt entry names where available. Individual hexadecapeptides are represented as horizontal tiles, coloured by the selecting chemokine. Left *Y*-axis scale shows peptide log2E, and right *Y*-axis scale the residue log2E. Peptide log2E was calculated as described above. Residue log2E (rlog2E) for each residue was calculated as the sum of log2Es of peptides overlapping a residue, and the curve smoothed using a rolling median over a window of 7 residues. Regions of interest (roi) were identified where rlog2E exceeded the upper boundary of the 95% confidence interval of median rlog2E. Structural features were obtained from the UniProt database which includes data from AlphaFold models. Known chemokine binding sites are indicated. Chemokine-binding sites for EV672 to CCL8 and EVA4 to CCL5 were obtained from published data[28,34]. Chemokine-binding sites on EVA1 for CCL3 were extracted from PDB structure 3FPU. Chemokine-binding sites on EV974 for CCL17 and CCL7, were extracted from PDB structures 7S4N and 7SOO[35]. ck:bind chemokine binding sites, cys cysteine, dsb disulfide-bonded cysteine, roi region of interest, cilog2E 95% confidence interval of median rlog2E for the entire protein. Source data are provided as a Source Data file.

dose-response experiments with HD2 against CCL8, CCL5, CCL7, CXCL10 and CXCL6 (Fig. 6). While EVA4 inhibits the CC chemokines (Fig. 6f–h), it did not inhibit CXCL10 or CXCL6 (Fig.6i, j), and dose response curves could not be obtained. The IC_{50} of the HD2 peptide ranged from a median 1.9E-8 molar (0.019 μM) for CCL8 to 1.4E-5 molar (14 μM) for CXCL6 (Fig. 6k).

Alanine-scanning mutagenesis identifies contiguous residues in HD2 necessary for binding

A molecular-level understanding of the binding mechanism is needed for the development of peptides as therapeutics and is usually obtained from structural analyses. As HD2 binds many chemokines this becomes a challenging task, and we explored if we could elucidate this using phage display mutagenesis. We examined the role of each residue in HD2 for binding in phage-display. We generated a library of HD2 mutations that had NNK substituted at each residue and performed phage-display selection against a panel of 24 biotinylated chemokines, in parallel, as described above. This strategy allowed us to evaluate the impact not only of Ala substitutions[41], but also conservative, hydrophilic and hydrophobic substitutions[47], by comparing with the binding of parental HD2, which was also included in the library. Ala substitution removes side chains beyond the β-carbon and can be used to infer the role of side-chain functional groups without affecting the conformational flexibility of the backbone[41]. Analysis following selection with the chemokine panel showed that several mutations have a large and significant impact on mean log2E when compared to parental HD2 (Fig. 7a). Contiguous regions of three or more residues that significantly reduce binding upon Ala substitution compared to parental HD2 are E2-Y5 and P10-Y14. These residues are within the two motifs identified previously. We next judged the impact of Ala mutation by

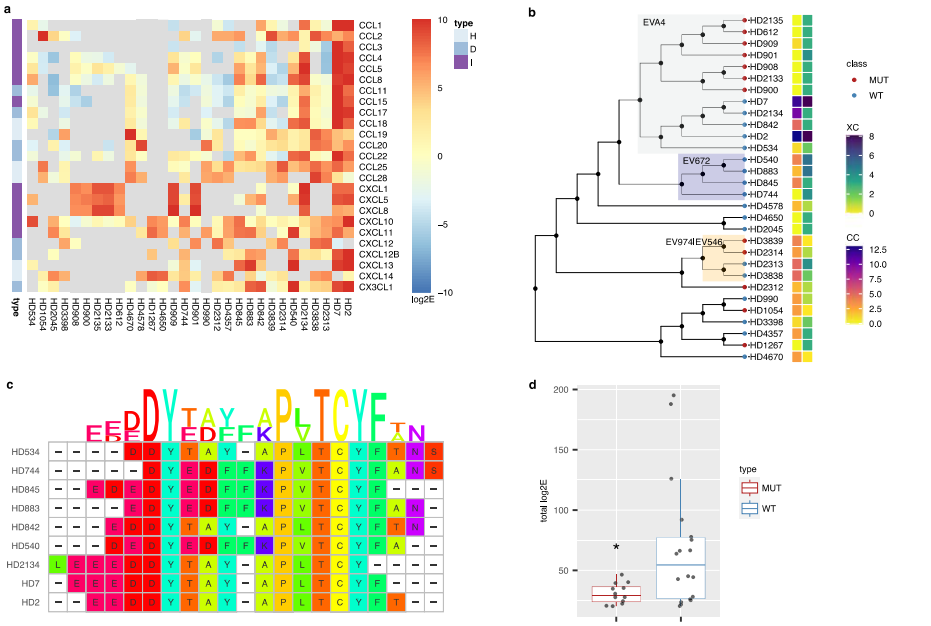

Fig. 3 | Promiscuous peptides. a Tileplot showing log2E of 30 peptides that specifically bind at least 3 chemokines with log2E > 5. Rows show the selecting chemokine and columns the peptide. Peptides are arranged by total numbers of chemokines bound with log2E > 5. Scale bar shows log2E values. Grey tiles indicates that the peptide was not recovered following the screen. Chemokine types (I = inflammatory, D = dual, H = homoeostatic) are indicated. **b** Neighbour-joining tree of peptides. Peptide identities are indicated at the tree tips. The ancestral node was defined by midpoint rooting. Peptides derived from EVA4, EV672 and EV974 are indicated in azure, navy, and orange respectively. The heatmap shows the number of CC or XC chemokines bound with log2E > 5. Mutant (MUT) and wild-type (WT) tip nodes are indicated. **c** Sequence alignment and logo for wild-type EVA4 and EV672-derived peptides. Amino acid residues are coloured using the Taylor scale. **d** Box-whisker plot showing the effect of Cys mutation to Ala or Ser (MUT) compared to wild-type (WT) for the subset of 30 peptides. *Y*-axis indicates the total log2E. Individual peptide data are indicated as points. The box-whisker plot shows the median as centre, 25th and 75th percentile as bounds, and 1.5*interquartile range as whiskers. A statistically significant difference between WT and MUT groups, using one-way ANOVA was observed, $p = 0.0231$, $F = 5.782$, df=1, $n = 18$ WT and 12 MUT independent peptide samples. Source data are provided as a Source Data file.

calculating the change in log2E (Δlog2E) between the mutant and parental HD2. A positive value of Δlog2E indicates increased binding, and a negative value decreased binding compared to parental HD2. A tile plot of the data (Fig. 7b) shows that while certain chemokines are relatively tolerant to single-point alanine mutagenesis (e.g., CCL8), others (e.g., CXCL10) were not. Analysis of conservative residue substitutions, identified from the Dayhoff PAM250 substitution matrix (Fig. 7c, Supplementary Fig. 4a) indicates that these substitutions have no significant deleterious effect on Δlog2E at the N-terminal motif, but that certain residues in the C-terminal motif (P10, T12 and C13) cannot be substituted. As may be seen, the log2E for the parental HD2 was ~0 in these analyses indicating a lack of enrichment. Examination of our data shows that there are several mutations that enhance binding to chemokines (e.g., anionic mutations at T6 and A7 or hydrophobic mutations at L11, see Fig. 7f, and Supplementary Fig. 4) providing a likely explanation of this result as they would compete with the parental HD2 peptide for binding.

Hydrophile-scanning mutagenesis identifies an N-terminal anionic patch in HD2

Ionic bonds are major interactions at protein interfaces, and occur between charged anionic and cationic residues[48]. Hydrophile scanning uses systematic mutation to anionic (e.g. glutamic or aspartic) or cationic (e.g. lysine, arginine) residues and complements alanine-scanning mutagenesis[47]. Analysis of these HD2 mutations present in the dataset generated above, shows that glutamic or aspartic acid (anionic) substitution at the N-terminus is not deleterious for binding, and in some cases, e.g., at T6, improve binding, whereas they are significantly deleterious at the C-terminus (Fig. 7d, Supplementary Figs. 4b, c, 5a, b). In contrast, cationic (lysine or arginine) mutations are generally deleterious through the peptide (Fig. 7e, and Supplementary Figs. 4d, e, 5c, d). Taken together these results indicate that an anionic N-terminal patch (EEDD) in HD2 mediates crucial interactions with target chemokines.

Hydrophobe-scanning mutagenesis identifies a role for C-terminal hydrophobicity in HD2

Protein interfaces are frequently characterised by hydrophobic interactions, leading to exclusion of these residues from the water exposed surface[48]. We therefore asked whether systematic mutation to the hydrophobic residues (i.e, valine, isoleucine, methionine and leucine[49]) would allow us to identify HD2 residues that likely mediated hydrophobic interactions with chemokines. Analysis of these mutations, from the phage-display dataset generated above, showed that certain

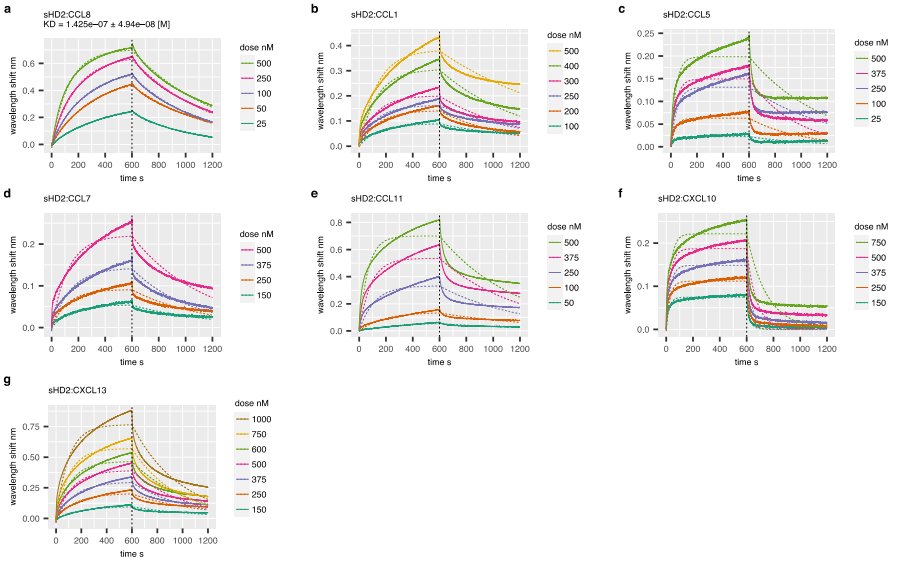

Fig. 4 | Binding of chemokines using biolayer interferometry. **a**–**g** Representative BLI dose-response sensorgrams showing purified sHD2 (SUMO:HD2) binding to indicated doses of chemokines. Plots display wavelength shift (*Y*-axis; nm) versus time (*X*-axis; seconds). Vertical dotted line indicates the onset of dissociation. Raw data are indicated by solid lines and fitted data (using a 1:1 binding model) by dotted lines. K_D estimates (mean ± standard error) are indicated where a good fit to the 1:1 binding model was obtained. Source data are provided as a Source Data file.

residues at the C-terminus—L11, T12, F15 and T16—can be substituted with a hydrophobic residue without significant deleterious effect (Fig. 7f and Supplementary Figs. 4f–i, 5e–h)).

Alanine-scanning mutagenesis identifies functionally important residues in HD2

To determine if alanine substitutions impacted the ability of HD2 to inhibit chemokine function we performed chemotaxis assays with synthetic peptides. We examined the effect of HD2 alanine mutants on migrated cell counts in chemotaxis assays using chemokines CCL5, CCL7, CCL8, CXCL6 and CXCL10, and compared it to parental HD2 as control (Supplementary Fig. 6). We observed that while several mutations (at residues E1, E2, D4, Y5, Y8, P10, L11, C13, Y14, F15), significantly affect ability to inhibit chemotaxis (as evidenced by an increase in migrated cell count relative to parental HD2) by CCL5, CCL7, CCL8 and CXCL6 and CXCL10, only P10A significantly affects chemotaxis by CCL8. This data is summarised by chemokine in Fig. 8a, where the effect of residue mutated to change in migrated cell count is shown. We performed a meta-analysis of the alanine-mutant chemotaxis experiments by pooling all biological replicate datapoints to obtain an overview of residues critical for chemokine inhibition (Fig. 8b). This analysis revealed that key residues that significantly impact function over all chemokines when mutated to alanine are P10, L11, C13 and Y14. We next asked whether chemotaxis inhibition was correlated with binding in phage-display. We examined the relationship between change in migrated cell count (Δmigrated) with change in log2E (Δlog2E) for each peptide:chemokine pair where such data was available (Fig. 8c). We observed that these two properties are highly correlated. Mutant peptide:chemokine pairs with lower Δlog2E (i.e., poor binding) have higher Δmigrated values (i.e., poor chemotaxis inhibition). Thus, poor binding in the phage-display experiment correlates with reduced inhibition of chemotaxis, indicating that the most likely explanation for loss of inhibition by a mutant is reduced binding affinity.

HD2 binds CC and CXC chemokines at distinct locations

To understand how the peptide HD2 may bind and inhibit CC- and CXC- class chemokines we modelled the chemokine:HD2 complex using two different methods, AlphaFold2-Multimer[50] and AutoDock CrankPep[51] (Fig. 9, Supplementary Figs. 7, 8). For each model, five alternative docking poses were identified using AlphaFold2-Multimer and ten using AutoDock CrankPep. We calculated the Rosetta cross-interface binding energy for each docked structure (Supplementary Table 7) as this parameter shows highest AlphaFold model classification accuracy[52]. In all cases but one, the cross-interface binding energy was less than −16, the suggested cut-off value[52], supporting the docked models. To identify peptide-proximal regions on the chemokines, rather than analysing the single highest-ranked pose from each method, which is less likely to retrieve the native docking pose[53], we aggregated data from the docking poses into heat maps of weighted proximity scores (Fig. 9a, b, Supplementary Figs. 7–9). AlphaFold2-Multimer analysis suggested that HD2 is in proximity to the N-terminus, N-loop, and residues within the β3-strands, 30s and 40s loops of CCL2, CCL3, CCL5, CCL7 and CCL8, but in proximity to the β1-strand and α-helix of CXCL6, CXCL10 and CXCL11 (Fig. 9a–c, Supplementary Fig. 7). Analysis using AutoDock CrankPep indicated overall concordance with the AlphaFold2-Multimer results, except for CXCL11 and CXCL6, where the peptide is in proximity to the N-terminus (Supplementary Fig. 8). The results of HD2 (EEDDYTAYAPLTCYFT) docking using AlphaFold2-Multimer and AutoDock CrankPep are remarkably

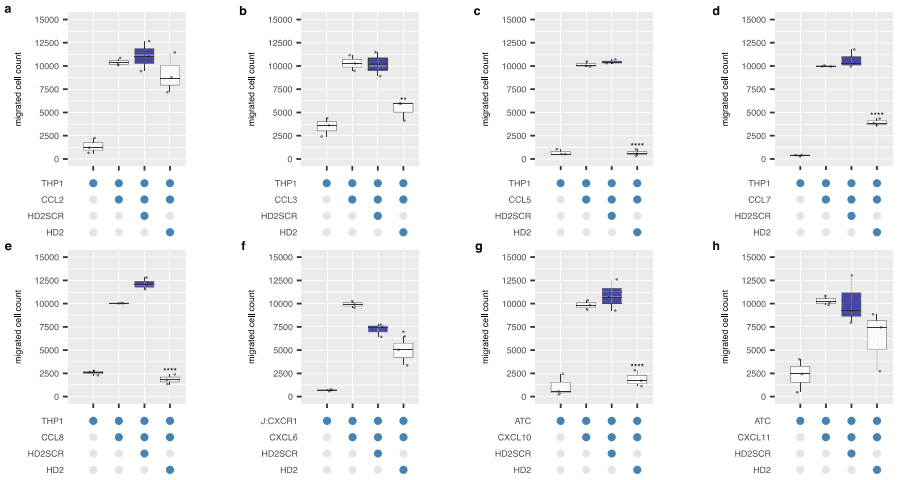

Fig. 5 | Effect of exemplar peptide on chemotaxis. a–h Box-whisker plots showing the effect of the exemplar peptide HD2 on cell migration induced by indicated human chemokines. All experiments were performed as three technical and three biological replicates, and individual biological replicate data points (mean of technical replicates) are shown. *Y*-axis in each panel shows cell count normalised to the median value of migrated cells in the presence of chemokine alone, set at 10000 cells. *X*-axis shows constituents of each experiment as blue-filled dots. Chemokine and cell type names are indicated. HD2SCR is a scrambled version of HD2 used as negative control. All peptides were at 10 μM final concentration and chemokines at EC80 doses. Each box-whisker plot shows the median as centre, 25th and 75th percentile as bounds, and 1.5*interquartile range as whiskers. Statistically significant differences (compared to control, coloured blue, $n = 3$ biologically independent experiments per group), were identified using a two-sided Dunnett's test with correction for multiple comparisons and are indicated by asterisks: ****$p \le 0.0001$, ***$p \le 0.001$, **$p \le 0.01$. Exact p-values by panel are: (**b**) $p = 0.009456$; (**c**–**e**) $p = 0.000000$; (**f**) $p = 0.033149$; (**g**) $p = 0.000016$. Source data are provided as a Source Data file.

consistent with the previously reported NMR chemical shift perturbation model of a highly similar peptide Ev4Glu[14]-Asn[31] (EEEDDYTAYAPLTAYFTN) in complex with CCL5[28] (Fig. 10), providing confidence in the docking methods we employed. AlphaFold2-Multimer models of EVA4 with target chemokines[35] suggested that it is in proximity to residues in the N-terminus and the N-loop, and residues within the 30s and 40s loops of CCL2, CCL3, CCL5, CCL7 and CCL8 (Supplementary Fig. 9). These results are also consistent with NMR analysis of CCL5:EVA4 interactions reported previously[28]. The HD2 segment within the chemokine:EVA4 models occupies a similar position to that observed in the corresponding chemokine:HD2 models (Supplementary Fig. 9a–e), and the chemokine residues in proximity to EVA4 in these models are similar to those in proximity to HD2 (Supplementary Fig. 9g).

HD2 binding partially occludes receptor-binding sites

As models of chemokines with their receptors are not uniformly available, we also modelled chemokine:receptor complexes using AlphaFold2-Multimer (Fig. 9, Supplementary Figs. 7, 9), to identify the receptor-proximal regions of these chemokines. These analyses suggest that CCR1, CCR2, and CCR5 are in proximity to the N-terminus, N-loop, β1 and β3-strands and residues within the 30s and 40s loops, while CXCR3 and CXCR1 are also in proximity to residues in the α-helix respectively (Fig. 9a–c, Supplementary Fig. 7a–f). These analyses also show that the distal N-termini of the CXC-chemokine receptors CXCR3 and CXCR1 are predicted to bind to the β1-strands of cognate CXC-chemokines by wrapping around the chemokine, and are consistent with reported models of CC and CXC-chemokine interactions with chemokine receptors[54,55]. The overlap between peptide-proximal and receptor-proximal regions (summarised in Fig. 9c) suggests that the peptide likely functions by partially occluding the receptor-proximal regions, interfering with binding. Analysis of the average number of chemokine bonds from the AlphaFold2-Multimer models for each HD2 residue indicated that the largest numbers of interactions, on average, are formed by the sequences E1:Y5 and L11:F15, i.e., the sequences EEDDY and LTCYF (Fig. 9d), with the unpaired Cys residue itself contributing many interactions.

Discussion

In this study we performed phage-display selection in parallel with multiple chemokines, coupled to deep sequencing, to systematically identify overlapping hexadecapeptides from 21 biochemically characterised class A evasins that bind chemokines. By pooling the results from 25 independent experiments conducted with CC- and CXC-class chemokines we were able to identify regions of interest within the parental proteins that bound chemokines in a "one-to-many" manner. These regions of interest map to interaction sites identified previously by hydrogen-deuterium-exchange mass spectrometry of the EV672:CCL8 complex[34], by NMR for EVA4:CCL5 complex[28], and by X-ray crystallography for EV974 complexes with CCL17 and CCL7[29].

A surprising and important result of our study is that several peptides—unlike the parental class A evasin proteins from which they are derived[25]—bind, and in the case of the peptide HD2, inhibit both CC and CXC class chemokines. The peptide HD2 is from the same region of EVA4 as an octadecapeptide Ev4Glu[14]-Asn[31] which was synthesised based on NMR analysis of the EVA4:CCL5 interface[28]. Unlike HD2, the octadecapeptide has a Cys-Ala mutation, and was reported to inhibit a single chemokine, CCL5[28]. As shown in the present study, the example peptide HD2 also shares sequence homology with several EV672-derived peptides, including HD845. HD845 was previously described

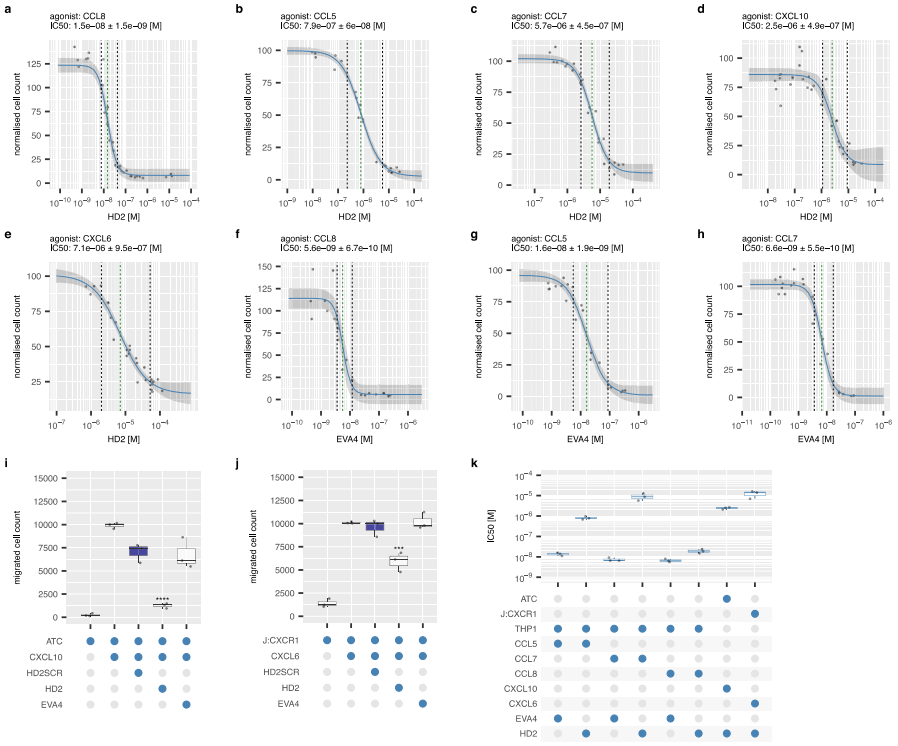

Fig. 6 | Effect of HD2 and EVA4 on chemotaxis response. a–h Representative dose-response curves showing effect of human chemokine induced THP1 or activated T cell (ATC) or Jurkat CXCR1 (J:CXCR1) migration by HD2 or EVA4. *Y*-axis shows percent migrated cells normalised to chemokine alone (set at 100%). *X*-axis shows inhibitor concentration (molar). Technical replicates at each inhibitor concentration ($n = 3$) are shown as individual data points. The dose-response curves (solid blue lines) and 95% confidence intervals (grey ribbons) were calculated using a 4-parameter log-logistic plot. Dotted green lines indicate IC_{50} and dotted black lines IC_{20} and IC_{80}. The IC_{50} (M, estimated from the *X*-intercept) ± standard error of the estimate is indicated in each plot. **i, j** Box-whisker plots showing the effect of HD2, scrambled version HD2SCR, and parental evasin EVA4 on cell migration induced by CXCL10 and CXCL6 respectively. All experiments were performed as three technical and three biological replicates, and individual biological replicate data points (mean of technical replicates) are shown. HD2, HD2SCR and EVA4 were at 20 μM final concentration in (**i**) and 10 μM in (**j**). *Y*-axis shows cell count normalised to the median value of migrated cells in the presence of chemokine alone, set at 10000 cells. *X*-axis shows constituents of each experiment as blue-filled dots. Each box-whisker plot shows the median as centre, 25th and 75th percentile as bounds, and 1.5*interquartile range as whiskers. Statistically significant differences (compared to control, coloured blue, $n = 3$ biologically independent experiments per group), were identified using a two-sided Dunnett's test with correction for multiple comparisons and are indicated by asterisks: $^{****}p \le 0.0001$, $^{***}p \le 0.001$. Exact *p*-values by panel are: (**i**) $p = 0.000020$; (**j**) $p = 0.000556$. (**k**) Summary IC_{50} values for inhibition by HD2 peptide and parental evasin EVA4. *Y*-axis shows IC50 (molar) and *X*-axis the constituents of each experiment. Data is shown as a box-whisker plot with median as centre, 25th and 75th percentile as bounds, and 1.5*interquartile range as whiskers, of biological replicates ($n = 3$) shown as individual data points. Source data are provided as a Source Data file.

as BK1.5, and together with other peptides of the BK series, were designed based on HDX-MS analysis of the EV672:CCL8 interface[34]. None of the previously described class A evasin-derived peptides were shown to have anti-chemokine activity against CXC-class chemokines. Potential explanations for the lack of CXC-binding capacity of the parental evasin is that CXC-chemokine interacting residues on the peptide may be unavailable in the parental protein. For instance, the unpaired Cys residue in the peptide is invariably disulfide bonded in the parental evasin. Multiple lines of evidence—including sequence conservation in binding peptides, mutation of Cys to Ala or Ser resulting in loss of binding activity in phage display, and loss of functional activity in chemotaxis assays—suggest that the unpaired Cys residue in these peptides is important. Cys residues are known to have non-covalent interactions[56], and it is possible that these enhance chemokine binding and inhibition. This result is consistent with the loss of activity previously observed with a Cys-Ala mutation in the EV672-derived peptide BK1.5 (which is identical to HD845 reported here)[34].

Following the discovery of the peptides by phage-display, we demonstrated that not only does the exemplar peptide HD2 bind multiple CC and CXC-chemokines using an independent approach—biolayer interferometry—but that it also inhibits multiple CC and CXC-chemokines in chemotaxis assays. These results suggest that the broad-spectrum chemokine-inhibiting activities of HD2 could be applied for therapeutic development. A key requirement for such

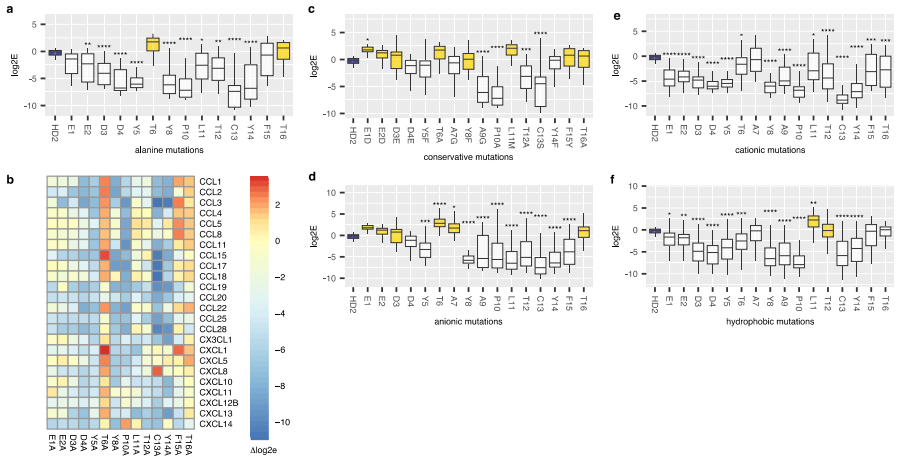

Fig. 7 | Effect of HD2 mutations on phage binding. Box-whisker plots (**a**, **c**–**f**) showing impact of HD2 residue mutation to alanine, conservative, anionic (glutamic acid, aspartic acid), cationic (lysine, arginine), and hydrophobic (leucine, isoleucine, methionine, and valine) residues respectively (*X*-axis) upon log2E (*Y*-axis). Each box-whisker plot shows the median as centre, 25th and 75th percentile as bounds, and 1.5*interquartile range as whiskers. Statistically significant differences (compared to control, coloured blue), using Dunnett's test with correction for multiple comparisons, are indicated by asterisks: $^{****}p \le 0.0001$, $^{***}p \le 0.001$, $^{**}p \le 0.01$, $^{*}p \le 0.05$, $n = 48$ per group for anionic or cationic mutations, 24 for wild-type, alanine, and conservative mutations, and 96 per group for hydrophobic mutations, except L11 where it was 72. Exact *p*-values are provided in Supplementary Table 5. Boxes showing a positive value for difference from control (identified from a two-sided Dunnett's test) are coloured yellow. **b** Tile plot of HD2 alanine mutations with tile colour showing Δlog2E, which is the difference in log2E between the parental wild-type peptide and the mutant variant following phage-display selection. Rows show the selecting chemokine and columns the mutation. Scale bar shows Δlog2E values. Source data are provided as a Source Data file.

progression, for instance in computer-aided rational drug design, is an understanding of the pharmacophore, i.e., the electronic and steric features required for binding and functional inhibition of the target[57,58]. Sequence conservation across peptides derived from EVA4 and EV672 that bound both CC and CXC chemokines indicated the presence of conserved residues in two motifs, E(E/D)(E/D)DY at the N-terminus; and (L/V)TCYF at the C-terminus. We applied saturation mutagenesis phage-display to dissect the functional importance of these residues. By examining the binding characteristics of alanine, hydrophilic and hydrophobic mutants for 24 different CC and CXC-chemokines, we show that the two motifs are biochemically distinctive, with the former characterised by an anionic patch and the latter by hydrophobic, aromatic and cysteine residues. These types of residues are some of the major drivers of protein complex formation[48]. We confirmed, using alanine scanning mutagenesis, the relative importance of these residues in functionally inhibiting multiple CC and CXC-chemokines and showed that functional inhibition strikingly correlates with binding in phage-display. The two motifs are separated by a conserved Pro residue which, while not contributing significantly to inter-chain bond formation, appears to be important for binding and inhibition by HD2. This is consistent with the role of the Pro residue in the analogous peptide BK1.1 (which is HD845 with a Cys-Ala mutation) observed previously[34], and suggests that it plays a role in peptide conformation, a known function of Pro residues[59].

To further elucidate the pharmacophore, we complemented these biochemical studies with two different in silico approaches that do not require prior knowledge of the binding pose of the peptide and use substantially different computational approaches. We initially applied AlphaFold2-Multimer[50], which is an implementation of the AlphaFold2[60,61] machine-learning algorithm "trained for multimeric inputs with known stoichiometry", and has been used for peptide:protein docking[62]. In these studies, we used a 1:1 stoichiometry based on our previous observations that the predominant binding stoichiometry of BK1.1 to CCL8 is 1:1[34]. We found using AlphaFold2-Multimer that the exemplar peptide, HD2, is predicted to bind to distinct sites in CC and CXC-chemokines: i.e., in CC to the N-terminus, and in CXC to the first β-strand. These results were confirmed in the large part using AutoDock CrankPep[51,63] which folds flexible peptides and docks them into rigid targets[51,63]. The reason for only partial and not full concordance between the two methods may lie in the differences in the folding algorithms, and how they rank binding modes. Our analysis shows that HD2 binding sites in both CC and in CXC-chemokines overlaps with the receptor-binding regions of the chemokine—i.e., the sites predicted by AlphaFold2-Multimer to bind the chemokine receptor—suggesting that HD2 occludes distinct receptor-binding regions in CC and in CXC-chemokines, interfering with their binding to cognate receptors. Confidence in our docking approach is increased by the observation that the NMR-based model[28] of CCL5 with Ev4Glu[14]-Asn[31] (which differs from HD2 by three residues) is highly consistent with the models of HD2 docked to CCL5 produced by AlphaFold2-Multimer and AutoDock CrankPep. Using Arpeggio[64], an algorithm that calculates interactions at protein-protein interfaces, we show that the N-terminal motif of HD2 contributes ionic and the C-terminal motif hydrophobic interactions, consistent with the results of the anionic, cationic, and hydrophobic substitution experiments. A limitation of these studies is that we have not confirmed the in silico predicted interactions and structure-activity relationships using approaches such as NMR or X-ray crystallography, which need to be performed in the future.

In summary, we have identified, using phage display and deep sequencing, a series of peptides from class A evasins that display broad-chemokine binding and inhibition activity spanning both CC

https://doi.org/10.1038/s41467-023-41488-z

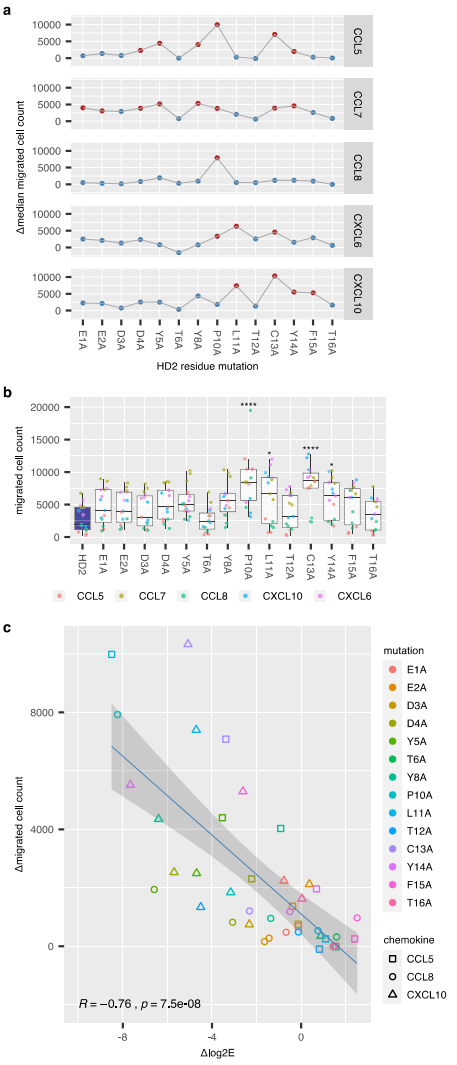

Fig. 8 | Effect of HD2 alanine mutations on chemotaxis. a Faceted plots of change in median migrated cell count between alanine mutant and wild-type HD2 peptide obtained in cell migration assays (*Y*-axis, Δmedian migrated cell count) versus alanine mutated residue (*X*-axis). Chemokines used for each experiment are indicated in the strip to the right of each plot. Statistically significant differences compared to parental HD2 are shown as red dots. **b** Box-whisker plot showing impact of HD2 residue mutation to alanine (*X*-axis) upon migrated cell count (*Y*-axis) for all chemokines studied. All experiments were performed as three biological replicates, and individual data points are indicated, and coloured by the chemokine used. The box-whisker plot shows the median as centre, 25th and 75th percentile as bounds, and 1.5*interquartile range as whiskers. Statistically significant differences (compared to control, coloured blue), using Dunnett's test with correction for multiple comparisons, are indicated by asterisks: ****$p \le 0.0001$, ***$p \le 0.001$, **$p \le 0.01$, *$p \le 0.05$, $n = 15$ observations per group (three biological replicates for each chemokine). Exact *p*-values are: C13A 1.62e−05; L11A 2.86e−02; P10A 2.79e−06; Y14A 4.17e−02. **c** Correlation of phage binding and inhibitory potency for alanine mutant HD2 peptides. Scatterplot of Δmedian migrated cell count (*Y*-axis, obtained in cell migration assays) versus Δlog2E (*X*-axis, obtained in phage-display experiments) for peptide:chemokine pairs. Individual data points indicate peptide chemokine pairs for which both cell migration and Δlog2E were available. Linear regression plot with 95% confidence interval, Spearman correlation coefficient (*R*) and statistical significance (*p*) are shown. Source data are provided as a Source Data file.

and CXC-class chemokines. The pharmacophore mediating this activity was characterised using a combination of sequence conservation across peptides recovered, analysis of alanine, hydrophilic and hydrophobic mutants, and integration with computational modelling. Our analyses suggest that these peptides occlude different parts of the chemokine receptor-binding sites and contain two motifs, one with an anionic patch primarily contributing ionic interactions, and the second containing an essential Cys residue and contributing hydrophobic interactions. The pharmacophoric features thus identified could be exploited to develop shorter linear peptides, cyclic peptides and peptidomimetics—i.e. synthetic agents that mimic the 3D-spatial and physicochemical properties of parental peptides but overcome their pharmacokinetic limitations[65]. Such synthetic agents may be generated using unnatural or D-amino acids so that key interactions with the target are maintained. The binding affinity and inhibitory potency of the peptides described are not yet in the range that would be desirable for use as therapeutic agents. These parameters could be enhanced by directed in vitro molecular evolution using deep mutational scanning combined with phage-display[66]. Further enhancement of inhibitory potency is also possible by conjugation to immunoglobulin Fc-chains to increase target avidity[67]. We suggest that the peptides and pharmacophore identified in this study could form templates for broad-spectrum anti-chemokine peptibodies or peptidomimetics that could be developed as therapeutics to target inflammatory disease. The phage-display, saturation mutagenesis and computational docking pipeline developed here could provide a new route to the discovery of such therapeutics that disrupt redundant and hence resilient protein-protein interaction networks in immuno-inflammation and cancer[9,68].

Methods

Human blood samples

Peripheral blood cells were obtained from anonymized donor leucocyte cones purchased from NHS Blood Transfusion Services, with ethics approval obtained from the University of Oxford Medical Sciences Interdivisional Research Ethics Committee, CUREC1 approval reference R75963/RE001.

Chemokines

Sources of chemokines for phage-display experiments, BLI, and cell migration are provided in Supplementary Tables 1 and 3.

Plasmids

HIS:SUMO peptides were constructed using NEB Builder HiFi Assembly (E5520, NEB) with a plasmid backbone derived from HIS6:SUMO:CCL8[22]. The CXCR1-expression plasmid (D1398) expresses a human CXCR1-IRES2-blasticidin resistance cassette from a CMV-T7 promoter and was constructed using GoldenGate Assembly from idempotent parts[20]. The EVA4 expression plasmid P1922 (8xHis-EVA4_RHISA) was constructed in plasmid pHLSec[69] using an In-Fusion cloning kit (Takara) following the instructions of the manufacturer, and contains EVA4_RHISA mature peptide (i.e., residues 24–127) with a N-terminal His-tag. Plasmid sequences were confirmed by Sanger sequencing (Azenta/Genewiz UK).

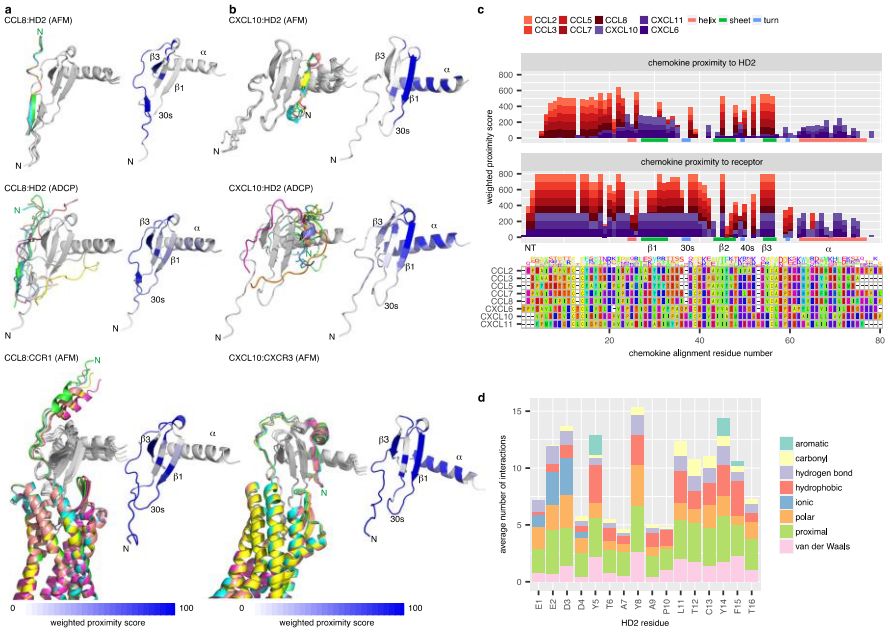

Fig. 9 | Predicted binding modes of HD2 and receptors to chemokines. a *Left panels:* Ribbon diagrams showing predicted poses for CCL8:HD2 using AlphaFold2-Multimer (*top*) or AutoDock CrankPep (*middle*) and for CCL8:CCR1 using AlphaFold2-Multimer (*bottom*). Chemokines are in grey, and the peptide or receptor in colour, with the top-ranked pose coloured green. *Right panels:* Corresponding heatmaps of weighted proximity scores mapped onto ribbon diagrams of CCL8. **b** *Left panels:* Ribbon diagrams showing predicted poses for CXCL10:HD2 using AlphaFold2-Multimer (*top*) or AutoDock CrankPep (*middle*) and for CXCL10:CXCR3 using AlphaFold2-Multimer (*bottom*). *Right panels:* Corresponding heatmaps of weighted proximity scores mapped onto ribbon diagrams of CXCL10. **c** Stacked bar charts of weighted proximity scores (*Y*-axis) for HD2 (*top panel*) and for receptor (*middle panel*), plotted for each chemokine residue (*X*-axis) following multiple sequence alignment (*bottom panel*). Models of chemokine:HD2 and chemokine:receptor (CCL2:CCR2, CCL3:CCR1, CCL5:CCR5, CCL7:CCR1, CCL8:CCR1, CXCL10:CXCR3, CXCL11:CXCR3 and CXCL6:CXCR1) were generated using AlphaFold2-Multimer. Secondary structural elements for CCL8 are indicated at the bottom of the top and middle panels. Chemokines and secondary structural elements are coloured as indicated in the legend. Amino acid residues are coloured using the Taylor scale. **d** Stacked bar chart of chemokine:HD2 interchain interactions identified by Arpeggio from AlphaFold2-Multimer predictions. *X*-axis shows HD2 peptide residue and *Y*-axis the average number of interactions per residue. Interaction types are coloured as shown in the legend; "proximal" indicates residues within 5 Å of the chemokine chain. NMR nuclear magnetic resonance, AFM AlphaFold2-Multimer, ADCP AutoDock CrankPep, N N-terminus of the top-ranked pose, β1, β3 β-strands, α: α-helix. Source data are provided as a Source Data file.

Cell lines

Jurkat E6.1 cells (ATCC TIB-152) were a gift from Pauline van Diemen (Oxford). THP1 cells (ECACC 88081201) were obtained from ECACC. Cell lines were confirmed mycoplasma free by monthly testing using a MycoAlert™ kit (LT07-118, Lonza) following the manufacturer's instructions. The J:CXCR1 cell line was generated by transfecting Jurkat E6.1 cells by electroporation with PvuI-linearised plasmid D1398 and selecting in RPMI-1640 (R0883, Sigma), 10% FBS (F9665, Sigma), 5 mM L-Glutamine (G7513, Sigma), and 5 µg/mL blasticidin (203350, Sigma). T-cells were isolated, activated and expanded as follows. Peripheral blood mononuclear cells were isolated from human leucocyte cones by density gradient centrifugation using Lymphoprep™ density gradient medium (07801, STEMCELL Technologies) and a SepMate™ isolation tube (85450, STEMCELL Technologies). CD8+ T-cells were isolated using two rounds of the human CD8+ T-cell isolation kit (480011, BioLegend). Isolated CD8+ T-cells were activated in ImmunoCult™-XF T-cell expansion medium (10982, STEMCELL Technologies) with an anti-CD3/anti-CD28 T-cell activator at 25 µl/ml (10991, STEMCELL Technologies) and supplemented with 10 ng/ml recombinant human IL-2 (200-02, PeproTech) with 1% penicillin/streptomycin. During activation, T-cells were passaged every 2–3 days in TexMACS medium (130-097-196, Miltenyi Biotec), supplemented with 10 ng/ml human IL-2 (200-05-250, Peprotech) and incubated at 37 °C in 5% CO_2. At day 10-13 after initial activation, CD8+ T-cells were frozen at 20×10^6 cell/ml in TexMACS medium supplemented with 10% DMSO (D2650, Sigma) in liquid nitrogen. 24 h prior to use, activated CD8$^+$ T-cells were recovered in TexMACs medium at 0.3 × 10^6 cell/ml and incubated at 37 °C in 5% CO_2.

Phage display library design

Wild-type class A evasin nucleotide sequences (excluding the signal peptide encoding sequence) were codon-optimised for *E.coli* expression using GeneDesigner, using default settings (i.e. codon bias threshold 0.1, and removing splicing, RNA destabilising, prokaryotic ribosome binding site, Shine-Dalgarno sequences, optimising the 5′ structure, and removing repeats). Codon optimisation was also repeated after mutating each Cys residue to Ala and Ser. We designed 81-mer oligonucleotides such that they encoded hexadecapeptides

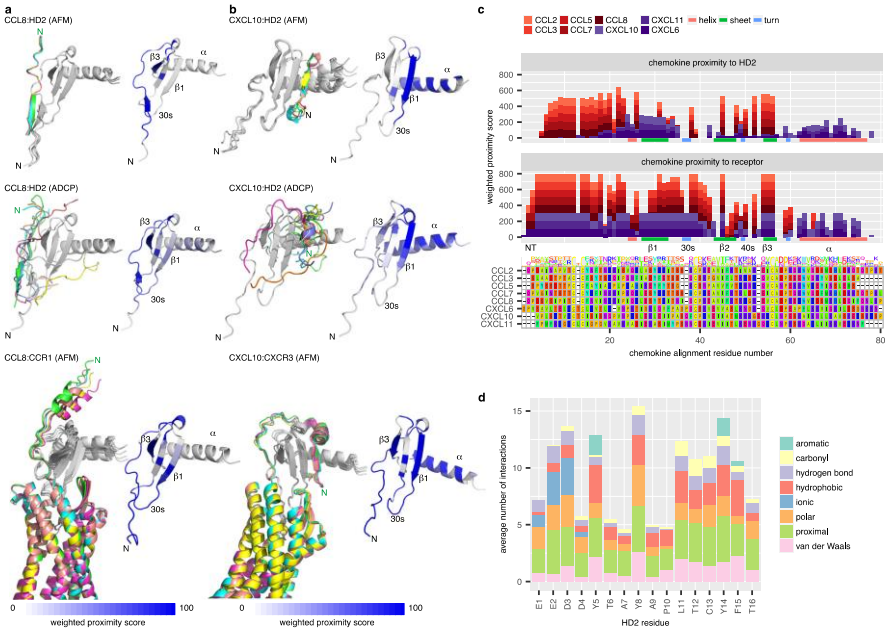

Fig. 9 | Predicted binding modes of HD2 and receptors to chemokines. a *Left panels:* Ribbon diagrams showing predicted poses for CCL8:HD2 using AlphaFold2-Multimer (*top*) or AutoDock CrankPep (*middle*) and for CCL8:CCR1 using AlphaFold2-Multimer (*bottom*). Chemokines are in grey, and the peptide or receptor in colour, with the top-ranked pose coloured green. *Right panels:* Corresponding heatmaps of weighted proximity scores mapped onto ribbon diagrams of CCL8. **b** *Left panels:* Ribbon diagrams showing predicted poses for CXCL10:HD2 using AlphaFold2-Multimer (*top*) or AutoDock CrankPep (*middle*) and for CXCL10:CXCR3 using AlphaFold2-Multimer (*bottom*). *Right panels:* Corresponding heatmaps of weighted proximity scores mapped onto ribbon diagrams of CXCL10. **c** Stacked bar charts of weighted proximity scores (*Y*-axis) for HD2 (*top panel*) and for receptor (*middle panel*), plotted for each chemokine residue (*X*-axis) following multiple sequence alignment (*bottom panel*). Models of chemokine:HD2 and chemokine:receptor (CCL2:CCR2, CCL3:CCR1, CCL5:CCR5, CCL7:CCR1, CCL8:CCR1, CXCL10:CXCR3, CXCL11:CXCR3 and CXCL6:CXCR1) were generated using AlphaFold2-Multimer. Secondary structural elements for CCL8 are indicated at the bottom of the top and middle panels. Chemokines and secondary structural elements are coloured as indicated in the legend. Amino acid residues are coloured using the Taylor scale. **d** Stacked bar chart of chemokine:HD2 interchain interactions identified by Arpeggio from AlphaFold2-Multimer predictions. *X*-axis shows HD2 peptide residue and *Y*-axis the average number of interactions per residue. Interaction types are coloured as shown in the legend; "proximal" indicates residues within 5 Å of the chemokine chain. NMR nuclear magnetic resonance, AFM AlphaFold2-Multimer, ADCP AutoDock CrankPep, N N-terminus of the top-ranked pose, β1, β3 β-strands, α: α-helix. Source data are provided as a Source Data file.

Cell lines

Jurkat E6.1 cells (ATCC TIB-152) were a gift from Pauline van Diemen (Oxford). THP1 cells (ECACC 88081201) were obtained from ECACC. Cell lines were confirmed mycoplasma free by monthly testing using a MycoAlert™ kit (LT07-118, Lonza) following the manufacturer's instructions. The J:CXCR1 cell line was generated by transfecting Jurkat E6.1 cells by electroporation with PvuI-linearised plasmid D1398 and selecting in RPMI-1640 (R0883, Sigma), 10% FBS (F9665, Sigma), 5 mM L-Glutamine (G7513, Sigma), and 5 µg/mL blasticidin (203350, Sigma). T-cells were isolated, activated and expanded as follows. Peripheral blood mononuclear cells were isolated from human leucocyte cones by density gradient centrifugation using Lymphoprep™ density gradient medium (07801, STEMCELL Technologies) and a SepMate™ isolation tube (85450, STEMCELL Technologies). CD8+ T-cells were isolated using two rounds of the human CD8+ T-cell isolation kit (480011, BioLegend). Isolated CD8+ T-cells were activated in ImmunoCult™-XF T-cell expansion medium (10982, STEMCELL Technologies) with an anti-CD3/anti-CD28 T-cell activator at 25 µl/ml (10991, STEMCELL Technologies) and supplemented with 10 ng/ml recombinant human IL-2 (200-02, PeproTech) with 1% penicillin/streptomycin. During activation, T-cells were passaged every 2–3 days in TexMACS medium (130-097-196, Miltenyi Biotec), supplemented with 10 ng/ml human IL-2 (200-05-250, Peprotech) and incubated at 37 °C in 5% CO_2. At day 10-13 after initial activation, CD8+ T-cells were frozen at 20×10^6 cell/ml in TexMACS medium supplemented with 10% DMSO (D2650, Sigma) in liquid nitrogen. 24 h prior to use, activated $CD8^+$ T-cells were recovered in TexMACs medium at 0.3×10^6 cell/ml and incubated at 37 °C in 5% CO_2.

Phage display library design

Wild-type class A evasin nucleotide sequences (excluding the signal peptide encoding sequence) were codon-optimised for *E.coli* expression using GeneDesigner, using default settings (i.e. codon bias threshold 0.1, and removing splicing, RNA destabilising, prokaryotic ribosome binding site, Shine-Dalgarno sequences, optimising the 5′ structure, and removing repeats). Codon optimisation was also repeated after mutating each Cys residue to Ala and Ser. We designed 81-mer oligonucleotides such that they encoded hexadecapeptides

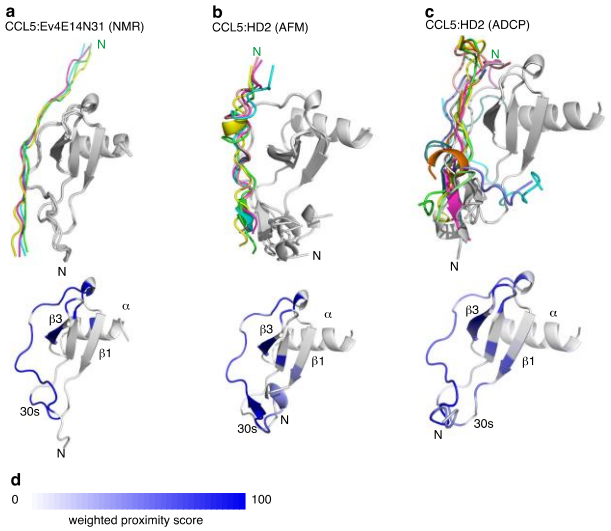

Fig. 10 | Comparison of NMR-predicted binding to predictions by AlphaFold2-Multimer and AutoDock CrankPep. a–c *Top panels:* Ribbon diagrams showing the predicted poses of indicated peptides bound to CCL5. Chemokines are in grey, and the peptide poses in colour, with the top-ranked pose coloured green. *Bottom panels*: Corresponding heatmaps of weighted proximity scores mapped onto ribbon diagrams of CCL5. Chemokine structural features (α-helix, β-strands and 30s loop) are indicated. **a** Poses obtained following the previously reported HADDOCK[70] analysis of NMR chemical shift perturbation data of peptide Ev4E14N31 (Ev4Glu^{14}-Asn^{31}, EEEDDYTAYAPLTAYFTN) in complex with CCL5[28]. **b**, **c** Poses obtained following AlphaFold2-Multimer (AFM) and AutoDock CrankPep (ADCP) analysis respectively of peptide HD2 (EEDDYTAYAPLTCYFT) docked to CCL5. **d** Heatmap scale for weighted proximity score. NMR nuclear magnetic resonance, AFM AlphaFold2-Multimer, ADCP AutoDock CrankPep, N N-terminus of the top-ranked pose, β1, β3: β-strands, α α-helix. Source data are provided as a Source Data file.

overlapping by a single residue, and had the sequence 5′-GCAGCCTCTTCATCTGGC, and GGTGGAGGATCCGGA-3′ at respective ends to enable amplification and cloning. A total of 4741 distinct peptides (including peptides where Cys was mutated to Ala or Ser) were designed as oligonucleotides and synthesised as a pool (Genscript, 12 K chip).

Phage display library construction

The plasmid prSTOP4 (kind gift from Dr Sachdev Sidhu, University of Toronto) was modified to have an *NsiI* restriction site and was amplified using primers (Sigma):

pRSTOP4Nsi_fwd: 5′-GGAGGCGCCGAGGGTGAC and pRSTOP4Nsi_rev: 5′-ATAGGCATTTGTAGCAATAGAAAAAACGAACATAGATGCAAG.

Oligonucleotide pools (Genscript) were amplified using primers (Sigma): oligo_fwd: 5′-CTATTGCTACAAATGCCTATGCAGCCTCTTCA TCTGGC and oligo_rev2: 5′-TCGTCACCCTCGGCGCCTCCTCCG-GATCCTCCACC. Oligonucleotide PCR products were cloned into plasmid prSTOP4Nsi using NEB Builder HiFi Assembly (E5520, NEB) following the instructions of the manufacturer. The vector pool was used to transform electrocompetent ElectroMAX™ DH5α-E™ cells (11319019, Invitrogen). Plasmid DNA was harvested by MaxiPrep (GeneJet Plasmid Maxiprep Kit (K0491, Thermo Scientific)) and was transformed into SS320 phage display electrocompetent cells (60512, Lucigen), following the manufacturer's protocol, resuspended in 950 µL recovery media for each electroporation, transferred to 50 mL Falcon tubes, 100 µL 10^{11} CFU/mL M13KO7 helper phage (N0315S, NEB) added and shaken at 37 °C, 220 RPM for 1 h. 1 mL recovery culture was added to 2YT medium containing 50 ug/mL carbenicillin (C9231, Sigma) and 25ug/mL kanamycin (K1377, Sigma), and grown overnight at 37 °C, 220 RPM. Phage was generated as described[70]. Briefly, phage was precipitated from the culture supernatant by adding 22.5 mL of supernatant to 4.5 mL 20% PEG 8000 (89510, Sigma)/2.5 M NaCl (S9625, Sigma), incubating on ice for 30 min, centrifuging at 12,857*g*, 4 °C for 10 min, resuspending the phage pellet in 1 mL of PBT (PBS (P4417, Sigma), BSA (A7030, Sigma) 0.20%, Tween 20 (P1379, Sigma) 0.05%), followed by centrifugation at 15,871*g*, 4 °C, for 10 min. Glycerol (G5516, Sigma) (10% final (v/v)) was added to supernatant, which was aliquoted and stored at −80 °C. For mutant libraries, 81-mer mutant oligonucleotides replacing NNK at each of the 16 peptide encoding residues were designed with the sequence arms described above. Oligonucleotides were individually amplified and cloned into plasmid prSTOP4Nsi.

Phage display library screening

Phage display screening was performed using a protocol as described[71] with certain modifications. Experiments were performed in 96-well plates (Greiner Bio-One, 655180). Briefly, biotinylated chemokines (1 µg, Almac or ProteinFoundry, Supplementary Table 1) were immobilised on 5 µl streptavidin-coated magnetic beads (Dynabeads™ M-280 Streptavidin, Invitrogen, 11205D) and incubated overnight at 4 °C. Chemokine-bound beads were blocked for 2 h in blocking buffer (PBS (phosphate-buffered saline, Sigma, P4417) + 0.2% BSA (bovine serum albumin, Sigma, A7030), and phage library (100 µL) allowed to bind for 2 h at a concentration of 10^{10} CFU/mL. Beads were washed 15

times with PT buffer (PBS + 0.05% Tween 20 (Sigma, P1379)) to remove unbound phage and transferred to a fresh plate. Beads were incubated with 100 μL of phage-resistant Omnimax *E.coli* (Invitrogen, A10469) at optical density (OD_{600}) 0.6-0.8 and shaken at 37 °C for 30 min, following which 10 μL M13K07 helper phage (NEB, N0315S, final concentration 10^{10} cfu/mL) was added and shaken at 37 °C for 45 min. Cells were transferred to 1 mL of 2YT medium pH 7 (MP Biomedicals™, 113012031) supplemented with 150 μg/mL carbenicillin (Sigma, C9231) and 75 μg/mL kanamycin (Sigma, K1377) in a 96-deep well block with V-bottom (Corning, CLS3960) and grown overnight shaking at 37 °C, 200 RPM. Plates were either centrifuged at 2000*g* (4 °C for 30 min) or transferred to screw cap tubes and pelleted by centrifugation at 4000*g* and 4 °C for 15 min. 540 μL of supernatant was transferred to a new 96-deep well plate, 60 μL 10×PBT (10×PBS + 2% BSA + 0.5% Tween 20) added and stored at 4 °C until further use in subsequent rounds. Phage display was carried out for three rounds.

Next generation sequencing

Inserts from the input library and from the final phage population following selection were amplified by PCR using primers: 5′-ACACTCTTTCCCTACACGACGCTCTTCCGATCTCTAGCGCTATGCCTATGCAGCCTCTTCA and 5′-GACTGGAGTTCAGACGTGTGCTCTTCCGATCTCGTCTGCGATGACAACAACCATCGCCCA, (Life Technologies). The PCR products were cleaned up using Monarch® PCR & DNA Cleanup Kit (5 μg) (T1030, NEB), 260/280 ratio determined by Nanodrop, quantified using a Qubit dsDNA Quantitation, High Sensitivity Kit (Q32851, Thermo Scientific) and subsequently sequenced at Azenta/GeneWiz using the AmpliconEZ protocol.

Next generation sequence analysis

Paired end read Fastq files were joined by the read id. Sequences containing both forward and reverse demultiplexing regions (5′-CTAGCGCT and 5′-CGCAGACG) and both constant regions (5′-ATGCCTATGCAGCCTCTTCATCTGGC and 5′-GGTGGAGGATCCGGAGGAGGCGCCGAGGGTGACGATCCCGCAAAAGCGGCCTTTAACTCCCTGCAAGCCTCAGCGACCGAATATATCGGTTATGCGTGGGCGATGGTTGTTGTCAT were analysed. Insert sequences from each read were identified and reads with non-identical insert sequences or ambiguous sequences were excluded, as were inserts that were incorrect in size (i.e., not 48 nucleotides). Insert sequences were translated to peptide. Only inserts present in the designed library were counted and frequency determined. Library cloning efficiency was calculated as the ratio of distinct cloned peptide inserts to the number of inserts in the designed library and was 98%. Hexadecapeptide enrichment (E) following selection was calculated as ratio of output peptide frequency to input peptide frequency and expressed as log2E. Where proportion of count in input library was not available it was replaced with the lowest input proportion in the experiment rather than replacing it with 0. This is needed to avoid a value of E that is infinity. For mutagenesis experiments, where proportion of count in output was not available it was replaced with the lowest output proportion in the experiment rather than zero, which would result in a -Infinity log2E.

Peptide mapping to parental protein sequences

Enriched peptides were mapped to parental proteins using custom R-scripts. Parental protein sequences were obtained from UniProt (https://www.uniprot.org) using RCurl. Briefly, collated enrichment data were filtered to include only those peptide-chemokine combinations where there was enrichment (i.e., log2E > 0), and wild-type and mutant peptides were mapped to the originating wild-type protein. Residue log2E was calculated as the sum of log2Es of peptides overlapping a residue. The rolling median of residue log2E was calculated using the "rollmedian" function in R-package zoo, with $k = 7$ and fill=NA. Confidence interval of the median was calculated using the "cimed" function in R-package asbio.

Annotation of parental proteins

PDB files for evasin complexes with chemokines 7S4N and 7SO0 (for EV974) and 3FPU (for EVA1) were retrieved from RCSB PDB (https://www.rcsb.org) using bio3d[72] and chemokine-binding site residues were identified using the bio3d "binding.site" function with the default cut-off of 5 Å. AlphaFold models were downloaded from https://alphafold.ebi.ac.uk/download and structural features extracted using bio3d.

Peptide sequence analysis

Tile-plots were constructed using pheatmap. Neighbour-joining trees were constructed by aligning peptide sequences using "ClustalW" with the Gonnet substitution matrix using R package msa, and aligned sequences were used to construct a matrix of pairwise distances. Neighbour-joining trees were constructed with 100 bootstrap replicates and midpoint-rooting using R packages ape, phytools, and ggtree. Peptide logos were constructed using R-packages ggmsa and ggseqlogo, and coloured using the Taylor colouring scheme.

Peptides

Peptides for all cell migration experiments were obtained from GenScript at >95% purity and were synthesised using Fmoc solid-phase synthesis to give peptides with a C-terminal amide. LC-MS data provided by the supplier show that HD2 peptide is at the expected molecular weight i.e., it is monomeric (Supplementary Fig. 10). Peptide sequences are provided in Supplementary Table 2. The HD2SCR sequence TLETDTFYECPDAYAY was designed by generating 50 random shuffles using the function "stri_rand_shuffle" (R-package stringi_1.7.6) and then selecting the peptide with the maximal "osa" string distance to wild-type using R-package stringdist_0.9.8.

Protein expression and purification

HIS:SUMO:peptide plasmids were transformed into BL21(DE3) cells (C2527H, NEB) and grown in 5 mL LB (L3022, Sigma) + 50 ug/mL Kanamycin (420411, Millipore) media overnight at 37 °C, with shaking at 200 RPM. 1% of this primary culture was inoculated into a secondary culture and grown for approximately 2 h at 37 °C, with shaking at 200 RPM. At OD600 of 0.4, the culture was induced with 1 mM IPTG (R0392, Thermo Scientific) and grown for 4 h at 37 °C, with shaking at 200 RPM. The induced cells were harvested at 3800 g in a Thermo Scientific Megafuge 16R using a swinging bucket rotor and the media was discarded. The pellet from a 200 mL culture was resuspended in 30 mL of binding buffer [Phosphate Buffer Saline, PBS (P4417, Sigma), 500 mM NaCl (S3014, Sigma), pH 7.2] containing 1 mM PMSF (P7626, Sigma). The suspension was sonicated using a Bandelin Sonopuls HD2070 for 45 min on ice using 0.7 s on- 0.3 s off cycle at 40% power. The lysate was centrifuged at 8500*g* in a Sorvall LYNX 4000 centrifuge for 20 min at 4 °C and the supernatant collected. 5 μL of DNase I (M0303, NEB) was added to the supernatant and incubated for 15 min in ice. Supernatant was filtered and passed over IMAC Sepharose 6 Fast Flow column resin (17-0921-07, GE Healthcare) [pre-treated with 0.2 M $NiCl_2$ (339350, Sigma) and equilibrated with binding buffer (PBS, 500 mM NaCl pH 7.2)]. The resin was incubated with the lysate supernatant for 1 h at 4 °C on a platform rocker for continuous mixing. 30 mL wash buffer (PBS, 500 mM NaCl, 20 mM imidazole (I5513, Sigma), pH 7.2) was applied to the resin. The peptide was then eluted in 5 mL elution buffer (PBS, 500 mM NaCl, 500 mM imidazole, pH 7.2), and buffer exchange in PBS was performed using Amicon Ultra Centrifugal Units 3 K (UFC9003, Millipore). EVA4 was expressed in HEK293F cells (R79007, ThermoFisher Scientific) by transient transfection of P1922 plasmid using polyethylenimine (24765, Polysciences) in HEK293F cells followed by culturing in Freestyle 293 expression medium (12338026, ThermoFisher) at 37 °C, 8% CO_2, at 130 rpm for 5 days. Protein was purified from filtered supernatants using nickel-charged IMAC Sepharose 6 Fast Flow resin as described above.

Elutions were concentrated using an Amicon Ultra-15 Centrifugal Filter Unit and purified by size exclusion chromatography (SEC) on an AKTA Start system using HiLoad 16/600 Superdex 75 (GE28-9893-33, GE Healthcare), in SEC buffer (PBS + 150 mM NaCl). Fractions showing absorption at 280 nm were analysed by electrophoresis on a Bolt Bis-Tris Plus Mini Protein Gel, 12% (NW00122, Invitrogen) in Bolt MES SDS Buffer (B000202, Invitrogen), stained with Quick Blue Protein Stain (LU001000, LuBio) and were pooled.

Biolayer interferometry

The binding of His-SUMO tagged peptide fusions to various chemokines (Supplementary Table 3) was investigated by biolayer interferometry (BLI) using Ni-NTA biosensors (18-5101, ForteBio). All BLI data were obtained at 25 °C using a ForteBio-Sartorius Octet RED 384 instrument and Octet 384-well tilted bottom microplate (18-5080, Sartorius). The biosensors were preincubated overnight at room temperature in BLI buffer (PBS, 500 mM NaCl, 0.01% BSA (A7638, Sigma) + 0.002% Tween (P2287, Sigma)). His-SUMO tagged peptide fusions at 1 mg/mL (for cross-binding screen assay) and at 0.25 mg/mL (for kinetic assays) were immobilised on the Ni-NTA biosensors for 500 s using the BLI buffer. The HIS:SUMO fusion-loaded biosensors were then washed in the BLI buffer to allow signal stabilisation. To study the association with the analyte (chemokines), the biosensors were then dipped in chemokine solutions of various concentrations (1 μM for cross-binding screen assays, a range of 25–750 nM for kinetic assays) made in the BLI buffer, for either 300 s for cross-binding screen assays, or 600 s for kinetic assays. This was followed by the dissociation step, where the biosensors were incubated in BLI buffer for 300 s for screening assays and 600 s for kinetic assays. For chemokine cross-binding screens, wavelength shift was normalised by subtracting the signal from buffer control, and normalising the highest Rmax (i.e., with CCL8 and HD2) obtained in the experiment to 1. Kinetic data was analysed using buffer subtracted wavelength shift and a 1:1 binding model. We calculated mean K_D and its standard error from at least three fits where full R^2 (i.e., how well the fit and experimental data correlate) was >0.95, full X^2 (i.e., measure of error between experimental data and fitted line) was <3, and K_D standard error was $<K_D$.

THP1 cell migration

For THP1 migration assays, 300000 cells/well were added to the top chamber of a 5-μm 96-well Transwell insert (3387, Corning) in 50 μL of cell migration media (RPMI-1640 (R0883, Sigma), 0.5% FBS (F9665, Sigma), 4 mM L-Glutamine (G7513, Sigma), 0.05% DMSO (D4540, Sigma)). The bottom chamber contained 150 μL of migration media with chemokine and peptide added. Cells were migrated at 37 °C in 5% CO_2 for 4 h.

J:CXCR1 cell migration

J:CXCR1 migration assays were performed exactly as for THP1 assays except that a 3-μm Transwell insert (3385, Corning) was used.

Activated T-cell migration

For activated-T cell migration assays, 100000 cells/well were added to the top chamber of a 3-μm Transwell insert (3385, Corning) in 50 μL of migration media (HBSS (14025-092, Life Technologies), 0.1% protease free bovine serum albumin (A7030, Sigma), 0.05% DMSO (D4540, Sigma)). The bottom chamber contained 150 μL of migration media with chemokine and peptide added. Cells were migrated at 37 °C in 5% CO_2 for 2 h.

Analysis of cell migration

Following the migration assay the migration plate was shaken at 850 RPM for 10 min, and media from bottom plate transferred to a round-bottomed 96 well plate (353910, Falcon). Cell counts were determined using an Atune NxT Flow Cytometer Plate Reader with Cytkick autosampler (ThermoFisher), based on cell size parameters FSC-H/SSC-H, and and a previously defined gate setting for each cell type (Supplementary Fig. 11). All experiments were performed as three technical and three biological replicates. Statistical significances between control and experimental groups was evaluated using Dunnett's test[73]. IC_{50} experiments were performed at the EC_{80} dose of chemokine. EC_{80} was calculated by fitting a chemokine dose-response curve with a 3-parameter log-logistic model (fixing the top to 100%) using the function "drm" in R-package drc[74]. IC_{50} was calculated by fitting an inhibitor response curve with a 4-parameter log-logistic model using the function "drm" in R-package drc[74]. All IC_{50} values reported had p-value < 0.05.

Modelling of chemokine complexes with peptides, receptors and evasins

Models were generated using AlphaFold2-Multimer at the COSMIC[2] Science Gateway using default parameters and a full database search using UniProt mature protein sequences[50,75]. The five highest confidence models were identified in each case from the confidence score and carried forward for heat map generation. As experimental structures often contain missing sidechain atoms, direct use of these structures will interfere with the atom-wise scoring function of AutoDock CrankPep (ADCP), and, also, as certain chemokines e.g., CXCL6, lack PDB structures, to maintain consistency, we first generated chemokine structures using AlphaFold for input to ADCP. The highest-ranking structure for each chemokine was reduced with "reduce", then the functions "prepare_receptor", "agfr", and "adcp" were called from ADFRsuite 1.0. Default parameters were used for "prepare_receptor" and "agfr", while "adcp" was run with $N = 300$, $n = 48000000$ and nc = 0.8 for all runs. For ADCP the ten highest ranked poses (based on automatically calculated lowest free energy) were carried forward for heat map generation. PDB files from previously reported HADDOCK[76] analysis of NMR chemical shift perturbation data of peptide $Ev4Glu^{14}$-Asn^{33} in complex with CCL5[28] were kindly provided by Prof. Ingrid Dijkgraaf, Maastricht. Binding site heatmaps were generated by identifying residues within 5 Å distance of the two chains using bio3d[72] for each docking pose. Weighted proximity scores were calculated as follows: A per-residue-score equal to the confidence score (AlphaFold) or calculated free energy (ADCP) was ascribed for each pose within a model, this was aggregated over the different poses in the model, and then normalised to a maximum score of 100 to allow comparison between models. For NMR-HADDOCK models the 4 generated poses were weighted equally for the calculation of the weighted proximity score. Docked poses were aligned using PyMol "extra_fit" to align multiple poses to the top-ranked pose.

Arpeggio analysis

Arpeggio[64] contacts between the two chains of the five AlphaFold multimer models for each complex were identified from the ".bs_contacts" file produced. Column identities for the file were taken from https://bitbucket.org/harryjubb/arpeggio/src/master/README.md.

Rosetta analysis

We performed model relaxation using Rosetta 3.13 (relax.static.linuxgccrelease) followed by calculation of the cross-interface binding energy (dG_cross) with Rosetta InterfaceAnalyser (InterfaceAnalyzer.static.linuxgccrelease) using the default ref2015 weightset[77–79].

Statistical information

For cell-based experiments sample size was not formally calculated. Cell numbers, numbers of technical and biological replicates are based on optimisation of such experiments[20–23,34]. Statistical analyses were performed using the R-base package stats and DescTools. Statistical tests used were one-way ANOVA followed by a two-sided

Dunnett's post-hoc multiple comparison procedure for comparing several treatments with a control, with 95% family wise confidence level[73]. Data are displayed as Tukey box-whisker plots using the ggplot function geom_boxplot, and displays median, lower and upper hinges (25th and 75th percentiles), and whiskers from hinge to 1.5* interquartile range.

Software

Biolayer interferometry data was collected and analysed using ForteBio Data Analysis HT 11.1. Flow sorting data was collected and analysed using Attune Cytometric Software v5.1.1. Structural models were generated using AlphaFold2-Multimer at the COSMIC[2] Science Gateway[50,75], and ADFRSuite 1.0[51] (https://ccsb.scripps.edu/adcp/downloads/) and reduce ((https://github.com/rlabduke/reduce) on the Oxford University BioMedical Research Computing Cluster (BMRCC). Data analysis was performed using R version 4.2.3, RStudio version 2023.03.2 + 454, running on arch64-apple-darwin20 (64-bit) with macOS Ventura 13.4.1. R packages used were: ape_5.7-1, asbio_1.9-2, bio3d_2.4-4, Biobase_2.58.0, BiocGenerics_0.44.0, BiocParallel_1.32.6, Biostrings_2.66.0, dendsort_0.3.4, DescTools_0.99.48, dplyr_1.1.2, drc_3.0-1, flextable_0.9.1, forcats_1.0.0, GenomeInfoDb_1.34.9, GenomicAlignments_1.34.1, GenomicRanges_1.50.2, ggmsa_1.4.0, ggnewscale_0.4.8, ggplot2_3.4.2, ggpubr_0.6.0, ggseqlogo_0.1, ggtree_3.6.2, ggupset_0.3.0, gridExtra_2.3, gtable_0.3.3, IRanges_2.32.0, janitor_2.2.0, jsonlite_1.8.4, lubridate_1.9.2, maps_3.4.1, MASS_7.3-58.2, MatrixGenerics_1.10.0, matrixStats_0.63.0, msa_1.30.1, officer_0.6.2, openxlsx_4.2.5.2, pals_1.7, pheatmap_1.0.12, phytools_1.5-1, purrr_1.0.1, R.methodsS3_1.8.2, R.oo_1.25.0, R.utils_2.12.2, RColorBrewer_1.1-3, readr_2.1.4, Rsamtools_2.14.0, S4Vectors_0.36.2, scales_1.2.1, seqinr_4.2-30, ShortRead_1.56.1, strex_1.6.0, stringr_1.5.0, SummarizedExperiment_1.28.0, tibble_3.2.1, tidyr_1.3.0, tidyverse_2.0.0, viridis_0.6.3, viridisLite_0.4.1, XVector_0.38.0, zoo_1.8-12. Arpeggio analysis used Python 2.7, biopython 1.79, and Arpeggio[64] (https://bitbucket.org/harryjubb/arpeggio/src/master/). Open-Source PyMOL (https://pymolwiki.org/index.php/MAC_Install) was used for scripting and PyMOL 2.5.2 (https://pymol.org/2/) was used for visualization of structural models. Rosetta analysis used Rosetta 3.13[77].

Reporting summary

Further information on research design is available in the Nature Portfolio Reporting Summary linked to this article.

Data availability

The authors declare that the data supporting the findings of this study are available within the paper and its supplementary files. Plasmids described and sequences are available on request from the corresponding author. Previously published structures used in our analyses were obtained from the PDB with accession codes as follows: 3FPU, 7S4N, 7SO0. Source data are provided with this paper.

Code availability

Code used in this study is available in the source data provided with this paper.

References

1. Zlotnik, A. & Yoshie, O. The chemokine superfamily revisited. *Immunity* **36**, 705–716 (2012).
2. Marquez, A. B., van der Vorst, E. P. C. & Maas, S. L. Key chemokine pathways in atherosclerosis and their therapeutic potential. *J. Clin. Med.* **10**, 3825 (2021).
3. Szekanecz, Z. & Koch, A. E. Successes and failures of chemokine-pathway targeting in rheumatoid arthritis. *Nat. Rev. Rheumatol.* **12**, 5–13 (2016).
4. Camba-Gomez, M., Arosa, L., Gualillo, O. & Conde-Aranda, J. Chemokines and chemokine receptors in inflammatory bowel disease: recent findings and future perspectives. *Drug Discov. Today* **27**, 1167–1175 (2022).
5. Coperchini, F., Chiovato, L., Croce, L., Magri, F. & Rotondi, M. The cytokine storm in COVID-19: an overview of the involvement of the chemokine/chemokine-receptor system. *Cytokine Growth Factor Rev.* **53**, 25–32 (2020).
6. Janssens, R., Struyf, S. & Proost, P. The unique structural and functional features of CXCL12. *Cell Mol. Immunol.* **15**, 299–311 (2018).
7. Kufareva, I., Gustavsson, M., Zheng, Y., Stephens, B. S. & Handel, T. M. What do structures tell us about chemokine receptor function and antagonism? *Annu. Rev. Biophys.* **46**, 175–198 (2017).
8. von Hundelshausen, P. et al. Chemokine interactome mapping enables tailored intervention in acute and chronic inflammation. *Sci. Transl. Med.* **9**, 1–14 (2017).
9. Mantovani, A. Redundancy and robustness versus division of labour and specialization in innate immunity. *Semin Immunol.* **36**, 28–30 (2018).
10. Whitacre, J. M. Biological robustness: paradigms, mechanisms, and systems principles. *Front. Genet.* **3**, 67 (2012).
11. Bhattacharya, S. & Kawamura, A. Using evasins to target the chemokine network in inflammation. *Adv. Protein Chem. Struct. Biol.* **119**, 1–38 (2020).
12. Harding, S. D., Faccenda, E., Southan, C., Maffia, P. & Davies, J. A. A new guide to immunopharmacology. *Nat. Rev. Immunol.* **18**, 729 (2018).
13. Bachelerie, F. et al. International union of basic and clinical pharmacology. LXXXIX. Update on the extended family of chemokine receptors and introducing a new nomenclature for atypical chemokine receptors. *Pharm. Rev.* **66**, 1–79 (2014).
14. Solari, R., Pease, J. E. & Begg, M. Chemokine receptors as therapeutic targets: why aren't there more drugs? *Eur. J. Pharmacol.* **746**, 363–367 (2015).
15. Wikel, S. K. Tick modulation of host immunity: an important factor in pathogen transmission. *Int J. Parasitol.* **29**, 851–859 (1999).
16. Hajnicka, V. et al. Anti-interleukin-8 activity of tick salivary gland extracts. *Parasite Immunol.* **23**, 483–489 (2001).
17. Frauenschuh, A. et al. Molecular cloning and characterization of a highly selective chemokine-binding protein from the tick Rhipicephalus sanguineus. *J. Biol. Chem.* **282**, 27250–27258 (2007).
18. Deruaz, M. et al. Ticks produce highly selective chemokine binding proteins with antiinflammatory activity. *J. Exp. Med.* **205**, 2019–2031 (2008).
19. Hayward, J. et al. Ticks from diverse genera encode chemokine-inhibitory evasin proteins. *J. Biol. Chem.* **292**, 15670–15680 (2017).
20. Singh, K. et al. Yeast surface display identifies a family of evasins from ticks with novel polyvalent CC chemokine-binding activities. *Sci. Rep.* **7**, 4267 (2017).
21. Alenazi, Y. et al. Genetically engineered two-warhead evasins provide a method to achieve precision targeting of disease-relevant chemokine subsets. *Sci. Rep.* **8**, 6333 (2018).
22. Eaton, J. R. O. et al. The N-terminal domain of a tick evasin is critical for chemokine binding and neutralization and confers specific binding activity to other evasins. *J. Biol. Chem.* **293**, 6134–6146 (2018).
23. Lee, A. W. et al. A knottin scaffold directs the CXC-chemokine-binding specificity of tick evasins. *J. Biol. Chem.* **294**, 11199–11212 (2019).
24. Aryal, P. et al. Swapping N-terminal regions among tick evasins reveals cooperative interactions influencing chemokine binding and selectivity. *J. Biol. Chem.* **298**, 102382 (2022).
25. Bhattacharya, S. & Nuttall, P. A. Phylogenetic analysis indicates that evasin-like proteins of ixodid ticks fall into three distinct classes. *Front. Cell Infect. Microbiol.* **11**, 769542 (2021).

26. Devkota, S. R. et al. Engineering broad-spectrum inhibitors of inflammatory chemokines from subclass A3 tick evasins. *Nat. Commun.* **14**, 4204 (2023).
27. Dias, J. M. et al. Structural Basis of Chemokine Sequestration by a Tick Chemokine Binding Protein: The Crystal Structure of the Complex between Evasin-1 and CCL3. *PLoS ONE* **4**, e8514 (2009).
28. Denisov, S. S. et al. Structural characterization of anti-CCL5 activity of the tick salivary protein evasin-4. *J. Biol. Chem.* **295**, 14367–14378 (2020).
29. Bhusal, R. P. et al. Structure-guided engineering of tick evasins for targeting chemokines in inflammatory diseases. *Proc. Natl Acad. Sci. USA* **119**, e2122105119 (2022).
30. Bonvin, P., Power, C. A. & Proudfoot, A. E. Evasins: therapeutic potential of a new family of chemokine-binding proteins from ticks. *Front. Immunol.* **7**, 208 (2016).
31. Angelini, A. et al. Directed evolution of broadly crossreactive chemokine-blocking antibodies efficacious in arthritis. *Nat. Commun.* **9**, 1461 (2018).
32. Abraham, M. et al. Development of novel promiscuous anti-chemokine peptibodies for treating autoimmunity and inflammation. *Front. Immunol.* **8**, 1432 (2017).
33. Oliveira, A. L. et al. The chemistry of snake venom and its medicinal potential. *Nat. Rev. Chem.* **6**, 451–469 (2022).
34. Darlot, B. et al. Engineered anti-inflammatory peptides inspired by mapping an evasin-chemokine interaction. *J. Biol. Chem.* **295**, 10926–10939 (2020).
35. Deruaz, M. et al. Evasin-4, a tick-derived chemokine-binding protein with broad selectivity can be modified for use in preclinical disease models. *FEBS J.* **280**, 4876–4887 (2013).
36. Ivarsson, Y. et al. Large-scale interaction profiling of PDZ domains through proteomic peptide-phage display using human and viral phage peptidomes. *Proc. Natl Acad. Sci. USA* **111**, 2542–2547 (2014).
37. Wigington, C. P. et al. Systematic discovery of short linear motifs decodes calcineurin phosphatase signaling. *Mol. Cell* **79**, 342–358.e312 (2020).
38. Davey, N. E. et al. Discovery of short linear motif-mediated interactions through phage display of intrinsically disordered regions of the human proteome. *FEBS J.* **284**, 485–498 (2017).
39. Benz, C. et al. Proteome-scale mapping of binding sites in the unstructured regions of the human proteome. *Mol. Syst. Biol.* **18**, e10584 (2022).
40. McLaughlin, M. E. & Sidhu, S. S. Engineering and analysis of peptide-recognition domain specificities by phage display and deep sequencing. *Methods Enzymol.* **523**, 327–349 (2013).
41. Weiss, G. A., Watanabe, C. K., Zhong, A., Goddard, A. & Sidhu, S. S. Rapid mapping of protein functional epitopes by combinatorial alanine scanning. *Proc. Natl Acad. Sci. USA* **97**, 8950–8954 (2000).
42. Pearson, W. R. Rapid and sensitive sequence comparison with FASTP and FASTA. *Methods Enzymol.* **183**, 63–98 (1990).
43. Rogers, J. M., Passioura, T. & Suga, H. Nonproteinogenic deep mutational scanning of linear and cyclic peptides. *Proc. Natl Acad. Sci. USA* **115**, 10959–10964 (2018).
44. Gustavsson, M., Dyer, D. P., Zhao, C. & Handel, T. M. Kinetics of CXCL12 binding to atypical chemokine receptor 3 reveal a role for the receptor N terminus in chemokine binding. *Sci. Signal* **12**, eaaw3657 (2019).
45. Kawamura, T. et al. A general method for site specific fluorescent labeling of recombinant chemokines. *PLoS ONE* **9**, e81454 (2014).
46. Salanga, C. L. & Handel, T. M. Chemokine oligomerization and interactions with receptors and glycosaminoglycans: the role of structural dynamics in function. *Exp. Cell Res.* **317**, 590–601 (2011).
47. Boersma, M. D., Sadowsky, J. D., Tomita, Y. A. & Gellman, S. H. Hydrophile scanning as a complement to alanine scanning for exploring and manipulating protein-protein recognition: application to the Bim BH3 domain. *Protein Sci.* **17**, 1232–1240 (2008).
48. Moreira, I. S., Fernandes, P. A. & Ramos, M. J. Hot spots–a review of the protein-protein interface determinant amino-acid residues. *Proteins* **68**, 803–812 (2007).
49. Aledo, J. C. Methionine in proteins: the Cinderella of the proteinogenic amino acids. *Protein Sci.* **28**, 1785–1796 (2019).
50. Evans, R. et al. Protein complex prediction with AlphaFold-Multimer. *bioRxiv* https://doi.org/10.1101/2021.10.04.463034 (2022).
51. Zhang, Y. & Sanner, M. F. AutoDock CrankPep: combining folding and docking to predict protein-peptide complexes. *Bioinformatics* **35**, 5121–5127 (2019).
52. Yin, R., Feng, B. Y., Varshney, A. & Pierce, B. G. Benchmarking AlphaFold for protein complex modeling reveals accuracy determinants. *Protein Sci.* **31**, e4379 (2022).
53. Weng, G. et al. Comprehensive evaluation of fourteen docking programs on protein-peptide complexes. *J. Chem. Theory Comput.* **16**, 3959–3969 (2020).
54. Zheng, Y. et al. Structure of CC chemokine receptor 5 with a potent chemokine antagonist reveals mechanisms of chemokine recognition and molecular mimicry by HIV. *Immunity* **46**, 1005–1017.e1005 (2017).
55. Ngo, T. et al. Crosslinking-guided geometry of a complete CXC receptor-chemokine complex and the basis of chemokine subfamily selectivity. *PLoS Biol.* **18**, e3000656 (2020).
56. Kilgore, H. R. & Raines, R. T. n–>pi* interactions modulate the properties of cysteine residues and disulfide bonds in proteins. *J. Am. Chem. Soc.* **140**, 17606–17611 (2018).
57. Giordano, D., Biancaniello, C., Argenio, M. A. & Facchiano, A. Drug design by pharmacophore and virtual screening approach. *Pharm. (Basel)* **15**, 646 (2022).
58. Hruby, V. J. & Cai, M. Design of peptide and peptidomimetic ligands with novel pharmacological activity profiles. *Annu. Rev. Pharm. Toxicol.* **53**, 557–580 (2013).
59. Ganguly, H. K. & Basu, G. Conformational landscape of substituted prolines. *Biophys. Rev.* **12**, 25–39 (2020).
60. Tunyasuvunakool, K. et al. Highly accurate protein structure prediction for the human proteome. *Nature* **596**, 590–596 (2021).
61. Jumper, J. et al. Highly accurate protein structure prediction with AlphaFold. *Nature* **596**, 583–589 (2021).
62. Johansson-Akhe, I. & Wallner, B. Improving peptide-protein docking with AlphaFold-Multimer using forced sampling. *Front. Bioinform.* **2**, 959160 (2022).
63. Zhang, Y. & Sanner, M. F. Docking flexible cyclic peptides with AutoDock CrankPep. *J. Chem. Theory Comput.* **15**, 5161–5168 (2019).
64. Jubb, H. C. et al. Arpeggio: a web server for calculating and visualising interatomic interactions in protein structures. *J. Mol. Biol.* **429**, 365–371 (2017).
65. Li Petri, G., Di Martino, S. & De Rosa, M. Peptidomimetics: an overview of recent medicinal chemistry efforts toward the discovery of novel small molecule inhibitors. *J. Medicinal Chem.* **65**, 7438–7475 (2022).
66. Fowler, D. M. & Fields, S. Deep mutational scanning: a new style of protein science. *Nat. Methods* **11**, 801–807 (2014).
67. Ning, L., He, B., Zhou, P., Derda, R. & Huang, J. Molecular design of peptide-Fc fusion drugs. *Curr. Drug Metab.* **20**, 203–208 (2019).
68. Lavi, O. Redundancy: a critical obstacle to improving cancer therapy. *Cancer Res.* **75**, 808–812 (2015).
69. Aricescu, A. R., Lu, W. & Jones, E. Y. A time- and cost-efficient system for high-level protein production in mammalian cells. *Acta Crystallogr. D: Biol. Crystallogr.* **62**, 1243–1250 (2006).
70. Frei, J. C. & Lai, J. R. Protein and antibody engineering by phage display. *Methods Enzymol.* **580**, 45–87 (2016).
71. Miersch, S. et al. Scalable high throughput selection from phage-displayed synthetic antibody libraries. *J. Vis. Exp.* **17**, 51492 (2015).
72. Grant, B. J., Skjaerven, L. & Yao, X. Q. The Bio3D packages for structural bioinformatics. *Protein Sci.* **30**, 20–30 (2021).

73. Dunnett, C. W. A multiple comparison procedure for comparing several treatments with a control. *J. Am. Stat. Assoc.* **50**, 1096–1121 (1955).
74. Ritz, C. *Dose-response Analysis Using R* (CRC Press, Taylor & Francis Group, 2020).
75. Cianfrocco, M. A., Wong-Barnum, M., Youn, C., Wahgner, R. & Leschziner, A. COSMIC2: A Science Gateway for Cryo-Electron Microscopy Structure Determination. In: *PEARC17: Proceedings of the Practice and Experience in Advanced Research Computing 2017 on Sustainability, Success and Impact* 1–5 (2017). https://doi.org/10.1145/3093338.3093390.
76. van Zundert, G. C. P. et al. The HADDOCK2.2 web server: user-friendly integrative modeling of biomolecular complexes. *J. Mol. Biol.* **428**, 720–725 (2016).
77. Leman, J. K. et al. Macromolecular modeling and design in Rosetta: recent methods and frameworks. *Nat. Methods* **17**, 665–680 (2020).
78. Stranges, P. B. & Kuhlman, B. A comparison of successful and failed protein interface designs highlights the challenges of designing buried hydrogen bonds. *Protein Sci.* **22**, 74–82 (2013).
79. Alford, R. F. et al. The Rosetta all-atom energy function for macromolecular modeling and design. *J. Chem. Theory Comput.* **13**, 3031–3048 (2017).

Acknowledgements

This research was funded by British Heart Foundation Chair Award (CH/09/003/26631), BHF Program Grant (RG/18/1/33351), Oxford BHF Regenerative Medicine Award (RM/17/2/33380) and Oxford BHF Centre of Research Excellence (RE/13/1/30181) Awards to S.B. M.P. is funded by a studentship from the Radcliffe Department of Medicine and the Clarendon Scholarship Fund and CC by a studentship from the Wellcome Programme in Genomic Medicine and Statistics. S.D. is funded by a Rubicon Fellowship from NWO. C.O. is supported by the Engineering and Physical Sciences Research Council through a postdoctoral fellowship (EP/W522582/1), and by Schmidt Futures through an Eric and Wendy Schmidt AI in Science Postdoctoral Fellowship. The research on the BMRC Cluster was supported by the Wellcome Trust Core Award Grant Number 203141/Z/16/Z with additional support from the NIHR Oxford BRC. The views expressed are those of the author(s) and not necessarily those of the NHS, the NIHR or the Department of Health. The authors are grateful to Prof. Ingrid Dijkgraaf (Maastricht) for kindly making available PDB files from previously published[28] NMR/HADDOCK analysis.

Author contributions

Phage-display and mutant libraries were designed by S.B. and constructed by G.D., K.H. and J.K. Phage-display screens were performed by K.H., S.V. and J.K. NextGen sequencing data analysis was performed by S.B. BLI was performed by S.C. The cell lines J:CXCR1 and ATC were generated by G.S. and M.P., respectively. Chemotaxis assays were performed by S.V., M.P., J.K., P.M. and G.S. S.D. synthesised peptides. S.B. performed bioinformatic and statistical analyses. Computational modelling was performed by C.C., S.D. and S.B. with advice from G.M., C.O., and C.D. on establishing the modelling pipeline. S.B., G.D., and G.M. supervised and interpreted experiments and modelling outputs. All authors contributed to writing the manuscript.

Competing interests

The authors declare no competing interests.

Additional information

Supplementary information The online version contains supplementary material available at https://doi.org/10.1038/s41467-023-41488-z.

Correspondence and requests for materials should be addressed to Shoumo Bhattacharya.

Peer review information *Nature Communications* thanks the anonymous reviewers for their contribution to the peer review of this work. A peer review file is available.

Reprints and permissions information is available at http://www.nature.com/reprints

Publisher's note Springer Nature remains neutral with regard to jurisdictional claims in published maps and institutional affiliations.

Open Access This article is licensed under a Creative Commons Attribution 4.0 International License, which permits use, sharing, adaptation, distribution and reproduction in any medium or format, as long as you give appropriate credit to the original author(s) and the source, provide a link to the Creative Commons license, and indicate if changes were made. The images or other third party material in this article are included in the article's Creative Commons license, unless indicated otherwise in a credit line to the material. If material is not included in the article's Creative Commons license and your intended use is not permitted by statutory regulation or exceeds the permitted use, you will need to obtain permission directly from the copyright holder. To view a copy of this license, visit http://creativecommons.org/licenses/by/4.0/.

© The Author(s) 2023